2010

Modeling Springback in Stamped Automotive Structures

Abbas Ghaei
University of Windsor

Follow this and additional works at: https://scholar.uwindsor.ca/etd

MODELING SPRINGBACK IN STAMPED AUTOMOTIVE STRUCTURES

by

Abbas Ghaei

A Dissertation
Submitted to the Faculty of Graduate Studies
through Mechanical, Automotive & Materials Engineering
in Partial Fulfillment of the Requirements for
the Degree of Doctor of Philosophy at the
University of Windsor

Windsor, Ontario, Canada

2009

Modeling Springback in Stamped Automotive Structures

by

Abbas Ghaei

APPROVED BY:

_____

Dr. M. Jain, External Examiner
McMaster University

_____

Dr. F. Ghrib
Department of Civil and Environmental Engineering

_____

Dr. N. Zamani
Department of Mechanical, Automotive & Materials Engineering

_____

Dr. W. Altenhof
Department of Mechanical, Automotive & Materials Engineering

_____

Dr. D. Green, Advisor
Department of Mechanical, Automotive & Materials Engineering

_____

Dr. H. Wu, Chair of Defense
Department of Mechanical, Automotive & Materials Engineering

11 November 2009

Declaration of Previous Publication

This dissertation includes three original papers that have been previously published/submitted for publication in peer reviewed journals, as follows:

Thesis Chapter	Publication title/full citation	Publication status
Chapter 3	Semi-implicit Numerical Integration of Yoshida-Uemori Two-Surface Plasticity Model, International Journal of Mechanical Sciences.	Submitted
Chapter 4	Numerical Implementation of Yoshida-Uemori Two-Surface Plasticity Model Using a Fully-Implicit Integration Scheme, Computational Materials Science.	Submitted

I certify that I have obtained a written permission from the copyright owner(s) to include the above published material(s) in my dissertation. I certify that the above material describes work completed during my registration as graduate student at the University of Windsor.

I declare that, to the best of my knowledge, my dissertation does not infringe upon anyone's copyright nor violate any proprietary rights and that any ideas, techniques, quotations, or any other material from the work of other people included in my dissertation, published or otherwise, are fully acknowledged in accordance with the standard referencing practices. Furthermore, to the extent that I have included copyrighted material that surpasses the bounds of fair dealing within the meaning of the Canada Copyright Act, I certify that I have obtained a written permission from the copyright owner(s) to include such material(s) in my dissertation.

I declare that this is a true copy of my dissertation, including any final revisions, as approved by my dissertation committee and the Graduate Studies office, and that this dissertation has not been submitted for a higher degree to any other University or Institution.

ABSTRACT

In sheet metal forming, the discrepancy between the fully loaded shape at the end of forming stage and the unloaded configuration is called springback. Springback is a major factor in preventing accurate dimensions of final products. Therefore, it is very important that springback be quantitatively predicted and compensated in the die design stage.

In sheet metal stamping, especially when drawbead is used, the material experiences several cycles of bending-unbending-reverse bending. Therefore, in to order to accurately predict springback, the constitutive model must be able to accurately describe the material behaviour during cyclic loading. Yoshida-Uemori (YU) two-surface model is one of the most sophisticated models which is capable of reproducing the transient Bauschinger effect, permanent softening and workhardening stagnation.

In this work, two different yield functions, i.e. Hill's 1948 and Yld 2000-2d, were used in conjunction with YU two-surface model. Moreover, two different numerical procedures were developed for numerical implementation of these models: a) a semi-implicit approach and b) a fully-implicit approach. The numerical procedures were used to develop user material subroutines for ABAQUS commercial software. Then, the subroutines were used to evaluate the capability of the model in prediction of springback for a channel draw process. In addition, the isotopic hardening (IH) and combined isotropic-nonlinear kinematic hardening (IH+NKH) models were also used to predict the springback of the problem. Finally, the springback profiles obtained by each model were compared with the experimental data. For DP600, the error in springback prediction is around 3% when YU model is used. For HSLA and AA6022, the error associated with YU model is less than 3% and 13% at 25% and 100% drawbead penetrations, respectively. The YU model does not predict the springback accurately for AKDQ and the error is around 30%. The results also show that the IH model overestimates the springback for all materials. For DP600 and AA6022, the results obtained by IH+NKH

model are the same as those obtained by YU model. However, the YU model considerably improves the springback prediction compared to IH+NKH model for HSLA; while for AKDQ the IH+NKH model improves the springback prediction compared to YU model.

Dedicated to my parents and wife

Acknowledgements

This research project would not have been possible without the support of many people. I wish to express my gratitude to my advisor, Dr. Daniel Green who was abundantly helpful and offered invaluable assistance, support and guidance. It was a great opportunity for me to learn from his knowledge and experience.

I would also like to thank the dissertation committee members, Dr. Ghrib, Dr. Zamani and Dr. Altenhof for providing constructive comments and valuable suggestions.

The intellectual discussions with Dr. J.W. Yoon and Dr. Aboozar Taherizadeh are also appreciated.

I also wish to express my love and gratitude to my beloved family, especially my wife for her understanding and endless love through the duration of this research.

Finally, I would like to express my sincere gratitude to the following individuals and organizations:

- Professor Wagoner and Piao Kun of Ohio State University for carrying out the uniaxial tension-compression cyclic tests.
- Professor Thuillier at the Université de Bretagne-Sud, in France for carrying out the experimental cyclic simple shear tests.
- Industrial Research & Development Institute (IRDI) in Midland, Ontario for carrying out the NumiSheet 2005 Benchmark #3 channel draw tests
- General Motors of Canada for sponsoring the NumiSheet 2005 Benchmark #3 channel draw tests.
- Dr. Reid for carrying out the twist compression tests at IRDI on the NumiSheet 2005 Benchmark lubricants.

Table of Contents

Chapters:

1. Springback

2. Constitutive Model

3. **Semi-implicit Numerical Integration of Yoshida-Uemori Two-Surface Plasticity Model**

List of Tables

List of Figures

xvi

List of Appendices

Chapter 1

Springback

1.1. Introduction:

Once a deformed sheet-metal part is removed from the dies in which it was formed, the elastic component of strain is recovered, especially where bending, bending-unbending, and reverse bending are performed. The elastic recovery is accompanied by strain and consequently causes the final shape of the part to change. The discrepancy between the fully loaded shape at the end of the forming stage and the unloaded configuration is called springback. This phenomenon can also be explained on the stress-strain curve as shown in Fig. 1.1. Unloading (by removing all external forces and moments) from a total strain A would follow line AB, and segment OB would represent the permanent (plastic) deformation and BC the recovered (elastic) deformation. It can also be observed that the elastic recovery is greater for materials with higher strength. Springback is the most significant factor that makes it difficult to achieve the required dimensional accuracy of stamped components. Designing a die with incorrect springback compensation can lead to significant difficulties in downstream operations such as poor fit-up during welding and distortion of sub-assemblies. In some cases, tooling revisions may be required which could lead to delays in production. Therefore, it is very important that springback be accurately predicted and correctly compensated during the first die design.
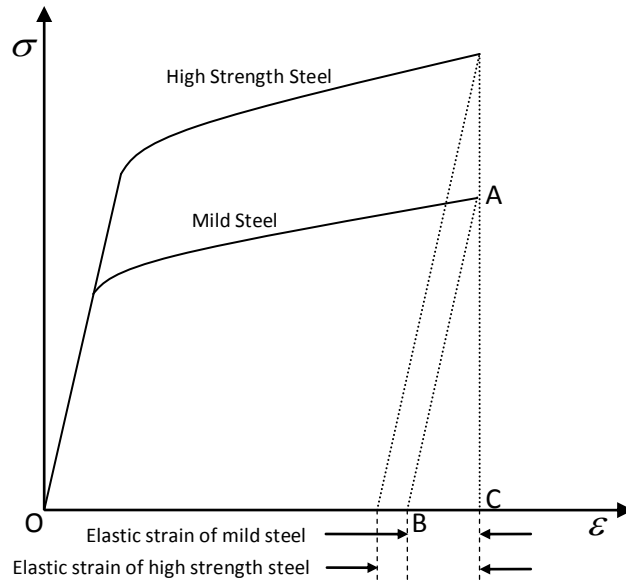
Fig. 1.1. Elastic recovery deformation during unloading

Springback after forming sheet steel can be classified in six categories:

1. **Sidewall opening**: The angle forming two sides enclosing a bending edge line deviates from the die angle (Fig. 1.2.a).
2. **Sidewall Curl**: The straight side wall becomes curved (Fig. 1.2.b).
3. **Edge line warping or bow**: The bending edge line deviates in curvature from the edge line of the die (Fig. 1.2.c).
4. **Twist**: Two neighbouring cross-sections rotate differently along their axis.
5. **Global shape change**: The desired shape of the part is not achieved after it is removed from the tooling.
6. **Surface distortion**: Local buckling occurs on the surface of a body panel after forming.
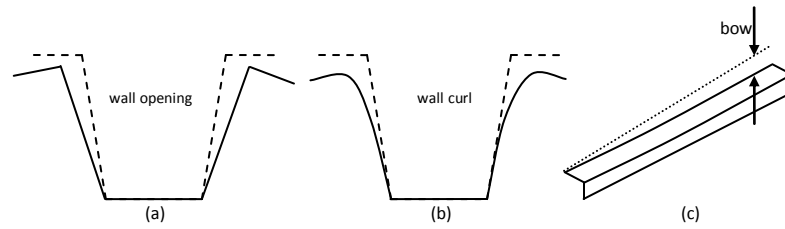
Fig. 1.2. Different types of springback

1.2. Springback Compensation:

Several approaches have been proposed to control springback. Most of them attempt to reduce springback by increasing the tension in the sheet. This can be achieved by increasing the blankholder force, especially at the end of the forming stage or by using drawbeads [1-6]. In general, a larger tension in the sidewall reduces the stress gradient through the sheet thickness causing less springback. However, the maximum tension in the sheet is limited by the fracture strength of the sheet material. Moreover this stretch-forming technique is generally not sufficient to eliminate springback. Some studies also suggest using a variable blank holder force during the punch trajectory. In this method, the blank holder force is low from the beginning until almost the end of the forming process and then it is increased at end of the process such that a large tensile stress is applied to the sheet material [5].

Another approach is to compensate for springback at the die design stage [7-8]. That is, regardless of what the springback might be, the die is designed so that the final part shape after springback corresponds to the target part shape. For instance, the ratio of tool radius to sheet thickness (R/t) is a design parameter which affects springback and can be modified to reduce it [9-10]. The first step in implementing such a strategy is the accurate prediction of the springback phenomenon. Assuming that springback can be predicted accurately, there still remains the problem of how to use such results to arrive at a suitable die design to produce a target part shape. That is, the springback predictions

3

allow "forward" analysis of forming and springback, while a "backward" analysis is needed to work from these results back toward an optimized die design. It is clear that a method is needed for guiding die design to compensate for springback (in a backward direction) using sophisticated springback prediction capabilities (forward direction). Such a development was reported by Karafillis and Boyce [8,11,12]. However, Gan and Wagoner [7] showed that this method suffers from a lack of convergence unless the forming operation is symmetric or has very limited geometric change during springback. They developed an alternate closed-loop design method that avoided many of the limitations of the Karafillis and Boyce model. They developed a displacement adjustment method that used simulated forming and springback displacements in the punch travel direction to predict the next die design iteration. They used their method for several arbitrary two-dimensional examples and showed that the advantages of their model were the convergence rate, the ease of implementation, and its general framework.

1.3. Prediction of Springback:

As mentioned in the previous section, in order to compensate for springback, it is necessary to quantitatively predict springback during the first die design stage. Generally, two methods are used for prediction of springback: analytical methods and numerical methods. Both types of methods have been extensively employed by researchers and die designers.

Several analytical solutions have been proposed for prediction of springback. Buranathiti and Cao [13] performed an analytical springback prediction of a straight flanging process by calculating the bending moment under plane-strain conditions. They used the model to predict springback for a few parts and compared the predicted results with experimental data. Yi *et al*. [14] developed an analytical model based on differential strains after relief from the maximum bending stress for six different deformation patterns. They used each deformation pattern to estimate springback by the residual

4

differential strains between outer and inner surfaces after elastic recovery. Zhang *et al*. [15] also developed an analytical model to predict springback in sheets bent in a U-die under plane-strain conditions. They used Hill's 1948 yield function and took into account the effects of deformation history, the evolution of sheet thickness and the shifting of the neutral surface. Lee *et al*. [16] proposed an analytical model for asymmetric elasto-plastic bending under tension followed by elastic unloading. They also compared the calculated springback amounts with the results of physical measurements and showed that their model predicted the main trends of the springback in magnesium alloy sheets reasonably well considering the simplicity of the analytical approach.

Although the use of analytical models is advantageous because of their simplicity, the application of these models is limited to simple geometries. The amount of springback also depends upon many process variables such as friction, temperature, variations in the thickness and mechanical properties of the incoming sheet material. Moreover, complex strain histories and highly nonlinear deformation of the material during the forming process add to the difficulty of predicting springback. Therefore, the most widely used method of predicting springback is to carry out computer simulations that rely on advanced material models to compute the stress distribution in the part and the final geometry of the part after elastic unloading. And most researchers have used the finite element method to predict springback.

Finite element (FE) simulation of springback is very sensitive to numerical parameters such as element type, mesh size as well as to the constitutive model that governs the behaviour of the deformable sheet. Several investigations have been conducted to study the effect of numerical parameters on the accuracy of the predicted profile after springback. Li *et al*. [17] simulated the draw-bend test and studied the sensitivity of the simulated springback to numerical parameters. They found that up to 51 integration points are required for an accurate simulation of springback. They also concluded that for small *R/t* ratios, nonlinear 3D solid elements are required for an accurate prediction of springback. Wagoner and Li [18] later performed an analytical study of the bending under tension followed by springback. They also performed a numerical analysis of this

problem and calculated the relative error as a function of number of integration points (NIP). They concluded that the relative error oscillates and in some cases even more than 51 integration points are required. Lee *et al.* [19] used the Taguchi method to study numerical factors affecting springback after the U-bending draw test in which drawbeads were not used. They determined the order of significance of each numerical parameter relative to its effect on the prediction of springback angle and radius of curvature. The results of their study show that the mesh size has the strongest effect on the accuracy of springback prediction. Mattiasson *et al*. [20] also found that springback simulation is much more sensitive to numerical tolerances than the simulation of the forming stage.

It is also worth mentioning that some researchers have used a combination of an analytical method and the finite element method to predict springback. These methods usually endeavour to use the advantages of each approach. Zhan *et al.* [21] developed a method based on springback angle model derived using an analytical method and simulation results from three-dimensional (3D) rigid-plastic finite element method (FEM). Lee *et al.* [22] proposed a simplified numerical procedure to predict springback in a 2D draw bend test that was developed based on a hybrid method which superposes bending effects onto membrane element formulation. This approach was shown to be especially useful to analyze the effects of various process and material parameters on springback.

1.4. Constitutive Model:

The accuracy of sheet metal forming and springback simulation depends not only on the forming conditions (friction, tool and binder geometry etc.), but also on the choice of the material constitutive model and its numerical implementation into finite element programs. Among these factors, the material constitutive law plays an important role in describing the mechanical behaviour of sheet metals, because it is essential to obtain an accurate stress distribution in a formed part if springback is to be correctly predicted. In

general, the behaviour of metals is quite complex, especially during the cyclic loading. So, an advanced constitutive model is usually required for an accurate prediction of springback. The importance of constitutive model will be further explained in the next chapter.

1.5. Motivations:

Springback has been one on the major concerns in sheet metal forming for decades. To reduce the weight of cars, the automotive industry is moving towards high strength materials that have a much lower weight-to-strength ratio than traditional steels. But as mentioned in section 1.1, the springback is generally larger for higher strength materials. Besides, the higher strength materials usually exhibit a larger Bauschinger effect which makes modelling of this phenomenon more important. The main purpose of this project is to implement advanced constitutive models into the finite element method and evaluate their ability to predict springback. For evaluation purposes, a channel draw process with drawbeads, presented as Benchmark #3 (BM3) in NumiSheet 2005 [23], was simulated using three different hardening models: isotropic hardening, nonlinear kinematic hardening and the Yoshida-Uemori two-surface plasticity model. The profile of the part after springback was predicted using each of these models and was compared with experimental profiles.

Chapter 2

Constitutive Model

2.1. Introduction:

Finite element analysis is the most commonly used method to simulate industrial sheet metal forming processes in order to assess forming severity, to improve the tooling design, and to predict springback. The accuracy of sheet metal forming and springback simulation depends not only on the forming conditions (friction, tool and binder geometry), but also on the choice of material constitutive model and their numerical implementations into a finite element program. Among these factors, the material constitutive law plays an important role in describing the mechanical behaviour of sheet metals, because it determines the accuracy of the stress distribution in a formed part and the subsequent springback. In sheet metal forming, the material commonly experiences bending, unbending and unloading over the die and punch radii and sometimes multiple bending-unbending cycles when it is formed through a drawbead. Cyclic loading paths have significant effects on stress and residual stress distributions, which are important in springback calculation. Accurate simulation of sheet metal forming requires an appropriate constitutive model that can effectively describe different phenomena usually observed in cyclic plasticity such as Bauschinger effect, a decrease in Young's modulus during unloading, permanent softening and so on. Moreover, sheet metal forming is a typical large-strain problem, and the springback is a process of small-scale re-yielding after large prestrain. Therefore, attention should be paid to the deformation behaviour of

large-strain cyclic plasticity and also the stress–strain responses at small-scale re-yielding after large prestrain.

Phenomenological constitutive models consist of three essential components: (1) a yield criterion, (2) a flow rule, (3) a strain-hardening rule. The yield criterion determines the stress state when yielding occurs; the flow rule describes the increment of plastic strain when yielding occurs; the hardening rule describes how the material is strain-hardened as the plastic strain increases; and the loading–unloading conditions specify the next step in the loading program. In this chapter, the notation and conventions used in this dissertation will be first explained and then the major components of a constitutive model will be introduced.

2.2. Notation and Conventions:

In this dissertation, scalars are shown by a lowercase letter, e.g. a, vectors and second-order tensor are expressed by a bold-faced lowercase letter (e.g. $\boldsymbol{a}$), and a fourth-order tensor is shown by a bold-faced capital letter (e.g. $\boldsymbol{A}$). In the index notation, the components of a second-order and a fourth-order tensor are denoted by $\boldsymbol{a}_{ij}$ and $\boldsymbol{T}_{ijkl}$ respectively. It should be noted that a second-order tensor has two subscripts and a fourth-order tensor has four subscripts. Summation and range conventions are used in the index notation. In the summation convention, a repeated index means summation of the term over the range of the index. For example, $\boldsymbol{A}_{kk} = \boldsymbol{A}_{11} + \boldsymbol{A}_{22} + \boldsymbol{A}_{33}$, if the range of the index is from 1 to 3. On the other hand, if the range of the index is from 1 to n, then $\boldsymbol{A}_{kk} = \boldsymbol{A}_{11} + \boldsymbol{A}_{22} + \cdots + \boldsymbol{A}_{nn}$, a sum of n terms. Note that the subscript n does not imply summation, and the index should not repeat more than once. The notation $\boldsymbol{A}_{kkk}$, for instance, is not defined. The repeated index k is called a dummy index because it can be replaced by another index with no difference in its outcome. For example, $\boldsymbol{A}_{kk} = \boldsymbol{A}_{ii} = \boldsymbol{A}_{jj} = \boldsymbol{A}_{11} + \boldsymbol{A}_{22} + \boldsymbol{A}_{33}$ [24].

The dot product of two second-order tensors is a scalar which is defined by the following relationship:

$$
\begin{aligned}
\boldsymbol{a} : \boldsymbol{b} = \boldsymbol{a}_{ij}\,\boldsymbol{b}_{ij} = \; & \boldsymbol{a}_{11}\boldsymbol{b}_{11} + \boldsymbol{a}_{12}\boldsymbol{b}_{12} + \boldsymbol{a}_{13}\boldsymbol{b}_{13} + \\
& \boldsymbol{a}_{21}\boldsymbol{b}_{21} + \boldsymbol{a}_{22}\boldsymbol{b}_{22} + \boldsymbol{a}_{23}\boldsymbol{b}_{23} + \\
& \boldsymbol{a}_{31}\boldsymbol{b}_{31} + \boldsymbol{a}_{32}\boldsymbol{b}_{32} + \boldsymbol{a}_{33}\boldsymbol{b}_{33}
\end{aligned}
\tag{2.1}
$$

The dyadic product of two vectors is a second-order tensor which is defined by the following relationship:

$$
\boldsymbol{a} \otimes \boldsymbol{b} = \boldsymbol{a}_i\,\boldsymbol{b}_j = \begin{bmatrix} \boldsymbol{a}_1\boldsymbol{b}_1 & \boldsymbol{a}_1\boldsymbol{b}_2 & \boldsymbol{a}_1\boldsymbol{b}_3 \\ \boldsymbol{a}_2\boldsymbol{b}_1 & \boldsymbol{a}_2\boldsymbol{b}_2 & \boldsymbol{a}_2\boldsymbol{b}_3 \\ \boldsymbol{a}_3\boldsymbol{b}_1 & \boldsymbol{a}_3\boldsymbol{b}_2 & \boldsymbol{a}_3\boldsymbol{b}_3 \end{bmatrix}
\tag{2.2}
$$

The transpose of a tensor is shown by $\boldsymbol{a}^T$ and is defined as follows:

$$
(\boldsymbol{a}_{ij})^T = \boldsymbol{a}_{ji}
\tag{2.3}
$$

2.3. Flow Rule:

The flow rule specifies the increment of plastic strain once the material has yielded. In general, it is assumed that plastic strain increment is obtained by differentiation of a plastic potential function as follows:

$$
d\boldsymbol{\varepsilon}^p = d\lambda \frac{\partial \Phi}{\partial \boldsymbol{\sigma}}
\tag{2.4}
$$

where $d\boldsymbol{\varepsilon}^p$ is the plastic strain increment, Φ is a potential function, $\boldsymbol{\sigma}$ is the stress tensor and $d\lambda$ is the scalar proportionality factor or plastic multiplier. If the potential function is assumed to be the same as the yield function, f, then the following relationship is obtained:

$$
d\boldsymbol{\varepsilon}^p = d\lambda \frac{\partial f}{\partial \boldsymbol{\sigma}}
\tag{2.5}
$$

The above equation states that the plastic strain increment is proportional to the gradient of the yield surface and is, therefore, normal to the yield surface. This is usually referred to as the normality condition. A flow rule obeying the normality condition is referred to as the associated flow rule. However, if any function other than the yield function is used as the potential function in Eq. (2.4), the plastic strain increment will not be normal to the yield surface. This theory is known as the non-associated flow rule which is mostly used for geotechnical materials. It is widely accepted that the associated flow rule works well for most of metals [24, 25].

2.4. Yield Criterion:

The yield stress σ_y is shown in the one-dimensional stress–strain curve of Fig. 2.1. According to this figure, the material behaves elastically if the applied stress is less than σ_y. However, as soon as the stress reaches σ_y plastic yielding occurs, which is called initial yielding. Therefore, the condition $\bar{\sigma} = \sigma_y$ is the yield criterion. The yield criterion defines the elastic region in the stress space (the stress axis in this one-dimensional case). When $\bar{\sigma} > \sigma_y$, which corresponds, for instance, to curve ABE in Fig. 2.1, the material undergoes strain-hardening, and the material is subjected to subsequent yielding. Generally, a yield criterion should be able to determine the elastic region in a multidimensional stress space. In principal three-dimensional stress space $(\sigma_1, \sigma_2, \sigma_3)$, an infinite number of yield points form a yield surface. In the nine-dimensional stress space $\boldsymbol{\sigma}_{ij}$ is represented by a hyper-surface shown in Figure 2.2. The yield surface is a function of stress so that the following conditions apply [24]:

$$
\begin{aligned}
f(\sigma_{ij}) &= 0 \qquad \text{plastic state} \\
f(\sigma_{ij}) &< 0 \qquad \text{elastic state} \\
f(\sigma_{ij}) &> 0 \qquad \text{impossible}
\end{aligned}
\tag{2.6}
$$

Many yield functions have been developed for different materials and applications in plasticity. In the next section, some of the commonly used yield functions in sheet metal forming are introduced.
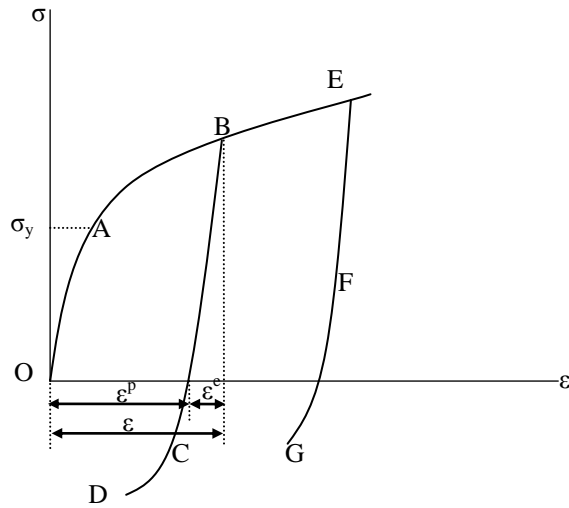
Fig. 2.1. The Schematic stress–strain curve [24]
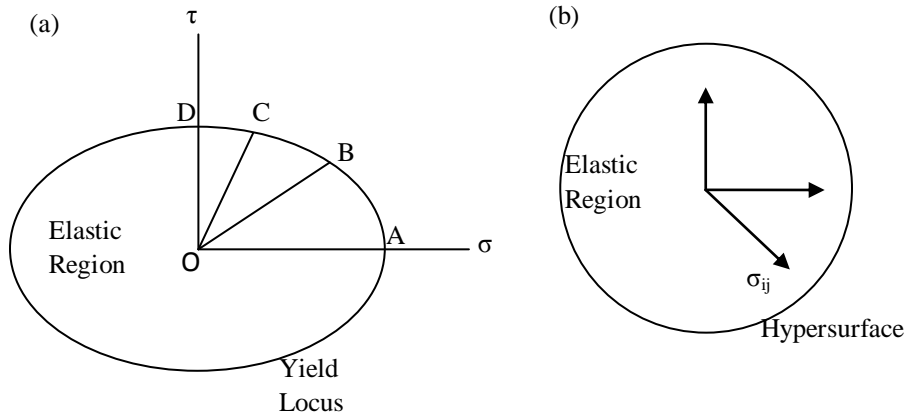
Fig. 2.2. (a) Yield locus in a two-dimensional stress space and (b) yield surface in the nine-dimensional stress space [24]

2.4.1. Maximum shear stress criterion:

The maximum shear stress criterion, also known as Tresca's criterion, is often used to predict the yielding of ductile materials. Yield in ductile materials is usually caused by the slippage of crystal planes along the maximum shear stress surface. With respect to 2D stress, the maximum shear stress is related to the difference in the two principal stresses. Therefore, this criterion requires the principal stress difference, along with the principal stresses themselves, to be equal to the yield shear stress:

$$\text{Max} \left[\frac{1}{2}|\sigma_1 - \sigma_2|, \frac{1}{2}|\sigma_2 - \sigma_3|, \frac{1}{2}|\sigma_1 - \sigma_3| \right] - k = 0 \tag{2.7}$$

where σ_1, σ_2, σ_3 are the principal stresses and k is the yield shear stress. According to this function, the uniaxial yield stress is equal to half of the yield shear stress. It should be noted that this yield function assumes the material is isotropic.
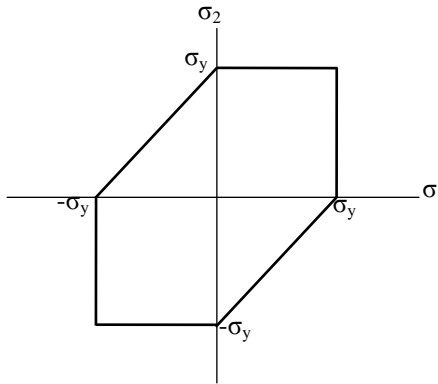
Fig. 2.3. Graphical representation of Tresca's yield function in a two-dimensional stress space

2.4.2. von Mises criterion:

The von Mises Criterion (1913), also known as the maximum distortion energy criterion, or octahedral shear stress theory, is often used to estimate the yield of isotropic ductile materials. The von Mises criterion states that failure occurs when the energy of

distortion reaches the same energy for yield/failure in uniaxial tension. Mathematically, this is expressed as follows:

$$\frac{1}{2}[(\sigma_1 - \sigma_2)^2 + (\sigma_1 - \sigma_3)^2 + (\sigma_2 - \sigma_3)^2] - \sigma_y{}^2 = 0 \qquad (2.8)$$

where σ_1, σ_2, σ_3 are the principal stresses and σ_y is the yield stress. A geometrical representation of this function in a 2D stress space is shown in Fig. 2.4.
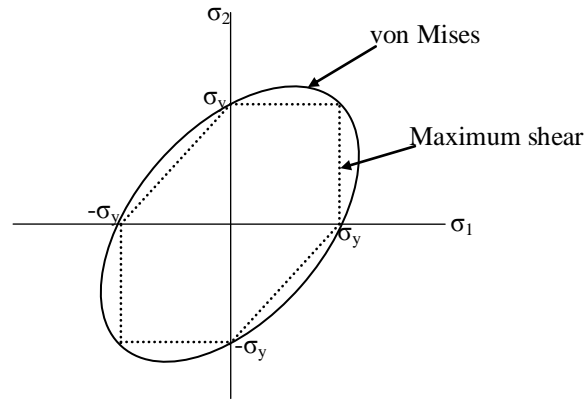
Fig. 2.4. Geometrical representation of Tresca and von Mises yield functions in a two-dimensional stress space

2.4.3. *Hosford's isotropic yield criterion:*

Hosford's [26] yield criterion for isotropic materials is a generalization of the von Mises yield criterion. It has the form:

$$\frac{1}{2}|\sigma_1 - \sigma_2|^n + \frac{1}{2}|\sigma_1 - \sigma_3|^n + \frac{1}{2}|\sigma_2 - \sigma_3|^n - \sigma_y^n = 0 \qquad (2.9)$$

where σ_1, σ_2, σ_3 are the principal stresses, n is a material-dependent exponent and σ_y is the yield stress. The exponent n does not need to be an integer. When $n = 1$ the criterion reduces to the Tresca yield criterion. When $n = 2$ the Hosford criterion reduces to the von

Mises yield criterion. For *n* = 6 and 8, this function fits closely to the experimental yield locus of BCC and FCC materials, respectively.
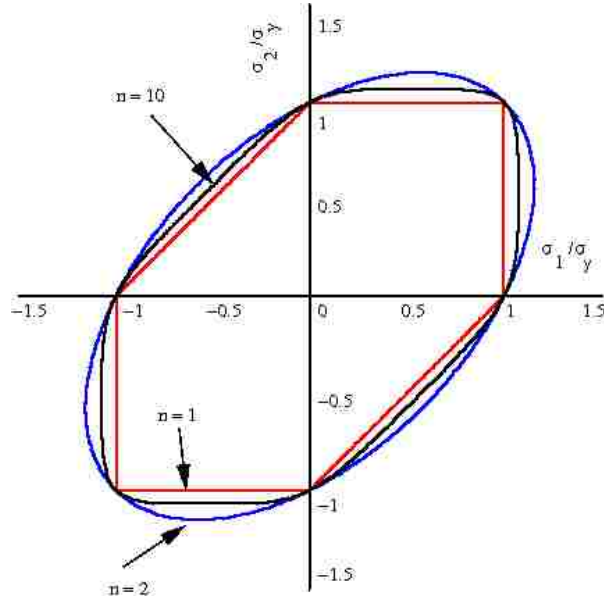
Fig. 2.5. Geometrical illustration of Hosford's isotopic yield functions in a two-dimensional stress space

2.4.4. Hill's quadratic yield criterion:

In 1948, Hill proposed an anisotropic yield criterion as a generalization of the von Mises criterion. It was assumed that the material has anisotropy with three orthogonal symmetry planes (for sheet metal). This function was defined by Hill [27] as follows:

$$
\frac{1}{2}\Big[F\big(\sigma_{yy} - \sigma_{zz}\big)^2 + G(\sigma_{zz} - \sigma_{xx})^2 + H\big(\sigma_{xx} - \sigma_{yy}\big)^2 \\
+ \ 2\big(L\sigma_{xy}{}^2 + I\sigma_{yz}{}^2 + K\sigma_{zx}{}^2\big) - 1\Big] = 0
\tag{2.10}
$$

where F, G, H, L, I and K are all material constants obtained by tests of material in different orientations. Using matrix notation, this function can be written as [28]:

$$\frac{3}{2}\boldsymbol{\sigma}^T \boldsymbol{N} \boldsymbol{\sigma} - \sigma_y{}^2 = 0 \tag{2.11a}$$

where $\boldsymbol{N}$ is a fourth order anisotropic tensor, σ_y is the yield stress, and $\boldsymbol{\sigma}$ is the stress tensor. The dimensionless coefficients of $\boldsymbol{N}$ are related to the coefficients of $F, G, .., K$ according to the following matrix:

$$\boldsymbol{N} = \begin{bmatrix} N_1 + N_2 & -N_1 & -N_2 & 0 & 0 & 0 \\ & N_1 + N_3 & -N_3 & 0 & 0 & 0 \\ & & N_2 + N_3 & 0 & 0 & 0 \\ & & & N_4 & 0 & 0 \\ & Sym. & & & N_5 & 0 \\ & & & & & N_6 \end{bmatrix} \tag{2.11b}$$

where

$$N_1 = \frac{2}{3} H \sigma_y^2, \ N_2 = \frac{2}{3} G \sigma_y^2, \ N_3 = \frac{2}{3} F \sigma_y^2, \ N_4 = \frac{2}{3} L \sigma_y^2,$$

$$N_5 = \frac{2}{3} I \sigma_y^2, N_6 = \frac{2}{3} K \sigma_y^2 \tag{2.11c}$$

2.4.5. Logan-Hosford yield criterion:

Logan and Hosford [29] proposed another yield criterion for anisotropic materials based on Hill's generalized yield criterion. This function is written as:

$$F|\sigma_1 - \sigma_2|^n + G|\sigma_1 - \sigma_3|^n + H|\sigma_2 - \sigma_3|^n - 1 = 0 \tag{2.12}$$

where F, G, H are material constants, $\sigma_1, \sigma_2, \sigma_3$ are the principal stresses, and the exponent n depends on the type of crystal (BCC, FCC, HCP, etc.) Accepted values of n are 6 for BCC materials and 8 for FCC materials.

2.4.6. Hill's generalized yield criterion:

In 1979, Hill [30] proposed a generalized form of Hill's quadratic yield function. This function has the following form:

$$F|\sigma_1 - \sigma_2|^m + G|\sigma_1 - \sigma_3|^m + H|\sigma_2 - \sigma_3|^m + L|2\sigma_1 - \sigma_2 - \sigma_3|^m$$
$$+ M|2\sigma_2 - \sigma_1 - \sigma_3|^m + N|2\sigma_3 - \sigma_2 - \sigma_1|^m - \sigma_y{}^m = 0 \qquad (2.13)$$

where σ_1, σ_2, σ_3 are the principal stresses (which are aligned with the directions of anisotropy), σ_y is the yield stress, and F, G, H, L, M, N are material constants. The value of m is determined by the degree of anisotropy of the material and must be greater than 1 to ensure convexity of the yield surface.

2.4.7. Yld2000-2d yield criterion:

In 2003, Barlat et al. [31] proposed a yield criterion for anisotropic materials. This function is usually used for aluminum alloys where the plastic anisotropy coefficients, or r-values, are not well predicted by the previously mentioned functions. This function was designated as Yld2000-2d and is written as follows [31]:

$$\frac{1}{2}(\Phi' + \Phi'') - \sigma_y{}^a = 0 \qquad (2.14a)$$

where a is a material coefficient, σ_y is the yield stress, Φ' and Φ'' are two isotropic functions and are defined as follows:

$$\Phi' = |X'_1 - X'_2|^a \ , \ \Phi'' = |2X''_2 + X''_1|^a + |2X''_2 + X''_1|^a \qquad (2.14b)$$

where X'_1, X'_2 are the principal values of tensor $\boldsymbol{X'}$ and X''_1, X''_2 are the principal values of tensor $\boldsymbol{X''}$. Tensors $\boldsymbol{X'}$ and $\boldsymbol{X''}$ are obtained by linear transformation the stress tensor as follows:

$$X' = L'\sigma \, , X'' = L''\sigma$$

where L' and L'' are related to the anisotropic coefficients of the material by:

$$\begin{bmatrix} L'_{11} \\ L'_{12} \\ L'_{21} \\ L'_{22} \\ L'_{66} \end{bmatrix} = \begin{bmatrix} 2/3 & 0 & 0 \\ -1/3 & 0 & 0 \\ 0 & -1/3 & 0 \\ 0 & 2/3 & 0 \\ 0 & 0 & 1 \end{bmatrix} \begin{bmatrix} \alpha_1 \\ \alpha_2 \\ \alpha_7 \end{bmatrix}$$

$$\begin{bmatrix} L''_{11} \\ L''_{12} \\ L''_{21} \\ L''_{22} \\ L''_{66} \end{bmatrix} = \frac{1}{9} \begin{bmatrix} -2 & 2 & 8 & -2 & 0 \\ 1 & -4 & -4 & 4 & 0 \\ 4 & -4 & -4 & 1 & 0 \\ -2 & 8 & 2 & -2 & 0 \\ 0 & 0 & 0 & 0 & 9 \end{bmatrix} \begin{bmatrix} \alpha_3 \\ \alpha_4 \\ \alpha_5 \\ \alpha_6 \\ \alpha_8 \end{bmatrix}$$

where α_1, α_2, …, α_8 are all material anisotropic coefficients. Generally, eight input data from the material are required to identify these constants. These data include the yield strength and r-value of the sheet in the rolling, transverse, diagonal directions and equibiaxial stress state, i.e. σ_0, σ_{45}, σ_{90}, σ_b, r_0, r_{45}, r_{90}, r_b. If r_b is not known or difficult to obtain, it is also possible to assume that $L''_{12} = L''_{21}$.

2.5. Hardening Rule:

There are three classes of materials: the strain-hardening material, the perfectly plastic material, and the strain-softening material. Generally, metals are strain hardening (or work-hardening) materials and geotechnical materials may exhibit strain-softening under certain conditions. In the multiaxial stress state, strain-hardening is considered in the form of hardening rules for subsequent yield surfaces. It has been observed that the yield surface, upon application of a deformation history, will undergo expansion, distortion, translation, and rotation [24]. In plasticity, the hardening rule is used to describe the material behaviour during the plastic deformation. As mentioned in section 1.4, cyclic

loading is a common type of loading in sheet metal forming. Therefore, in this section, the behaviour of sheet metals during cyclic loading is briefly explained and then the most commonly used hardening models in literature will be introduced.

2.5.1. *The behaviour of sheet metals during cyclic loading:*

The behaviour of metals during cyclic plastic deformation is quite complex. In particular, the behaviour during reverse loading is usually different from the behaviour in forward loading. Experimental cyclic tests, such as uniaxial tension-compression, are required to determine actual material behaviour during cyclic loading. However, it is difficult to carry out uniaxial cyclic tension-compression tests on thin sheet metal specimens because of the tendency for the sheet to buckle in compression. To overcome this problem, many experimental methods have been proposed to render the uniaxial compression of sheet specimens possible. Kuwabara et al. [32] and Boger et al. [33] respectively used fork-shaped dies and flat dies to provide a lateral support for the sheet and prevent its buckling during uniaxial tension-compression tests. Yoshida et al. [34] successfully bonded a few thin sheets of metal to provide support for the sheet during uniaxial compression. Cyclic simple shear tests have also attracted the attention of many researchers as the specimen is not compressed during the test. Miyauchi [35, 36], Genevois [37], Rauch [38] and Barlat et al. [39] have successfully used the simple shear test for reverse loading at large strains. From the experimental cyclic tests on mild and dual-phase steels, the following phenomena have been observed during cyclic plastic deformation of sheet metals [34]:

1. During reverse deformation, the transient Bauschinger deformation, characterized by an early re-yielding and smooth elastic–plastic transition with a rapid change of workhardening rate, is followed by the plastic deformation with an apparent permanent softening.

19

2. For the mild steel sheet, abnormal shapes of reverse stress–strain curves appear due to the workhardening stagnation which is caused by dissolution of dislocation cell walls during reverse loading

3. Cyclic stress amplitudes strongly depend on cyclic strain ranges, as well as the mean strains. The larger the strain ranges, the larger the saturated stress amplitudes.

4. Young's modulus decreases during unloading as the plastic strain increases and finally saturates to a particular value after a large amount of plastics strain.

A schematic illustration of the stress-strain response of sheet metals during uniaxial tension-compression test is shown in Fig. 2.6 [40]. This figure illustrates some of the phenomena that occur during cyclic deformation and that become more significant at large deformations.

2.5.2. Isotropic hardening:

Many metals, when deformed plastically, harden; that is, the stress required to cause further plastic deformation increases, often as a function of accumulated plastic strain. A uniaxial stress–strain curve with non-linear hardening is shown in Fig. 2.7 together with schematic representations of the initial and subsequent yield surfaces. In this instance, the subsequent yield surface is shown expanded compared with the original. When the expansion is uniform in all directions in stress space, the hardening is referred to as *isotropic*. In Fig. 2.7, loading is in the 2-direction, so the load point moves in the σ_2 direction from zero until it meets the initial yield surface at $\sigma_2 = \sigma_y$. Yield occurs at this point. In order for hardening to take place, and for the load point to stay on the yield surface (the consistency condition requires this), the yield surface must expand as σ_2 increases, shown in Fig. 2.7. The amount of expansion is often taken to be a function of accumulated plastic strain. So many functions have been proposed for the amount of expansion of the yield surface as a function of plastic strain. For the isotropic hardening, the yield function equation is written as:

$$f(\sigma, p) = \bar{\sigma} - \sigma_y(p) = 0 \tag{2.15}$$

where $\bar{\sigma}$ is the effective stress, p is the accumulated effective plastic strain, and $\sigma_y(p)$ is the yield stress which might be of the form :

$$\sigma_y(p) = \sigma_{y0} + r(p) \tag{2.16}$$

in which σ_{y0} is the initial yield stress and $r(p)$ is called the isotropic hardening function. There are many forms used for $r(p)$ but a common one is:

$$\dot{r}(p) = b(Q - r)\dot{p} \tag{2.17}$$

where b and Q are material constants, which gives an exponential shape to the uniaxial stress–strain curve which saturates with increasing plastic strain, since integrating Eq. (2.17) with initial condition $r(0) = 0$ gives:

$$r(p) = Q(1 - e^{-bp}) \tag{2.18}$$

So, Q is the saturated value of r so that the peak stress achieved with this kind of hardening, from Eq. (2.16), is therefore $(\sigma_{y0} + Q)$. Constant b determines the rate at which saturation is achieved. Fig. 2.7 shows an example of the uniaxial stress–strain behaviour predicted using this kind of isotropic hardening function [41]. Because of the uniform expansion of the yield surface, the yield stress in the reverse loading is equal to that in forward loading. Therefore, isotropic hardening is not able to describe the Bauschinger effect in reverse loading. In order to describe the Bauschinger effect, the kinematic hardening rules have been proposed which will be introduced in the next sections.
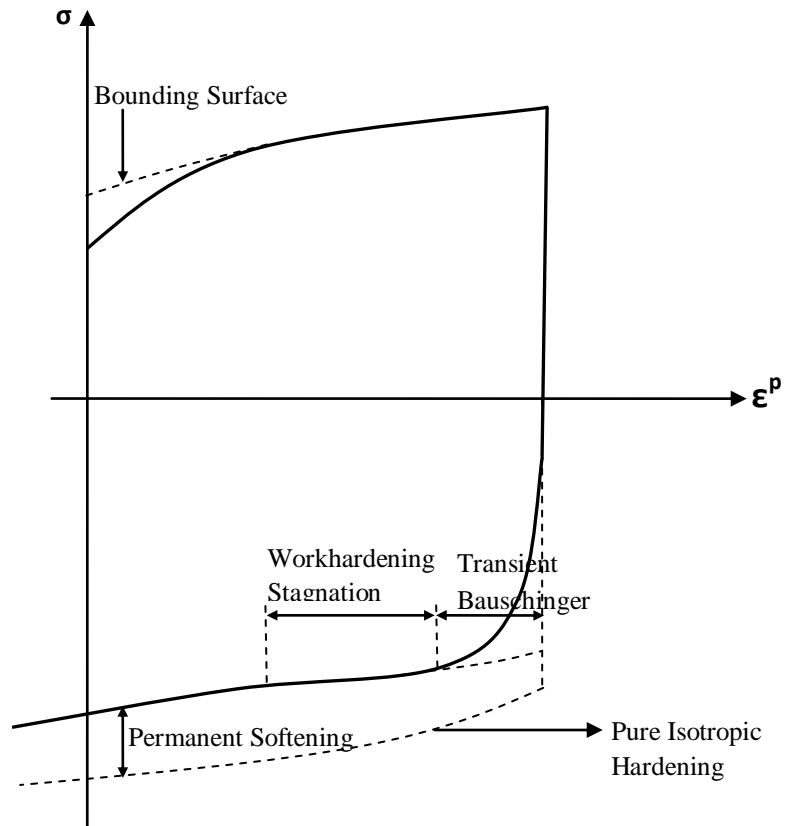
Fig.2.6. Schematic of the stress-strain behaviour under cyclic tension-compression [40]
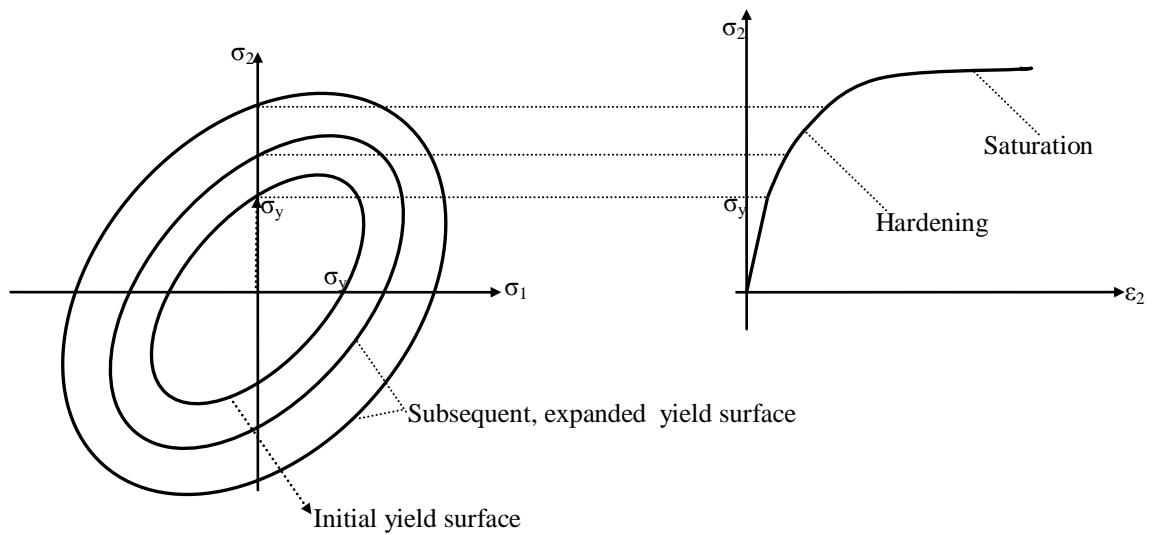
Fig. 2.7. Isotropic hardening, in which the yield surface expands with plastic deformation, and the corresponding uniaxial stress–strain curve [41]

2.5.3. Kinematic hardening:

In the case of monotonically increasing loading, it is often reasonable to assume that any hardening that occurs is isotropic. For the case of reversed loading, however, this is often not appropriate. Consider a material which hardens isotropically, shown schematically in Fig. 2.8. At a strain of ε_i, corresponding to load point (1) shown in the figure, the load is reversed so that the material behaves elastically (the stress is now lower than the yield stress) and linear stress–strain behaviour results until load point (2) is reached. At this point, the load point is again on the expanded yield surface, and any further increase in load results in plastic deformation. Figure 2.8(b) shows that isotropic hardening leads to a very large elastic region upon reverse loading, which is often not what would be seen in experimental data. In fact, a much smaller elastic region is expected and this results from what is often called the Bauschinger effect, and kinematic hardening. In kinematic hardening, the yield surface translates in stress space, rather than expanding. This is shown in Fig. 2.9.

In Fig. 2.9(a), the stress increases until the yield stress, σ_y, is reached. With continued loading, the material deforms plastically and the yield surface translates. When load point (1) is achieved, the load is reversed so that the material deforms elastically until point (2) is achieved when the load point is again in contact with the yield surface. The elastic region is much smaller than that predicted with isotropic hardening and shown in Fig. 2.8(b). In fact, for the kinematic hardening in Fig. 2.9, the size of the elastic region is $2\sigma_y$, whereas for isotropic hardening, it is $2(\sigma_y + r)$. In the case of plastic flow with kinematic hardening, note that the consistency condition still holds; i.e. the load point must always lie on the yield surface during plastic flow. In addition, normality still holds; the direction of the plastic strain increment is normal to the yield surface at the load point.
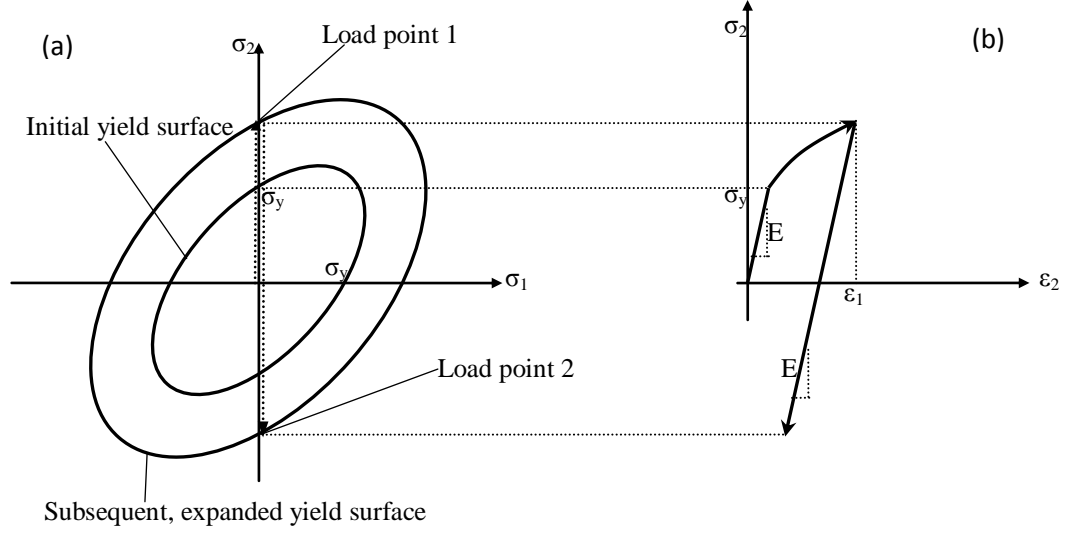
Fig. 2.8. Reversed loading with isotropic hardening showing (a) the yield surface and (b) the resulting stress–strain curve [41]

The yield function describing the yield surface must now also depend on the location of the surface in stress space. Consider the initial yield surface shown in Fig. 2.9. Under applied loading and plastic deformation, the surface translates to the new location shown such that the initial centre point has been translated by $|\boldsymbol{\alpha}|$. So, the stresses relative to the new centre of the yield surface should be checked for yield. Generally, the equation of the yield surface with the kinematic hardening is written as:

$$f(\boldsymbol{\sigma} - \boldsymbol{\alpha}) - \sigma_y = 0 \tag{2.19}$$

where $\boldsymbol{\alpha}$ is called the *backstress tensor* and determines the location of the centre of the yield surface. For example, Hill's quadratic yield function, written in the form of Eq. (2.11a) in the absence of kinematic hardening, should be converted to the following equation:

$$\frac{3}{2}(\boldsymbol{\sigma} - \boldsymbol{\alpha})^T \boldsymbol{N}(\boldsymbol{\sigma} - \boldsymbol{\alpha}) - \sigma_y{}^2 = 0 \tag{2.20}$$

Because the backstress is a variable defined in stress space, it has the same components as stress. Several functions have been proposed to define the evolution of the backstress in stress space.

24
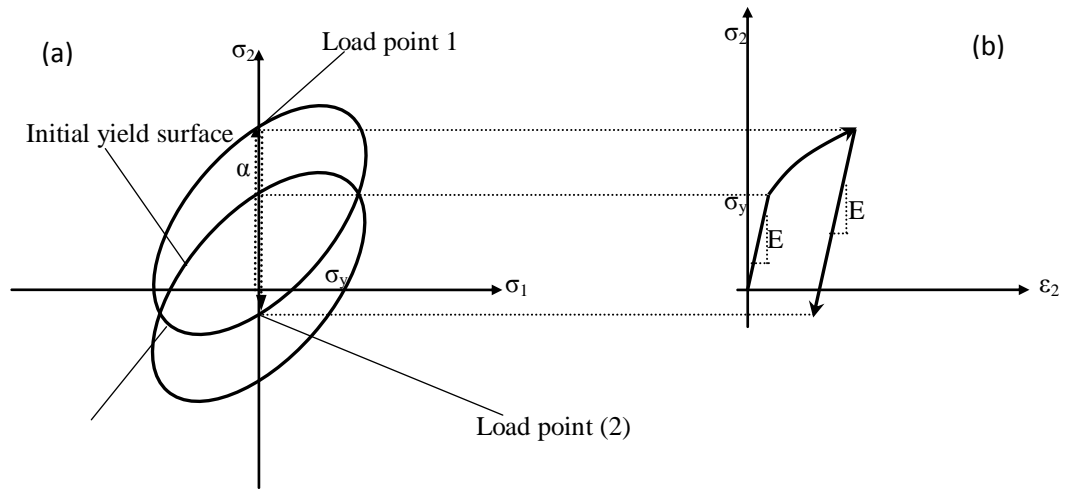
Fig. 2.9. Kinematic hardening showing (a) the translation, and (b) the resulting stress–strain curve with shifted yield stress in compression [41]

In order to reproduce the Bauschinger effect, linear kinematic hardening model was first proposed by Prager [42]. In Prager's kinematic hardening rule, the evolution of backstress is assumed to be proportional to the plastic strain as follows:

$$d\boldsymbol{\alpha} = \frac{2}{3}c\,d\boldsymbol{\varepsilon}^p \tag{2.21}$$

where c is a material constant. Ziegler [43] modified Prager's rule and proposed another linear kinematic rule according to the following equation:

$$d\boldsymbol{\alpha} = d\mu(\boldsymbol{\sigma} - \boldsymbol{\alpha}) \text{ where } d\mu > 0 \tag{2.22}$$

in which $d\mu$ depends on the material. The difference between the Prager and Ziegler hardening rules is shown in Fig. 2.10. According to Prager, the center of yield surface translates in a direction normal to the yield surface at P and this increment of translation is denoted by $d\alpha^{(P)}$ in the figure. On the other hand, according to Ziegler, the increment of translation of the yield surface, denoted by $d\alpha^{(Z)}$, is along the direction of O′P. It should be noted that the two rules are the same if the current yield surface is a hypersphere,

which is true when the Mises yield surface is considered and a combined isotropic–kinematic hardening is applied.
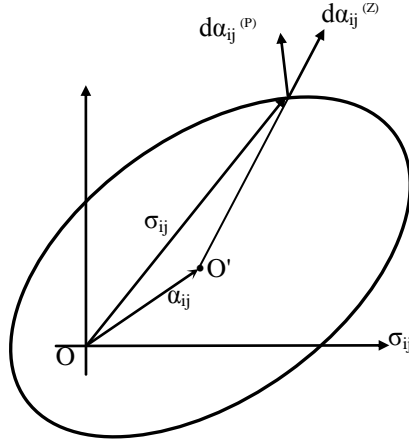
Fig. 2.10. Kinematic-hardening rules by Prager and Ziegler [24]

Neither linear kinematic hardening nor combined isotropic-linear kinematic-hardening rule can capture the transient behaviour curve during reverse loading. In order to capture this curve, Armstrong and Frederick [44] proposed the following nonlinear kinematic hardening model:

$$d\boldsymbol{\alpha} = \frac{2}{3}c\,d\boldsymbol{\varepsilon}^p - \gamma\boldsymbol{\alpha}\,dp \tag{2.23}$$

where c and γ are two material constants. In its uniaxial form, for monotonically increasing plastic strain, Eq. (2.23) can be integrated, taking $\boldsymbol{\alpha}$ to be zero at $\varepsilon^p = 0$, to give:

$$\alpha = \frac{c}{\gamma}(1 - e^{-\gamma\varepsilon^p}) \tag{2.24}$$

According to Eq. (2.24), the backstress saturates to the value c/γ as the plastic strain increases. So, the maximum stress saturates to $\sigma_y + c/\gamma$: constant γ is the time constant and determines the rate of saturation of stress and c/γ determines the magnitude. Later, Chaboche [45] modified the Armstrong-Frederick nonlinear kinematic model to better

reproduce the transient behaviour and ratcheting in fatigue. His proposed model is a decomposed nonlinear kinematic hardening as follows:

$$d\boldsymbol{\alpha} = \sum_{i=1}^{4} d\boldsymbol{\alpha}_i$$

$$d\boldsymbol{\alpha}_i = \frac{2}{3}c_i d\boldsymbol{\varepsilon}^p - \gamma_i \boldsymbol{\alpha}_i dp \text{ , for i=1,2,3} \tag{2.25}$$

$$d\boldsymbol{\alpha}_i = \frac{2}{3}c_i d\boldsymbol{\varepsilon}^p - \gamma_i \boldsymbol{\alpha}_i \left\langle 1 - \frac{\boldsymbol{\alpha}_i}{f(\boldsymbol{\alpha}_i)} \right\rangle dp \text{ , for i=4}$$

where $\boldsymbol{\alpha}_4$ is a threshold to make dynamic recovery term inactive within the threshold, c_i and γ_i are two material constants and dp and $f(\boldsymbol{\alpha}_i)$ are defined as follows:

$$f(\alpha_i) = \left[\frac{3}{2} a_i : a_i \right]^{0.5}$$

This model assumes that the backstress evolution is obtained by four components. The first three components are the same as that of Armstrong and Frederick. However, the fourth component contains a threshold level of backstress that makes the dynamic recovery term inactive within the threshold. Outside the threshold, the fourth component evolves according to the Armstrong–Frederick rule. Ohno and Wang [46] introduced a different threshold term to the Armstrong–Frederick rule in order to control the evolution of the decomposed kinematic hardening rules. Each decomposed rule stops evolving outside of its threshold, c_i/γ_i. This model is defined as follows:

$$d\boldsymbol{\alpha} = \sum_{i=1}^{M} d\boldsymbol{\alpha}_i$$

$$d\boldsymbol{\alpha}_i = \frac{2}{3}c_i d\boldsymbol{\varepsilon}^p - \gamma_i \boldsymbol{\alpha}_i \left\langle d\boldsymbol{\varepsilon}^p : \frac{\boldsymbol{\alpha}_i}{f(\boldsymbol{\alpha}_i)} \right\rangle \left(\frac{f(\boldsymbol{\alpha}_i)}{c_i/\gamma_i} \right)^{m_i} \tag{2.26}$$

where $f(\alpha_i)$ is the von Mises yield function and exponents m_i are proposed to be dependent on the non-coaxiality of the plastic strain rate and the backstress in this model.

In an effort to improve the Ohno-Wang model, McDowell [47] proposed a new expression for m_i, appeared in the above equation, with the purpose of improving its capability for multiaxial simulation as follows:

$$m_i = A_i \left\langle \boldsymbol{n}' : \frac{\boldsymbol{\alpha}_i}{f(\boldsymbol{\alpha}_i)} \right\rangle^{B_i}, \quad \boldsymbol{n}' = \frac{d\varepsilon^p}{dp} = \frac{3}{2\sigma_0}(\boldsymbol{s} - \boldsymbol{\alpha}) \tag{2.27}$$

where $\boldsymbol{s}$ is the deviatoric stress tensor. The expression for the exponents m_i include the constants B_i which can be calibrated using multiaxial ratcheting responses to influence the multiaxial ratcheting simulations without affecting the uniaxial simulations. Jiang and Sehitoglu [48] incorporated the non-coaxiality of plastic strain rate into the Ohno and Wang model and offered another generalized form of this model as follows:

$$d\boldsymbol{\alpha} = \sum_{i=1}^{M} d\boldsymbol{\alpha}_i$$

$$d\boldsymbol{\alpha}_i = \frac{2}{3} c_i d\varepsilon^p - \gamma_i \left(\frac{f(\boldsymbol{\alpha}_i)}{c_i / \gamma_i} \right)^{m_i} \boldsymbol{\alpha}_i dp$$

$$m_i = A_{0i} \left\langle 2 - \boldsymbol{n}' : \frac{\boldsymbol{\alpha}_i}{f(\boldsymbol{\alpha}_i)} \right\rangle \tag{2.28}$$

$$\boldsymbol{n}' = \frac{d\varepsilon^p}{dp} = \frac{3}{2\sigma_0}(\boldsymbol{s} - \boldsymbol{\alpha})$$

Similar to the McDowell model, the exponents m_i in this model assume constant values ($m_i = A_{0i}$) and the model reduces to the Ohno–Wang model for uniaxial loading. Chun et al. [40, 50] further improved the cyclic hardening model of Chaboche by using different backstress evolution laws for monotonic loading and reverse loading. In their approach, several backstress laws are deactivated upon loading reversal in order to obtain a different flow stress saturation level. The backstress is assumed to be obtained by the superposition of two different backstresses as follows:

$$\boldsymbol{\alpha} = \boldsymbol{\alpha}_1 + \boldsymbol{\alpha}_2 \tag{2.29}$$

Each component of the back-stress is made to evolve independently so that different kinematic shift can be realized for the initial and reversal loading:

$$\dot{\boldsymbol{\alpha}}_1 = \frac{c_1}{\bar{\sigma}}(\boldsymbol{\sigma} - \boldsymbol{\alpha})\dot{p} - \gamma \boldsymbol{\alpha}_1 \dot{p} \tag{2.30a}$$

$$\dot{\boldsymbol{\alpha}}_2 = \begin{cases} \dfrac{c_2}{\bar{\sigma}}(\boldsymbol{\sigma} - \boldsymbol{\alpha})\dot{p} & \text{for initial loading} \\ 0 & \text{for reverse loading} \end{cases} \tag{2.30b}$$

where c_1, c_2 and γ are material (hardening) parameters to be determined. The Modified Chaboche model is recovered when $\boldsymbol{\alpha}_2$ approaches zero (or $c_2 = 0$).

Yoshida et al. [34] developed two constitutive models called IH+NKH and IH+NLK+LK. The first model uses a combined isotropic-nonlinear kinematic hardening. A new evolution for the expansion of yield surface has been proposed in IH. In the second model, a linear term has been added to the Armstrong-Frederick model for evolution of backstress in LK. The NLK, LK and IH have the following forms, respectively:

$$d\boldsymbol{\alpha}_1 = c(\frac{2}{3}ad\boldsymbol{\varepsilon}^p - \boldsymbol{\alpha}_i dp)$$

$$d\boldsymbol{\alpha}_2 = \frac{2}{3}H'_\infty d\boldsymbol{\varepsilon}^p$$

(2.31)

where c, a and H'_∞ are all material constants. The results of their study show that neither IH+NLK model nor IH+NLK+LK model can accurately describe the phenomena observed in cyclic experiments. In order to accurately model the material behaviour, two-surface plasticity models have been employed by many researchers which will be discussed in the next section.

2.5.4. Two-surface plasticity models:

In parallel to modification of nonlinear kinematic hardening models, two-surface plasticity models, originally proposed by Dafalias and Popov [51] and Krieg [52], attracted a lot of attention by researchers because both the transient and long-term behaviour of the material can be fairly well described by these models. In two-surface models, the evolution of the inner surface is usually defined such that it describes the transient response of the material and the evolution of the bounding surface is usually responsible to describe the long-term response of the material.

The two-surface model proposed by Dafalias and Popov [51] defines a continuous variation of the plastic modulus $\frac{d\sigma}{d\varepsilon^p} = E_p$ between these two surfaces. In this model, a bounding surface is proposed in stress space in addition to the yield surface (sometimes also called the loading surface). The bounding surface always encloses the yield surface and is a generalization of the bounds observed in the experimental results for uniaxial random cyclic loading on a grade 60 steel specimen. The details of the experimental random cyclic loading curve were presented in [51].

Geng and Wagoner [53,54] developed a two-surface plasticity model with the purpose of improving the nonlinear kinematic hardening model to capture the permanent softening. Their hardening rule is expressed as in the Armstrong–Frederick formulation with an additional term to allow for translations and expansion of the limiting or bounding surface:

$$d\boldsymbol{\alpha} = \frac{c_p}{\sigma_0}(\boldsymbol{\sigma} - \boldsymbol{\alpha})dp - \gamma(\boldsymbol{\alpha} - \boldsymbol{\beta})dp \qquad (2.32)$$

where dp is the equivalent plastic strain rate; σ_0, c_p and γ are material parameters, with σ_0 representing the yield surface size, β is the centre of the bounding surface. The stress mapping point $\boldsymbol{\sigma_\beta}$ on the bounding surface is determined as follows:

$$\left(\boldsymbol{\sigma_\beta} - \boldsymbol{\beta}\right) = \frac{\sigma_{\beta 0}}{\sigma_0}(\boldsymbol{\sigma} - \boldsymbol{\alpha}) \qquad (2.33)$$

where $\sigma_{\beta 0}$ represents the size of the bounding surface. The translation and expansion of the bounding surface is specified with a mixed hardening rule:

$$d\boldsymbol{\beta} = \frac{mH^p}{\sigma_{\beta 0}}(\boldsymbol{\sigma_\beta} - \boldsymbol{\beta})dp \qquad (2.34)$$

$$d\sigma_{\beta 0} = (1 - m)H^p dp \qquad (2.35)$$

where H^p is the plastic modulus of the monotonic loading curve, and m is the ratio of the kinematic response (translation) to the isotropic response (expansion) of the bounding surface.

Yoshida and Uemori [40,55] developed another two-surface plasticity model. This model is composed of two nonlinear kinematic hardening rules and the isotropic hardening of the bounding surface. The model also pays special attention to the workhardening stagnation. This mode will be discussed later in the next chapter.

Lee et al. [56] also proposed another two-surface plasticity model based on the Dafalias and Popov model. In their model, both surfaces translate (kinematic hardening) and expand (isotropic hardening) in stress space. The kinematic hardening of the surfaces is defined by two different linear kinematic hardening rules. They also used their model to predict springback in a draw-bend test and showed their model improves the predicted springback results. It should be mentioned that this model does not take the workhardening stagnation into account. McDowell [57], Ohno and Kachi [58], Ohno and Satra [59], Xianjie et al. [60], Iwata [61] and White [62] have also developed two-surface plasticity models to improve modeling the material behaviour in cyclic loading.

2.5.5. Rotation of the yield surface:

The rotation of the yield surface has also been taken into account by some researchers. In an attempt to consider the rotation of the yield surface, Suprun [63] developed a new constitutive model with three plasticity constants. This model is actually an anisotropic work hardening model characterized by translation, reshaping and turning of the subsequent yield surface. The yield surface is initially a hypersphere; i.e. the material is initially isotropic, and then it is anisotropically extended to a hyperellipsoid. Meanwhile, this hyperellipsoid is allowed to rotate in the deviatoric stress space. The evolution law for this model is defined as a function of length of plastic deformation trajectory, the position of the loading point and the physical properties of the material. It should be pointed out that this model needs four parameters: the elastic limit, and three independent plastic constants.

Choi et al. [64,65] also considered the rotation of the yield surface for the description of the multi-axial elastoplastic behaviour. Their model enables the anisotropic yield surface to grow (isotropic hardening), translate (kinematic hardening) and rotate (rotation of the anisotropy axes) with respect to the deformation, while the shape of the yield surface remains essentially unchanged. Essentially, the model is formulated on the basis of an Armstrong–Frederick type kinematic hardening, the plastic spin theory for the reorientation of the symmetry axes of the anisotropic yield function, and additional terms coupling these expressions. The capability of the model is illustrated with multi-path

loading simulations in 'tension-shear' and 'reverse-shear' to assess its performance with 'cross' hardening and 'Bauschinger' effects.

2.5.6. *Distortion of the yield surface:*

It has been reported in the literature that the yield surface is distorted as the plastic deformation proceeds [66-69]. Since the plastic strain increment is obtained according to the normality rule in the associated flow rule, it is important to take this phenomenon into account. In an effort to model yield surface distortion Francois [70] proposed a method to take into account the yield surface distortion within the thermodynamic framework. The yield surface obtained by this method is an egg-shaped similar to those observed in experimental data. He also compared the experimental results with those simulation results for both proportional and non-proportional tension-torsion paths. Vincent et al. [71] managed to introduce nonlinear kinematic hardening model taking distortion of subsequent yield surface into account. They used the results of a polycrystalline model to get some reference predictions to utilize in the development of the constitutive laws and then quantitatively identified their model using experimental data on a type 316L stainless steel. This model is limited to two-dimensional loading paths for simplicity of constitutive equation. Later in 2004, Vincent et al. [72] extended this model to a general five-dimensional loading path.

2.5.7. *Yoshida-Uemori two-surface model:*

As mentioned in the first chapter, advanced material constitutive equations are required for more accurate simulation of sheet metal forming and subsequent springback. Cyclic loading is a very common type of loading in sheet metal forming processes as it is observed during the material flow over the punch radius, die radius and through a drawbead. Since the material behaviour is quite complex in cyclic loading, the hardening

rule should be able to accurately predict the material behaviour in cyclic loading. After a careful investigation of existing hardening models in the literature, it was found that the Yoshida-Uemori (YU) model [40] is one of the most sophisticated and comprehensive phenomenological models which is capable of reproducing the transient Bauschinger effect, permanent softening and workhardening stagnation in large elasto-plastic deformation.

2.6. Consistency Condition:

The plastic multiplier, $d\lambda$ in Eq. (2.4), is determined by use of the consistency condition. This condition states that the loading from a plastic state must again lead to a plastic state, the stress and plastic strain that exist after the infinitesimal changes $d\boldsymbol{\sigma}$, $d\boldsymbol{\varepsilon}^p$ and $d\sigma_y$ have taken place must still satisfy the yield function equation:

$$f(\boldsymbol{\sigma}, \boldsymbol{\varepsilon}^p, \sigma_y) = 0 \tag{2.36}$$

By use of the consistency condition, the increment of the yield function is zero, that is,

$$df = \frac{\partial f}{\partial \boldsymbol{\sigma}} d\boldsymbol{\sigma} + \frac{\partial f}{\partial \boldsymbol{\varepsilon}^p} d\boldsymbol{\varepsilon}^p + \frac{\partial f}{\partial \sigma_y} d\sigma_y = 0 \tag{2.37}$$

In Fig. 2.11, the stress at point A is $\boldsymbol{\sigma}^{(A)}$ and it is on the yield surface

$$f\left(\boldsymbol{\sigma}^{(A)}, \boldsymbol{\varepsilon}^{p(A)}, \sigma_y^{(A)}\right) = 0 \tag{2.38}$$

An infinitesimal loading has moved the stress point from A to B and it carries the yield surface with it, so that the stress at B is $\boldsymbol{\sigma}^{(B)}$ and the yield surface that B is on is:

$$f\left(\boldsymbol{\sigma}^{(B)}, \boldsymbol{\varepsilon}^{p(B)}, \sigma_y^{(B)}\right) = 0 \tag{2.39}$$

while

$$f\left(\boldsymbol{\sigma}^{(B)}, \boldsymbol{\varepsilon}^{p(A)}, \sigma_y^{(A)}\right) = 0 \tag{2.40}$$

Substituting (2.5) into (2.37), we have:

$$df = \frac{\partial f}{\partial \boldsymbol{\sigma}}d\boldsymbol{\sigma} + d\lambda \frac{\partial f}{\partial \boldsymbol{\varepsilon}^p}\frac{\partial f}{\partial \boldsymbol{\sigma}} + \frac{\partial f}{\partial \sigma_y}d\sigma_y = 0 \qquad (2.41)$$

which may be solved to obtain $d\lambda$ as:

$$d\lambda = -\frac{\left(\frac{\partial f}{\partial \sigma_y}\right)d\sigma_y + \left(\frac{\partial f}{\partial \boldsymbol{\sigma}}\right)d\boldsymbol{\sigma}}{\left(\frac{\partial f}{\partial \boldsymbol{\sigma}}\right)\left(\frac{\partial f}{\partial \boldsymbol{\varepsilon}^p}\right)} \qquad (2.42)$$
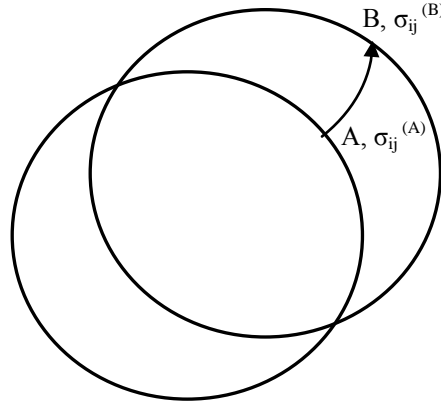
Fig. 2.11. The consistency condition[24]

2.7. Return Mapping Algorithm:

In any structural analysis, we need to address how to represent and model the deformations and the material behaviour. For the representation of the deformations, a displacement field needs to be assumed and the corresponding kinematic quantities, such as strains, strain rates, deformation gradient, etc. need to be calculated. Once, the kinematic variables are known, a material model is required to calculate the stresses in the structure. A numerical algorithm is required for stress integration of strain-driven problem formulations; these problems arise in the displacement-based and mixed finite element formulations. The task of stress integration is to determine the stresses, inelastic strains and internal variables at the end of the time increment. A numerical integration

method is usually required for integration of plasticity equations. According to α-method, the integral of function $f(t)$ in an interval Δt can be approximated as:

$$\int_{t}^{t+\Delta t} f(t)dt = [(1-\alpha)f_t + \alpha f_{t+\Delta t}]\Delta t \tag{2.42}$$

where $0 \leq \alpha \leq 1$ is the integration parameter, f_t denotes the value of f at time t and $f_{t+\Delta t}$ is the value of f at time $t + \Delta t$. The values $\alpha = 0$ and $\alpha = 1$ correspond to the Euler forward method and Euler backward method, respectively, while $\alpha = 0.5$ gives the trapezoidal rule. If the Euler backward method is used in integration of plasticity equations, the value of the function is required at the end of time increment $(t + \Delta t)$. Since, the stress is not known at the end of increment, Euler backward integration is referred to as the implicit method. Nevertheless, using Euler forward method is referred to as the explicit method since all quantities, including stresses, are known at the beginning of time increment t.

In the return mapping procedure, it is first assumed that the increment is purely elastic. An elastic constitutive law, e.g. Hooke's law, is used to calculate the so-called trial stress. If the trial stress lies inside or on the yield surface, the trial stress is accepted as the final solution and all internal variables are updated and the stress integration procedure is stopped. If the trial stress lies outside the yield surface, the plastic correction procedure is used to bring the stress back onto the yield surface at the end of time increment. In the plastic corrector procedure, the plasticity equations are integrated using Euler backward method and all equations are usually written in terms of one single parameter which is usually the effective plastic strain. Substituting these equations into the yield function leads to a nonlinear equation in terms of the effective plastic strain increment. This nonlinear equation is usually solved by the Newton-Raphson numerical method. Once the effective plastic strain is known, the plasticity equations are used to update all variables at the end of the time increment. This method is also known as elastic-predictor plastic-corrector and is illustrated in Fig. 2.12. The return mapping procedure will be used in the next chapters to implement the advanced constitutive models in a finite element program.

$\sigma^{Trial(n+1)}$

Plastic Corrector

$\sigma^{(n+1)}$

$\sigma^{(n)}$

$f(\sigma^{(n+1)})=0$

$f(\sigma^{(n)})=0$
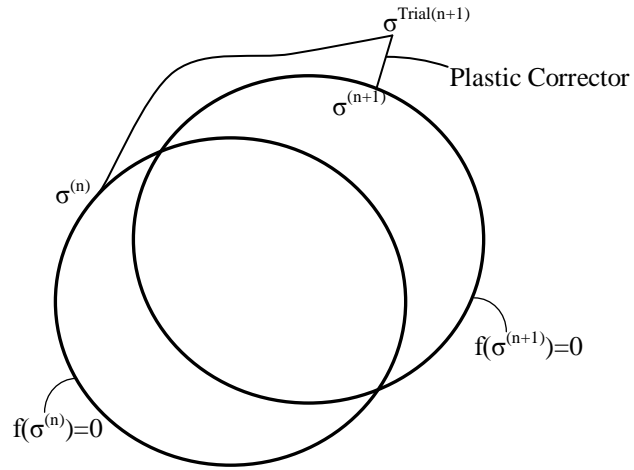
Fig. 2.12. The return-mapping algorithm in multidimensional stress space [24]

Chapter 3

Semi-implicit Numerical Integration of Yoshida-Uemori Two-Surface Plasticity Model

3.1. Introduction:

In order to reproduce the material behaviour in cyclic loading, the Yoshida-Uemori (YU) model [40], which is capable of describing the cyclic material behaviour relatively accurately, is used in this work. This model is able to describe transient Bauschinger effect, permanent softening and workhardening stagnation. To the best of our knowledge, the numerical procedure to implement this model has not published in the literature up to now. Moreover, the constitutive models utilizing this hardening law and anisotropic yield functions have not been developed in the literature. So, the return mapping algorithm is used in this project to develop two different numerical algorithms for implementation of this model into finite element codes. The first algorithm, which is limited to the use of quadratic yield functions, is presented in this chapter and the second one, which can be used with any yield function including nonquadratic yield functions, is described in the next chapter.

The YU model is a two-surface plasticity model that assumes kinematic hardening of the yield surface within the bounding surface and mixed isotropic–kinematic hardening of the bounding surface itself. In two-surface plasticity models, such as Dafalias and Popov [51] and Lee *et al.* [56], two independent hardening evaluations are usually

defined for the kinematic evolution of the yield and bounding surfaces. In these models, a proper equation is required to define the gap between the yield and bounding surfaces and this gap should be checked at each time increment to make sure that the yield surface stays either inside or tangent to the bounding surface at the loading point. However, in the YU model, the evolution of the yield surface is defined by the superposition of two kinematic hardening laws. The first one ($\boldsymbol{\beta}$) locates the centre of the bounding surface and the second one ($\boldsymbol{\theta}$) defines the relative kinematic motion of the yield surface with respect to the bounding surface. The relative kinematic motion ($\boldsymbol{\theta}$) is a function of the difference between the sizes of the two surfaces and is defined such that the inner surface never passes the outer surface. Therefore, the yield surface never passes through the bounding surface. This fact makes the numerical implementation of this model much easier compared to other two-surface models. Additionally, the model uses only a few numbers of material constants although it is capable of reproducing many cyclic phenomena relatively accurately. Most of the parameters (seven parameters in the basic version of this model) can be easily determined directly from the experimentally obtained stress–strain curves.

In order to consider the anisotropy of the sheet metal, the Hill's quadratic yield function is used to define the yield (inner) surface. As mentioned in section 2.7, there are generally two integration schemes to integrate the plasticity equations: implicit and explicit schemes. In this chapter, a semi-implicit approach is used to integrate the Yoshida-Uemori (YU) model and implement it as a user-defined material subroutine (UMAT). In the next chapter, an algorithm based on a fully implicit scheme is presented for implementation of this model as a UMAT for commercial finite element packages. The equations are derived in such a way that they would be applicable for all stress states including plane-stress problems.

3.2. Plastic Strain Rate:

At the presence of backstress, Hill's quadratic yield function (Eq. 2.11) is rewritten as:

$$f(\boldsymbol{\eta}) = \sqrt{(3/2)\boldsymbol{\eta}^T \boldsymbol{N} \boldsymbol{\eta}} - Y = 0 \quad \text{or} \quad f(\boldsymbol{\eta}) = \bar{\eta} - Y = 0 \qquad (3.1a)$$

where $\boldsymbol{N}$ is a fourth order anisotropic tensor defined in Eqs. 2.11, Y is the yield stress, and $\boldsymbol{\eta}$ is defined as the difference between the stress and the backstress, i.e. $\boldsymbol{\eta} = \boldsymbol{\sigma} - \boldsymbol{\alpha}$. Voigt notation is usually used in development of numerical algorithms for implementation into computer programs. In this notation, second-order tensors and fourth-order tensors are represented by one-dimensional arrays and two-dimensional arrays, respectively. Using Voigt notation, the stress and backstress tensors are represented by:

$$\boldsymbol{\sigma} = \begin{bmatrix} \sigma_{xx} \\ \sigma_{yy} \\ \sigma_{zz} \\ \sigma_{xy} \\ \sigma_{yz} \\ \sigma_{xz} \end{bmatrix}, \boldsymbol{\alpha} = \begin{bmatrix} \alpha_{xx} \\ \alpha_{yy} \\ \alpha_{zz} \\ \alpha_{xy} \\ \alpha_{yz} \\ \alpha_{xz} \end{bmatrix} \qquad (3.1b)$$

In order to calculate the plastic strain increment, the incremental deformation theory [73,74] is applied to the elasto-plastic formulation based on the materially embedded coordinate system. Under this scheme, the strain increments in the flow formulation are the discrete true (or logarithmic) strain increments, and the material rotates by the incremental angle obtained from the polar decomposition at each discrete step. It should be mentioned that the plastic strain increment can also be obtained by the multiplicative decomposition theory. Especially when material deformation follows minimum plastic work path (or logarithmic strain path), multiplicative theory formulation coincides with the current additive decomposition theory based on the incremental deformation theory (Han *et al.* [75]). In the incremental deformation theory, the effective plastic strain increment is obtained as follows:

$$\Delta p = \frac{\boldsymbol{\sigma} : \Delta \boldsymbol{\varepsilon}^p}{\overline{\sigma}} = \frac{\boldsymbol{\sigma} : \Delta \lambda \frac{\partial \overline{\sigma}}{\partial \boldsymbol{\sigma}}}{\overline{\sigma}} = \frac{\Delta \lambda \overline{\sigma}}{\overline{\sigma}} = \Delta \lambda \qquad (3.2a)$$

where $\Delta \lambda$ is the plastic multiplier, Δp is the effective plastic strain increment and $\overline{\sigma}$ is a first order homogenous function, that is $\overline{\sigma} = \boldsymbol{\sigma} \frac{\partial \overline{\sigma}}{\partial \boldsymbol{\sigma}}$. Now, using the associated flow rule and Eq. (3.2a), the plastic strain increment is obtained as follows:

$$\dot{\boldsymbol{\varepsilon}}^p = \frac{3\dot{p}}{2\overline{\eta}} N\boldsymbol{\eta} \qquad (3.2b)$$

3.3. The Yoshida-Uemori (YU) Model:

The materially embedded coordinate system (co-rotational coordinate system) is used here in this chapter, not only because it makes the derivation of numerical equations more convenient but also because it is usually required by many of the commercial programs such as ABAQUS. The YU model consists of two surfaces in stress space that are schematically shown in Fig. 3.1. The kinematic hardening of the yield surface describes the transient Bauschinger deformation characterized by early re-yielding and a subsequent rapid change of workhardening rate, which is mainly due to the motion of less stable dislocations, such as piled-up dislocations. The isotropic hardening of the bounding surface represents the global workhardening, which is associated with the formation of stable dislocation structures, such as cell walls. Permanent softening and workhardening stagnation are caused by the dissolution of dislocation cell walls that were created during forward deformation [76,77]. In order to describe such deformation characteristics under stress reversals, the kinematic hardening and non-IH region during stress reversals are assumed for the bounding surface. The model is able to describe the cyclic phenomena shown in Fig. 3.2 relatively accurately.

The inner surface, or yield surface, determines the elastic domain of the material in stress space. It is assumed that this surface translates in stress space without expansion.

The relative kinematic motion ($\boldsymbol{\theta}$) of the yield surface with respect to the bounding surface is expressed by:

$$\dot{\boldsymbol{\theta}} = c\left[\frac{a}{Y}\boldsymbol{\eta} - \sqrt{\frac{a}{\bar{\theta}}}\boldsymbol{\theta}\right]\dot{p} \tag{3.3a}$$

where $\boldsymbol{\eta}$ is the difference between the stress and backstress, $\boldsymbol{\theta}$ is the position of the yield surface with respect to the centre of the bounding surface, c is a material parameter that controls the rate of kinematic hardening and Y is the initial yield stress. Moreover, $\dot{p}$ is the effective plastic strain rate, $\bar{\theta}$ is the effective backstress, and a is the difference between the size of the bounding surface and the yield surface. These parameters are defined as follows:

$$\dot{p} = \sqrt{\frac{2}{3}\dot{\boldsymbol{\varepsilon}}^p : \dot{\boldsymbol{\varepsilon}}^p} \,; \bar{\theta} = \sqrt{(3/2)\boldsymbol{\theta}^T N\boldsymbol{\theta}} \,; a = B + R - Y \tag{3.3b}$$

where $\dot{\boldsymbol{\varepsilon}}^p$ denotes the plastic strain rate, and B and R are the initial size of the bounding surface and the isotropic hardening component, respectively. Eq. (3.3a) indicates that the yield surface moves in such a way that the current stress point existing on the yield surface is approaching the corresponding point on the bounding surface. Under the uniaxial stress state, Eq. (3.3a) yields:

$$\dot{\boldsymbol{\theta}} = ca\left[\dot{\varepsilon}^p - sgn(\boldsymbol{\theta})\sqrt{\frac{\bar{\theta}}{a}}|\dot{\varepsilon}^p|\right] \tag{3.4}$$

A combined isotropic-nonlinear kinematic hardening model is used to describe the evolution of the bounding surface. The isotropic hardening of the bounding surface is expressed by:

$$\dot{R} = k(R_{sat} - R)\dot{p} \tag{3.5}$$

where R_{sat} is the saturated value of the isotropic hardening stress, R, at infinitely large plastic strain, and k is a material parameter that controls the rate of isotropic hardening. The isotropic hardening of the bounding surface is used to describe the global

workhardening of the material. In order to describe the permanent softening observed during reverse loading, the kinematic hardening of the bounding surface is introduced. The kinematic hardening of the bounding surface is assumed by:

$$\dot{\boldsymbol{\beta}} = k\left[\frac{b}{Y}\boldsymbol{\eta} - \boldsymbol{\beta}\right]\dot{p} \tag{3.6}$$

where $\boldsymbol{\beta}$ is the kinematic hardening of the bounding surface and b is a material parameter. It should be noted that parameter k is assumed to be the same as in the evolution equation of the isotropic hardening stress (Eq. (3.5)). It should also be mentioned that $\dot{\boldsymbol{\beta}}$ is defined in the deviatoric stress space by Yoshida and Uemori where the linear term (i.e. the first term) of the equation is based on Prager's model. However, I assumed that the linear term of $\dot{\boldsymbol{\beta}}$ is in the direction of $\boldsymbol{\eta}$ according to Ziegler's model not only to avoid the strain softening error associated with Prager's rule but also to define both backstress equations in the same stress space and then simply add them together to calculate $\boldsymbol{\alpha}$. The evolution of the yield surface is defined by superposition of the above nonlinear kinematic motions as:

$$\dot{\boldsymbol{\alpha}} = \dot{\boldsymbol{\beta}} + \dot{\boldsymbol{\theta}} \tag{3.7}$$
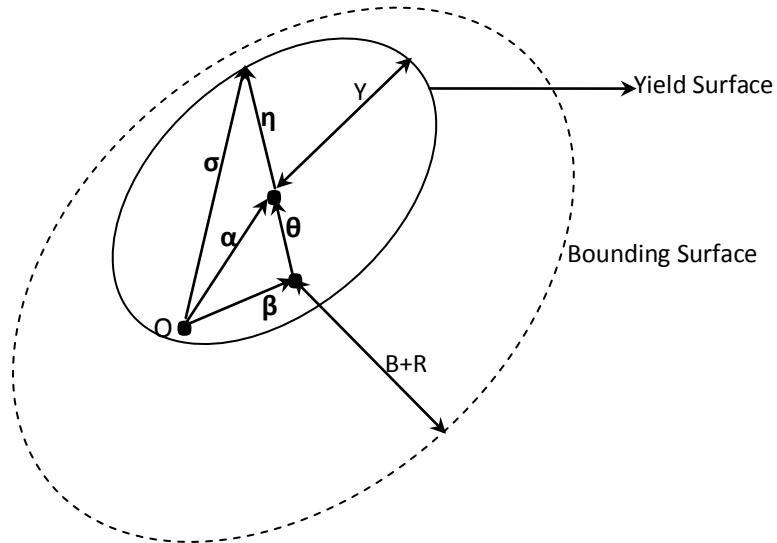
Fig. 3.1. Schematic illustration of Yoshida-Uemori model [40]

The size of yield surface is smaller than the bounding surface and makes it possible to capture the early re-yielding during reverse deformation. The kinematic hardening of the yield surface is used to describe the rapid change of workhardening in the transient Bauschinger region. The kinematic and isotropic hardenings of the bounding surface describe permanent softening and global workhardening of the material, respectively. It should be noted that the bounding stress in uniaxial loading is obtained by:

$$\sigma_{bound}^{forward} = B + R + \beta = B + \left(R_{sat} + b\right)\left(1 - e^{-kp}\right) \tag{3.8}$$
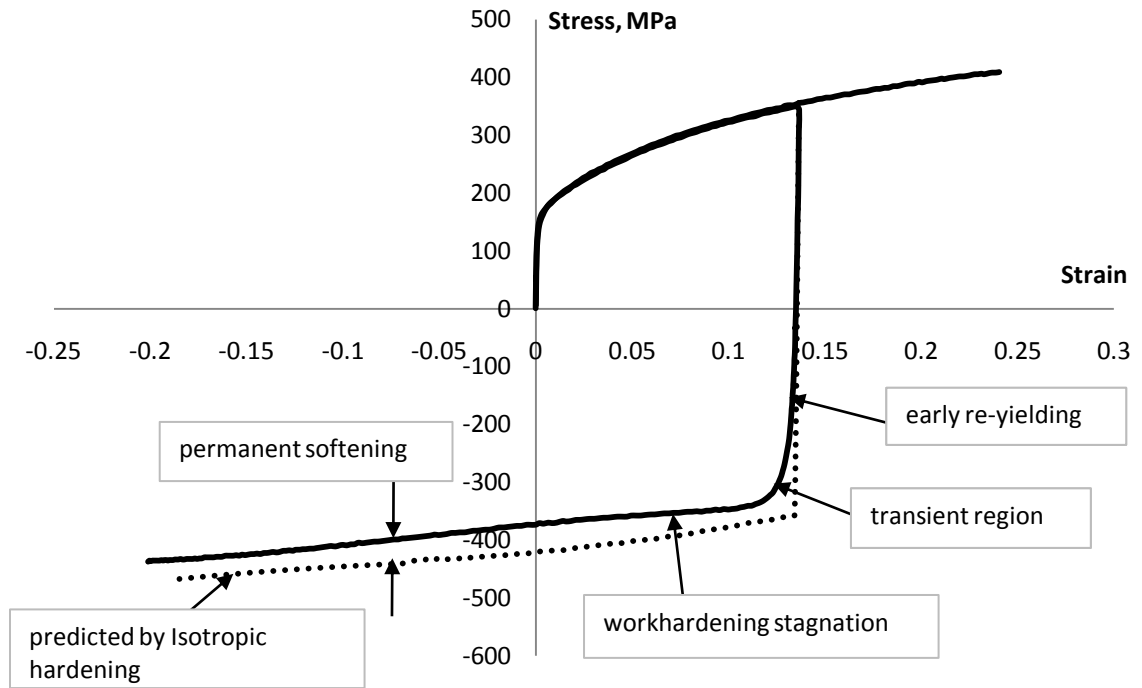
Fig. 3.2. Stress-strain response of a mild steel in a forward and reverse loading and the cyclic phenomena

At the beginning of deformation, both the yield and bounding surfaces are assumed to be at the origin in stress space, and the radius of the yield surface is smaller than that of the bounding surface. As plastic deformation takes place, the yield surface translates within the bounding surface which itself is both translating and expanding. The model also accounts for the workhardening stagnation which is discussed in section 3.4.2.

43

3.4. Stress Integration:

In the following equations of this chapter, subscript n is used to denote a quantity at the beginning of a time increment, whereas subscript $n + 1$ is used to denote a quantity at the end of the time increment. If no subscript is used, this quantity is evaluated at the end of the increment. It is generally more advantageous to use the Euler backward method (fully implicit integration scheme) in order to integrate the plasticity equations because it is unconditionally stable. In this scheme, all quantities are written at the end of each time increment to ensure that the yield function is satisfied at the end of the time increment. Therefore, this avoids drift from the yield surface which can occur in the Euler forward (explicit) method. When an implicit approach is used for integration of global finite element equations, the Euler backward scheme generally leads to much more rapid solutions as it allows larger time increments to be used. However, it is more challenging mathematically to use a fully implicit approach with complex hardening laws. For example, if a fully implicit approach were used here to integrate Eq. 3.4, then we would need to solve a system of equations for $\boldsymbol{\theta}$ in each direction because its evolution depends on $\boldsymbol{\theta}$. Therefore, a fully implicit approach usually is both more challenging to implement and more computationally expensive. In addition, the implicit approach may not be able to converge for very complex problems as more equations are to be solved in this approach.

A simpler approach is to integrate the effective plastic strain implicitly but the internal variables explicitly. This method is called semi-implicit integration. Since it is not unconditionally stable [78], a sufficiently small time increment should be used to ensure both stability and accuracy when this approach is used. In this study, a semi-implicit approach was used to integrate equations 3.3a and 3.6. A sub-step algorithm was also used in the user subroutine to control the size of strain increment and to control the integration error in the simulation. It is also worth mentioning that the strain increment is usually very small in the global finite element explicit approach and there is practically no need for such a sub-stepping algorithm. The semi-implicit integration of equations 3.3a and 3.6 leads to:

$$\Delta\boldsymbol{\theta} = c\left[\frac{a}{Y}\boldsymbol{\eta} - \sqrt{\frac{a}{\bar{\theta}_n}}\boldsymbol{\theta}_n\right]\Delta p \tag{3.9}$$

$$\Delta\boldsymbol{\beta} = k\left[\frac{b}{Y}\boldsymbol{\eta} - \boldsymbol{\beta}_n\right]\Delta p \tag{3.10}$$

$$\Delta\boldsymbol{\alpha} = \Delta\boldsymbol{\beta} + \Delta\boldsymbol{\theta} \tag{3.11}$$

It is noted that all variables except $\boldsymbol{\theta}$ and $\boldsymbol{\beta}$ are written at the end of the time increment. Using the return mapping algorithm, the trial stress and then the stress can be written in elastic predictor-plastic corrector form in terms of the trial stress and plastic return as:

$$\boldsymbol{\sigma}^{Tr} = \boldsymbol{\sigma}_n + \boldsymbol{D}\Delta\boldsymbol{\varepsilon} \tag{3.12}$$

$$\boldsymbol{\sigma} = \boldsymbol{\sigma}^{Tr} - \boldsymbol{D}\Delta\boldsymbol{\varepsilon}^p \tag{3.13}$$

$$\boldsymbol{\eta} = \boldsymbol{\sigma} - \boldsymbol{\alpha} = \boldsymbol{\sigma}^{Tr} - \boldsymbol{D}\Delta\boldsymbol{\varepsilon}^p - \boldsymbol{\alpha}_n - \Delta\boldsymbol{\alpha} = \boldsymbol{\eta}^{Tr} - \boldsymbol{D}\Delta\boldsymbol{\varepsilon}^p - \Delta\boldsymbol{\alpha} \tag{3.14}$$

where $\boldsymbol{\sigma}^{Tr}$ is the trial elastic stress, $\boldsymbol{\sigma}$ is stress at the end of an increment, $\boldsymbol{\alpha}_n$ and $\boldsymbol{\alpha}_n$ are backstresses at the beginning and end of an increment, respectively, $\boldsymbol{\varepsilon}_n^p$ and $\boldsymbol{\varepsilon}^p$ are the total plastic strains at the beginning and end of an increment, respectively, and $\boldsymbol{D}$ is the elasticity tensor. Eqs. (3.15a) and (3.15b) show the representation of $\boldsymbol{D}$ in Voigt notation for a general 3D stress space and plane stress space respectively.

$$\boldsymbol{D} = \begin{bmatrix} 2G^E + \lambda^E & \lambda^E & \lambda^E & 0 & 0 & 0 \\ \lambda^E & 2G^E + \lambda^E & \lambda^E & 0 & 0 & 0 \\ \lambda^E & \lambda^E & 2G^E + \lambda^E & 0 & 0 & 0 \\ 0 & 0 & 0 & G^E & 0 & 0 \\ 0 & 0 & 0 & 0 & G^E & 0 \\ 0 & 0 & 0 & 0 & 0 & G^E \end{bmatrix} \tag{3.15a}$$

$$\boldsymbol{D} = \frac{E}{1-v^2}\begin{bmatrix} 1 & v & 0 \\ v & 1 & 0 \\ 0 & 0 & \dfrac{1-v}{2} \end{bmatrix} \tag{3.15b}$$

where E, v, G^E and λ^E are the elastic modulus, Poisson's ratio, shear modulus and Lame's constant of the material, respectively. It should be emphasized that engineering

shear strains are used in Eqs. (3.15) to calculate the shear stresses. So, the strain tensors in Voigt notation for 3D and plane stress states are respectively represented as:

$$\boldsymbol{\varepsilon} = \begin{bmatrix} \varepsilon_{xx} \\ \varepsilon_{yy} \\ \varepsilon_{zz} \\ 2\varepsilon_{xy} \\ 2\varepsilon_{yz} \\ 2\varepsilon_{xz} \end{bmatrix}, \boldsymbol{\varepsilon} = \begin{bmatrix} \varepsilon_{xx} \\ \varepsilon_{yy} \\ 2\varepsilon_{xy} \end{bmatrix} \tag{3.15c}$$

The elasticity tensor for plane strain and axisymmetric states is simply obtained by eliminating the fifth and sixth columns and rows of Eq. (3.15a).

Substitution of Eq. (3.2b) and Eqs. (3.9)-(3.11) into Eq. (3.14) leads to the following equation:

$$\boldsymbol{\eta} = \boldsymbol{\sigma}^{Tr} - \boldsymbol{D}[\boldsymbol{\varepsilon} - \boldsymbol{\varepsilon}_n^p - \frac{3\Delta p}{2\sigma_y}\boldsymbol{N}\boldsymbol{\eta}] - \boldsymbol{\alpha}_n - c(\frac{a}{Y}.\boldsymbol{\eta} - \sqrt{\frac{a}{\bar{\boldsymbol{\theta}}_n}}.\boldsymbol{\theta}_n)\Delta p - k(\frac{b}{Y}b.\boldsymbol{\eta} - \boldsymbol{\beta}_n)\Delta p \tag{3.16}$$

After some mathematical manipulations, the following return map equation is obtained which is only in terms of a single parameter, i.e. Δp:

$$\boldsymbol{\eta} = \frac{1}{1 + \dfrac{a.c.\Delta p}{Y} + \dfrac{b.k.\Delta p}{Y}} \boldsymbol{\Xi}^{-1}\boldsymbol{D}^{-1}\left[\boldsymbol{\eta}^{Tr} + \sqrt{\frac{a}{\bar{\boldsymbol{\theta}}_n}}.c.\Delta p.\boldsymbol{\theta}_n + k.\Delta p.\boldsymbol{\beta}_n\right] \tag{3.17a}$$

where

$$\boldsymbol{\Xi}^{-1} = \left[\boldsymbol{D}^{-1} + \frac{(3/2)\Delta p}{Y + a.c.\Delta p + b.k.\Delta p}\boldsymbol{N}\right]^{-1} \tag{3.17b}$$

Substituting Eq. (3.17) into the yield function, i.e. Eq. (3.1), results in a nonlinear equation in terms of Δp which can be easily solved using the Newton-Raphson method. Once Δp is known, Eq. (3.17a) is first used to obtain $\boldsymbol{\eta}$, then Eqs. (3.9)-(3.11) are used to calculate the increment of backstress. Finally, the plastic strain increment and stress are obtained by using Eqs. (3.2b) and (3.13), respectively. It should be mentioned that for the

plane stress state, the thickness strain also needs to be updated. This thickness strain at the end of a time increment can be calculated using the following relationship:

$$\boldsymbol{\varepsilon}_{zz} = -\frac{v}{E}(\boldsymbol{\sigma}_{xx} + \boldsymbol{\sigma}_{yy}) - (\boldsymbol{\varepsilon}_{xx}^{p} + \boldsymbol{\varepsilon}_{yy}^{p}) \qquad (3.18)$$

where E, v are the elastic modulus and Poisson's ratio of the material respectively. σ_{xx}, σ_{yy}, ε_{xx}^{p} and ε_{yy}^{p} are all written at the end of the time increment.

3.4.1. The elastoplastic tangent modulus:

In the implementation of a plasticity model into an implicit finite element code, it is necessary to provide the tangent modulus or the material Jacobian matrix which is required for solving the equilibrium equations or momentum balance. In general, there are two methods to calculate the tangent modulus. In the first method, the plasticity equations in the rate form are used to obtain the derivative of stress with respect to strain. So, the following relationship is obtained:

$$\boldsymbol{D}_{c}^{ep} = \frac{\partial \boldsymbol{\sigma}}{\partial \boldsymbol{\varepsilon}} \qquad (3.19)$$

$\boldsymbol{D}_{c}^{ep}$ is called *continuum tangent modulus*. In the second method, the derivative of stress increment with respect to strain increment is calculated and the following equation is obtained:

$$\boldsymbol{D}^{ep} = \frac{\partial(\Delta \boldsymbol{\sigma})}{\partial(\Delta \boldsymbol{\varepsilon})} \qquad (3.20)$$

$\boldsymbol{D}^{ep}$ is called *consistent tangent modulus* because it is consistent with the stress integration algorithm. Simo and Taylor [79] showed that the consistent tangent modulus, i.e. Eq. (3.20), approaches to the continuum tangent modulus, i.e. Eq (3.19), as the increment size approaches to zero. In general, it is more challenging and difficult to

calculate the consistent tangent modulus. The advantage of using a consistent tangent modulus is that it results to the quadratic rate of asymptotic convergence for the Newton-Raphson method to solve the global finite element equilibrium equations as proved by Simo and Hughes [80]. Therefore, larger strain increment sizes can be generally solved when a consistent tangent modulus is used. Since a large increment size should not be used in the semi-implicit approach; the continuum tangent modulus was used in the user subroutine in order to prevent the user from using very large increments. In chapter 4, a fully implicit approach is used to integrate YU model and the consistent tangent modulus will be calculated.

Using the additive decomposition of strain and elastic constitutive equation, the stress is written as follows:

$$\boldsymbol{\sigma} = \boldsymbol{D}\boldsymbol{\varepsilon}^e = \boldsymbol{D}[\boldsymbol{\varepsilon} - \boldsymbol{\varepsilon}^p] \tag{3.21}$$

Time differentiation of this equation leads to:

$$\dot{\boldsymbol{\sigma}} = \boldsymbol{D}[\dot{\boldsymbol{\varepsilon}} - \dot{\boldsymbol{\varepsilon}}^p] = \boldsymbol{D}\left[\dot{\boldsymbol{\varepsilon}} - \frac{3\dot{\lambda}}{2\bar{\eta}}\boldsymbol{N}\boldsymbol{\eta}\right] \tag{3.22}$$

The plastic consistency condition states that the stress point must remain on the yield surface during plastic loading. So, the time differentiation of the yield function for the inner surface gives:

$$\dot{f} = \frac{3\boldsymbol{\eta}^T\boldsymbol{N}\dot{\boldsymbol{\eta}}}{2\bar{\eta}} = 0 \quad or \quad \boldsymbol{\eta}^T\boldsymbol{N}\dot{\boldsymbol{\eta}} = 0 \tag{3.23}$$

Substitution of Eq. (3.22) and Eq. (3.7) into Eq (3.22) gives:

$$\boldsymbol{\eta}^T\boldsymbol{N}\left[\boldsymbol{D}\dot{\boldsymbol{\varepsilon}} - \frac{3\dot{\lambda}}{2Y}\boldsymbol{D}\boldsymbol{N}\boldsymbol{\eta} - \frac{\dot{\lambda}}{Y}ca\boldsymbol{\eta} + \dot{\lambda}cY\sqrt{\frac{a}{\theta}}\dot{\boldsymbol{\theta}} - \frac{\dot{\lambda}}{Y}kb\boldsymbol{\eta} + \dot{\lambda}k\boldsymbol{\beta}\right] = 0 \tag{3.24}$$

The effective plastic strain rate is obtained by solving Eq. (3.24):

$$\dot{\lambda} = \frac{\boldsymbol{\eta}^T\boldsymbol{N}\boldsymbol{D}\dot{\boldsymbol{\varepsilon}}}{\varphi} \tag{3.25a}$$

where

$$\varphi = \boldsymbol{\eta}^T NDN\boldsymbol{\eta} + \frac{4}{9}(a.c + k.b)Y^2 - \frac{2}{3}Y.c\sqrt{\frac{a}{\theta}}\boldsymbol{\eta}^T N\boldsymbol{\theta} - \frac{2}{3}Y.k.\boldsymbol{\eta}^T N\boldsymbol{\beta} \qquad (3.25b)$$

Finally, Eq. (3.25a) is substituted back into Eq. (3.22) to find the tangent modulus:

$$\dot{\boldsymbol{\sigma}} = \left[\boldsymbol{D} - \frac{(DN\boldsymbol{\eta}) \otimes (DN\boldsymbol{\eta})}{\varphi} \right] \dot{\boldsymbol{\varepsilon}} \qquad (3.26)$$

where $\otimes$ denotes the dyadic product of two vectors.

3.4.2. Workhardening stagnation:

The experimentally obtained stress–strain curves on a mild steel exhibit apparent workhardening stagnation in a certain period of reverse deformation starting from the reverse re-yielding [34]. This phenomenon is also related to the cyclic strain-range, as well as the mean-strain.

As already mentioned, the workhardening stagnation is caused by the dissolution of dislocation cell walls during a reverse deformation. It can be expressed by the non-isotropic hardening (non-IH) of the bounding surface, since in the present model the isotropic hardening of the bounding surface represents the global workhardening due to the formation of stable dislocation structures, such as cell walls. Yoshida and Uemori defined a non-isotropic surface of J_2-type, g_σ, to account for workhardening stagnation. It is assumed that the centre of the bounding surface is located either inside this surface or on the boundary of this surface. Isotropic hardening of the bounding surface takes place if the centre of the bounding surface is located on the boundary of g_σ as shown in Fig. 3.3b. g_σ is defined as follows:

$$g_\sigma(\boldsymbol{\beta}, \boldsymbol{q}, r) = \frac{3}{2}[\boldsymbol{\beta} - \boldsymbol{q}]^T \boldsymbol{P}[\boldsymbol{\beta} - \boldsymbol{q}] - r^2 = 0 \qquad (3.27a)$$

$\dot{R} = 0$, otherwise $\hspace{6cm}$ (3.27b)

where $\boldsymbol{q}$ and r denote the centre and radius of g_σ, respectively, as shown in Fig. 3.3 and $\boldsymbol{P}$ is defined by:

$$P = \frac{1}{3}\begin{bmatrix} 2 & -1 & -1 & 0 & 0 & 0 \\ & 2 & -1 & 0 & 0 & 0 \\ & & 2 & 0 & 0 & 0 \\ & & & 3 & 0 & 0 \\ \textit{Sym.} & & & & 3 & 0 \\ & & & & & 3 \end{bmatrix}$$
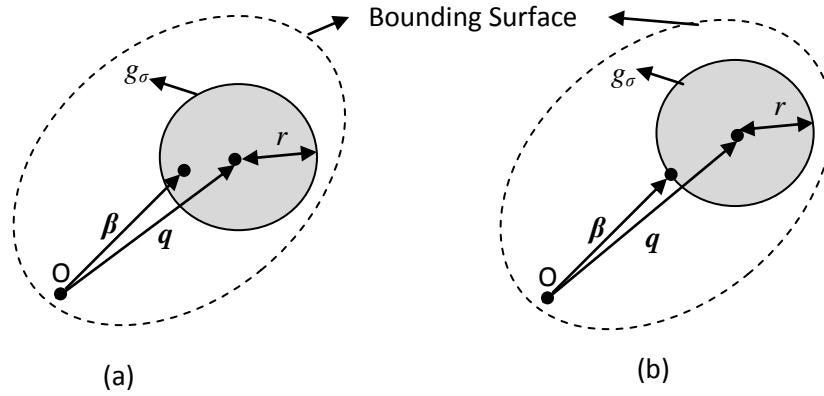
Fig. 3.3 Schematic illustration of stagnation surface: a) non-isotropic hardening ($\dot{R}$=0); b) isotropic hardening takes place ($\dot{R}$>0)

From some experimental stress–strain curves under a large-strain reverse deformation, it was found that the plastic strain region of workhardening stagnation increases with the accumulated plastic strain. Such a phenomenon can be expressed by the expansion of the surface g_σ with increasing plastic strain. Yoshida and Uemori assumed the kinematic motion of the surface g_σ such that the center of g_σ moves in the direction of $(\boldsymbol{\beta} - \boldsymbol{q})$, as:

$$\dot{\boldsymbol{q}} = \mu[\boldsymbol{\beta} - \boldsymbol{q}] = \mu\boldsymbol{\xi} \hspace{5cm} (3.28)$$

where $\xi = \beta - q$ and μ is obtained by imposing the consistency condition which states that the centre point of the bounding surface should be either on, or inside, the stagnation surface:

$$\mu = \frac{3\xi^T P \dot{\beta}}{2r^2} - \frac{r}{\dot{r}} \tag{3.29}$$

The following evolution equation for the evolution of r was assumed by Yoshida and Uemori:

$$\dot{r} = h \frac{3\xi^T P \dot{\beta}}{2r} \quad \text{when } \dot{R} > 0 \tag{3.30a}$$

$$\dot{r} = 0 \quad \text{when } \dot{R} = 0 \tag{3.30b}$$

where $(0 \leq h \leq 1)$ denotes a material parameter that determines the rate of expansion of surface g_σ. The larger value of h gives a rapid expansion of the non-IH surface, and as a result, it leads to the prediction of less cyclic hardening. Since the non-IH (workhardening stagnation) appears during reverse deformation after prestrain, the initial value of r may be assumed to be zero.

A description of the integration of the stagnation equations is now presented. Integration of Eq. (3.30a) and (3.28) using the Euler backward method leads to:

$$r^2 = r_n^2 + 3h\xi^T P \Delta\beta \tag{3.31}$$

$$\Delta q = \Delta\mu\xi \tag{3.32}$$

Furthermore, Eq. (3.32) is used to calculate ξ:

$$\xi = \beta - q = \beta - q_n - \Delta q = \beta - q_n - \Delta\mu\xi \tag{3.33}$$

$$\xi = \frac{\xi_n}{1 + \Delta\mu} \tag{3.34}$$

where $\xi_n = \beta - q_n$.

Substituting Eqs. (3.34) and (3.31) into Eq. (3.27a) yields the following quadratic equation:

$$\frac{3}{2}\boldsymbol{\xi}_n^T\boldsymbol{P}\boldsymbol{\xi}_n - 3h\boldsymbol{\xi}_n^T\boldsymbol{P}\Delta\boldsymbol{\beta}[1 + \Delta\mu] - r_n^2[1 + \Delta\mu]^2 = 0 \tag{3.35}$$

The analytical solution to this equation is obtained as follows:

$$\Delta\mu = \frac{3h\boldsymbol{\xi}_n^T\boldsymbol{P}\Delta\boldsymbol{\beta} + \sqrt{[3h\boldsymbol{\xi}_n^T\boldsymbol{P}\Delta\boldsymbol{\beta}]^2 + 4r_n^2\left[\frac{3}{2}\boldsymbol{\xi}_n^T\boldsymbol{P}\boldsymbol{\xi}_n\right]}}{2r_n^2} - 1 \tag{3.36}$$

Once $\Delta\mu$ is known, $\boldsymbol{\xi}$ is obtained using Eq. (3.34) and then $\boldsymbol{\beta}$ is found by Eq. (3.33) at the end of the time increment. The radius of the stagnation surface, r, is also obtained by Eq. (3.31). Therefore, the location and radius of the stagnation surface is found at the end of the increment.

At the beginning of deformation, it is assumed that the isotropic hardening does not take place. The stress integration algorithm is run first to calculate the stress and all internal variables, i.e. $\boldsymbol{\beta}$, $\boldsymbol{\theta}$, $\boldsymbol{\alpha}$, R. Then, the stagnation surface calculations are done to find the final position and size of the stagnation surface, i.e. $\boldsymbol{q}$ and r. If the centre of the bounding surface is located inside the stagnation surface, all solutions are accepted as final solutions. However, if the centre of the bounding surface is located on the boundary of the stagnation surface, this means that isotropic hardening should take place. Therefore, the current strain increment should be divided into two sub-increments. In the first sub-step, the centre of the bounding surface moves within the stagnation surface until it arrives at the boundary of the stagnation surface. In the second sub-step, the centre of the bounding surface remains on the boundary of the stagnation surface and isotropic hardening takes place. It is generally difficult and time consuming to find when the centre of the bounding surface reaches the boundary of the stagnation surface. Nevertheless, if the strain increment size is selected to be small, the change from non-isotropic hardening to isotropic hardening can be neglected. In other words, if the centre of the bounding surface lies on the boundary of the stagnation surface at the end of a time increment, it can be assumed that isotropic hardening takes place for this increment. As mentioned at

the beginning of this section, sub-step algorithm is utilized to make sure that the increment size is small enough for the subroutine. Therefore, in order to reduce computation time, the stagnation condition (Eq. 3.27) is checked at the end of each increment. After isotopic hardening occurs, the current status is saved in a state variable for the next increment. The isotropic hardening of the bounding surface takes place until unloading occurs. In the first unloading increment, the stress integration algorithm calculates the stress and all internal variables. Then, the final position and size of the stagnation surface is obtained. The final position of the bounding surface shows that the centre of the bounding surface is located inside the stagnation surface. So, the algorithm determines that isotropic hardening should not take place. The stress integration is re-run to calculate the stress and internal variables assuming that isotropic hardening does not take place. In summary, the isotropic hardening assumption is first made based on the previous increment. At the end of the increment, the solution is accepted if the assumption was correct. If not, the isotropic assumption will be changed and the stress integration subroutine is re-run. The numerical algorithm for implementation of this model is shown in Table A.1.

3.4.3. Decrease of unloading elastic modulus:

Luo and Ghosh [81] have reported that the elastic modulus during unloading and reloading is different from the initial elastic modulus in the un-deformed state. Levy *et al.* [82] also reported that the apparent unloading modulus is smaller than the initial elastic modulus and experimentally obtained the variation of unloading modulus as a function of plastic strain for AKDQ and DP600 sheet materials. Benito *et al.* [83] also observed that the elastic modulus of polycrystalline pure iron decreases with plastic deformation during a tensile test at room temperature. They measured the residual stresses and texture and observed the dislocation structure by TEM. Since they did not observe any significant change in texture during the deformation, they concluded that the decrease of elastic modulus was not due to either a change of texture or to residual stresses. They stated that

the dislocation arrangement change results in diminution of elastic modulus and proposed a relationship between these two parameters. Yang *et al.* [84], Cleveland and Ghosh [85] and Morestin and Boivin [86] have also reported the decrease of unloading modulus. Since the decrease of unloading modulus has a significant effect on the prediction of springback, the following empirical equation was used by Yoshida and Uemori [40,55] in YU model to take the decrease of unloading modulus into account:

$$E = E_0 - [E_0 - E_a][1 - \exp(-\zeta p)] \tag{3.37}$$

where E_0 and E_a are Young's modulus for as-received and infinitely large prestrained materials, respectively, and ζ is a material constant which determines the rate of decrease of the effective unloading modulus with respect to plastic strain. In simulation of BM#3, which is presented in the next section, the elastic modulus was taken to be constant during the forming stage, and the reduced unloading modulus was used in the springback simulation stage.

3.5. Hourglass Control:

If an element in reduced integration mode is used in ABAQUS/Standard, the hourglass stiffness needs to be calculated. Because ABAQUS/Standard calculates the hourglass stiffness by using the elastic properties of the material, it requires the hourglass stiffness when a UMAT is used in the simulation. So, the user must define the hourglass stiffness factor for hourglass control based on the total stiffness approach as part of the element section definition. It should be mentioned that the hourglass stiffness factor is not required for enhanced hourglass control in ABAQUS.

Normally the hourglass control stiffness is defined from the elasticity associated with the material. In most cases it is based on a typical value of the initial shear modulus of the material, which may, for example, be given as part of the elastic material definition. For an isotropic elastic or hyperelastic material G^E is the shear modulus. For a non-isotropic

elastic material an average shear modulus is used to calculate the hourglass stiffness. The default values for the stiffness factors are defined below.

- For membrane or solid elements:

$$r_F = 0.005G^E \tag{3.38}$$

- For membrane hourglass control in a shell:

$$r_F = 0.005 \frac{\int_{-t/2}^{t/2} G^E . dt}{t} \tag{3.39}$$

where r_F denotes the hourglass stiffness factor and t is the thickness of the shell. The above formulations are used to obtain the hourglass stiffness factor for the element [87].

3.6. Transverse Shear Stiffness:

If user subroutine UMAT is used to describe the material of beams or shells that calculate transverse shear energy, the user must specify the transverse shear stiffness as part of the beam or shell section definition to define the transverse shear behaviour. For all shell elements in ABAQUS/Standard that use transverse shear stiffness and for the finite-strain shell elements in ABAQUS/Explicit, the transverse shear stiffness is computed by matching the shear response for the shell to that of a three-dimensional solid for the case of bending about one axis.

In all shell elements in ABAQUS/Standard that are valid for thick shell problems or that enforce the Kirchhoff constraint numerically and in the finite-strain shell elements in ABAQUS/Explicit, ABAQUS computes the transverse shear stiffness by matching the shear response for the case of the shell bending about one axis, using a parabolic variation of transverse shear stress in each layer. In calculating the transverse shear

stiffness, ABAQUS assumes that the shell section directions are the principal bending directions (bending about one principal direction does not require a restraining moment about the other direction). For composite shells with orthotropic layers that are not symmetric about the shell midsurface, the shell section directions may not be the principal bending directions. In such cases the transverse shear stiffness is a less accurate approximation and will change if different shell section directions are used. ABAQUS computes the transverse shear stiffness only once at the beginning of the analysis based on initial elastic properties given in the model data. Any changes to the transverse shear stiffness that occur due to changes in the material stiffness during the analysis are ignored.

The transverse shear stiffness should be specified as the initial, linear elastic stiffness of the shell in response to pure transverse shear strains. For a homogeneous shell made of a linear, orthotropic elastic material, where the strong material direction aligns with the element's local 1-direction, the transverse shear stiffness should be:

$$K_{11}^{ts} = \frac{5}{6} G_{13}^E t \,, K_{22}^{ts} = \frac{5}{6} G_{23}^E t \ \text{ and } K_{12}^{ts} = K_{21}^{ts} = 0 \tag{3.40}$$

where G_{13}^E and G_{23}^E are the material's shear moduli in the out-of-plane direction. The number 5/6 is the shear correction coefficient that results from matching the transverse shear energy to that for a three-dimensional structure in pure bending [87].

3.7. Identification of Material Constants:

YU model contains seven material parameters ($Y, c, B, R_{sat}, b, k, h$). There are generally two ways to obtain the material parameters. The first method is to use an optimization method to fit the simulation stress-strain curve to that of the experiment. The second method is to use a systematic way to identify the material constants from the stress-strain

curve in cyclic deformation. In this project, the second method was used to find the constants for YU model. Now, each of these methods are described.

3.7.1. Optimization method:

Let $\boldsymbol{x} = [Y, c, B, R_{sat}, b, k, h]$ denote a set of material parameters to be identified. The purpose is to find the vector x that minimizes the objective function:

$$F(\boldsymbol{x}) = \sum_{i=1}^{L} s^i F^i(\boldsymbol{x}), \quad A_j \leq x_j \leq B_j, (j = 1,2,\dots,N) \tag{3.41}$$

where L is the total number of individual forward or reverse deformations (denoted by i). A_j and B_j are the lower and upper limits of the searching area for a material parameter x_i. $F^i(\boldsymbol{x})$ is the dimensionless function defined as the square difference in stress between the experimental data, $\sigma_{s(\exp)}^i$, and the corresponding calculated results for an assumed set of material parameters $\boldsymbol{x}$, $\sigma_{(\text{cal})}^i(x, \varepsilon_s^i)$ as:

$$F^i(\boldsymbol{x}) = \left\{ \sum_{s=1}^{S_i} [\sigma_{s(\exp)}^i - \sigma_{(\text{cal})}^i(x, \varepsilon_s^i)]^2 \right\} / \left\{ \sum_{s=1}^{S_i} [\sigma_{s(\exp)}^i]^2 \right\} \tag{3.42}$$

where S_i is the total numbers of data points in i-th stress–strain response. In Eq. (3.41), S^i is the weight coefficient which determines the relative contribution of i-th set of experimental data. For the minimization of the objective function, Yoshida and Uemori successfully used an optimization technique based on the iterative multipoint concept [88-90] and found the set of material parameters simultaneously.

3.7.2. Systematic method:

In this method, the cyclic stress-strain curve is used to calculate the parameters as follows:

- Y is equal to the initial yield stress

- The cyclic curve is extrapolated at the beginning of each cycle to find the bounding stress curve. The bounding stress curve is used in the first cycle to fit the experimental curve to Eq. (3.8). Therefore, parameters B, $(R_{sat} + b)$ and k will be found.

- In order to find b, we need to find $\sigma_{B0}^{(p)}$ which is equal to the difference between the experimental yield stress and predicted yield stress by isotropic hardening model at the beginning of reverse loading. From Eq. (3.6), the amount of softening at the beginning of reverse loading is given by:

$$\sigma_{B0}^{(p)} = 2\beta_0 = 2b(1 - e^{-kp_0}) \tag{3.43}$$

where β_0 denotes the kinematic hardening of the bounding surface at the stress reversal point, and p_0 is the plastic prestrain at the beginning of reverse loading. From Eq. (3.43), the parameter b is obtained. Since $(R_{sat} + b)$ is already known from the previous step, R_{sat} is also obtained.

- Parameter c is identified from the stress–strain curve of the transient Bauschinger deformation. From Eq. (3.4), for reverse deformation after large forward prestrain, we have

$$c \approx \frac{2}{p}\left[(1 + ln2) - \sqrt{\frac{|\theta|}{a}} + ln\left(1 + sgn(\theta)\sqrt{\frac{|\theta|}{a}}\right)\right] \tag{3.44}$$

- Parameter h is identified by the numerical simulation of such cyclic stress–strain responses so as to obtain the best-fit curves to the corresponding experimental results.

3.8. Verification of the User Material Subroutine:

In this section, the UMAT and VUMAT based on Hill's quadratic yield function and YU model are used to simulate a few problems and verify it is able to work properly under different loading conditions. The simulation results will be evaluated either quantitatively or qualitatively. As a first evaluation, every problem can be simulated by both UMAT and VUMAT to compare the results. The following problems were simulated by both UMAT and VUMAT and it was found that both UMAT and VUMAT yielded almost the same results. Therefore, in the following the simulation results are referred to UMAT and I will not distinguish between UMAT and VUMAT. The material is assumed to be ADKQ in the following simulations. The experimental yield stress and r-values in each direction is given in Table 3.1. The material coefficient associated with YU model were found by fitting the simulation results to the experimental stress-strain curve obtained by the cyclic shear test. In addition, the experimental yield stresses in each direction were used to find the Hill's coefficients. The material constants associated with YU model and Hill's quadratic yield function are shown in Tables 3.2 and 3.3 respectively.

Table 3.1. The experimental yield stress and r-values in different directions

Yield stress, MPa		r-value	
σ_0	158.3	r_0	1.546
σ_b	183.0	r_{45}	1.508
σ_{90}	166.7	r_{90}	1.942
τ_{xy}	84.0		

Table 3.2. The Yoshida-Uemori material constants

Material	Y (MPa)	c	B (MPa)	R_{sat} (MPa)	b (MPa)	k	h	E_0 (GPa)	E_a (GPa)	ζ
AKDQ	158	300	190	240	10	8.5	0.7	206	178	160

Table 3.3. Coefficients of Hill's 1948 yield function

Material	F	G	H	N
AKDQ	0.329	0.419	0.581	1.776

3.8.1. Uniaxial tension:

The uniaxial tension loading can be used as a very simple and initial test to verify the UMAT. This type of loading is interesting as it causes a homogenous deformation in the structure and only one element is required in the simulation. The advantage of using one element is that the solution will not depend on the mesh size. The uniaxial tension is a very simple type of loading and in many cases it is easy to obtain an analytical solution for the problem. Therefore, if the user can analytically integrate the plasticity equations for uniaxial stress state, the relative error associated with the numerical integration of the model can be easily estimated. So, the uniaxial tension of a square part in the plane stress state is first simulated. A square of 1 mm by 1 mm was simulated using the user material subroutine. The bottom side of the square was fixed in the Y-direction and the node located in the left bottom corner was fixed in both X and Y-directions. The right and top sides of the square were displaced 0.2 mm in the Y-direction. A first-order quadrilateral element in the reduced integration mode, denoted as CPS4R, was used to mesh the part. The schematic of the finite element model is shown in Fig. 3.4.

As mentioned in section 3.3, the bounding stress for uniaxial monotonic loading is obtained by Eq. (3.8). Therefore, as plastic deformation occurs, the stress should start from the yield strength and gradually approach to the stress in the bounding stress. Depending on the material constants, the stress should reach the bounding stress after a

certain amount of stress. The bounding stress was obtained using Eq. (3.8) for AKDQ and plotted in Fig. 3.5. The stress versus plastic strain obtained by simulation was also plotted in Fig. 3.5. This figure shows that the stress starts from the yield stress, which is below the bounding stress, approaches and finally reaches the bounding stress after a large amount of plastic strain.
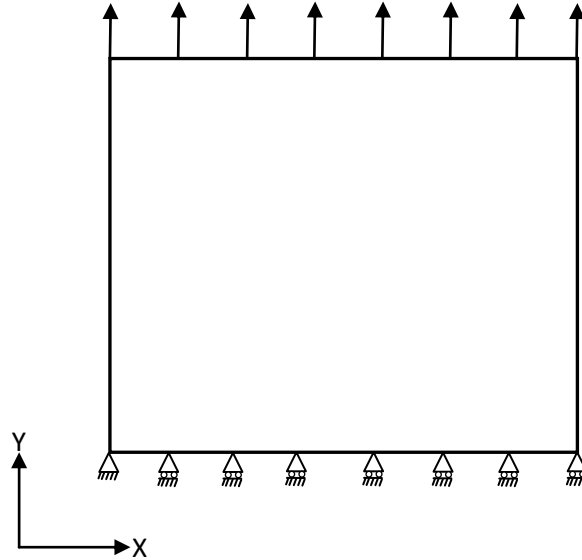
Fig. 3.4. Schematic representation of the finite element model for the uniaxial tension test

The uniaxial tension test can also be used to evaluate the implementation of the yield function. Hill's anisotropic coefficients were obtained from the uniaxial tensile yield stress of the material in the rolling, and transverse directions, and from the equibiaxial and shear yield stresses. Therefore, if the yield stress obtained by simulation in each of these stress states correlates with their corresponding experimental value, it can be concluded that the yield function was correctly implemented for each type of loading. Here, the uniaxial tension, equibiaxial loading and shear test were all simulated by UMAT and the yield stress in each problem was obtained by simulation. It was found that the UMAT reproduces the experimental yield stresses for all of these stress states. Therefore, Hill's function was considered to be correctly implemented.
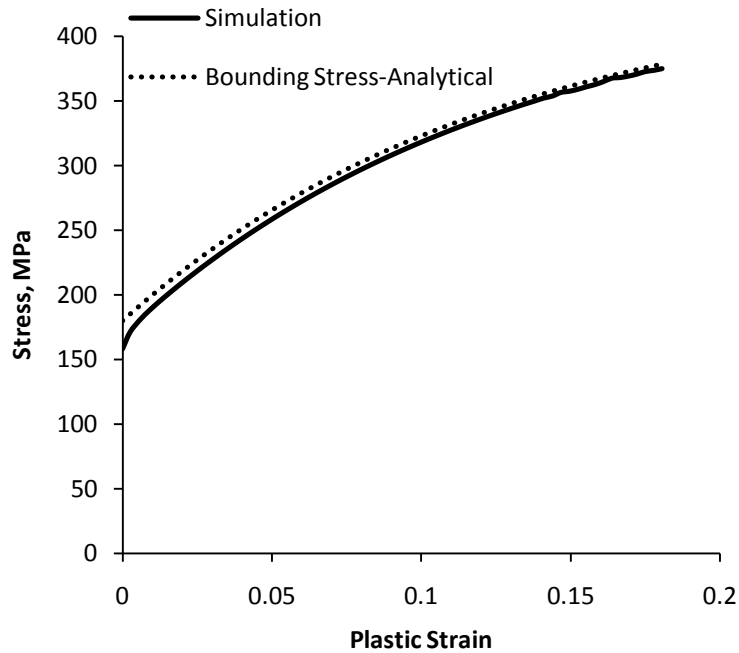
Fig. 3.5. The stress and bounding stress in uniaxial tension

3.8.2. Biaxial loading:

Uniaxial tension evaluates the user material subroutine during loading in only one direction. It is also useful to evaluate the user material subroutine during a multiaxial loading. The biaxial bulge test is one of the most popular tests in sheet metal forming and it is also a good example of multiaxial loading. Since all cyclic phenomena occur during reverse loading, the YU model must predict the same results as isotropic hardening in monotonic loading. Therefore, it is expected that both isotropic hardening and YU model predict the same results for the bulge test as the loading is monotonous in this test. The equibiaxial loading of a 1 mm square sheet was simulated with both our UMAT and an ABAQUS built-in material model which is based on Hill's quadratic yield function and the isotropic hardening law. The left and bottom sides of the square were fixed in the X and Y-directions, respectively. The right and top sides of the square were displaced 0.1 mm in both X and Y-directions. A 4-node element with linear shape function in the reduced integration mode, denoted as CPS4R, was used to mesh the part. The schematic

of the finite element model is shown in Fig. 3.6. Fig. 3.7 compares the stress-strain response of the material obtained by UMAT and ABAQUS built-in material model (isotropic hardening model) in the equibiaxial loading. This figure shows that, as expected, the results obtained by UMAT and isotropic hardening model are identical.
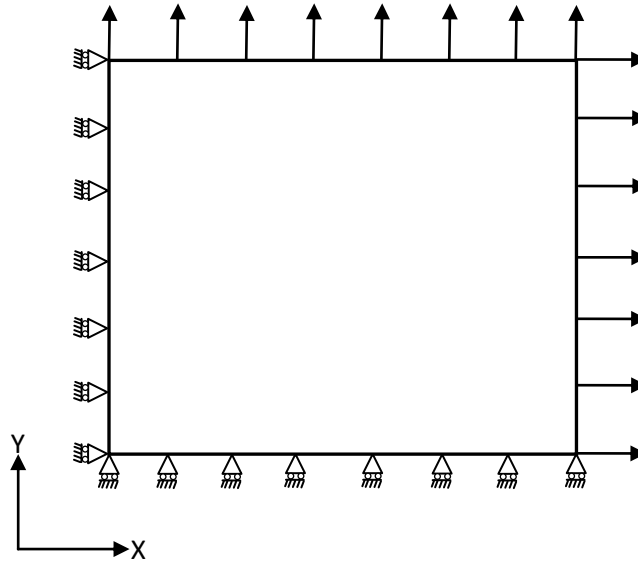
Fig. 3.6. Schematic representation of the finite element model for the biaxial bulge test
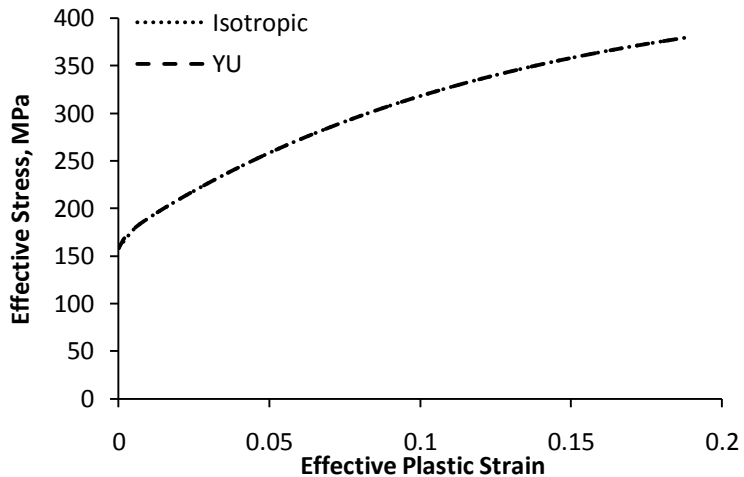
Fig. 3.7. Stress-strain response of the material in equibiaxial loading obtained by YU model (UAMT) and isotropic model (ABAQUS built-in material model)

3.8.3. Bending of a cantilever beam:

As explained in the previous problem, the YU model and isotropic hardening must predict the same amount of stress in monotonic loading. So, any monotonic loading problem can be simulated by using UMAT and then compared with the stress results obtained by isotropic hardening of ABAQUS built-in material model. Bending of a cantilever beam in one direction is an example of monotonic loading. This problem can evaluate the accuracy of the stress integration in the UMAT for forward bending compared with ABAQUS. A rectangle of 1 mm wide and 10 mm long was fixed at one end and vertically displaced downward 2 mm at the other end which is schematically shown in Fig. 3.8. A first-order quadrilateral element in the reduced integration mode, denoted as CPS4R, was used to mesh the part. The mesh size was selected to be 0.25 mm by 0.25 mm in the X and Y-directions. Figs. 3.9 and 3.10 show the von Mises stress contour on the deformed part obtained by ABAQUS built-in material model based on isotropic hardening and the UMAT based on YU model, respectively. A comparison of these two contours shows that both the ABAQUS built-in material model and the UMAT yield practically the same results for this problem. Fig. 3.11 also shows the predicted stress on the top surface of the beam obtained by ABAQUS built-in material model and UMAT.
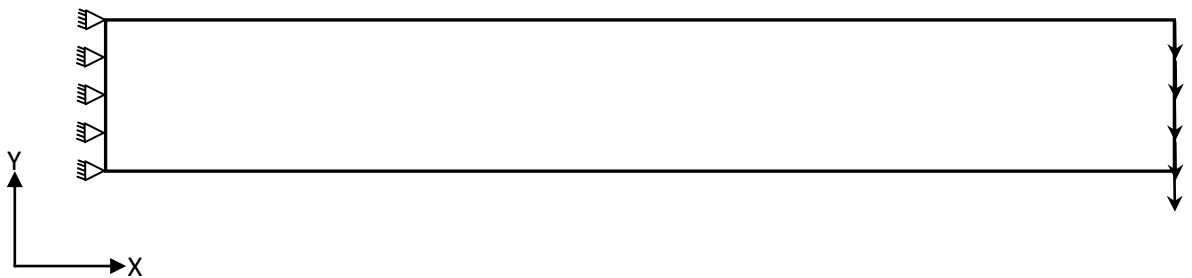
Fig. 3.8. Schematic of the cantilever beam and the boundary conditions
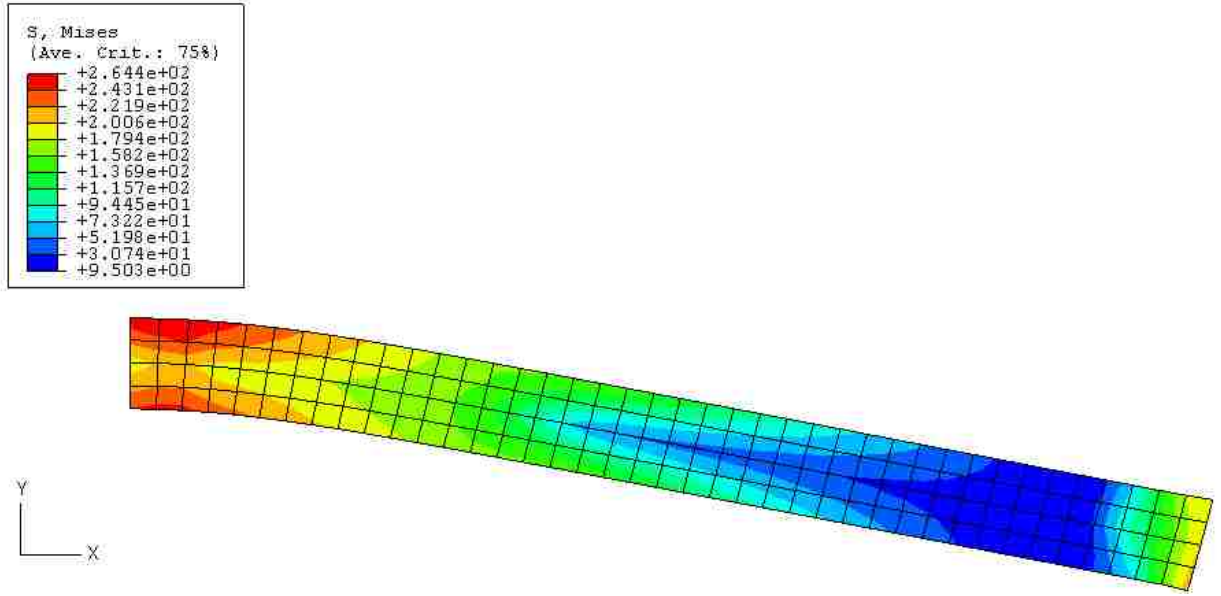
Fig. 3.9. von Mises stress contour on the deformed part obtained by ABAQUS built-in material model based on isotropic hardening model
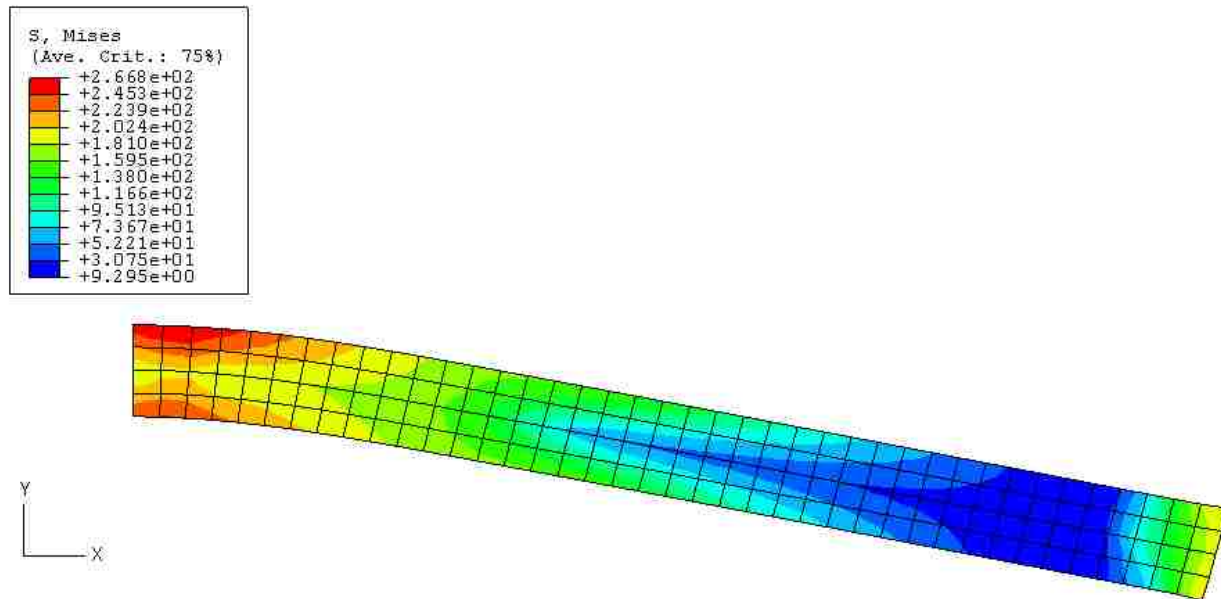
Fig. 3.10. von Mises stress contour on the deformed part obtained by UAMT based on the YU model
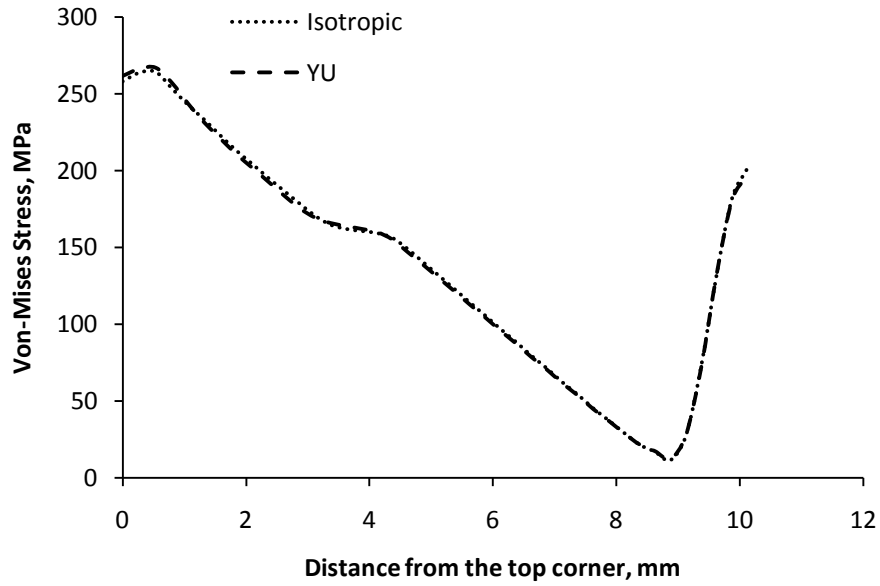
Fig. 3.11. von Mises stress along the top surface of beam

3.8.4. Combined tension-shear:

Again the isotropic hardening and YU model are used to simulate a combined tension-shear loading. The element CPS4R is again used to mesh a 1 mm by 1 mm square. The bottom side was fixed in all directions. The top side is displaced 0.1 mm in the X-direction and 0.15 mm in the Y-direction. Fig. 3.12 shows a schematic of the problem and boundary conditions. Fig. 3.13 compares the effective stress-strain response of the material obtained by ABAQUS built-in material and UMAT. As can be seen, the results obtained by ABAQUS built-in material model and UMAT are almost identical.
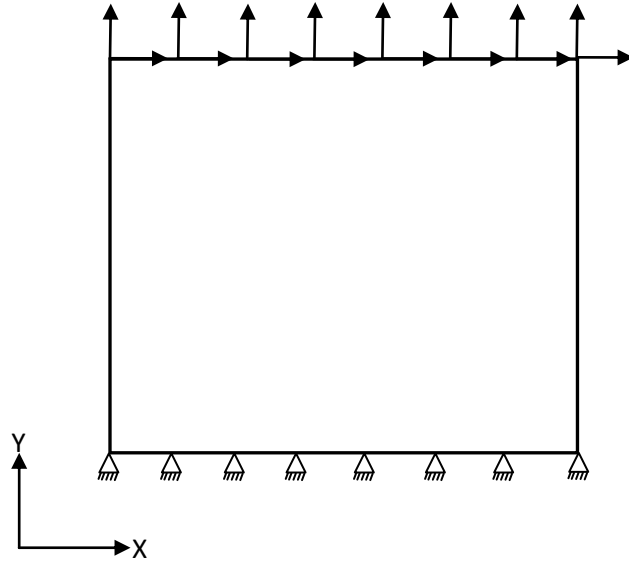
Fig. 3.12. Schematic of the combined shear-tension problem and the boundary conditions
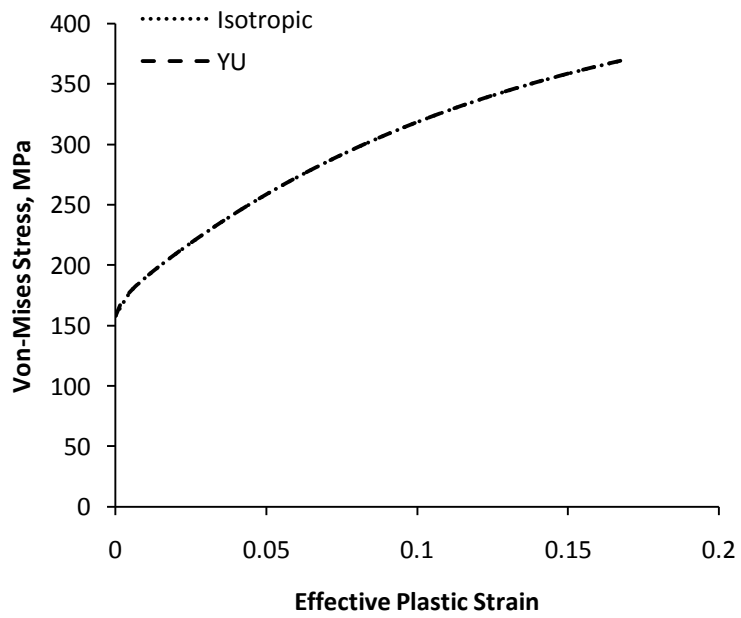
Fig. 3.13. Stress-strain response of the material obtained by UMAT and ABAQUS built-in material model

3.8.5. Evaluation of UMAT under cyclic loading:

In all of the above problems, the UMAT was used to simulate a variety of monotonic loading conditions. Therefore, they do not evaluate the accuracy of the stress integration during the cyclic loading conditions. In the remaining problems of this chapter, the cyclic loading of the biaxial bulge test and cyclic bending of a cantilever beam are simulated using both UMAT and an ABAQUS built-in material model based on combined isotropic-nonlinear kinematic hardening (NKH). The NKH model is not able to capture the workhardening stagnation. Therefore, it is not able to describe the cyclic behaviour of AKDQ very well and cannot be compared with YU model. In order to compare NKH with YU model, it is assumed that the experimental cyclic stress-strain behaviour of a fictitious material was obtained by NKH as shown in Fig. 3.14. The material constants associated with each model is shown in Table 3.4 for this material. Now, it is expected that both YU and NKH models predict almost the same results for different problems at different cyclic loading conditions. The cyclic biaxial loading and cyclic bending of a cantilever beam are simulated using YU and NKH models and compare the results.

Table 3.4. The material constants associated with YU and NKH models for fictitious material

YU model		NKH model	
E	210 GPa	E	210 GPa
Y	160 MPa	Y	160 MPa
c	200	Q	100 MPa
B	180 MPa	b	8
R_{sat}	120 MPa	C	5000 MPa
b	200 MPa	γ	20
k	17		
h	0.01		
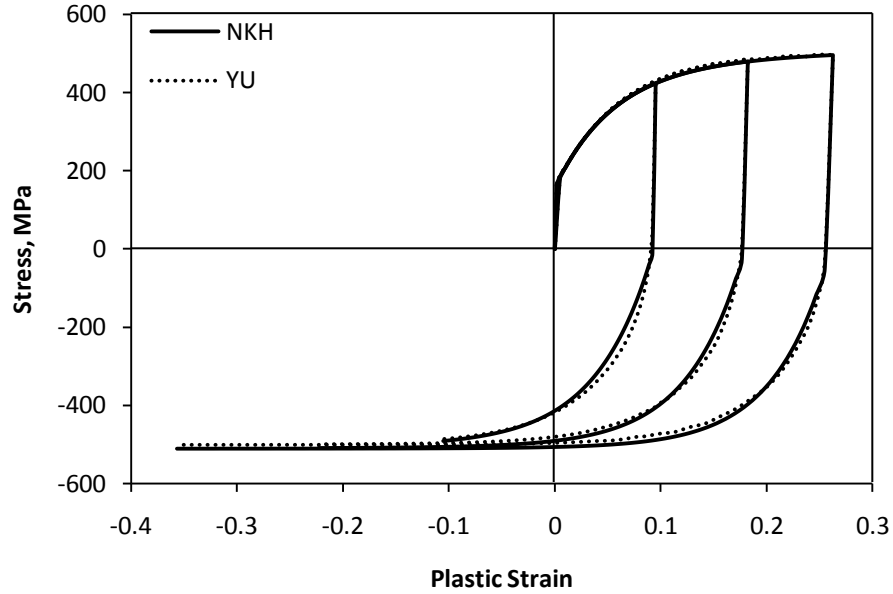
Fig. 3.14. Stress-strain response of a fictitious material obtained by UMAT (YU model) and ABAQUS built-in material (NKH model)

The equibiaxial loading of a square of 1x1 mm is first simulated by both our UMAT and NKH models. The left and bottom sides of the square are fixed the X and Y-directions, respectively. In the first loading step, the right and top sides of the square were displaced 0.1 mm in the X and Y-directions. In the second loading step, the right and top sides of the square were displaced 0.2 mm in the negative X and Y-directions. Fig. 3.6 shows the schematic of the problem in the first loading step. A four-node element with linear shape function in the reduced integration mode, denoted as CPS4R, was used to mesh the part. Fig. 3.15 compares the stress-strain response of the material obtained by UMAT and NKH models in the cyclic equibiaxial loading. The figure shows that the YU model predicts almost the same response as NKH model.
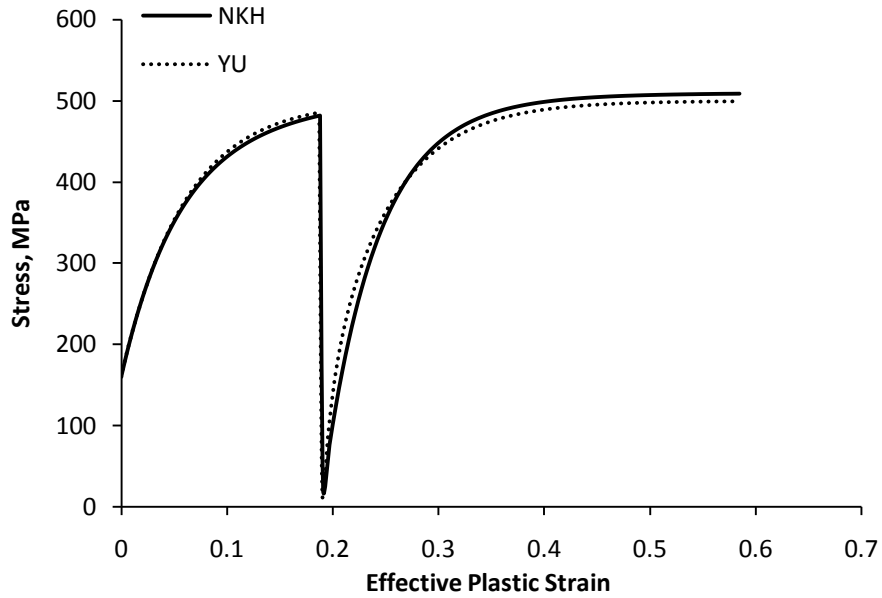
Fig. 3.15. Comparison of stress-strain response obtained by NKH and YU models in cyclic equibiaxial loading

In order to evaluate the UMAT in bending-reverse bending, the cyclic bending of cantilever beam was simulated using both YU and NKH. A rectangle of 1 mm wide and 10 mm long was fixed at one end. The other end was first displaced 2 mm downward and then displaced 4 mm in the opposite direction. This type of loading causes a bending-unbending-reverse bending deformation in the material. A first-order quadrilateral element in the reduced integration mode, denoted as CPS4R, was used to mesh the part. The mesh size was selected to be 0.25 mm by 0.25 mm in the X and Y-directions. A schematic of the problem and the boundary conditions in the first loading step is shown in Fig. 3.8. The problem was simulated with both our UMAT and an ABAQUS built-in material model based on NKH. Fig. 3.16 shows the predicted stress on the top surface of the beam obtained by ABAQUS built-in material model and UMAT.
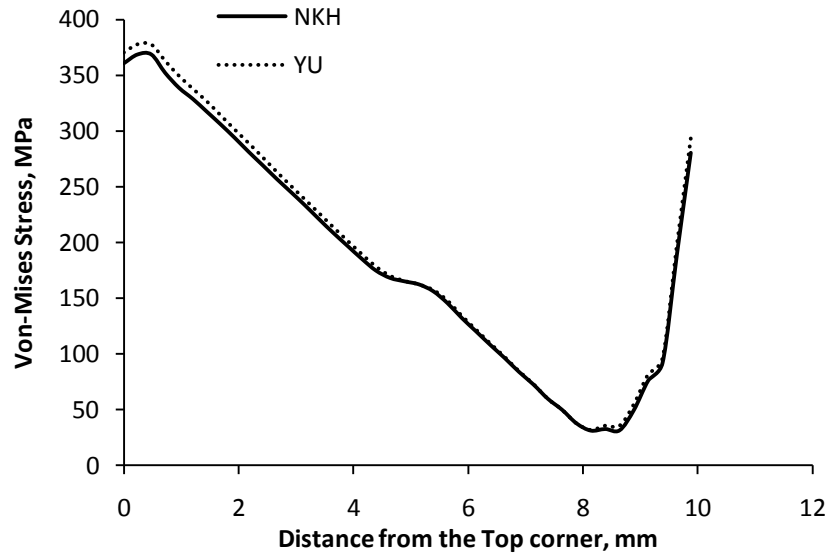
Fig. 3.16. von Mises stress along the top surface of beam at the end of reverse bending

The above simulations show that the UMAT is able to accurately predict the stress field in the part in several loading conditions such as tension, equibiaxial loading, bending and cyclic loading. The uniaxial tension is different direction also shows that UMAT correctly predicts the yield stress in the rolling, transverse directions. Moreover, simulation of equibiaxial bulge test and pure shear show that the UMAT correctly predicts the yield stress in these loading conditions for orthotropic sheet. The UMAT also correctly predicts the stress for combined loading such as combined shear-tension and combined bending-shear, i.e. cantilever beam. Therefore, it can be concluded that the material user subroutine has been correctly implemented.

Chapter 4

Fully Implicit Numerical Integration of Yoshida-Uemori Two-Surface Plasticity Model

4.1. Introduction:

In chapter 3, the Yoshida-Uemori two-surface plasticity model (YU) was introduced and a semi-implicit scheme was used to integrate this model. The Hill's quadratic yield function was used to consider the anisotropy of the material. As mentioned in chapter 3, the semi-implicit integration scheme is conditionally stable, and therefore, may not be able to converge to the solution if a large strain increment is used. The main advantages of the semi-implicit approach are its simplicity of implementation and its computational efficiency. In this chapter, a fully implicit integration scheme is used to integrate all equations including the backstress and a numerical algorithm is developed for implementation of this model into a finite element program. The numerical algorithm is implemented such that any general yield function could be used in the model. Both Hill's quadratic function and Yld2000-2d function, proposed by Barlat et al. [31], are adopted to develop user-defined material subroutines for ABAQUS-Explicit (VUMAT) and ABAQUS-Standard (UMAT). Yld2000-2d is a non-quadratic yield function developed for highly anisotropic materials such as aluminum alloys. This function will be introduced in detail in section 4.6.

The YU model is a two-surface plasticity model with two nonlinear kinematic evolutions for each surface. The outer surface grows uniformly in stress space while the size of the inner surface is kept constant. Since the inner surface does not change its size, the model is able to capture early re-yielding during reverse loading. The isotropic hardening of the bounding surface is also used to represent the strain hardening of the material. A non-isotropic hardening surface is also defined in this model to account for the workhardening stagnation. Two nonlinear kinematic hardening evolutions for each surface make it possible to describe the transient and permanent behaviour of the material during reverse loading. So, this model is capable of reproducing the transient Bauschinger effect, permanent softening and workhardening stagnation in large elasto-plastic deformation relatively accurately. This model was introduced in section 3.3. In the next section, the return mapping procedure is used to develop a numerical algorithm for implementation of this model into a finite element program.

4.2. Stress Integration:

In the following equations, the subscript n is used to denote a quantity at the beginning of the nth time increment. If no subscript is used, this quantity is evaluated at the end of the increment. The Euler backward method (implicit) is used to integrate all plasticity equations including the backstress. So, all variables are referred to their values at the end of the time increment during integration. Using this method, integration of Eqs. (3.3a), (3.6) and (3.7) in the materially embedded coordinate system leads to the following equations:

$$\Delta\boldsymbol{\theta} = \left[\frac{a.c}{Y}\boldsymbol{\eta} - c\sqrt{\frac{a}{\bar{\theta}}}\boldsymbol{\theta}\right]\Delta p \qquad (4.1)$$

$$\Delta\boldsymbol{\beta} = \left[\frac{k.b}{Y}\boldsymbol{\eta} - k\boldsymbol{\beta}\right]\Delta p \qquad (4.2)$$

$$\Delta\boldsymbol{\alpha} = \Delta\boldsymbol{\beta} + \Delta\boldsymbol{\theta} \qquad (4.3)$$

The following general equation is assumed to define the yield surface in stress space:

$$f = \bar{\eta} - Y = 0 \tag{4.4}$$

where Y is the initial yield strength of the material and $\bar{\eta}$ is the effective value for $\boldsymbol{\eta}$. According to the associated flow rule, the increment of plastic strain is obtained by taking the derivative of the yield function with respect to stress. And, the plastic strain increment is obtained as follows:

$$\Delta \boldsymbol{\varepsilon}^p = \Delta p \frac{\partial \bar{\sigma}}{\partial \boldsymbol{\sigma}} = \Delta p \frac{\partial \bar{\eta}}{\partial \boldsymbol{\sigma}} = \Delta p \boldsymbol{m} \tag{4.5}$$

where $\boldsymbol{m}$ denotes the normal to the yield surface and Δp is the effective plastic strain increment which is obtained by solving the yield equation in the return map procedure. In the return map method, it is first assumed that the total strain increment is fully elastic. Then, the yield surface equation is used to find the effective stress. If the effective stress is less than, or equal to, the flow stress, then the deformation is fully elastic and the trial stress is accepted as the solution. If the effective stress is larger than the flow stress, the correction for effective plastic strain and all internal state variables is found and the new stress is updated by reducing the increment of plastic strain from the total strain increment. This iteration continues until the updated stress state satisfies the yield function equation. Mathematically, the return map equation is written as follows:

$$\boldsymbol{\sigma} = \boldsymbol{\sigma}^{Tr} - \boldsymbol{D}[\Delta \boldsymbol{\varepsilon}^p] \tag{4.6}$$

where $\boldsymbol{\sigma}$ is the stress at the end of the time increment, $\boldsymbol{D}$ is the elasticity tensor and $\boldsymbol{\sigma}^{Tr}$ denotes the trial stress. This incremental relationship is expressed in a materially embedded coordinate system. Therefore, it is objective with respect to material rotation. The trial stress is obtained by the elastic constitutive law, assuming that the total strain increment is elastic, as follows:

$$\boldsymbol{\sigma}^{Tr} = \boldsymbol{\sigma}_n + \boldsymbol{D}[\Delta \boldsymbol{\varepsilon}] \tag{4.7}$$

The updated stress is obtained by substituting the plastic strain increment from Eq. (4.5) into Eq. (4.6):

$$\boldsymbol{\sigma} = \boldsymbol{\sigma}^{Tr} - \boldsymbol{D}[\Delta p\boldsymbol{m}] \tag{4.8}$$

Now, the updated stress is used to calculate the effective stress based on the yield function. So, the yield condition at the end of time increment leads to the following equation:

$$f = \bar{\sigma}(\boldsymbol{\sigma}^{Tr} - \Delta p\boldsymbol{Dm}) - Y = 0 \tag{4.9}$$
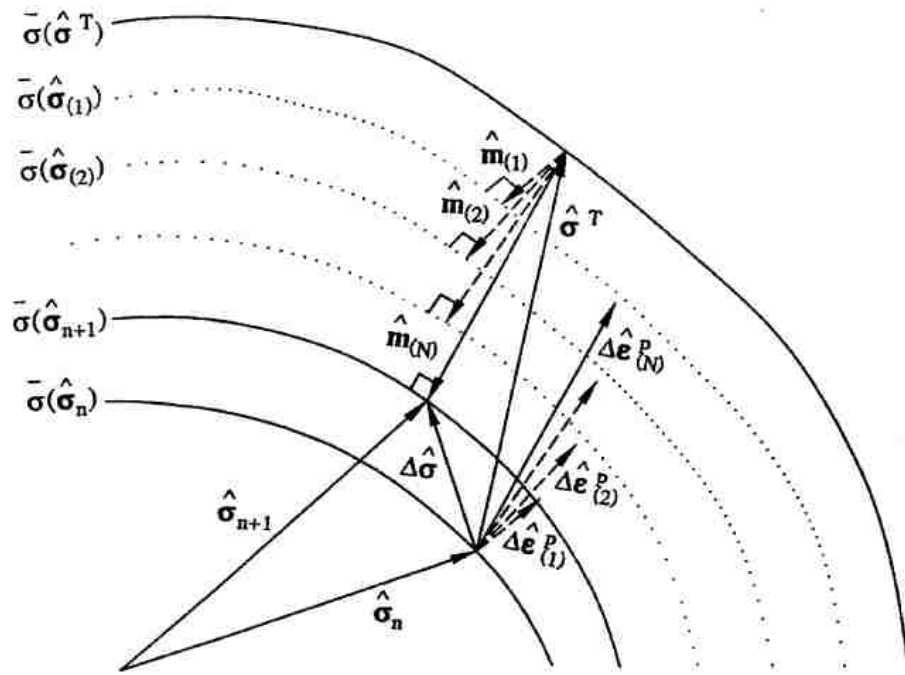
Fig. 4.1. Schematic view for multi-stage return mapping method [91]

The Newton-Raphson method is usually used to solve Eq. (4.9). For nonquadratic yield functions and at large strain increments, it is usually difficult to find the solution of Eq. (4.9) numerically. Therefore, a multi-stage return mapping procedure is employed in this work to control the potential residual and guarantee the convergence to the solution. This method was proposed by Yoon et al. [74] and is applicable to a non-quadratic yield

function and a general hardening law without the need of a line search algorithm, even for a relatively large strain increment (10%) [91]. For sub-step k, the nonlinear equation, Eq. (4.9), is modified with the given residual as follows:

$$f(\Delta p_{(k)}) = \bar{\sigma}(\boldsymbol{\sigma}^{Tr} - \Delta p_{(k)}\boldsymbol{D}\boldsymbol{m}_{(k)}) - Y = f_{(k)} \tag{4.10}$$

where

$$f(\Delta p_{(0)} = 0) = f_{(0)}, \{f_{(k)}|f_{(0)} > f_{(1)} > \cdots > f_{(k)} > \cdots f_{(N)}(f_{(N)} = 0), k = 0{\sim}N\},$$

$$\Delta f = (f_{(k-1)} - f_{(k)}) < Y \text{ and } f_{k=1\sim(N-1)} \text{ are prescribed values.}$$

As shown in Fig. 4.1, the normal to the yield surface, $\boldsymbol{m}$, in each sub-step is estimated from its direction from the previous sub-step. Then the exact normal direction is obtained by solving Eq. (4.10) based on the Euler backward method. Now, the stress updating procedure can be developed by rearranging Eq. (4.10), (4.8), (4.1) and (4.2) as follows:

$$G_1 = \bar{\sigma}(\boldsymbol{\sigma}_{(k)}) - Y - f_{(k)} = 0 \tag{4.11a}$$

$$\boldsymbol{G}_2 = \boldsymbol{D}^{-1}[\boldsymbol{\sigma}_{(k)} - \boldsymbol{\sigma}^{Tr}] + \Delta p_{(k)}\boldsymbol{m}_{(k)} = 0 \tag{4.11b}$$

$$\boldsymbol{G}_3 = \boldsymbol{\theta}_{(k)} - \boldsymbol{\theta}_n - \left[\frac{a.c.\Delta p_{(k)}}{Y}\right]\boldsymbol{\eta}_{(k)} + \left[c.\Delta p_{(k)}.\sqrt{\frac{a}{\bar{\theta}}}\right]\boldsymbol{\theta}_{(k)} = 0 \tag{4.11c}$$

$$\boldsymbol{G}_4 = \boldsymbol{\beta}_{(k)} - \boldsymbol{\beta}_n - \left[\frac{k.b.\Delta p_{(k)}}{Y}\right]\boldsymbol{\eta}_{(k)} + [\Delta p_{(k)}.k]\boldsymbol{\beta}_{(k)} = 0 \tag{4.11d}$$

where $\boldsymbol{\sigma}_{(k)} = \boldsymbol{\sigma}^{Tr} - \Delta p_{(k)}\boldsymbol{D}\boldsymbol{m}_{(k)}$. In order to find the correction for each variable at each iteration, the above system of equations is linearized around the current values of the state variables:

$$G_1 + \boldsymbol{m}{:}d\boldsymbol{\sigma} - \boldsymbol{m}{:}d\boldsymbol{\beta} - \boldsymbol{m}{:}d\boldsymbol{\theta} = 0 \tag{4.12a}$$

$$\boldsymbol{G}_2 + \left[\boldsymbol{D}^{-1} + \Delta p\frac{\partial \boldsymbol{m}}{\partial \boldsymbol{\sigma}}\right]d\boldsymbol{\sigma} - \left[\Delta p\frac{\partial \boldsymbol{m}}{\partial \boldsymbol{\sigma}}\right]d\boldsymbol{\beta} - \left[\Delta p\frac{\partial \boldsymbol{m}}{\partial \boldsymbol{\sigma}}\right]d\boldsymbol{\theta} + \boldsymbol{m}d\Delta p = 0 \tag{4.12b}$$

$$\boldsymbol{G}_3 - \left[\frac{a.c.\Delta p}{Y}\right]d\boldsymbol{\sigma} + \left[\frac{\partial \boldsymbol{G}_3}{\partial \boldsymbol{\theta}}\right]d\boldsymbol{\theta} + \left[\frac{a.c.\Delta p}{Y}\right]d\boldsymbol{\beta} + \left[\frac{\partial \boldsymbol{G}_3}{\partial \Delta p}\right]d\Delta p = 0 \tag{4.12c}$$

$$G_4 - \frac{k.b.\Delta p}{Y}d\boldsymbol{\sigma} + \frac{\partial G_4}{\partial \boldsymbol{\beta}}d\boldsymbol{\beta} + \left[\frac{k.b}{Y}\Delta p\right]d\boldsymbol{\theta} - \left[\frac{k\Delta p}{Y}\boldsymbol{\eta} + k\boldsymbol{\beta}\right]d\Delta p = 0 \qquad \text{(4.12d)}$$

where

$$\frac{\partial G_3}{\partial \boldsymbol{\theta}} = 1 + \frac{a.c.\Delta p}{Y} + c.\Delta p.\sqrt{\frac{a}{\bar{\bar{\theta}}}} - \frac{c.\Delta p.\sqrt{a}.\left(\boldsymbol{\theta}:\frac{\partial \bar{\theta}}{\partial \boldsymbol{\theta}}\right)}{2\bar{\theta}\sqrt{\bar{\theta}}}$$

$$\frac{\partial G_3}{\partial \Delta p} = -\frac{a.c}{Y}\boldsymbol{\eta} - \frac{H.c.\Delta p}{Y}\boldsymbol{\eta} + c.\sqrt{\frac{a}{\bar{\bar{\theta}}}}\boldsymbol{\theta} + \frac{H.c.\Delta p}{2\sqrt{a.\bar{\theta}}}\boldsymbol{\theta}$$

$$\frac{\partial G_4}{\partial \boldsymbol{\beta}} = 1 + \frac{k.b}{Y}\Delta p + k.\Delta p$$

$$H = \frac{\partial R}{\partial \Delta p} = k(R_{sat} - R)$$

Solving the above system of equations gives the correction for the effective plastic strain increment ($d\Delta p$), stress ($d\boldsymbol{\sigma}$) and the kinematic motions ($d\boldsymbol{\beta}$ and $d\boldsymbol{\theta}$). Then each variable is updated, and iterations continue until the above equations (Eqs. 4.12) are satisfied within a prescribed tolerance.

The implementation of workhardening stagnation and decrease of elastic modulus for this algorithm is the same as for the semi-implicit algorithm, and therefore are omitted here for the sake of brevity. The implementation of workhardening stagnation has been described in sections 3.4.2 and the decrease of unloading modulus is taken into account using Eq. (3.37).

4.3. Consistent Tangent Modulus:

In the implementation of a plasticity model into an implicit finite element code, it is necessary to provide the tangent modulus or the material Jacobian matrix which is required to solve the equilibrium equations or momentum balance. The elastoplastic tangent modulus which was obtained in chapter 3 is called *continuum tangent modulus*.

The continuum tangent modulus is developed by the plasticity equations in the rate form. However, if the stress integration algorithm is linearized to obtain the derivative of the stress increment with respect to strain, the resulting tangent modulus will be consistent with the stress integration algorithm and is called *consistent tangent modulus*. It has been shown [79] that as the increment size approaches zero, the continuum tangent modulus approaches to the consistent tangent modulus. The consistent tangent modulus preserves the quadratic rate of asymptotic convergence in Newton's method at finite strain increments [79].

In order to find the consistent tangent modulus, the following equation is used:

$$\boldsymbol{\sigma} = \boldsymbol{\sigma}_n + \boldsymbol{D}[\boldsymbol{\varepsilon} - \boldsymbol{\varepsilon}_n] - \Delta p \boldsymbol{D} \boldsymbol{m} \tag{4.24}$$

Differentiation of Eq. (4.24) yields:

$$d\boldsymbol{\sigma} = \boldsymbol{D}[d\boldsymbol{\varepsilon}] - d\Delta p \boldsymbol{D} \boldsymbol{m} - \Delta p \boldsymbol{D} \left[\frac{\partial \boldsymbol{m}}{\partial \boldsymbol{\sigma}} d\boldsymbol{\sigma} - \frac{\partial \boldsymbol{m}}{\partial \boldsymbol{\sigma}} d\boldsymbol{\alpha} \right] \tag{4.25}$$

where

$$d\boldsymbol{\alpha} = d\boldsymbol{\theta} + d\boldsymbol{\beta} = \boldsymbol{n} dp \tag{4.26a}$$

$$\boldsymbol{n} = \left[\frac{a.c}{Y} \boldsymbol{\eta} - c. \sqrt{\frac{a}{\bar{\theta}}} \boldsymbol{\theta} + \frac{k.b}{Y} \boldsymbol{\eta} - k.\boldsymbol{\beta} \right] \tag{4.27b}$$

Substituting Eq. (4.26a) into Eq. (4.25) gives:

$$d\boldsymbol{\sigma} = \boldsymbol{\Xi}^{-1} \left[d\boldsymbol{\varepsilon} - (\boldsymbol{m} - \frac{\partial \boldsymbol{m}}{\partial \boldsymbol{\sigma}} \Delta p \boldsymbol{n}) dp \right] \tag{4.28a}$$

where $(\partial \boldsymbol{m}/\partial \boldsymbol{\sigma})$ is the derivative of the normal to yield surface and $\boldsymbol{\Xi}^{-1}$ is the modified elastic tangent matrix and is defined as follows:

$$\boldsymbol{\Xi}^{-1} = \left[\boldsymbol{D}^{-1} + \Delta p \frac{\partial \boldsymbol{m}}{\partial \boldsymbol{\sigma}} \right]^{-1} \tag{4.28b}$$

Now, the consistency condition is used to obtain dp. Differentiation of the yield function, i.e. Eq. (4.4), leads to the following equation:

$$df = \boldsymbol{m}:d\boldsymbol{\sigma} - \boldsymbol{m}:d\boldsymbol{\alpha} = 0 \tag{4.29}$$

Substituting $d\boldsymbol{\sigma}$ from Eq. (4.28a) and $d\boldsymbol{\alpha}$ from Eq. (4.26a) gives the following equation for dp:

$$dp = \frac{\boldsymbol{m}\boldsymbol{\Xi}^{-1}d\boldsymbol{\varepsilon}}{\boldsymbol{m}\boldsymbol{\Xi}^{-1}(\boldsymbol{m} - \Delta p\frac{\partial\boldsymbol{m}}{\partial\boldsymbol{\sigma}}\boldsymbol{n}) + \boldsymbol{mn}} \tag{4.30}$$

Finally, the consistent tangent modulus is obtained by substituting dp from Eq. (4.30) back into Eq. (4.28a):

$$d\boldsymbol{\sigma} = \boldsymbol{D}^{ep}\,d\boldsymbol{\varepsilon} \tag{4.31}$$

where

$$\boldsymbol{D}^{ep} = \boldsymbol{\Xi}^{-1} - \frac{\left[\boldsymbol{\Xi}^{-1}(\boldsymbol{m} - \Delta p\frac{\partial\boldsymbol{m}}{\partial\boldsymbol{\sigma}}\boldsymbol{n})\right] \otimes [\boldsymbol{\Xi}^{-1}\boldsymbol{m}]}{\boldsymbol{m}\boldsymbol{\Xi}^{-1}(\boldsymbol{m} - \Delta p\frac{\partial\boldsymbol{m}}{\partial\boldsymbol{\sigma}}\boldsymbol{n}) + \boldsymbol{mn}} \tag{4.32}$$

The numerical algorithm used in the user-defined material subroutine is shown in Table A.2. Using this algorithm, we can develop a general user material subroutine for YU model which may include any desired yield function. The desired yield function and its first and second derivatives can be defined in the subroutine and be called from within the UMAT. In this project, the Hill's quadratic yield function and Yld2000-2d were used.

It should also be mentioned that for shell elements, the transverse shear stiffness must be calculated and be returned to the finite element software. As mentioned in section 3.6, Eq. (3.40) was used in this work to calculate the transverse shear stiffness. For reduced integration elements, the hourglass stiffness needs to be calculated. So, Eqs. (3.38, 3.39) were used to calculate the hourglass stiffness.

4.4. Yield Function:

Sheet anisotropy is one of the parameters that has to be taken into account for an accurate simulation in sheet metal forming. Geng and Wagoner [54] conducted a study on the role of anisotropy on springback prediction and found that the simulated springback depends not only on the hardening behaviour but also on the anisotropy of the sheet. The numerical procedure developed in section 3 can be easily used with any yield function which is written in the form of Eq. (8) and whose first and second derivatives can be explicitly stated. In this work, two different yield functions were used to develop two user material subroutines: a) Hill's quadratic yield function, b) Yld2000-2d. In order to complete the stress algorithm, the first and second derivatives of these functions are derived.

4.4.1. Hill's quadratic yield function:

For YU model, Hill's quadratic yield function is written as follows:

$$\left(\frac{3}{2}\boldsymbol{\eta}^T \boldsymbol{N}\boldsymbol{\eta}\right)^{1/2} - Y = 0 \tag{4.33}$$

where $\boldsymbol{N}$ is a fourth-order anisotropic tensor that was defined in section 2.4.4. So, the effective quantity for $\boldsymbol{\eta}$ is defined by:

$$\bar{\eta} = \left(\frac{3}{2}\boldsymbol{\eta}^T \boldsymbol{N}\boldsymbol{\eta}\right)^{1/2} \tag{4.34}$$

According to Eq. (4.5), the normal to the yield surface is obtained as follows:

$$\boldsymbol{m} = \frac{\partial \bar{\eta}}{\partial \boldsymbol{\sigma}} = \frac{3}{2}\frac{\boldsymbol{N}\boldsymbol{\eta}}{\bar{\eta}} \tag{4.35}$$

The numerical algorithm explained in this chapter also requires calculation of the second derivative of the yield function, i.e. $(\partial \boldsymbol{m}/\partial \boldsymbol{\sigma})$. Differentiation of Eq. (4.35) gives:

$$\frac{\partial \boldsymbol{m}}{\partial \boldsymbol{\sigma}} = \frac{\frac{3}{2}\boldsymbol{N} - \boldsymbol{m}\otimes\boldsymbol{m}}{\bar{\eta}} \tag{4.36}$$

Now, the fully-implicit numerical algorithm developed in this chapter is completely defined for Hill's quadratic yield function.

4.4.2. Yld2000-2d:

In order to describe the anisotropy of sheet metals, Barlat et al. proposed Yld2000-2d anisotropic yield function. This function is not quadratic in general and it is particularly intended for aluminum alloy sheets. For YU model, this function is written as follows [31]:

$$f = \bar{\eta} - Y = \left[\frac{\Phi' + \Phi''}{2}\right]^{\frac{1}{a'}} - Y = 0 \tag{4.37}$$

Φ' and Φ'' are two isotropic functions and are defined by:

$$\Phi' = |X'_1 - X'_2|^{a'}, \Phi'' = |2X''_2 + X''_1|^{a'} + |2X''_2 + X''_1|^{a'} \tag{4.38}$$

where a' is a material coefficient, X'_1, X'_2 are the principal values of tensor $\boldsymbol{X}'$ and X''_1, X''_2 are the principal values of tensor $\boldsymbol{X}''$. Tensors $\boldsymbol{X}'$ and $\boldsymbol{X}''$ are obtained by linear transformation the stress tensor as follows:

$$\boldsymbol{X}' = \boldsymbol{L}'\boldsymbol{\eta}, \boldsymbol{X}'' = \boldsymbol{L}''\boldsymbol{\eta}$$

where $\boldsymbol{L}'$ and $\boldsymbol{L}''$ are related to the anisotropic coefficients of the material by:

$$
\begin{bmatrix} L'_{11} \\ L'_{12} \\ L'_{21} \\ L'_{22} \\ L'_{66} \end{bmatrix} = \begin{bmatrix} 2/3 & 0 & 0 \\ -1/3 & 0 & 0 \\ 0 & -1/3 & 0 \\ 0 & 2/3 & 0 \\ 0 & 0 & 1 \end{bmatrix} \begin{bmatrix} \alpha_1 \\ \alpha_2 \\ \alpha_7 \end{bmatrix}
$$

$$
\begin{bmatrix} L''_{11} \\ L''_{12} \\ L''_{21} \\ L''_{22} \\ L''_{66} \end{bmatrix} = \frac{1}{9} \begin{bmatrix} -2 & 2 & 8 & -2 & 0 \\ 1 & -4 & -4 & 4 & 0 \\ 4 & -4 & -4 & 1 & 0 \\ -2 & 8 & 2 & -2 & 0 \\ 0 & 0 & 0 & 0 & 9 \end{bmatrix} \begin{bmatrix} \alpha_3 \\ \alpha_4 \\ \alpha_5 \\ \alpha_6 \\ \alpha_8 \end{bmatrix}
$$

where $\alpha_1, \alpha_2, \ldots, \alpha_8$ are all material anisotropic coefficients. For the isotropic case, all independent coefficients α_k (for k=1 to 8) reduce to one. Generally, eight input data from the material are required to identify these constants. These data include the yield stress and r-value of the sheet in the rolling, transverse and diagonal directions and also in an equibiaxial stress state, i.e. $\sigma_0, \sigma_{45}, \sigma_{90}, \sigma_b, r_0, r_{45}, r_{90}, r_b$. The parameter r_b characterizes the slope of the yield surface in balanced biaxial tension, i.e. $r_b = \dot{\varepsilon}_{yy}/\dot{\varepsilon}_{xx}$. r_b can be determined with three different methods: experimentally measured, calculated with another yield function, or computed from a polycrystal model if the crystallographic texture of the material is known. If r_b is either unknown or difficult to obtain, it is reasonable to assume that $L''_{12} = L''_{21}$ and determine the coefficients using only seven input data.

The principal values of X' and X'' are obtained as follows:

$$
X' = \begin{bmatrix} X'_1 \\ X'_2 \end{bmatrix} = \begin{bmatrix} \dfrac{X'_{xx} + X'_{yy}}{2} + \sqrt{\left(\dfrac{X'_{xx} - X'_{yy}}{2}\right)^2 + \left(X'_{xy}\right)^2} \\ \dfrac{X'_{xx} + X'_{yy}}{2} - \sqrt{\left(\dfrac{X'_{xx} - X'_{yy}}{2}\right)^2 + \left(X'_{xy}\right)^2} \end{bmatrix}
\tag{4.39}
$$

$$\mathbf{X''} = \begin{bmatrix} X''_1 \\ X''_2 \end{bmatrix} = \begin{bmatrix} \dfrac{X''_{xx} + X''_{yy}}{2} + \sqrt{\left(\dfrac{X''_{xx} - X''_{yy}}{2}\right)^2 + \left(X''_{xy}\right)^2} \\[4mm] \dfrac{X''_{xx} + X''_{yy}}{2} - \sqrt{\left(\dfrac{X''_{xx} - X''_{yy}}{2}\right)^2 + \left(X''_{xy}\right)^2} \end{bmatrix} \tag{4.40}$$

The derivative of the yield function can be calculated using the chain rule:

$$\mathbf{m} = \frac{\partial \bar{\eta}}{\partial \boldsymbol{\sigma}} = \left[2a'\bar{\eta}^{(a'-1)}\right]^{-1}\left[\frac{\partial \Phi'}{\partial X'}\frac{\partial X'}{\partial X'_{\alpha\beta}}\frac{\partial X'_{\alpha\beta}}{\partial \boldsymbol{\sigma}} + \frac{\partial \Phi''}{\partial X''}\frac{\partial X''}{\partial X''_{\alpha\beta}}\frac{\partial X''_{\alpha\beta}}{\partial \boldsymbol{\sigma}}\right] \tag{4.41}$$

where $\alpha\beta$ stands for *xx, yy* and *xy*. Now, each term can be calculated by differentiation:

$$\frac{\partial \Phi'}{\partial X'} = \begin{bmatrix} a'(X'_1 - X'_2)^{a'-2}|X'_1 - X'_2| \\ -a'(X'_1 - X'_2)^{a'-2}|X'_1 - X'_2| \end{bmatrix} \tag{4.42}$$

$$\frac{\partial X'}{\partial X'_{\alpha\beta}} = \begin{bmatrix} \dfrac{1}{2}\left(1 + \dfrac{X'_{xx} - X'_{yy}}{\sqrt{\Delta'}}\right) & \dfrac{1}{2}\left(1 - \dfrac{X'_{xx} - X'_{yy}}{\sqrt{\Delta'}}\right) & \dfrac{2X'_{xy}}{\sqrt{\Delta'}} \\[4mm] \dfrac{1}{2}\left(1 - \dfrac{X'_{xx} - X'_{yy}}{\sqrt{\Delta'}}\right) & \dfrac{1}{2}\left(1 + \dfrac{X'_{xx} - X'_{yy}}{\sqrt{\Delta'}}\right) & -\dfrac{2X'_{xy}}{\sqrt{\Delta'}} \end{bmatrix} \tag{4.43}$$

$$\frac{\partial X'_{\alpha\beta}}{\partial \boldsymbol{\sigma}} = \mathbf{L'} \tag{4.44}$$

$$\frac{\partial \Phi''}{\partial X''} = \begin{bmatrix} a'(2X''_2 - X''_1)^{a'-2}|2X''_2 - X''_1| + 2a'(2X''_1 - X''_2)^{a'-2}|2X''_1 - X''_2| \\ 2a'(2X''_2 - X''_1)^{a'-2}|2X''_2 - X''_1| + a'(2X''_1 - X''_2)^{a'-2}|2X''_1 - X''_2| \end{bmatrix} \tag{4.45}$$

$$\frac{\partial X''}{\partial X''_{\alpha\beta}} = \begin{bmatrix} \dfrac{1}{2}\left(1 + \dfrac{X''_{xx} - X''_{yy}}{\sqrt{\Delta''}}\right) & \dfrac{1}{2}\left(1 - \dfrac{X''_{xx} - X''_{yy}}{\sqrt{\Delta''}}\right) & \dfrac{2X''_{xy}}{\sqrt{\Delta'}} \\[4mm] \dfrac{1}{2}\left(1 - \dfrac{X''_{xx} - X''_{yy}}{\sqrt{\Delta''}}\right) & \dfrac{1}{2}\left(1 + \dfrac{X''_{xx} - X''_{yy}}{\sqrt{\Delta''}}\right) & -\dfrac{2X''_{xy}}{\sqrt{\Delta''}} \end{bmatrix} \tag{4.46}$$

$$\frac{\partial X''_{\alpha\beta}}{\partial \boldsymbol{\sigma}} = \mathbf{L''} \tag{4.47}$$

where

$$\Delta' = \left(X'_{xx} - X'_{yy}\right)^2 + 4(X'_{xy})^2 \tag{4.48}$$

$$\Delta'' = \left(X''_{xx} - X''_{yy}\right)^2 + 4(X''_{xy})^2 \tag{4.49}$$

So, the first derivative of the yield function is obtained using Eqs. (4.41-4.49). In order to find the second derivative, Eq. (4.41) is integrated according to the chain rule:

$$\frac{\partial \boldsymbol{m}}{\partial \boldsymbol{\sigma}} = \frac{\partial^2 \bar{\eta}}{\partial \boldsymbol{\sigma}^2} = \frac{\bar{\eta}^{(1-a')}}{2a'} \frac{\partial^2 \Phi}{\partial \boldsymbol{\sigma}^2} - \frac{1-a'}{\bar{\eta}} \boldsymbol{m} \otimes \boldsymbol{m} \tag{4.50}$$

$$
\begin{aligned}
\frac{\partial^2 \Phi}{\partial \boldsymbol{\sigma}^2} = \Bigg\{ &\left(\frac{\partial^2 \Phi'}{\partial X' \partial X'} \frac{\partial X'}{\partial X'_{\alpha\beta}} \frac{\partial X'_{\alpha\beta}}{\partial \boldsymbol{\sigma}} \right) \frac{\partial X'}{\partial X'_{\alpha\beta}} \frac{\partial X'_{\alpha\beta}}{\partial \boldsymbol{\sigma}} \\
&+ \left(\frac{\partial^2 \Phi''}{\partial X'' \partial X''} \frac{\partial X''}{\partial X''_{\alpha\beta}} \frac{\partial X''_{\alpha\beta}}{\partial \boldsymbol{\sigma}} \right) \frac{\partial X''}{\partial X''_{\alpha\beta}} \frac{\partial X''_{\alpha\beta}}{\partial \boldsymbol{\sigma}} \Bigg\} \\
&+ \Bigg\{ \frac{\partial \Phi'}{\partial X'} \left(\frac{\partial^2 X'}{\partial X'_{\alpha\beta} \partial X'_{\alpha\beta}} \frac{\partial X'_{\alpha\beta}}{\partial \boldsymbol{\sigma}} \right) \frac{\partial X'_{\alpha\beta}}{\partial \boldsymbol{\sigma}} \\
&+ \frac{\partial \Phi''}{\partial X''} \left(\frac{\partial^2 X''}{\partial X''_{\alpha\beta} \partial X''_{\alpha\beta}} \frac{\partial X''_{\alpha\beta}}{\partial \boldsymbol{\sigma}} \right) \frac{\partial X''_{\alpha\beta}}{\partial \boldsymbol{\sigma}} \Bigg\}
\end{aligned}
\tag{4.51}
$$

where $\Phi = \Phi' + \Phi''$.

$$\left[\frac{\partial^2 \Phi'}{\partial X' \partial X'} \right] = a'(a'-1)|X'_1 - X'_2|^{a'-2} \begin{bmatrix} 1 & -1 \\ -1 & 1 \end{bmatrix} \tag{4.52}$$

$$
\begin{aligned}
\left[\frac{\partial^2 \Phi''}{\partial X'' \partial X''} \right] = a'(a'-1) \times \Bigg[& |2X''_2 - X''_1|^{a'-2} + 4|2X''_1 - X''_2|^{a'-2} \\
& 2|2X''_2 - X''_1|^{a'-2} + 2|2X''_1 - X''_2|^{a'-2} \\
& 2|2X''_2 - X''_1|^{a'-2} + 2|2X''_1 - X''_2|^{a'-2} \\
& 4|2X''_2 - X''_1|^{a'-2} + |2X''_1 - X''_2|^{a'-2} \Bigg]
\end{aligned}
\tag{4.53}
$$

84

$$\left[\frac{\partial^2 X'_1}{\partial X'_{\alpha\beta}\,\partial X'_{\alpha\beta}}\right]$$

$$=\begin{bmatrix} \dfrac{1}{4\Delta'}-\dfrac{\left(X'_{xx}-X'_{yy}\right)^2}{16\Delta'^3} & -\dfrac{1}{4\Delta'}+\dfrac{\left(X'_{xx}-X'_{yy}\right)^2}{16\Delta'^3} & -\dfrac{\left(X'_{xx}-X'_{yy}\right)X'_{xy}}{4\Delta'^3} \\[4mm] -\dfrac{1}{4\Delta'}+\dfrac{\left(X'_{xx}-X'_{yy}\right)^2}{16\Delta'^3} & \dfrac{1}{4\Delta'}-\dfrac{\left(X'_{xx}-X'_{yy}\right)^2}{16\Delta'^3} & \dfrac{\left(X'_{xx}-X'_{yy}\right)X'_{xy}}{4\Delta'^3} \\[4mm] -\dfrac{\left(X'_{xx}-X'_{yy}\right)X'_{xy}}{4\Delta'^3} & \dfrac{\left(X'_{xx}-X'_{yy}\right)X'_{xy}}{4\Delta'^3} & \dfrac{1}{\Delta'}-\dfrac{X'^2_{xy}}{\Delta'^3} \end{bmatrix} \quad (4.54)$$

$$\left[\frac{\partial^2 X''_1}{\partial X''_{\alpha\beta}\,\partial X''_{\alpha\beta}}\right]$$

$$=\begin{bmatrix} \dfrac{1}{4\Delta''}-\dfrac{\left(X''_{xx}-X''_{yy}\right)^2}{16\Delta''^3} & -\dfrac{1}{4\Delta''}+\dfrac{\left(X''_{xx}-X''_{yy}\right)^2}{16\Delta''^3} & -\dfrac{\left(X''_{xx}-X''_{yy}\right)X''_{xy}}{4\Delta''^3} \\[4mm] -\dfrac{1}{4\Delta''}+\dfrac{\left(X''_{xx}-X''_{yy}\right)^2}{16\Delta''^3} & \dfrac{1}{4\Delta''}-\dfrac{\left(X''_{xx}-X''_{yy}\right)^2}{16\Delta''^3} & \dfrac{\left(X''_{xx}-X''_{yy}\right)X''_{xy}}{4\Delta''^3} \\[4mm] -\dfrac{\left(X''_{xx}-X''_{yy}\right)X''_{xy}}{4\Delta''^3} & \dfrac{\left(X''_{xx}-X''_{yy}\right)X''_{xy}}{4\Delta''^3} & \dfrac{1}{\Delta''}-\dfrac{X''^2_{xy}}{\Delta''^3} \end{bmatrix} \quad (4.55)$$

$$\left[\frac{\partial^2 X'_1}{\partial X'_{\alpha\beta}\,\partial X'_{\alpha\beta}}\right]=-\left[\frac{\partial^2 X'_2}{\partial X'_{\alpha\beta}\,\partial X'_{\alpha\beta}}\right] \quad (4.56)$$

$$\left[\frac{\partial^2 X''_1}{\partial X''_{\alpha\beta}\,\partial X''_{\alpha\beta}}\right]=-\left[\frac{\partial^2 X''_2}{\partial X''_{\alpha\beta}\,\partial X''_{\alpha\beta}}\right] \quad (4.57)$$

4.5. Verification of the User Material Subroutine:

In chapter 3, several loading cases were simulated and the results obtained by UMAT were compared with the results obtained with either an analytical method or with ABAQUS built-in material models such as isotropic hardening or combined isotropic-nonlinear kinematic hardening. The simulation results showed that UMAT was able to produce the results obtained by ABAQUS built-in material models for many different loading conditions. In this section, the fully-implicit UMAT and the semi-implicit UMAT are used to simulate various loading conditions, and the comparison of results will provide a validation of the fully-implicit UMAT. The UMAT is based on Hill's quadratic yield function and the YU hardening model and was used with ABAQUS/Standard for

these simulations, and the results are presented in sections 4.7.1 to 4.7.5. The material was assumed to be an AKDQ steel grade in the following simulations unless otherwise stated. The experimental yield stresses and r-values in the three significant material directions are given in Table 3.1. The material coefficients associated with the YU model were found by fitting the simulation results to the experimental stress-strain curve obtained by the cyclic shear test. In addition, the experimental yield stresses in each direction were used to find Hill's coefficients. The material constants associated with YU model and Hill's quadratic yield function are shown in Tables 3.2 and 3.3, respectively. Furthermore, the implementation of the Yld2000-2d yield function is also presented in section 4.7.6. Since this function is usually used for aluminum alloys, AA6022-T43 was used to verify the implementation of this model.

4.5.1. Uniaxial tension:

In general, the backstress equations are nonlinear with respect to the effective plastic strain. So, when the Euler backward stress integration method is used, regardless of the integration scheme the strain increment must be small in order to converge to the solution. Therefore, both semi-implicit and fully-implicit approaches require a sub-step algorithm to make sure that the strain increment is sufficiently small throughout the simulation. However, the advantage of a fully-implicit approach is that, although the backstress equations, i.e. Eqs. (4.11c, 4.11d), will not be satisfied at the end of a time increment if the strain increment is larger than a critical value, the user can be easily notified that the strain increment is too large. In order to study the relative error associated with numerical integration, a square of 1 mm^2 subject to during a uniaxial tensile loading was simulated. The bottom side was fixed in the Y-direction and the left bottom corner was fixed in the X-direction. Then, the upper side was displaced in the Y-direction. The schematic illustration of this problem and the boundary conditions are shown in Fig. 3.4. One CPS4R element was used to mesh the part. Initially, UMATs based on semi-implicit and fully-implicit approaches with no sub-step algorithm were used to simulate this problem.

When no sub-step algorithm is used, the error associated with numerical integration depends on the strain increment size. The relative error is defined by the following relationship:

$$Error = \frac{|\sigma - \sigma^*|}{\sigma^*} \times 100 \tag{4.58}$$

where σ is the stress calculated by UMAT and σ^* is the calculated stress with sufficiently large number of sub-increments to make sure that the algorithm converged to the solution. The relative error associated with each integration scheme is plotted in Fig. 4.2. This figure shows that the relative error increases as the size of the strain increment increases. Moreover, the relative error associated with the fully-implicit method is smaller compared to the semi-implicit method. The reason for this lies in the fact that the explicit integration of backstress does not guarantee convergence to the solution at large strain increments. In general, the amount of relative error depends on the nonlinearity of the material. In order to eliminate the amount of error, the size of the strain increment must be small. In this work, an automatic sub-step algorithm was used to refine the strain increment when it is too large for the algorithm. If the effective strain increment is larger than a critical value, the increment size is divided into a few sub-increments to guarantee that the strain increment size is smaller than the critical value.

In order to find the critical strain, the uniaxial tension was simulated using different values for the critical strain. The upper side was displaced 0.1 mm in the Y-direction causing a uniform strain of around 10%. Fig. 4.3 shows the relative error with respect to the critical value for semi-implicit and fully implicit approaches. This figure shows that the relative error increases dramatically for the semi-implicit approach if the critical strain is larger than 0.5%. This figure also shows that the relative error is smaller for the fully-implicit approach compared to the semi-implicit approach. In all subsequent simulations with this UMAT, a conservative value of 0.1% was selected as the critical strain. That is, if the strain increment is larger than 0.1%, the sub-step algorithm divides it such that the strain increment in each sub-step never exceeds 0.1%. This example was repeated to obtain the critical strain for the other materials which will be used in this work and it was found that this critical strain is small enough for all materials used in this

work. In general, the user of this subroutine can repeat this example to obtain a critical value for other materials. It is noted that the critical value depends upon both the material coefficients and the strain increment size. So, it is expected that the critical strain obtained by this test be small enough for other loading conditions and element types. Alternatively, if the user runs the simulation with a smaller strain increment and the stress does not change significantly, it can be concluded that the strain increment was sufficiently small.
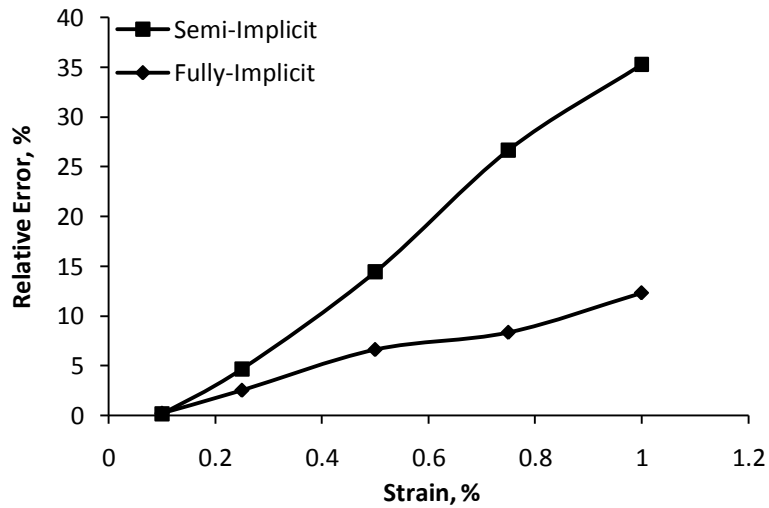

Fig. 4.2. The relative error with respect to strain increment size (without sub-step algorithm)
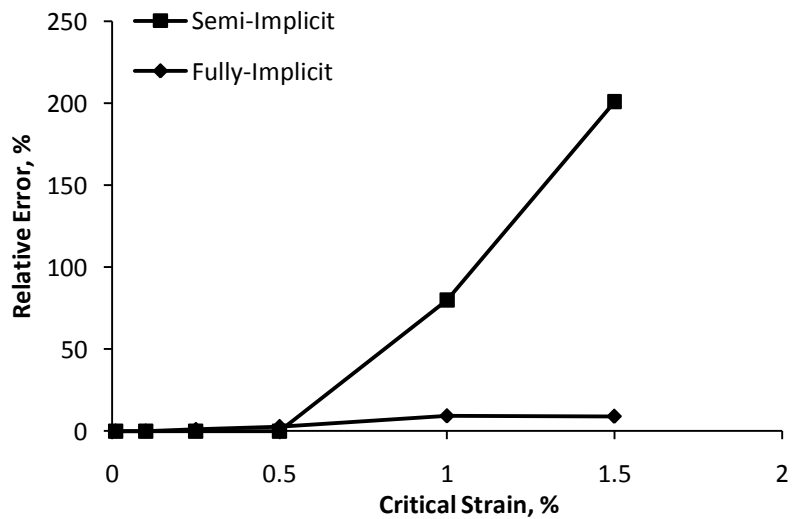

Fig. 4.3. The relative error with respect to the critical strain increment size

4.5.2. Uniaxial cyclic tension-compression:

The uniaxial tension-compression problem is a very simple type of loading and can be used as an initial test to verify the UMAT. Uniaxial tension-compression loading causes a homogenous deformation. Therefore a single element represents an adequate discretization of the model and the solution does not depend on the mesh size. In this problem, a square of 1 mm^2 was loaded in uniaxial tension-compression. The bottom side was fixed in the Y-direction and the left bottom corner was fixed in the X-direction. The upper side was first pulled 0.2 mm in the Y-direction and then compressed 0.4 mm in the negative Y-direction. A schematic illustration of the problem and the boundary conditions at the end of first loading step is shown in Fig. 3.4. A first-order quadrilateral element in the reduced integration mode, denoted as CPS4R, was used to mesh the part. The problem was simulated using both the semi-implicit and the fully-implicit UMATs. Fig. 4.4 shows that the semi-implicit and fully-implicit approaches result in the same stress-strain response for uniaxial loading. Since the semi-implicit UMAT was already verified in section 3.8, this comparison provides an initial validation of the fully-implicit UMAT.
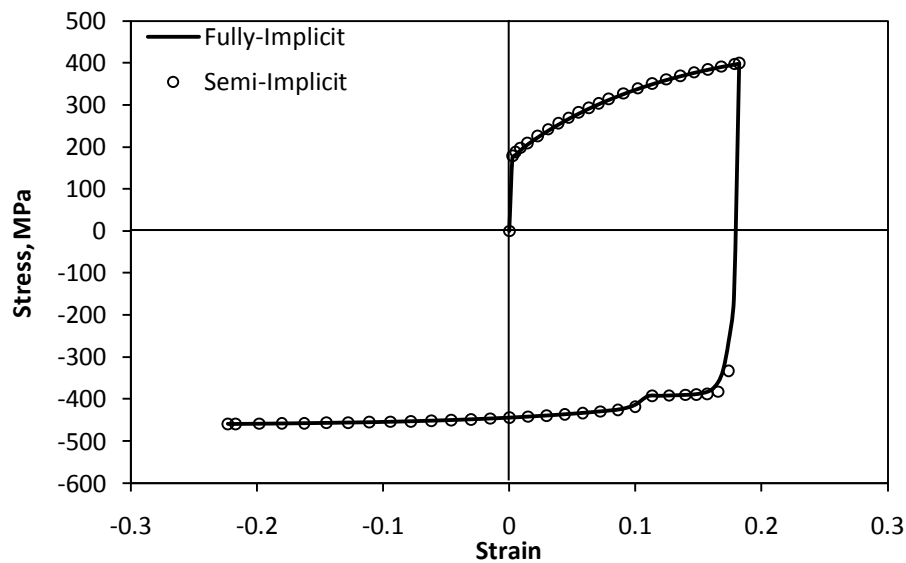

Fig. 4.4. Comparison of fully-implicit and semi-implicit in uniaxial tension-compression loading

4.5.3. Biaxial loading:

In this example, the biaxial bulge test was simulated to evaluate the fully-implicit UMAT in the equibiaxial stress state. A square of 1 mm^2 was simulated by both semi-implicit and fully-implicit UMATs. The left and bottom sides of the square were fixed the X and Y-directions, respectively. In the first loading step, the right and top sides of the square were simultaneously displaced 0.2 mm in the X and Y-directions, respectively. In the second loading step, the right and top sides of the square were simultaneously displaced 0.4 mm in the negative X and Y-directions, respectively. The finite element model and the boundary conditions are shown in Fig. 3.6. The comparison of the stress-strain response of the material in the X-direction is shown in Fig. 4.5. This figure shows both UMATs reproduce the same stress-strain response. It is again noted that the semi-implicit UMAT was already validated in section 3.8 and is now used as the reference against which the fully-implicit UMAT is evaluated.
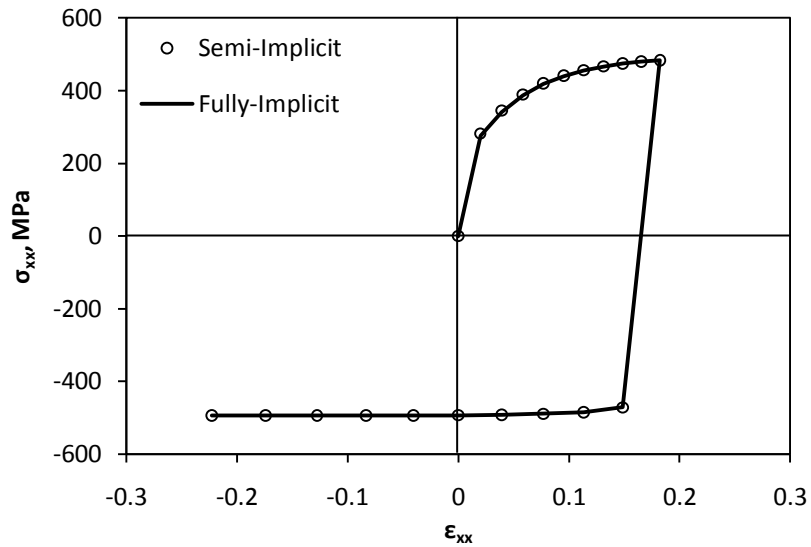

Fig. 4.5. Comparison of fully-implicit and semi-implicit in equibiaxial loading

4.5.4. Simple shear:

In order to verify the fully-implicit UMAT in the prediction of shear stresses, this subroutine was used to simulate the cyclic simple shear problem. A square of 1 mm^2 was fixed at the bottom side in the X and Y-directions. In the first loading step, the upper side was displaced 0.1 mm in the X-direction while it remained fixed in the Y-direction. In the second loading step, the upper side was displaced 0.2 mm in the negative Y-direction. Only one CPS4R element was used to mesh the part. The finite element model and the boundary conditions in the first loading step are shown in Fig. 4.6. Both the semi-implicit and fully-implicit approaches were used to simulate the problem. The deformed configuration of the model at the end of second loading step is shown in Fig. 4.7. The stress-strain response of the material obtained by semi-implicit and fully-implicit is shown in Fig. 4.8. Once again, it can be seen that the results obtained by both approaches are identical.
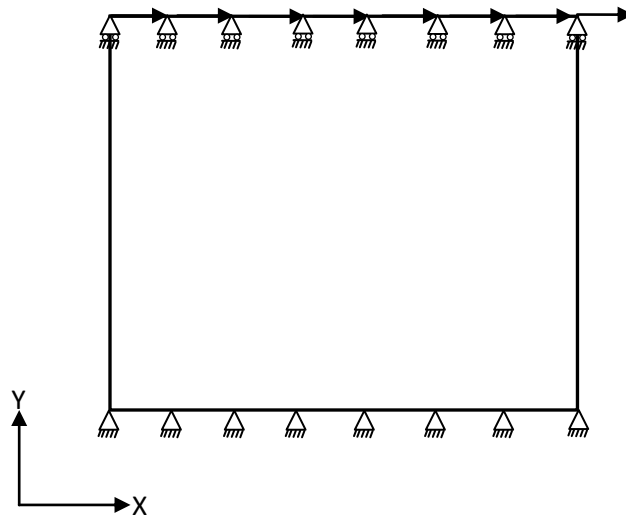
Fig. 4.6. Schematic of the simple shear problem and the boundary conditions
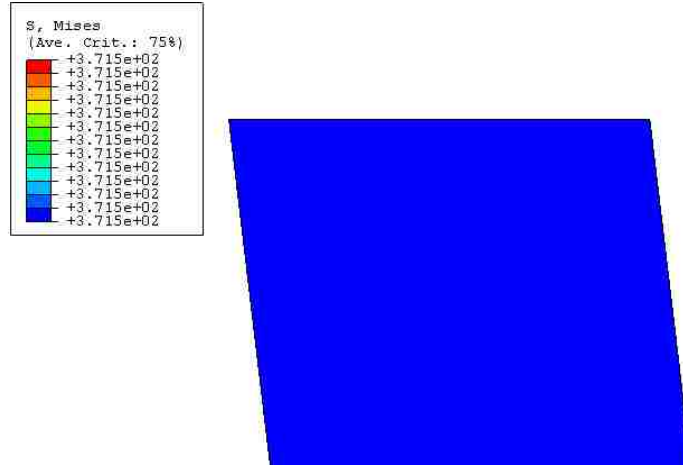
Fig. 4.7. The deformed configuration of the simple shear problem
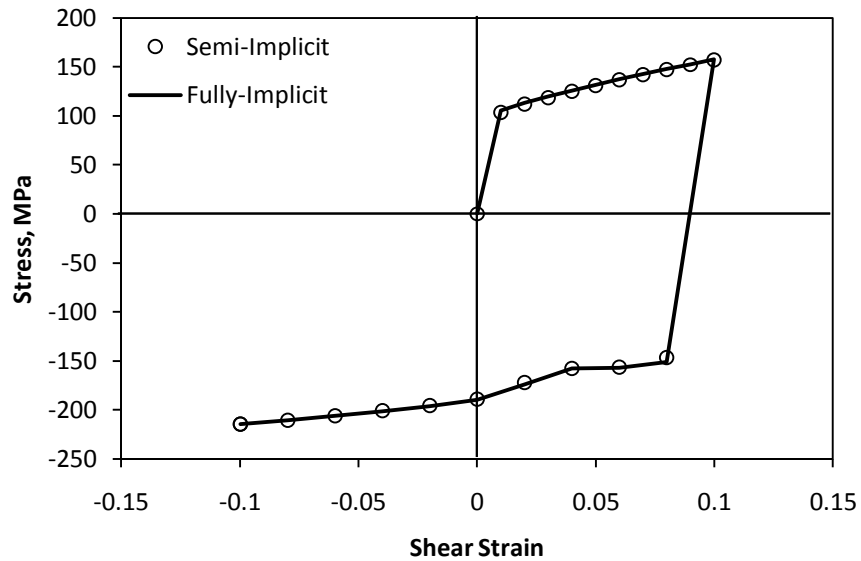
Fig. 4.8. Comparison of fully-implicit and semi-implicit in simple shear

4.5.5. *Bending of a cantilever beam:*

A rectangle 1 mm wide and 10 mm long was fixed at one end and displaced 2 mm at the other end. ABAQUS CPS4R element was used to mesh the part. The mesh size was selected to be 0.25 mm by 0.25 mm in the X and Y-directions. A schematic of the problem is shown in Fig. 3.8. Figs. 4.9 and 4.10 show the von Mises stress contour on the

deformed part obtained by fully-implicit and semi-implicit approaches, respectively. It can be seen that both UMATs predict essentially the same stress distributions. Fig. 4.11 also shows the predicted stress on the top surface of the beam obtained by each method. The stress history of the node located on the left top corner of the beam is also plotted in Fig. 4.12. These figures demonstrate that both methods result in the same stress distribution.

Fig. 4.9. von Mises stress contours on the deformed part obtained by fully-implicit scheme

Fig. 4.10. von Mises stress contours on the deformed part obtained by semi-implicit scheme

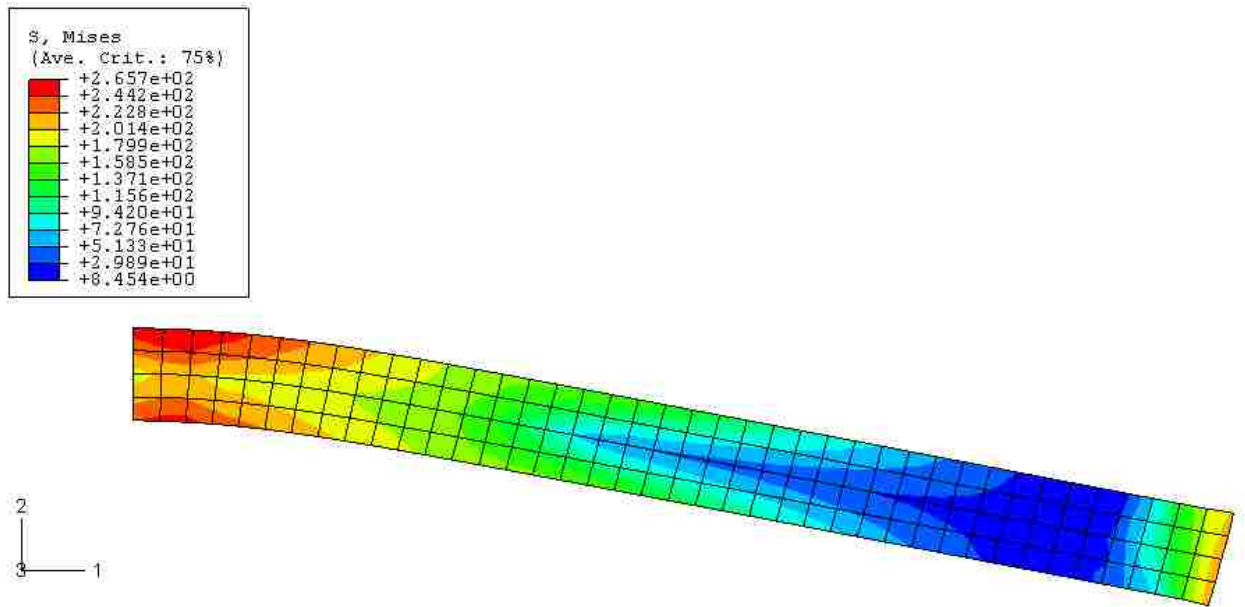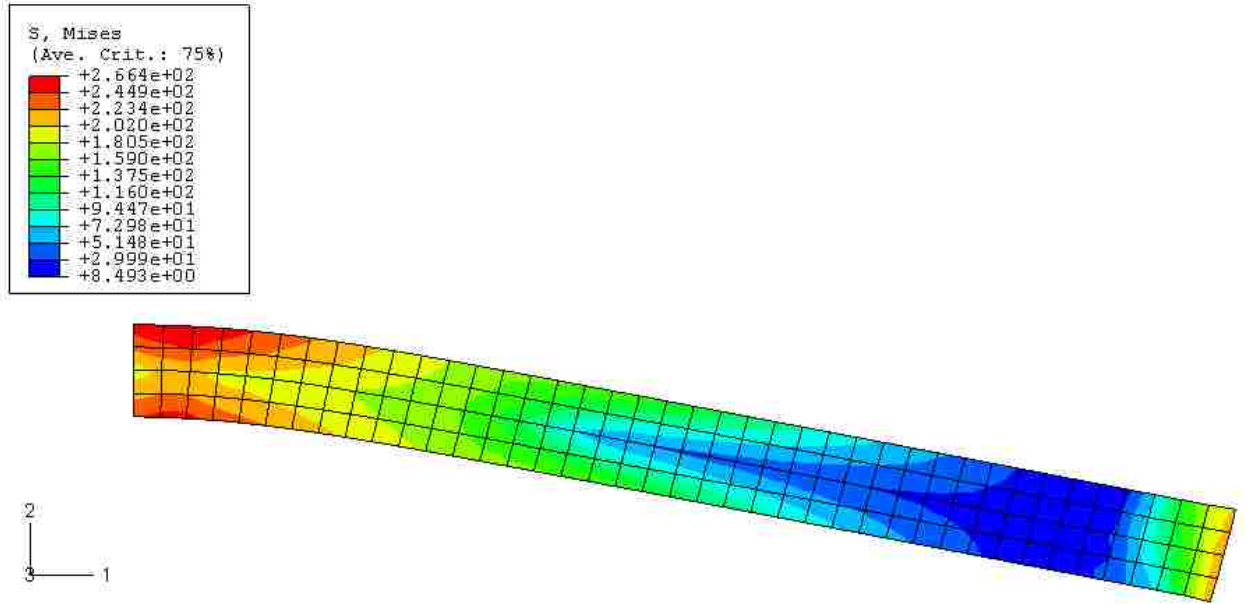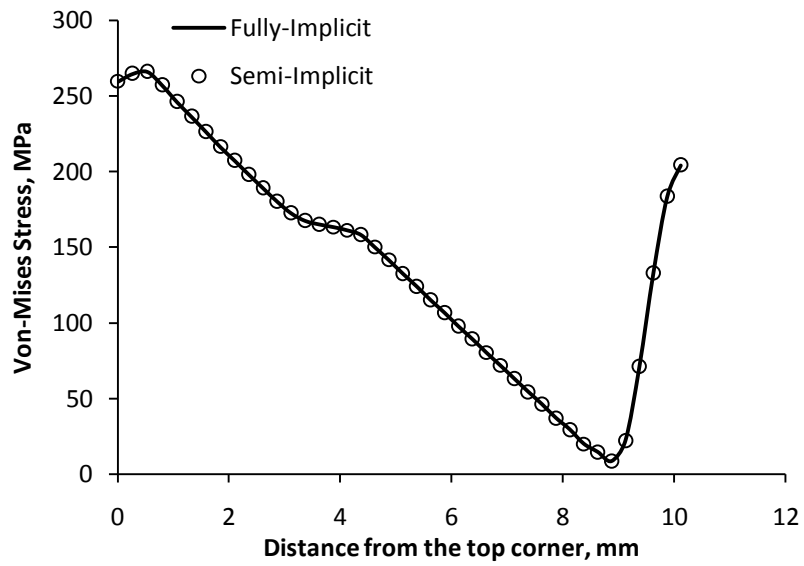Fig. 4.11. von Mises stress along the top surface of a cantilever beam
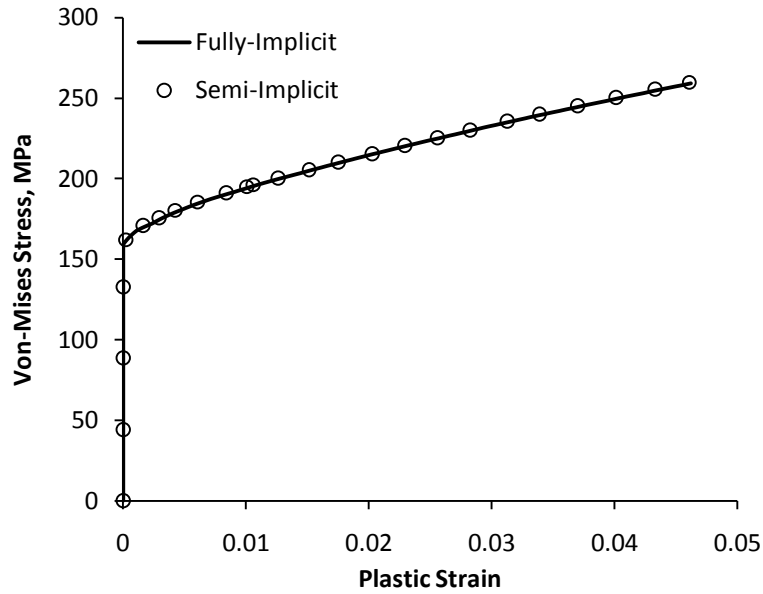
Fig. 4.12. History of nodal stress at the left top corner of a cantilever beam

4.5.6. Validation of Yld2000-2d function:

In this section, the implementation of Yld2000-2d is verified by simulation of uniaxial tension and equibiaxial tension of a square of unit length. Either seven or eight input data are required to obtain the Yld2000-2d anisotropic material parameters, i.e. α_k (k=1 to 8). The input data are usually yield stresses and r-values of the material in the rolling, transverse and diagonal directions and in the equibiaxial stress state. These input data were used by Barlat et al. [31] for AA2090-T3 to determine the material parameters α_k (k=1 to 8). The experimental input data and the yield function coefficients are listed in Tables 4.1 and 4.2, respectively. If the yield function is correctly implemented, the finite element simulation of the uniaxial tension and equibiaxial bulge tests must predict the corresponding experimental values. So, a square of unit length was simulated using the UMAT for uniaxial tensile tests in three directions and for equibiaxial tension. The material was assumed to be rigid-plastic so as to easily find out the predicted yield stress by simulation. The yield stresses and r-values obtained by simulation are also shown in Table 4.1. This table shows that the UMAT is able to accurately reproduce the anisotropy

of the sheet in rolling, transverse and diagonal directions and also in equibiaxial stress state.

Table 4.1. Normalized yield stress and r-values for AA2090-T3

	σ_0	σ_{45}	σ_{90}	σ_b	r_0	r_{45}	r_{90}	r_b
Experiment*	1.000	0.811	0.910	1.035	0.21	1.58	0.69	0.67
Simulation	0.999	0.811	0.910	1.035	0.21	1.58	0.69	0.67

* The experiments were obtained from reference [31]

Table 4.2. The anisotropic coefficients of AA6022-T43 for Yld2000-2d

α_1	α_2	α_3	α_4	α_5	α_6	α_7	α_8	a'
0.4865	1.3783	0.7536	1.0246	1.0363	0.9036	1.2321	1.4858	8

In this section, the user material subroutines were used to simulate several problems and the results were verified by the semi-implicit UMAT which itself had been verified in the previous chapter. The results show that the fully implicit integration of YU model has been performed correctly. TheYld2000-2d yield function was also verified by different tests such as uniaxial and biaxial bulge tests. A comparison of the results of semi-implicit and fully-implicit approaches also reveals that the fully-implicit method results in smaller relative error compared to semi-implicit at larger increments if no sub-increment algorithm is used in the subroutine. So, it can be generally suggested to use the semi-implicit method with ABAQUS-Explicit and the fully-implicit method with ABAQUS-Implicit code.

Chapter 5

Simulation of Springback

5.1. Introduction:

In sheet metal forming, a part is removed from the tooling after the forming stage. During this unloading stage, elastic deformation is recovered and causes the final shape of the part to change. The discrepancy between the fully loaded shape at the end of the forming stage and the unloaded configuration is called springback. Springback is the most significant factor that makes it difficult to achieve the required dimensional accuracy of stamped components. Designing a die with incorrect springback compensation can lead to significant difficulties in downstream operations such as poor fit-up during welding and distortion of sub-assemblies. In some cases, tooling revisions may be required which could lead to delays in production. Therefore, it is very important that springback be accurately predicted and correctly compensated during the first die design.

In order to study the ability of the YU model to predict springback, a channel draw process, presented as Benchmark #3 (BM3) in NumiSheet 2005 [23], was simulated using ABAQUS commercial finite element code. NumiSheet 2005 BM3 consists of drawing a rectangular blank into a deep, U-shaped channel section with the use of variable penetration drawbeads. This benchmark is extremely well suited to assessing the ability of a finite element model to predict springback for the following reasons: *a*) it provides experimental data for four different types of sheet materials, *b*) it covers a wide

range of strains by using four different drawbead penetrations, *c*) the deformation is severe in the drawbead region and *d*) the loading is cyclic because of a sequence of bending, unbending and reverse bending in the drawbeads. The complex contact condition in the drawbead region also presents a challenge for evaluation of the contact model. In this chapter, a brief introduction of BM3 is provided first and then the sensitivity of the predicted springback geometry to different model parameters is discussed. Finally, the effect of hardening model on the predicted springback profile is investigated.

5.2. Problem Description:

The objective of the NumiSheet 2005 BM3 is to document the forming characteristics of sheet metals in a deformation process dominated by cyclic bending and unbending. The channel draw die used for BM3 was designed and built by the Auto/Steel Partnership (A/SP). A schematic illustration of the tooling is shown in Fig. 5.1. The major dimensions of the tooling and drawbead are shown in Figs. 5.2-5.4 and are provided in Tables 5.1 and 5.2. Four different sheet materials were tested: AA6022-T43, AKDQ, HSLA and DP600. It is worth to mention that all steels used were hot-dip galvanized. A summary of mechanical properties of these materials is shown in Table 5.3. Blanks were 1067 mm long and 254 mm wide and were drawn into the die to form a wide, plane-strain channel section. The sheet thickness was 0.8 mm for HSLA and 1 mm for the other materials. Four spacer blocks were also mounted in the die to ensure that the distance between the die and the binder surfaces was consistently 0.42 mm greater than the nominal thickness of the sheet throughout the forming stage (see Fig.5.3). This gap helped to minimize the effect of friction on the process. A blankholder force of 637 kN was generated by four 140 mm diameter hydraulic actuators set at 10.3 MPa and was applied using cushion pins under the blankholder. The magnitude of this blankholder force was sufficient to set the beads and maintain a fixed clearance between the upper die and binder throughout the forming process [23].

Two drawbead inserts were built into each side of the die as shown in Fig.5.1. The detail of the drawbead geometry can be seen in Fig. 5.3. Channel sections were drawn at each of four different drawbead penetrations: 25%, 50%, 75% and 100%. 0% drawbead penetration is defined by contact of the drawbead on the sheet surface, but no plastic bending takes place in the drawbead region; 100% is achieved when the centre of the male bead radii and the centre of the female shoulder radii all lie on a strait horizontal line. The distance D_b, shown in Fig. 5.3, is given in Table 5.2 for nominal 25%, 50%, 75% and 100% penetrations. Green *et al*. [92] studied the influence of drawbead penetration on the forming and springback behaviour of plane-strain channel sections.
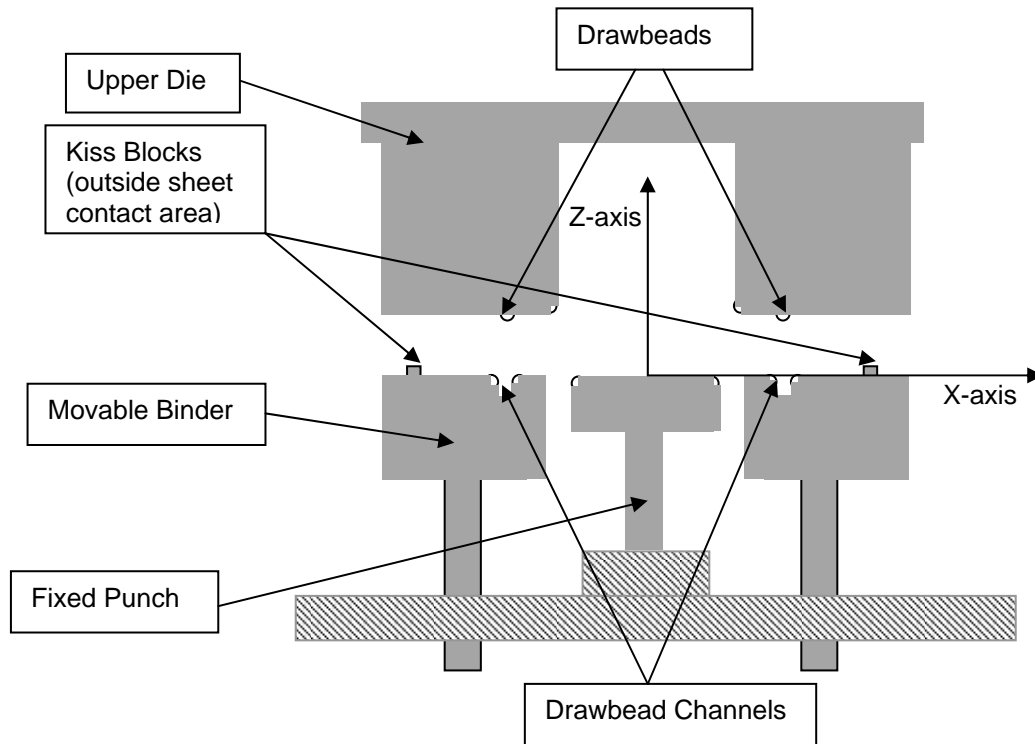

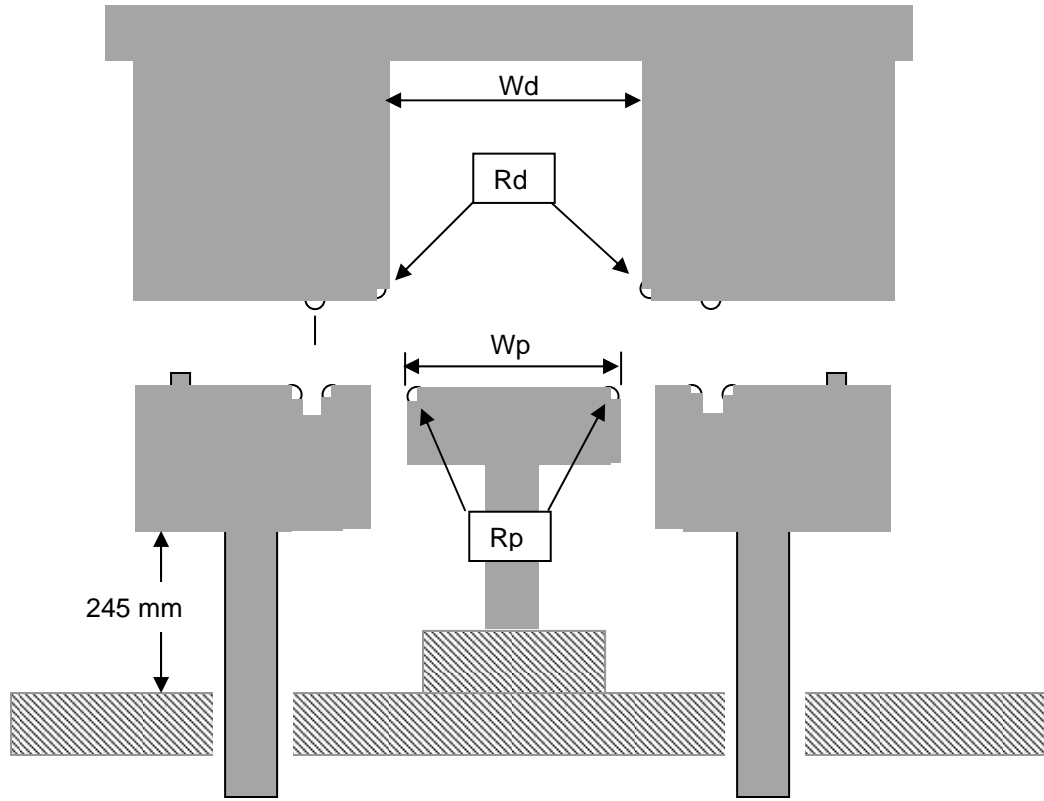Fig. 5.1. Tooling Components and Coordinate System in Side-View [23]
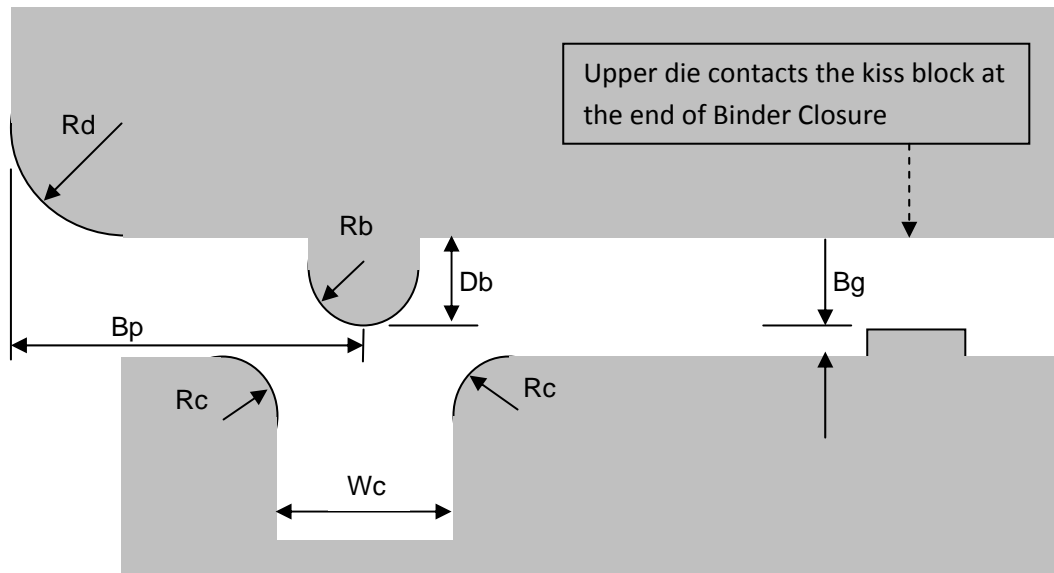
Fig. 5.2. Major Tooling Dimensions [23]

Fig. 5.3. Kiss block and Drawbead Dimensions and Location. Note the upper die and lower binder are shown in an OPEN position [23].

Table 5.1. Tooling, drawbead and processing parameters in Figs. 5.2 and 5.3 [23]

Description	Symbol	Value (mm)
Upper Die		
Width of Die Cavity	Wd	319.90
Radius of Die Profile	Rd	12.00
Punch		
Width of Punch	Wp	224.00
Radius of Punch Profile	Rp	12.00
Binder		
Binder Gap	Bg	See Table 5.2
Drawbead		
Bead Position	Bp	31.05
Depth of Bead	Db	6.85
Radius of Bead	Rb	4.00
Width of Channel	Wc	10.80
Radius of Channel	Rc	4.00
BLANK		
Width	BW	254.00
Length	BL	1066.80

Table 5.2. Binder gap and drawbead depth for the standard benchmark[23]

Material	Bg (mm)	D_b (mm) 25%	D_b (mm) 50%	D_b (mm) 75%	D_b (mm) 100%
AKDQ	1.42	2.34	4.75	6.85	9.09
HSLA	1.18	2.34	4.75	6.85	9.09
DP600	1.42	2.34	4.75	6.85	N/A
AA6022	1.42	2.34	4.75	6.85	9.09

   Once a channel section was drawn, it was removed from the die and allowed to spring back freely. Fig. 5.5 shows a typical example of a drawn channel section after springback. In order to measure the curvature in the channel sidewalls (i.e. after springback), 3 to 5 channel sections drawn with a given drawbead configuration were scanned using a Virtek LaserQC™ 2D laser scanner. Each channel section was carefully placed on its edge on the glass surface of the LaserQC™ in order to avoid applying any constraints to the channel and thereby distorting its natural shape. The glass surface was

also sufficiently slippery that the part would find its natural equilibrium. Channel sections were positioned in such a way that the laser could scan the edge of the RHS sidewall in contact with the glass without being obstructed. The scanning accuracy of the LaserQC™ is approximately 0.05 mm.

Table 5.3. Summary of mechanical properties of Numisheet2005 BM3 materials [23]

Material	Orientation	Thickness, mm	0.2 % Yield Stress, MPa	U.T.S. MPa	Uniform Elong. %	r-Value
AA6022	L	1.00	136.0	256.9	22.2	1.029
	T	1.00	127.6	238.3	24.0	0.728
	D	1.00	131.2	247.6	24.8	0.532
	Mean	**1.00**	**131.6**	**247.6**	**23.7**	**0.705**
AKDQ	L	1.00	158.3	315.0	26.4	1.546
	T	1.00	166.0	312.0	24.6	1.942
	D	1.00	164.7	317.0	25.1	1.508
	Mean	**1.00**	**163.0**	**314.7**	**25.4**	**1.626**
HSLA	L	0.80	394.3	463.7	16.4	0.581
	T	0.80	427.7	466.0	17.5	1.013
	D	0.80	395.3	447.0	17.0	1.166
	Mean	**0.80**	**405.8**	**458.9**	**16.9**	**0.981**
DP600	L	0.98	420.0	688.7	14.0	0.821
	T	0.98	425.7	697.0	13.5	0.969
	D	0.98	427.7	690.7	12.8	0.915
	Mean	**0.98**	**424.4**	**692.1**	**13.4**	**0.905**

L, T, D stand for the longitudinal, transverse and diagonal (45º) directions of the coil

Mean r-values are calculated as (L+T+2D)/4; other mean values are simply averages
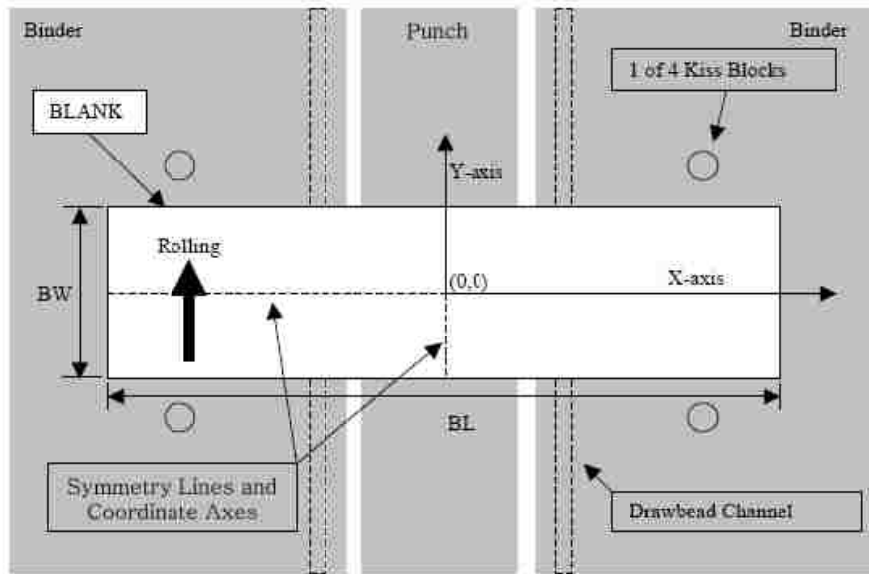
Fig. 5.4. Blank size and location, rolling direction of sheet coil, and XY coordinate system in plan-view [23]
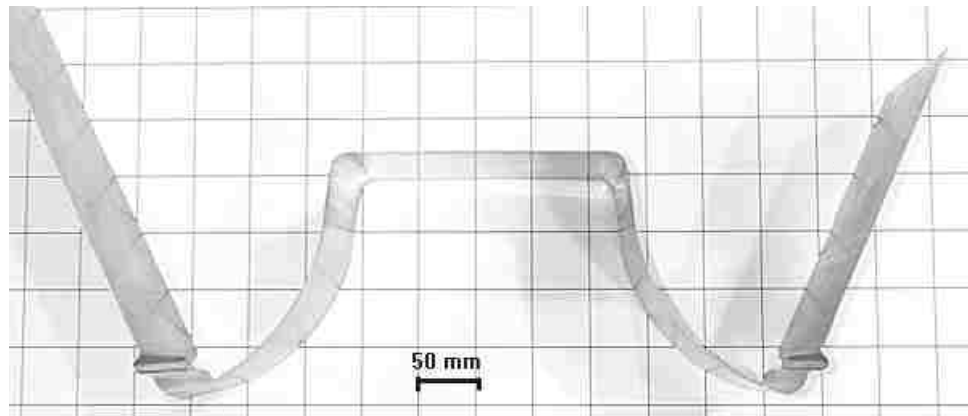

Fig. 5.5. Photograph of a drawn channel section after springback

5.3. Material Parameters:

Two sets of data are required for the YU model to completely define the material response: *a)* the anisotropic coefficients, *b)* the YU hardening parameters. The

anisotropic coefficients are usually obtained by uniaxial tension tests in different directions. For some particular yield functions, additional tests such as equibiaxial tests might be required. The YU hardening parameters were obtained by performing cyclic tests such as uniaxial tension-compression or cyclic shear tests on the material.

Two different yield functions were used in this project to implement the YU model: *a)* Hill's quadratic yield function and *b)* the Yld2000-2d non-quadratic yield function proposed by Barlat *et al.* [31]. Hill's quadratic yield function was used to simulate the channel draw for all four materials used in BM3, i.e. AKDQ, HSLA, DP600 and AA6022. However, Yld2000 was only used to simulate drawing AA6022 channel sections as this function was specifically developed for aluminum alloys. So, Hill's anisotropic coefficients were obtained for all four materials and the Yld2000 anisotropic parameters were only calculated for AA6022.

5.3.1. *Hill's quadratic yield function parameters:*

Hill's quadratic yield function can be written as:

$$
\begin{aligned}
\Big[F\big(\sigma_{yy} - \sigma_{zz}\big)^2 &+ G(\sigma_{zz} - \sigma_{xx})^2 + H\big(\sigma_{xx} - \sigma_{yy}\big)^2 \\
&+ 2\big(L\sigma_{xy}{}^2 + I\sigma_{yz}{}^2 + K\sigma_{zx}{}^2\big) - (\sigma_{ref})^2 \Big] = 0
\end{aligned}
\tag{5.1}
$$

where *F, G, H, L, I* and *K* are all material constants and σ_{ref} is the yield stress in the reference direction. In a general 3D stress space, six coefficients are used in Hill's 1948 yield function. Therefore, at least six input data from the material are required to determine these coefficients. Any combination of the yield strength and/or r-values of the material in different directions can be used to calculate these constants. For instance, one combination is the yield strength in the rolling direction and r-values in the rolling, transverse and diagonal directions. Let σ_0 denote the yield stress in the rolling direction and r_0, r_{90}, r_{45} denote the r-values in the rolling, transverse and diagonal directions, respectively. Uniaxial tension in the rolling (reference) direction gives:

$$G + H = (\frac{\sigma_{ref}}{\sigma_0})^2 = 1 \qquad (5.2)$$

The equation for r-values in each direction gives the following equations:

$$r_0 = \frac{\dot{\varepsilon}_{yy}^p}{\dot{\varepsilon}_{zz}^p} = \frac{\frac{\partial f}{\partial \sigma_{yy}}}{\frac{\partial f}{\partial \sigma_{zz}}} = \frac{H}{G} \qquad (5.3)$$

$$r_{90} = \frac{\dot{\varepsilon}_{xx}^p}{\dot{\varepsilon}_{zz}^p} = \frac{\frac{\partial f}{\partial \sigma_{xx}}}{\frac{\partial f}{\partial \sigma_{zz}}} = \frac{H}{F} \qquad (5.4)$$

In order to calculate the equation for r_{45}, we need to transform the stress into the anisotropic axes first. Then, Eq. (5.1) must be used to calculate the plastic strain in the anisotropic directions. Finally, the strains must be transformed back into the original coordinate system and the transverse strain is extracted. Following this procedure leads to the following equation:

$$r_{45} = \frac{2L - (F + G)}{2(F + G)} \qquad (5.5)$$

Solving Eqs. (5.2-5.5) gives:

$$G = \frac{1}{1 + r_0}$$

$$H = \frac{r_0}{1 + r_0}$$

$$F = \frac{r_0}{(1 + r_0)r_{90}} \qquad (5.6)$$

$$L = \frac{1}{1 + r_0}\left(\frac{1}{2} + r_{45}\right)\left(1 + \frac{r_0}{r_{90}}\right)$$

In order to calculate I and K, the shear yield stresses or r-values in the xz and yz planes are required. However, in the plane-stress and plane-strain states these values are not required since no stress is applied in these directions. In the simulation of BM3, either the plane-stress assumption or the plane-strain assumption was adopted. Therefore, only the

constants in Eqs. (5.6) are required for simulation. The experimental yield stress and r-values for BM3 materials are shown in Table 5.4. Eqs. (5.6) were used to calculate the anisotropic constants for these materials, and Hill's material coefficients are shown in Table 5.5.

Table 5.4. The experimental values for BM3 materials

Material	σ_0(MPa)	r_0	r_{45}	r_{90}
AKDQ	158	1.546	1.508	1.942
HSLA	394	0.581	1.166	1.013
DP600	420	0.821	0.915	0.969
AA6022	136	1.029	0.532	0.728

Table 5.5. Coefficients for Hill's 1948 yield function

Material	F	G	H	L
AKDQ	0.313	0.393	0.607	1.417
HSLA	0.433	0.567	0.433	1.498
DP600	0.465	0.549	0.451	1.435
AA6022	0.697	0.493	0.507	1.228

5.3.2. Yld2000-2d yield function parameters:

Yield stress and r-values in the rolling and transverse directions ($\sigma_0, \sigma_{90}, r_0, r_{90}$), yield stress and r-value in the balanced biaxial yield stress (σ_b, r_b) provide six input data to calculate the coefficients. The parameter r_b defines the slope of the yield surface at the balanced biaxial stress state ($r_b = \dot{\varepsilon}_{yy}/\dot{\varepsilon}_{xx}$) and can be evaluated by performing compression of circular disks in the sheet normal direction and measuring the aspect ratio of the specimen after deformation. If it is not possible to perform compression of a

circular disk, the parameter r_b can also be estimated by either Yld96 or a polycrystal model. Loading of the material in the uniaxial and equibiaxial stress states yields the following equations:

$$f = \emptyset - 2(\bar{\sigma}/\sigma)^{a'} = 0 \tag{5.7}$$

$$g = q_x \frac{\partial \emptyset}{\partial s_{xx}} - q_y \frac{\partial \emptyset}{\partial s_{yy}} = 0 \tag{5.8}$$

where s_{ij} denotes the deviatoric stress, q_x, q_y are defined in Table 5.6 and $\emptyset$ is given in Eq. (5.9). It is worth noting that Eq. (5.7) satisfies the yield function and Eq. (5.8) satisfies the r-value. The function $\emptyset$ can be written as:

$$\emptyset = |\alpha_1 \gamma - \alpha_2 \delta|^{a'} + |\alpha_3 \gamma + 2\alpha_4 \delta|^{a'} + |2\alpha_5 \gamma + \alpha_6 \delta|^{a'} \tag{5.9}$$

where γ, δ are defined in Table 5.6 for uniaxial and biaxial stress states. Eqs. (5.7, 5.8) provide six equations in terms of α_1 to α_6. So, six independent coefficients α_1 to α_6 can be found by solving this set of equations simultaneously.

Table 5.6. The definition of q_x, q_y, γ and δ for uniaxial and biaxial loading

	γ	δ	q_x	q_y
0°	2/3	-1/3	$1 - r_0$	$2 + r_0$
90°	-1/3	2/3	$2 + r_{90}$	$1 - r_{90}$
Biaxial	-1/3	-1/3	$1 + 2r_b$	$2 + r_b$

In order to find α_7 and α_8, the yield stress and r-value obtained by uniaxial tension test at 45° to the rolling direction are used. If the material is loaded in uniaxial tension at 45° to the rolling direction, the following equation should satisfy the yield surface:

$$\left| \frac{\sqrt{(K'_2)^2 + 4\alpha_7{}^2}}{2} \right|^{a'} + \left| \frac{3K''_1 - \sqrt{(K''_2)^2 + 4\alpha_8{}^2}}{4} \right|^{a'}$$

$$+ \left| \frac{3K''_1 + \sqrt{(K''_2)^2 + 4\alpha_8{}^2}}{4} \right|^{a'} - 2(\bar{\sigma}/\sigma_{45})^{a'} = 0 \qquad (5.10)$$

where

$$K'_2 = \frac{\alpha_1 - \alpha_2}{3}$$

$$K''_1 = \frac{2\alpha_5 + \alpha_6 + \alpha_3 + 2\alpha_4}{9} \qquad (5.11)$$

$$K''_2 = \frac{2\alpha_5 + \alpha_6 - \alpha_3 - 2\alpha_4}{3}$$

The equation which satisfies r-value in the diagonal direction is written as follows:

$$G = \frac{\partial \emptyset}{\partial \sigma_{xx}} + \frac{\partial \emptyset}{\partial \sigma_{yy}} - \frac{2a\bar{\sigma}^{a'}}{\sigma(1 + r_{45})} \qquad (5.12)$$

Eqs. (5.10, 5.12) provide two equations for α_7 and α_8 which can be solved to obtain these coefficients. Usually, the Newton-Raphson method is used to solve these equations. In this work, the above-mentioned procedure was used to develop a computerized program for calculating α_1 to α_8. The program was used to determine the coefficients α_k for AA6022-T43. Table 5.7 shows the experimental data for AA6022-T43 and Table 5.8 lists the material coefficients for Yld2000-2d.

Table 5.7. Experimental mechanical properties of AA6022-T43

σ_0	σ_{90}	σ_b	σ_{45}	r_0	r_{90}	r_b	r_{45}
136.0	127.6	136.1	131.2	1.029	0.728	1.000	0.532

Table 5.8. The anisotropic coefficients of AA6022-T43 for Yld2000-2d

α_1	α_2	α_3	α_4	α_5	α_6	α_7	α_8	a'
0.9380	1.0451	0.9291	1.0298	0.9874	1.0359	0.9528	1.1010	8

5.3.3. YU model parameters:

As explained in section 3.7, the parameters associated with the YU model can be identified by either an optimization method or a systematic method. The optimization method calculates the parameters simultaneously by fitting the simulation to the experimental stress-strain curve; while the systematic method uses a graphical method to identify the material constants from the stress-strain curve in cyclic deformation. The cyclic stress-strain response of the material is required for identification procedure. So, uniaxial tension-compression tests were first carried out on all BM3 materials. The uniaxial tests were performed using a special instrument developed at Ohio State University by Boger et al. [3]. This testing apparatus uses flat plates pressurized with pneumatic cylinders to provide a lateral support for the sheet specimen and prevent it from buckling during uniaxial compression tests. In this approach, the geometry of the specimen was designed to minimize the buckling outside the constrained region. A schematic illustration of this anti-buckling mechanism is shown in Fig. 5.6. Figs. 5.7-5.10 show the cyclic response of the BM3 materials in uniaxial tension-compression tests in the rolling direction. As can be seen in these figures, the maximum strain in compression is only about -0.03 because the risk of buckling increases beyond this. So, cyclic shear tests were also performed on all BM3 materials except for AA6022-T43 because the original batch of material was no longer available.
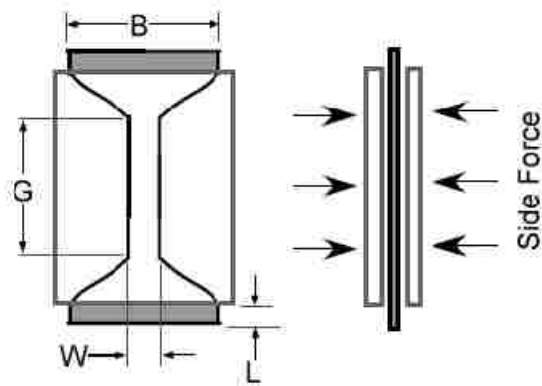
For 6022-T4 (thickness = 2.5 mm):
G = 36.8 mm, W = 15.2 mm
B = 50.8 mm, L > 3 mm

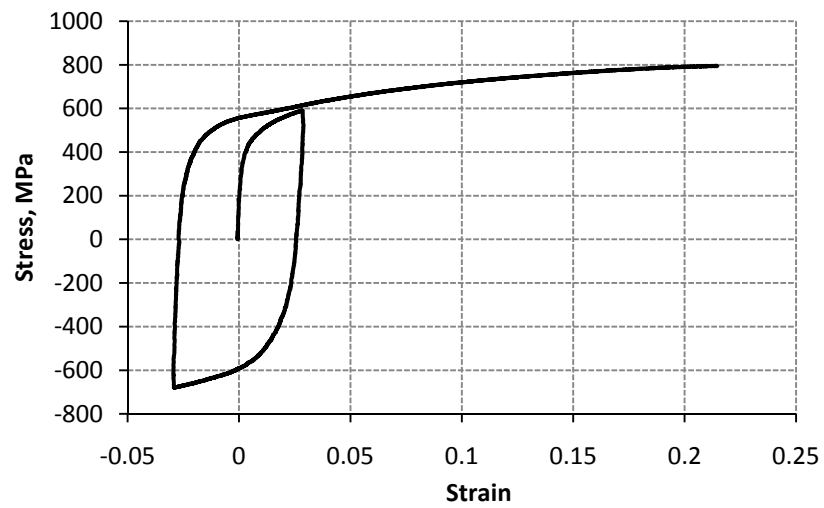Fig. 5.6. Schematic of the flat dies and dimensions of specimens [3]

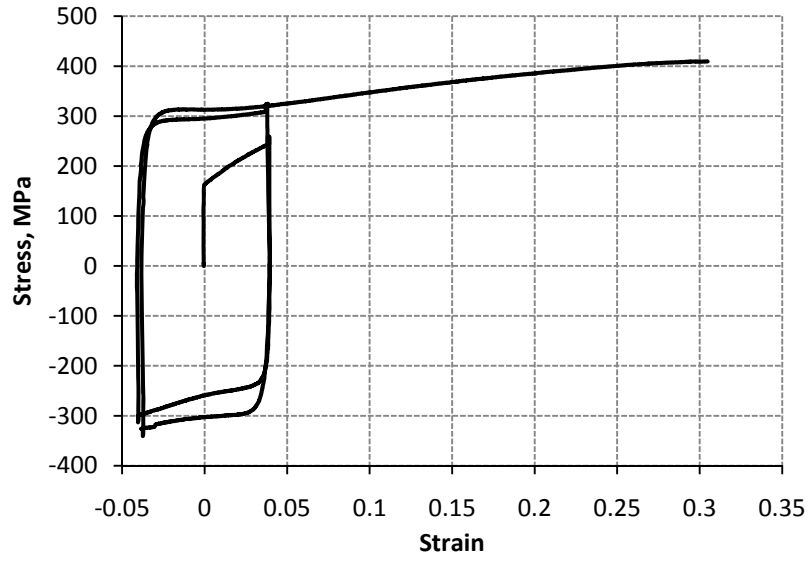Fig. 5.7. The uniaxial tension-compression response of DP600

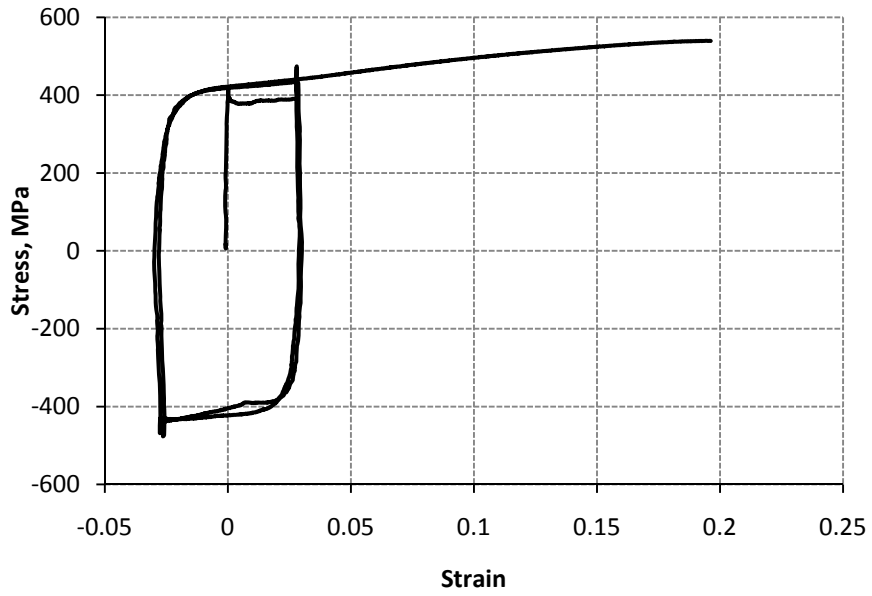Fig. 5.8. The uniaxial tension-compression response of AKDQ

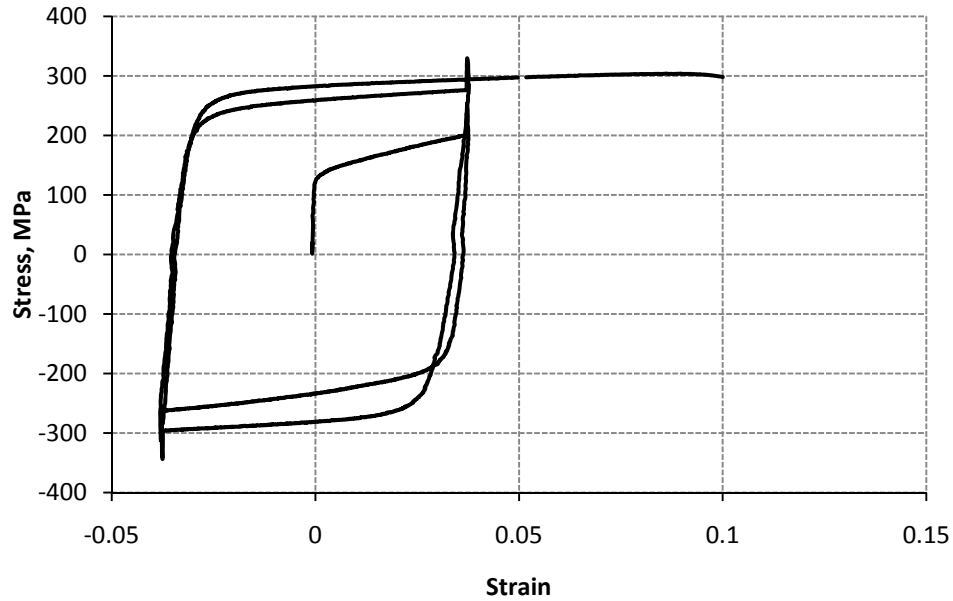Fig. 5.9. The uniaxial tension-compression response of HSLA

111

Fig. 5.10. The uniaxial tension-compression response of AA6022-T43

The cyclic simple shear tests were carried out at the Université de Bretagne-Sud, in France. A schematic of this testing apparatus, especially designed for the study of metallic sheets, used in the shear test is shown in Fig. 5.11. The sample (1) is clamped between two grips (2) and (3), securely attached to the fixed part (4) and the moving part (5) of the apparatus, respectively. The relative motion between (4) and (5) is obtained by pairs of linear guides symmetrically positioned with respect to the sample. The device is directly connected to a tensile test machine. The clamping of the sample under the grips is obtained by the tightening of six screws with a torque wrench; the torque is dependent on the tested material. The optimal value is obtained with the lowest torque that minimizes the sliding between the sample and the grips.
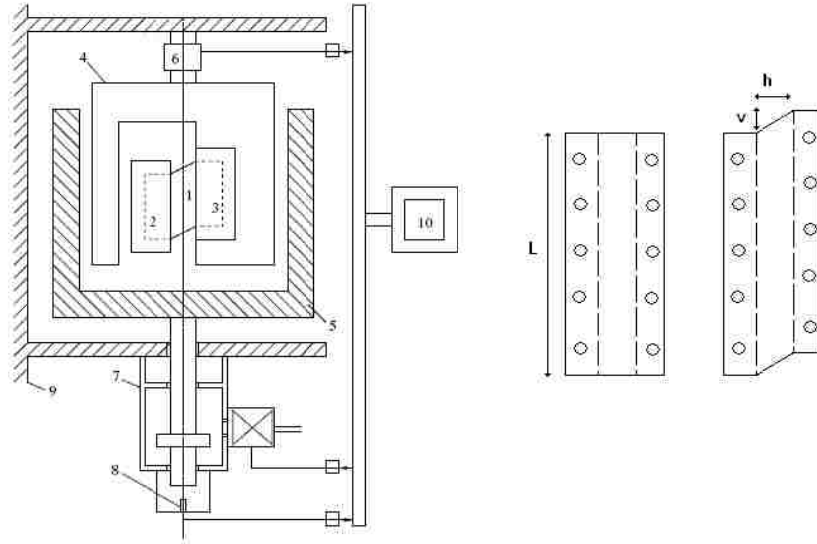
Fig. 5.11. The schematic of simple shear device [93]

Simple shear tests were performed on BM3 sheet steels at different prestrain magnitudes. A systematic method, explained in section 3.7.2, was used to obtain the YU hardening parameters for these materials. Figs. 5.12-5.14 show the experimental stress-strain response of DP600, AKDQ and HSLA obtained by simple shear test. The identified material constants are used to simulate the stress-strain response of these materials. As can be seen, the YU model is able to accurately describe the stress-strain response of these materials. In order to compare isotropic hardening (IH) model with the YU model, the predicted response by IH model is also shown for the largest strain magnitude. It is observed that the IH model over-predicts the stress as it is not able to model the cyclic phenomena. A comparison of the uniaxial tension-compression test and simple shear test reveals that the maximum compressive strain in the uniaxial test was much smaller than the reversal strain in the simple shear test. We also know that the strain level in BM3 is around 30% for shallowest drawbead penetration which is much larger than the strain achieved in the uniaxial test. So, we used the constants obtained by simple shear test as shown in Table 5.9. As mentioned before, the AA6022-T43 was no longer available for the simple shear test. So, we used the cyclic tension-compression curve to obtain the constants for AA6022-T43. Fig. 5.15 compares the predicted response by YU model with that of experiment.
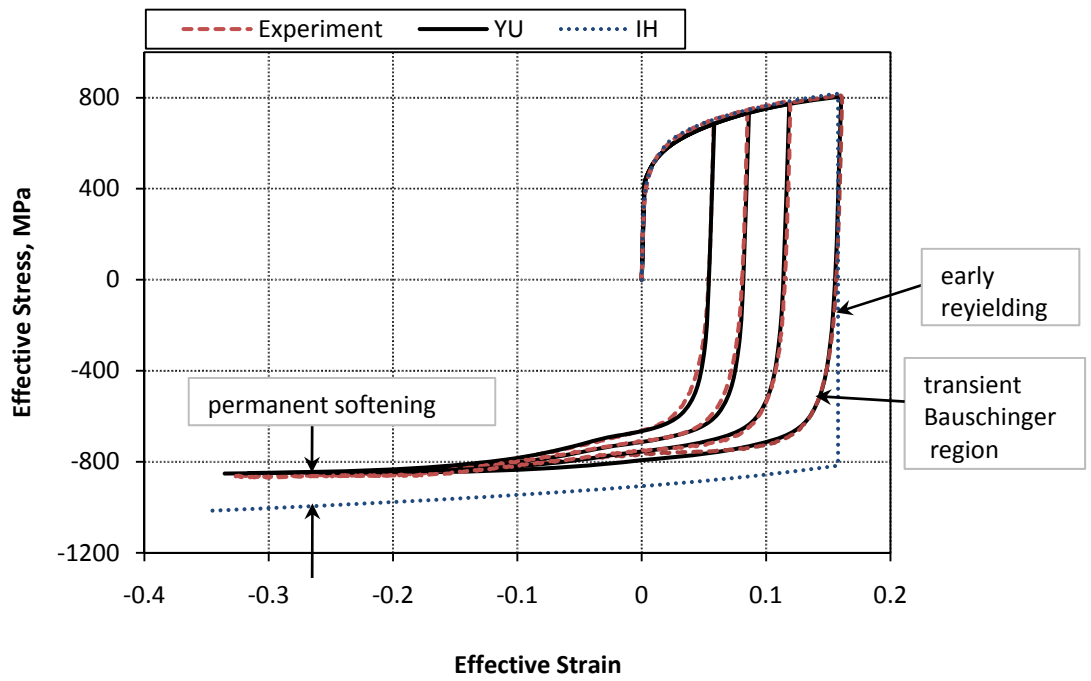
Fig. 5.12. Comparison of predicted stress-strain response of DP600 with experimental data
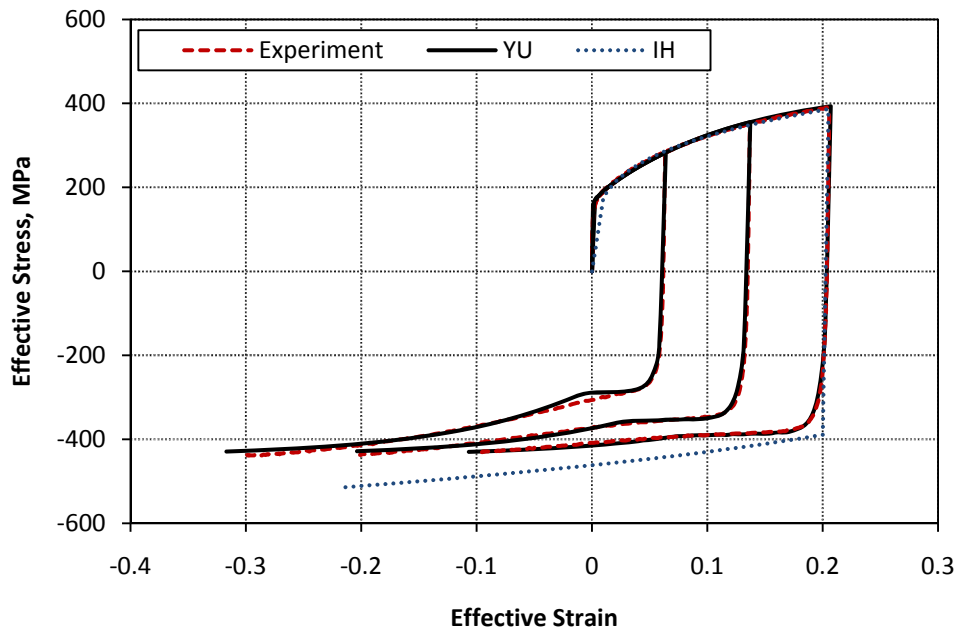

Fig. 5.13. Comparison of predicted stress-strain response of AKDQ with experimental data
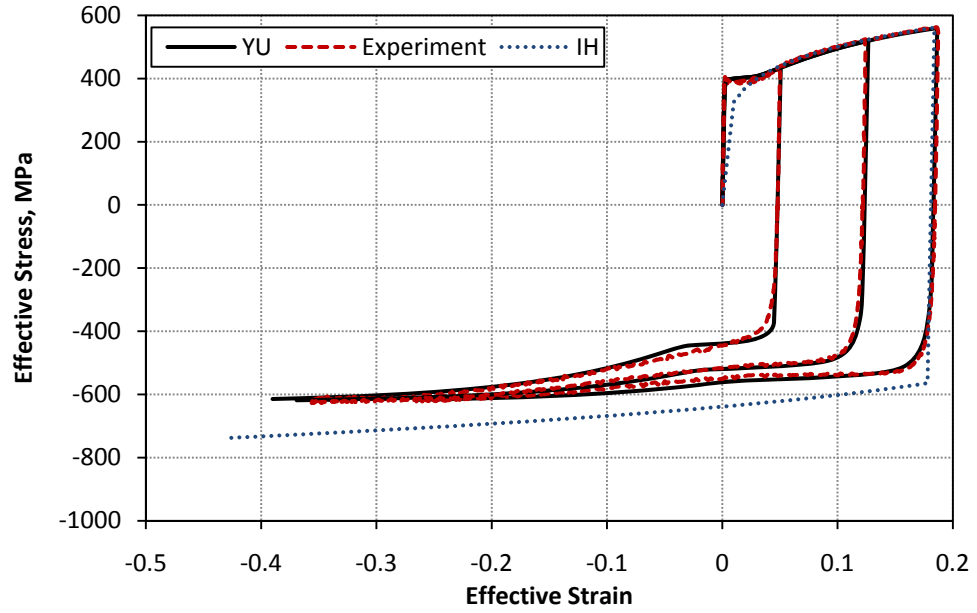
Fig. 5.14. Comparison of predicted stress-strain response of HSLA with experimental data
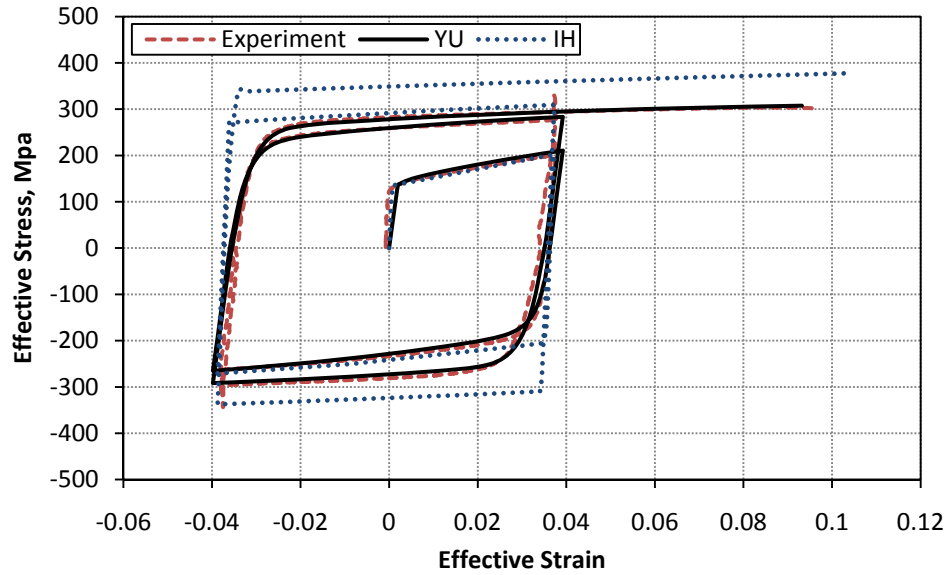

Fig. 5.15. Comparison of predicted stress-strain response of AA6022 with experimental data

Table 5.9. The Yoshida-Uemori material constants (Eqs. 3.3-3.6, 3.37)

Material	Y (MPa)	C	B (MPa)	R_{sat} (MPa)	b (MPa)	k	h	E_0 (GPa)	E_a[**] (GPa)	ζ[**]
AKDQ	158	300	190	240	10	8.5	0.7	206	178	160
HSLA*	394	200	400	195	30	8	0.8	206	178	160
DP600	420	200	555	190	110	12	0.9	206	163	135
AA6022	135	700	150	130	40	13	0.01	70	61	120

*The initial size of the stagnation surface was set equal to 5 MPa.

** These constants were obtained from reference [82]

5.4. Finite Element Model:

Finite element (FE) simulation of springback is very sensitive to the finite element model parameters such as element type, mesh size, friction and constitutive model. This section is therefore dedicated to studying the effect of different process parameters on the predicted springback of the sidewall of drawn channel sections. After careful investigation of the process parameters, the optimized conditions will be used to simulate BM3 using YU material model. In the finite element model, the deformation of tooling was neglected as it is very small compared to that of the sheet material and all the tooling was modelled as rigid entities. Furthermore, only half of the sheet was modelled due to symmetry and the corresponding symmetric boundary condition was applied. The penalty contact algorithm was used to model the contact between the blank and each tool. The sensitivity of the analysis to the friction coefficient will also be discussed.

It is generally preferable to use a global implicit integration scheme for both forming and springback stages as the dynamic effects are not taken into account in this scheme [53, 94, 95]. However, deformation in the forming stage is usually complex and it is difficult to get convergence for such a problem. Therefore, the explicit-implicit approach has also been popular in springback simulation [96-99]. For BM3, it is very difficult to simulate the forming stage with an implicit solver because of the very severe deformation in the drawbead region. It also becomes more difficult when an advanced constitutive

model is used in the simulation. So, an explicit-implicit approach was used in this work. That is, the forming stage was simulated using ABAQUS-Explicit and the results were imported into ABAQUS-Standard that uses an implicit integration scheme for the simulation of unloading. For all steels, Hill's quadratic yield function was used to describe the anisotropy of the steel sheets. For AA6022, both Hill's quadratic and Yld2000-2d yield functions were used. Three hardening models were also used with the yield function for all materials: *a)* isotropic hardening, *b)* combined isotropic-nonlinear kinematic hardening, and *c)* Yoshida-Uemori model.

5.4.1. The effect of element type on springback:

Since the blanks were 254 mm wide, it is reasonable to assume a plane-strain deformation. Both shell and solid elements were used to model the blank sheet to study the ability of each element type to simulate springback for this benchmark. In the model with shell elements, only a small portion of the blank in the width direction was modelled and appropriate symmetric boundary conditions were imposed to ensure plane-strain deformation. The shell element used in this case is denoted as S4R in ABAQUS which is a 4-node shell element in reduced integration mode. The mesh convergence study showed that a mesh size 0.5 mm in the longitudinal direction represented an appropriate discretization of the model. In the model with solid elements, a 4-node (first order) plane-strain element in reduced integration mode denoted as CPE4R in ABAQUS was used. The hourglass energy of the system and the convergence study showed that at least four elements along the thickness were required for CPE4R element. The aspect ratio of the solid elements was consistently chosen to be one, and this discretization resulted in convergence in all cases.
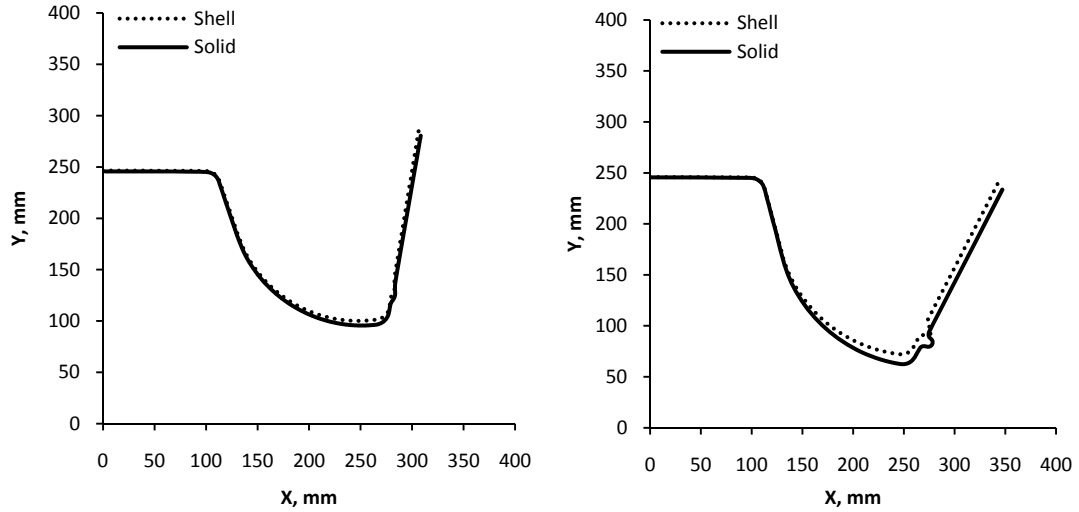
Fig. 5.16. Comparison of the predicted profile using shell and solid elements for AKDQ at 25% (left) and 100% (right) drawbead penetrations

The sidewall profile predicted with each type of element is shown in Figs. 5.16-5.17 as an example for two materials at two different drawbead penetrations. A comparison between the simulated profile by solid and shell elements shows that both elements predict almost the same profile for springback. Therefore, it appears that a fine mesh with shell elements can produce the same springback profile as with solid elements even though the ratio *R/t* (tool radius to sheet thickness) is less than 5 in the drawbead region. It would seem that both shell and solid elements can be used for the simulation of this benchmark.
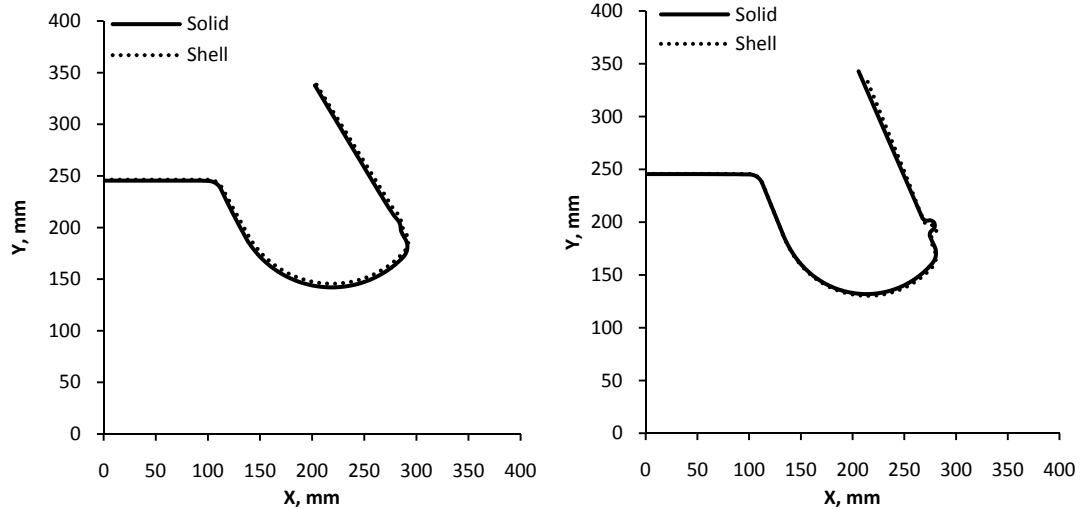
Fig. 5.17. Comparison of the predicted profile using shell and solid elements for HSLA at 25% (left) and 100% (right) drawbead penetrations

5.4.2. The effect of number of integration points on springback:

The number of integration points (NIP) through the sheet thickness is of critical significance when using shell elements. In general, more integration points are required when a larger stress gradient is to be captured by the element. Therefore, the required NIP depends on the drawbead penetration and the material in this problem. Figs. 5.18-5.19 show the effect of NIP on the predicted sidewall profile after springback for different materials and for the deepest drawbead penetrations which need more integration points through the thickness. A comparison of the predicted profile with the experimental profile shows that the predicted profile is underestimated for HSLA and AKDQ when only 5 integration points (the default value in ABAQUS) are used through the thickness. However, the use of 5 integration points results in an overestimation of springback for DP600. This observation shows that the predicted springback profile oscillates around the converged solution which is consistent with the observation of Wagoner and Li [18]. These figures show that at least 9 integration points are required for HSLA and AA6022 to guarantee convergence. However, a larger number of integration points are required for DP600 and AKDQ. These figures show that at least 29 and 49 are

required for AKDQ and DP600, respectively, to guarantee the convergence of the numerical solution. Material nonlinearity and the strength of material are among the important factors affecting NIPs through the thickness. Usually, more NIPs are required for higher strength materials and more nonlinear materials. Note that the maximum compressive and tensile stresses depend upon yield stress.
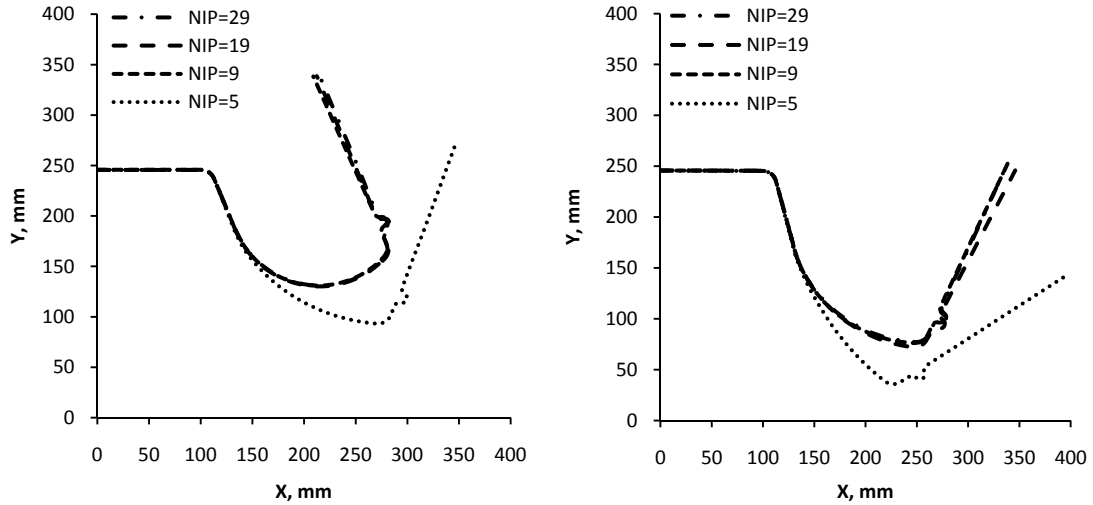

Fig. 5.18. The effect of NIP on springback profile for HSLA (left) and AKDQ (right) at 100% drawbead penetration
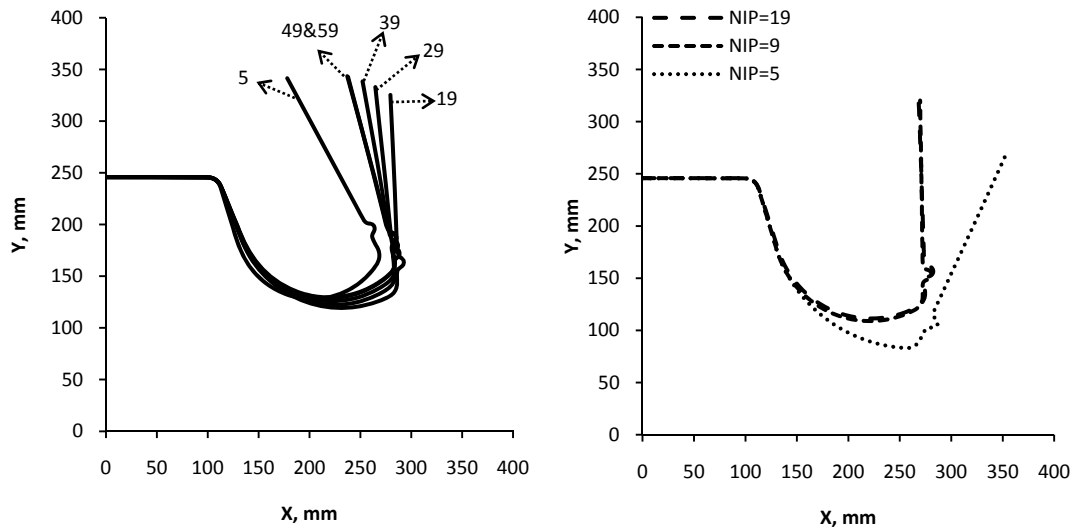

Fig. 5.19. The effect of NIP on springback profile for DP600 (left) and AA6022 (right) at 75% and 100% drawbead penetrations, respectively

120

5.4.3. The effect of friction coefficient on springback:

As discussed in section 5.2, the distance between the die and binder surfaces was always 0.42 mm more than the nominal thickness of the sheet during the drawing process in order to minimize the effect of friction. It is therefore expected that friction has a minor effect on the amount of springback in this problem. A constant friction coefficient of 0.16 for AA6022-T43 and 0.12 for the other materials was used, as suggested by data obtained from twist compression tests [100]. However, different values of the coefficient of friction were used in the simulations to investigate the sensitivity of the predicted profile to the friction coefficient.

At the beginning of forming stage, the sheet is first bent over the die radius. After the punch travels a certain distance, the material points located before the drawbead region flow through the drawbead region and will finally end up in the sidewall. Since only a little area is in contact with binder, the contact area does not change significantly throughout the forming stage. So, the forming stage of this problem is expected to be a kind of steady state process. The experimental punch force, as shown at the end of this chapter, confirms that the punch force converges to a certain value for all materials and all drawbead penetrations. This suggests that the friction should be constant throughout the forming stage. Therefore, the change of friction coefficient during the forming stage is not considered here in this work.

Figs. 5.20-5.21 show the effect of friction on the predicted profile after springback. The friction coefficient of 0.16 did not result in convergence of simulation for AKDQ during springback stage. In general, a greater coefficient of friction results in a greater tension in the sidewall and consequently reduces the amount of springback. Although the validity of this observation is confirmed by Figs. 5.20-5.21, the springback profile is not very sensitive to the coefficient of friction at shallow drawbead penetration (25%) where the restraining force is relatively low and the tension in the sidewall is not sufficiently large to considerably reduce springback. However, at deeper drawbead penetrations the springback profile is somewhat sensitive to the coefficient of friction. It is also worth

121

mentioning that a very small coefficient of friction may cause instability in the numerical simulation and convergence may not be obtained. A large coefficient of friction may also result in failure of the sheet in the sidewall. Therefore, the choice of a reasonable coefficient of friction is important in the simulation of the channel draw process even if the contact area between the sheet and the binder is minimized.
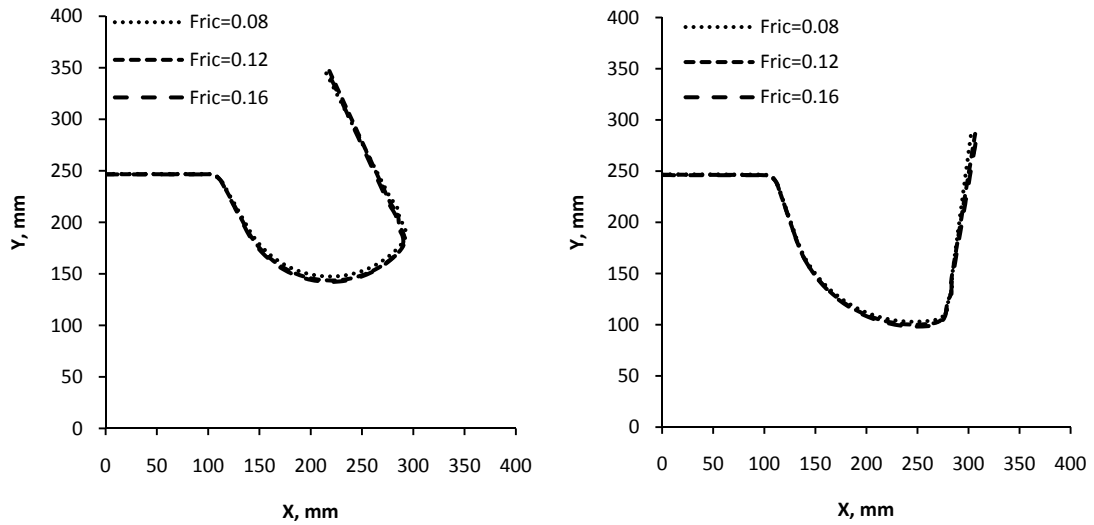

Fig. 5.20. The effect of coefficient of friction on springback profile of DP600 (left) and AKDQ (right) at 25% drawbead penetration
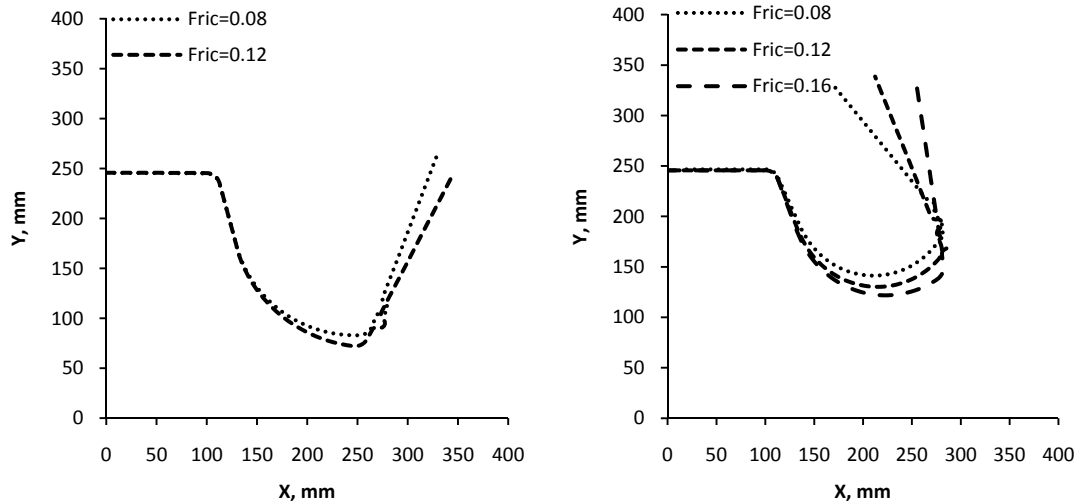

Fig. 5.21. The effect of coefficient of friction on springback profile of AKDQ (left) and HSLA (right) at 100% drawbead penetration

5.5. Results:

During the experimental work of BM3, it was found that DP600 channel sections drawn with 100% drawbead penetration occasionally fractured in the sidewall, therefore this condition was excluded from the investigation. All other combinations of sheet material and drawbead penetration were simulated using ABAQUS commercial software, resulting in a series of 15 different simulations. Three different material models were used in the simulations: *a)* isotropic hardening (IH), *b)* combined isotropic-nonlinear kinematic hardening (IH+NKH), *c)* Yoshida-Uemori two-surface model (YU). So, the results obtained by each model are first presented and then compared.

5.5.1. Error between the simulated and experimental curve:

In order to quantify the error between the simulation and experiment, consider point C on the experimental curve and its corresponding point C′ on the simulated curve, as shown in Fig. 5.22. The error in the x-direction and y-direction are obtained as follows:

$$(\delta_x)_c = (X_c - X_{c'})$$
$$\left(\delta_y\right)_c = (Y_c - Y_{c'})$$

(5.13)

So, the error at point C can be written as:

$$\delta_c = \sqrt{(\delta_x)_c^2 + \left(\delta_y\right)_c^2}$$

(5.14)

In fact, the error at each point is equal to the distance between that point and the corresponding point on the simulated curve. The sum of errors between the simulated and experimental curve can be calculated by the line integral over the experimental curve. So, the area between two curves can be used as a measure of the error between the experimental and simulated profiles. In order to normalize the error, this area is divided by the area under the experimental curve from point A to point B as follows:

$$\text{Error} = \frac{\text{Area between the curves}}{\text{Area under the experimental curve from A to B}} \qquad (5.15)$$

Since the area of interest is the sidewall region, only the curves from points A up to point B are considered. Note that point A is the end point of the punch radius.
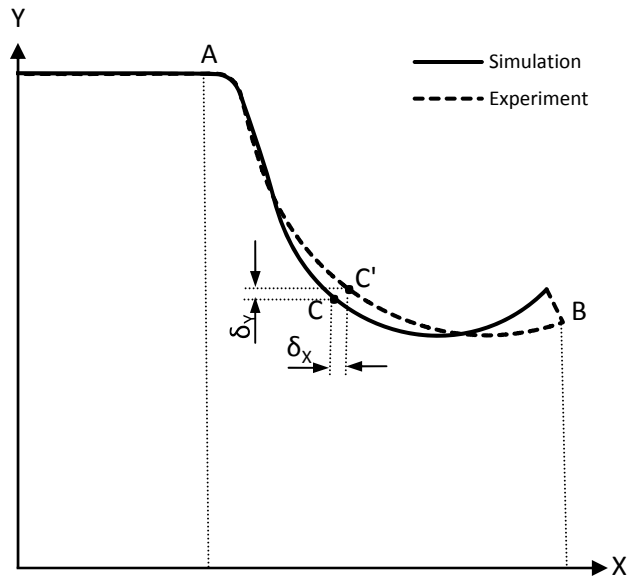

Fig. 5.22. Schematic illustrating the error between the simulated and experimental curves

5.5.2. Isotropic hardening model (IH):

Hollomon's power law relationship between the stress and the amount of plastic strain can be written as:

$$\sigma = K(\bar{\varepsilon}^p)^n \qquad (5.16)$$

where σ is the stress, K is the strength index, $\bar{\varepsilon}^p$ is the effective plastic strain and n is the strain hardening index. This law can be used to fit the experimental stress-strain curve of the material and be extrapolated to obtain the material response at larger strain magnitudes. Table 5.10 lists the coefficients in Hollomon's equation fitted to the uniaxial stress-strain curve of the material in the rolling direction of the sheet. Using the material coefficients in Table 5.10, the isotropic hardening model with Hill's quadratic yield

124

function was used to simulate BM3 of NumiSheet 2005. The simulations were carried out using the initial elastic modulus (IEM) and the reduced elastic modulus (REM) according to Eq. (3.37) and the corresponding constants are given in Table 5.9. For each simulation, the error between the simulation and experiment were calculated according to Eq. (5.15). Table 5.11 shows the percentage of relative error for each material at different drawbead penetrations. Figs. 5.23-5.30 compare the experimental channel sidewall profile with the profile predicted by the IH model for all four BM3 materials. These figures show that the IH model over-predicts springback and the reduced unloading modulus results in a larger springback. In IH model, the stress is over-predicted in the simulation which results in overestimation of springback. However, if the decrease of unloading modulus is not taken into account, the springback will be underestimated. So, the simulation of springback by IH model with initial elastic modulus may happen to be relatively accurate due to compensation of these two errors. This is the case for DP600 as can be observed from Figs. 5.23-5.30 and Table 5.11. In order to prove this, the experimental punch force during forming stage can be compared with that predicted by IH model. The punch force is the integral of stress. So, the punch force during the forming stage must be over-predicted if the stresses are over-estimated by the model. The results of simulations of BM3 by IH model confirm that this model considerably over-predicts the punch force for DP600. A comparison between the predicted and experimental punch force will be presented later in this chapter.

Table 5.10. Coefficients in Hollomon's equation for BM3 sheet materials

Material	K(MPa)	n
AA6022-T43	479.9	0.258
AKDQ	579.9	0.256
DP600	1080.7	0.152
HSLA	770.0	0.187

125

Table. 5.11. The percentage of relative error in prediction of springback by IH model

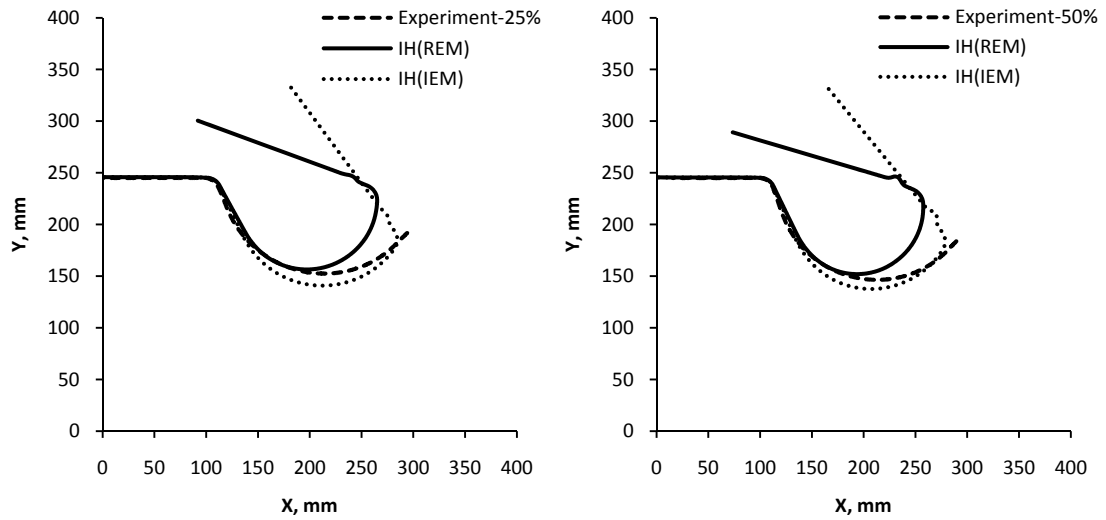| Drawbead Penetration	DP600		AKDQ		HSLA		AA6022	
	IEM	REM	IEM	REM	IEM	REM	IEM	REM
25%	4.74	6.12	18.25	24.67	6.27	15.11	12.01	6.32
50%	3.67	7.06	18.07	26.22	3.87	10.66	8.94	4.53
75%	3.05	10.12	16.81	24.49	6.55	13.83	4.50	7.00
100%	--	--	19.30	25.62	11.87	24.49	6.38	10.96

Fig. 5.23. Channel sidewall profiles predicted by the IH model for DP600 at 25% (left) and 50% (right) drawbead penetrations
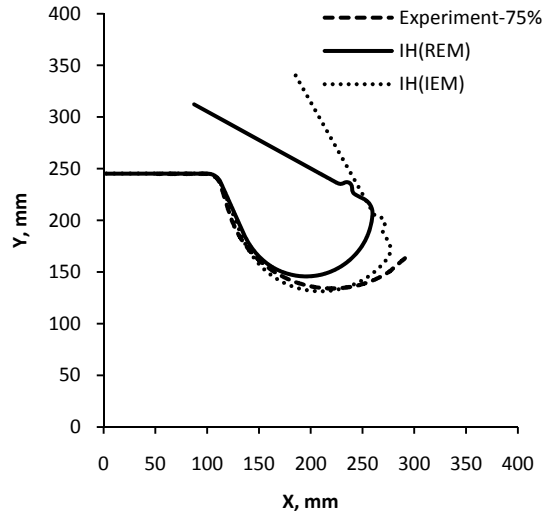
Fig. 5.24. Channel sidewall profiles predicted by the IH model for DP600 at 75% drawbead penetration

Fig. 5.25. Channel sidewall profiles predicted by the IH model for AKDQ at 25% (left) and 50% (right) drawbead penetrations

Fig. 5.26. Channel sidewall profiles predicted by the IH model for AKDQ at 75% (left) and 100% (right) drawbead penetrations
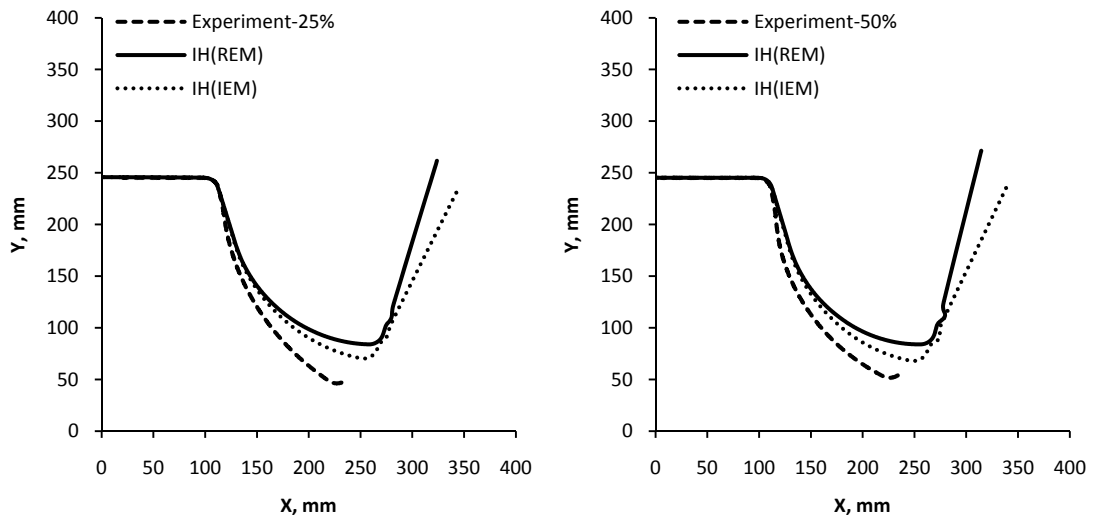

Fig. 5.27. Channel sidewall profiles predicted by the IH model for HSLA at 25% (left) and 50% (right) drawbead penetrations
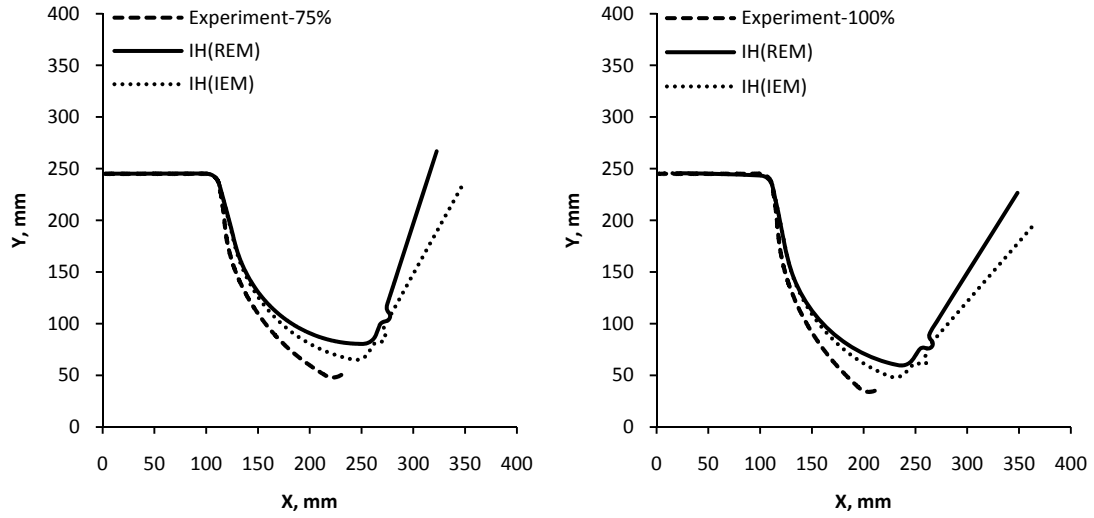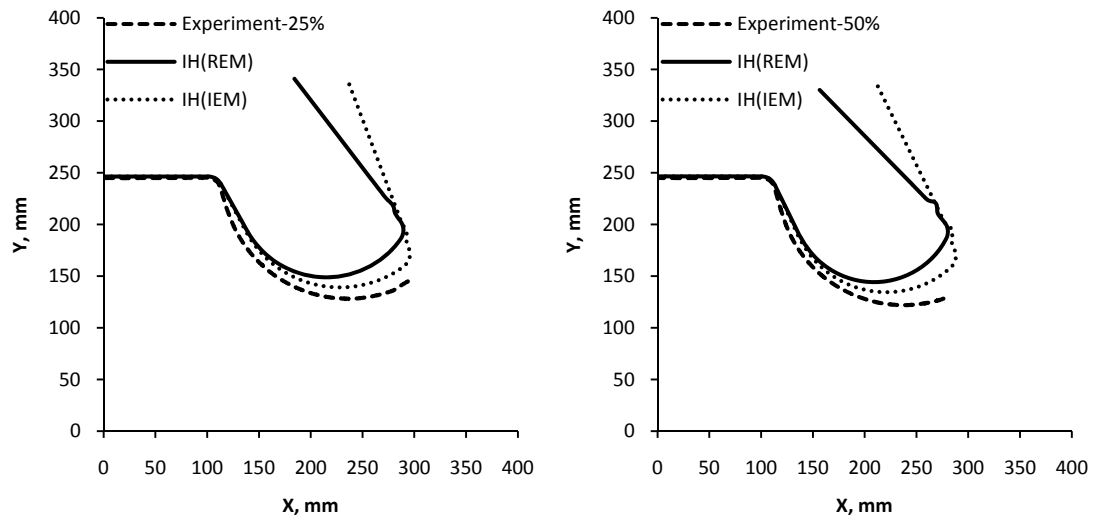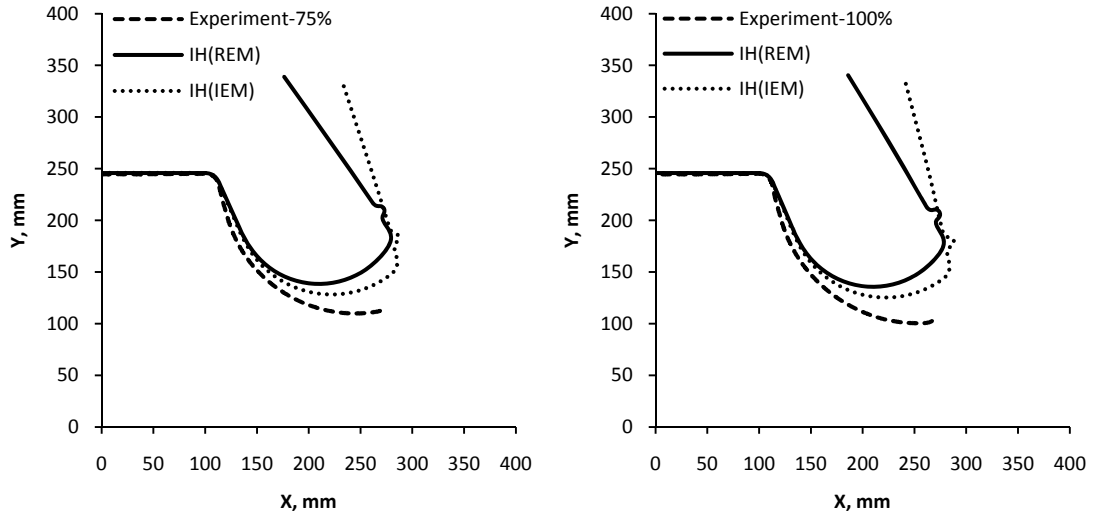
Fig. 5.28. Channel sidewall profiles predicted by the IH model for HSLA at 75% (left) and 100% (right) drawbead penetrations
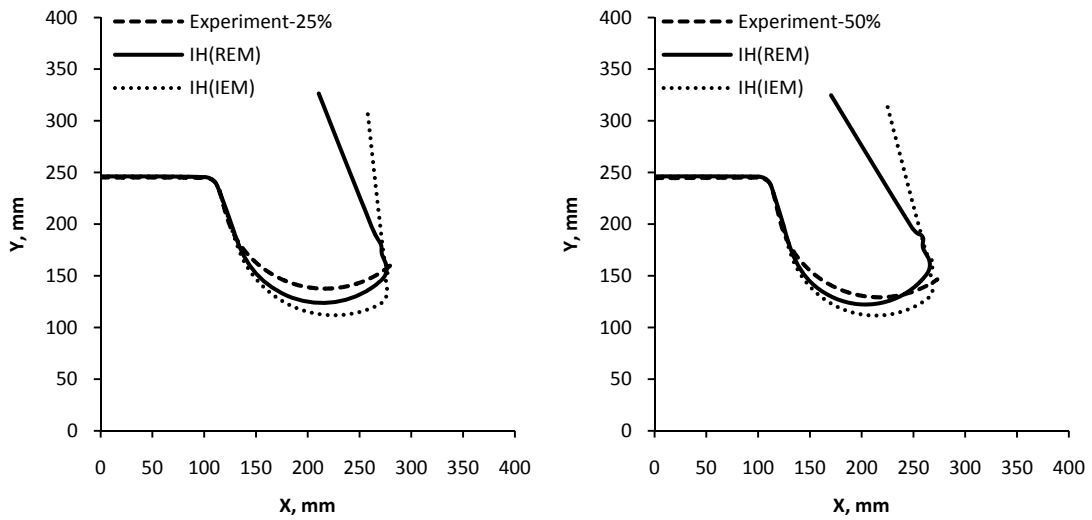

Fig. 5.29. Channel sidewall profiles predicted by the IH model for AA6022 at 25% (left) and 50% (right) drawbead penetrations
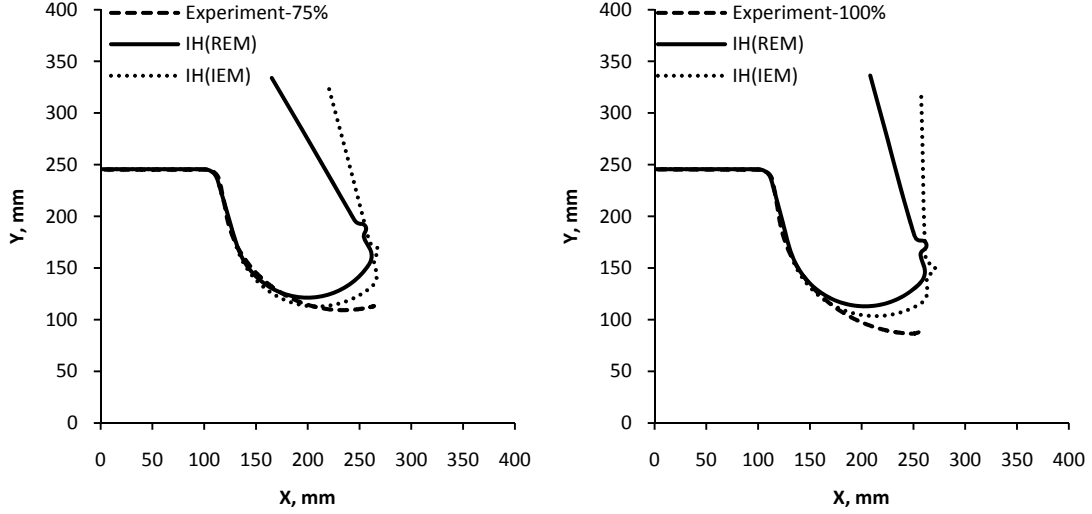
Fig. 5.30. Channel sidewall profiles predicted by the IH model for AA6022 at 75% (left) and 100% (right) drawbead penetrations

5.5.3. Combined isotropic-nonlinear kinematic hardening model (IH+NKH):

In the previous section, it was shown that the IH model overestimates the springback for BM3. In this section, Hill's quadratic yield function with the combined IH+NKH model is used to evaluate the capability of this model to predict springback. This model assumes the expansion of the yield surface as well as its translation in stress space. The following equation is used for the isotropic hardening:

$$R = Q'(1 - e^{-b'p}) \tag{5.14}$$

where Q' and b' are two material parameters. Q' is the maximum change in the size of the yield surface, and b' defines the rate at which the size of the yield surface changes as plastic straining develops. The translation of the yield surface is defined by:

$$\dot{\alpha} = \frac{C'}{\sigma_y}(\boldsymbol{\sigma} - \boldsymbol{\alpha})\dot{p} - \gamma'\boldsymbol{\alpha}\dot{p} \tag{5.17}$$

where C' and γ' are material parameters and σ_y is the yield stress or the current size of the yield surface. C' is the initial kinematic hardening modulus, and γ' determines the rate at which the kinematic hardening modulus decreases with increasing plastic deformation.

130

The kinematic hardening law can be separated into a deviatoric part and a hydrostatic part; only the deviatoric part has an effect on the material behaviour. When C' and γ' are zero, the model reduces to an isotropic hardening model. The least squares method was used to fit the simulated stress-strain curve to the experimental curve which was obtained either by simple shear tests or by uniaxial tension-compression tests. Table 5.12 lists the material constants associated with this model for the BM3 materials. Figs. 5.31-5.34 show the predicted response of the material by IH+NKH. As can be seen from these figures, IH+NKH is able to capture both permanent softening and the Bauschinger effect. However, the transient Bauschinger region is not accurately described by this model. The early re-yielding is not accurately described for DP600, HSLA and AA6022. For AKDQ, it seems that the amount of Bauschinger effect is not very large and therefore the IH+NKH model is able to describe the reverse yield stress relatively accurately. These figures also show that workhardening stagnation is not observed for AA6022. Therefore, IH+NKH model is able to better describe the reverse behaviour of DP600 and AA6022 compared to the other two materials. However, the reverse stress-strain response of the material is not described very well for AKDQ and HSLA because the model is not able to capture workhardening stagnation. Since there is a workhardening stagnation period at the beginning of forward loading for HSLA, the stress-strain response is not well described even during forward loading. In summary, it seems that IH+NKH describes the behaviour of AA6022 and DP600 relatively well but it is not able to describe the behaviour of AKDQ and HSLA. Fig. 5.33 shows that the IH+NKH model fails to accurately describe the cyclic behaviour of HSLA.

Table 5.12. Material coefficient for IH+NKH model

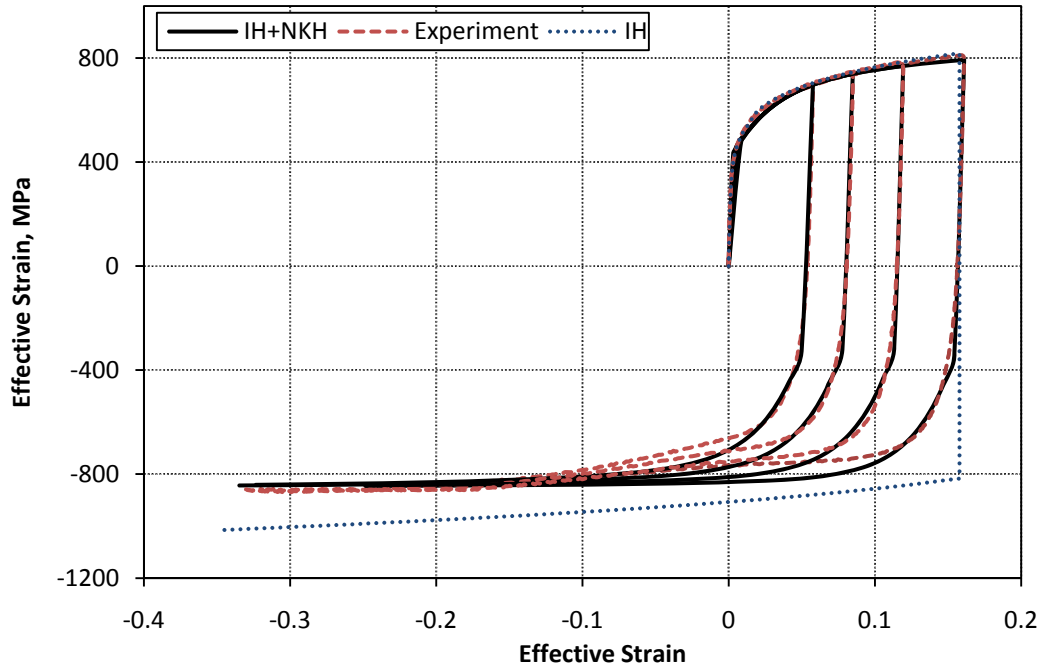| Material	σ_y (MPa)	C' (MPa)	γ'	Q' (MPa)	b'
AA6022-T43	136	1027	48.6	150	11
AKDQ	158	300	5	240	8.5
DP600	420	9500	40	190	8
HSLA	394	5000	140	180	7

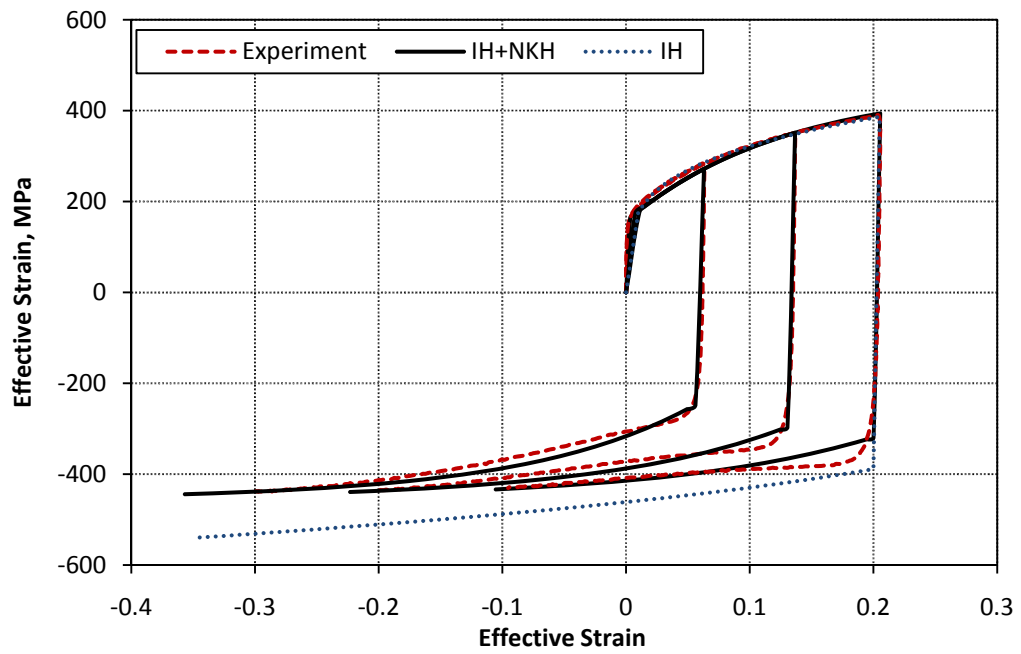Fig. 5.31. Predicted stress-strain response of DP600 using IH+NKH

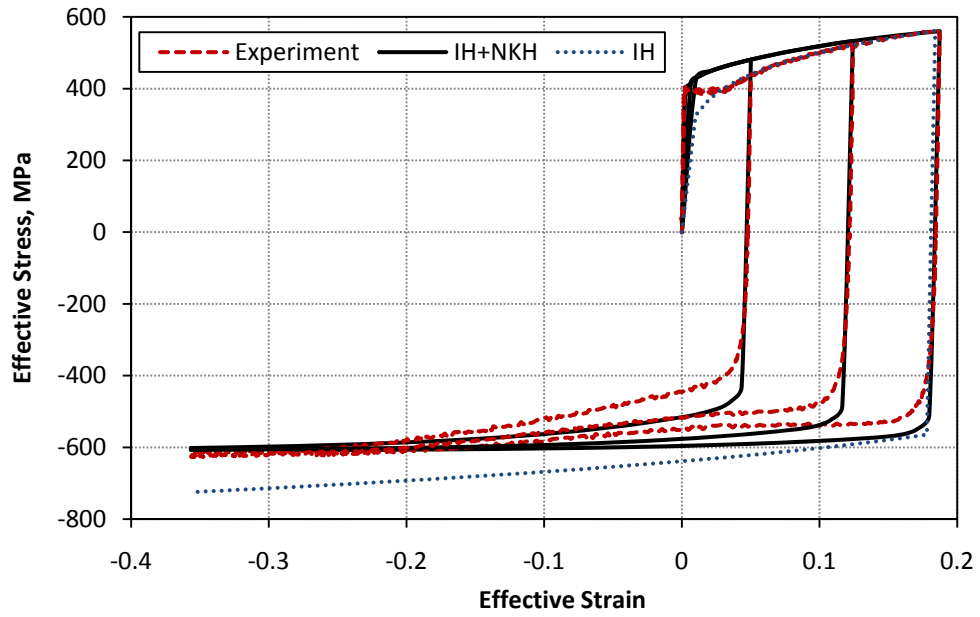Fig. 5.32. Predicted stress-strain response of AKDQ using IH+NKH

Fig. 5.33. Predicted stress-strain response of HSLA using IH+NKH
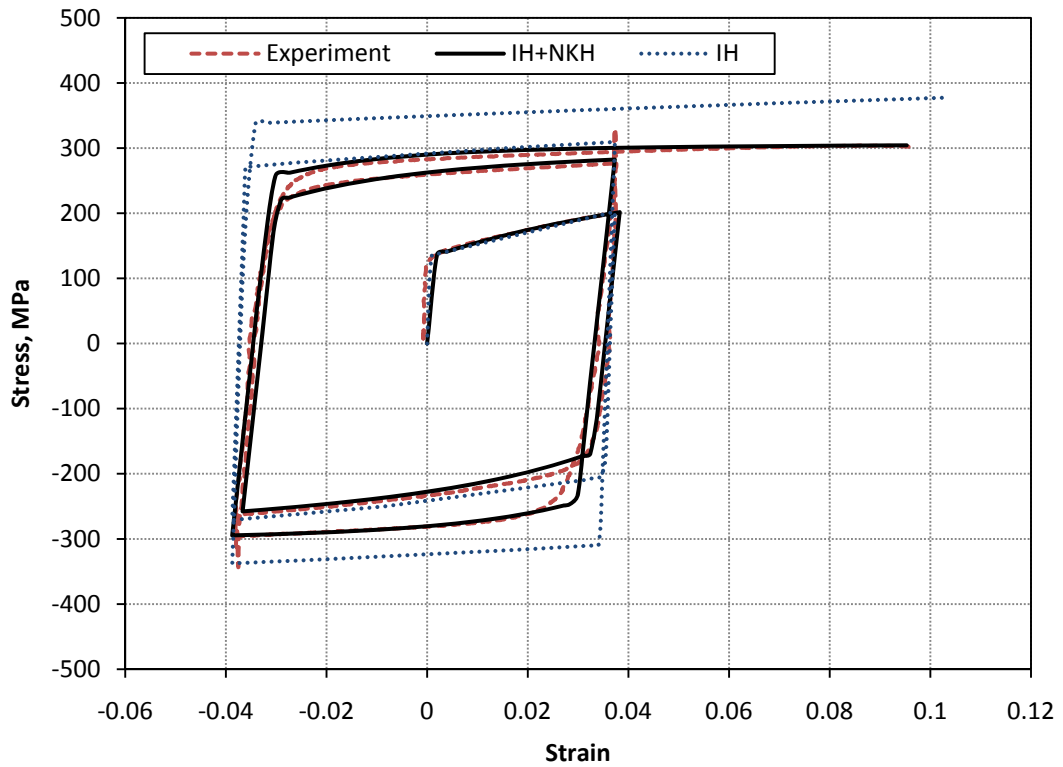

Fig. 5.34. Predicted stress-strain response of AA6022 using IH+NKH

Again, the relative error was calculated according to Eq. (5.15). Table 5.13 lists the percentage of relative error for each material at different drawbead penetrations. The predicted profile after springback using IH+NKH model is shown in Figs. 5.35-5.42. The springback stage was simulated using either the initial elastic modulus (IEM) or the reduced elastic modulus (REM) where the decrease in unloading modulus is taken into account. Figs. 5.35-5.36 show that springback in DP600 channel sidewalls are underestimated if the reduced elastic modulus is not used. If the reduced elastic modulus is considered, however, the predicted springback profile is relatively close the experimental profile. Figs. 5.37-5.38 show that, for AKDQ channels, the predicted sidewall curl is overestimated when the initial elastic modulus is used, and the overprediction is even more significant when the reduced elastic modulus is used. For HSLA, the discrepancy between the predicted and experimental profiles is even more than that of AKDQ. Finally, the predicted profile for AA6022 is predicted fairly well at shallow drawbead penetrations, i.e. 25% and 50%. However, the discrepancy between the simulation and experiment increases as the drawbead penetration increases. The results of these simulations show that the IH+NKH model improves the simulation results compared to the IH model, especially for DP600 and AA6022. So, it seems that the springback profiles are well predicted for materials where the cyclic stress-strain curve is well predicted by IH+NKH model. A more detailed discussion on the comparative ability of various hardening models to predict springback will be presented in section 5.5.5.

Table. 5.13. The percentage of relative error in prediction of springback by IH+NKH model

Drawbead Penetration	DP600		AKDQ		HSLA		AA6022	
	IEM	REM	IEM	REM	IEM	REM	IEM	REM
25%	8.12	3.19	14.95	20.1	3.20	8.65	7.55	3.35
50%	6.85	3.62	16.45	23.57	4.41	9.82	6.15	1.85
75%	7.63	2.71	9.37	15.93	8.02	13.64	2.79	3.60
100%	--	--	25.24	33.53	11.70	17.56	6.11	11.52

Fig. 5.35. Channel sidewall profiles predicted by the IH+NKH model for DP600 at 25% (left) and 50% (right) drawbead penetrations

Fig. 5.36. Channel sidewall profiles predicted by the IH+NKH model for DP600 at 75% drawbead penetrations

135

Fig. 5.37. Channel sidewall profiles predicted by the IH+NKH model for AKDQ at 25% (left) and 50% (right) drawbead penetrations

Fig. 5.38. Channel sidewall profiles predicted by the IH+NKH model for AKDQ at 75% (left) and 100% (right) drawbead penetrations

Fig. 5.39. Channel sidewall profiles predicted by the IH+NKH model for HSLA at 25% (left) and 50% (right) drawbead penetrations

Fig. 5.40. Channel sidewall profiles predicted by the IH+NKH model for HSLA at 75% (left) and 100% (right) drawbead penetrations
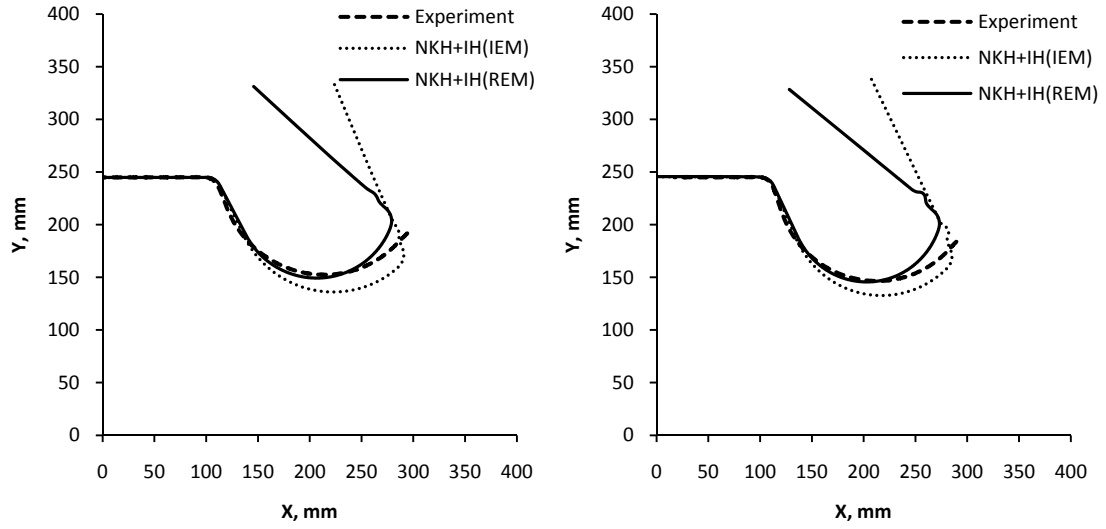
Fig. 5.41. Channel sidewall profiles predicted by the IH+NKH model for AA6022 at 25% (left) and 50% (right) drawbead penetrations

Fig. 5.42. Channel sidewall profiles predicted by the IH+NKH model for AA6022 at 75% (left) and 100% (right) drawbead penetrations

5.5.4. Yoshida-Uemori two surface model (YU):

In this section, Hill's quadratic yield function and the YU hardening model are used to predict the springback profile of BM3. The material coefficients for Hill's function and YU model are shown in Tables 5.5 and 5.9, respectively. The same finite element models as those used in sections 5.5.1 and 5.5.2 were used to obtain the predicted profile for BM3. Figs. 5.43-5.50 compare the experimental sidewall profiles with the predicted profiles. As can be seen, the predicted profiles are fairly close to the experiment for DP600 if the decrease in unloading modulus is taken into account. There is quite a large discrepancy between the experimental and simulated profiles for AKDQ at all drawbead penetrations. The simulated profile for HSLA is also overestimated if the unloading modulus decrease is taken into account. For AA6022, the profile is predicted fairly well at shallow drawbead penetrations. However, as the drawbead penetration increases, the predicted profile is overestimated.

Table. 5.14. The percentage of relative error in prediction of springback by YU model

Drawbead Penetration	DP600		AKDQ		HSLA		AA6022	
	IEM	REM	IEM	REM	IEM	REM	IEM	REM
25%	8.76	3.09	25.31	31.43	3.77	2.62	6.36	2.19
50%	7.34	2.89	28.70	35.08	1.66	5.00	5.17	2.09
75%	8.04	2.18	26.06	32.38	2.70	8.20	2.23	4.85
100%	--	--	25.41	31.09	6.97	12.64	6.98	12.46

Fig. 5.43. Channel sidewall profiles predicted by the YU model for DP600 at 25% (left) and 50% (right) drawbead penetrations
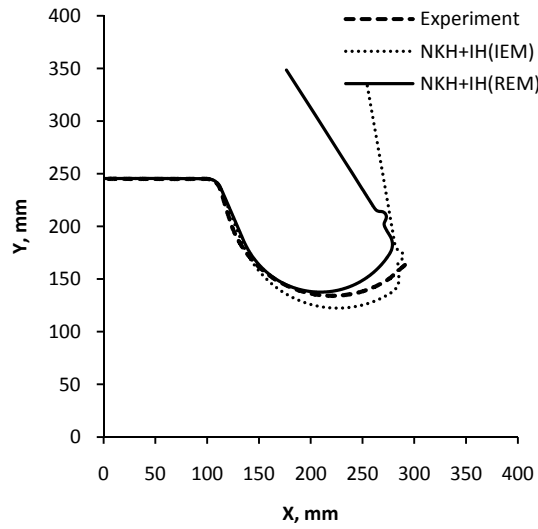

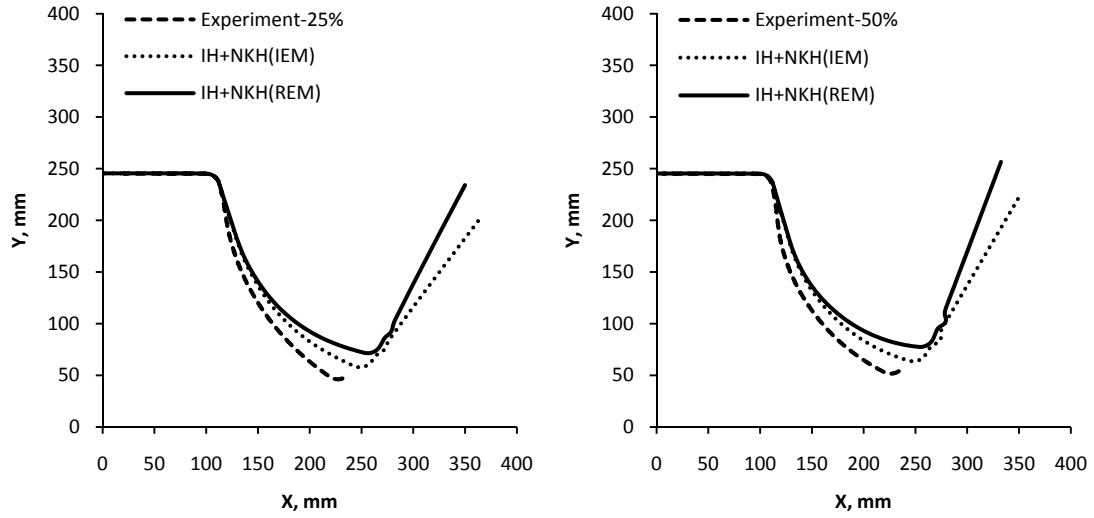Fig. 5.44. Channel sidewall profiles predicted by the YU model for DP600 at 75% drawbead penetrations

Fig. 5.45. Channel sidewall profiles predicted by the YU model for AKDQ at 25% (left) and 50% (right) drawbead penetrations
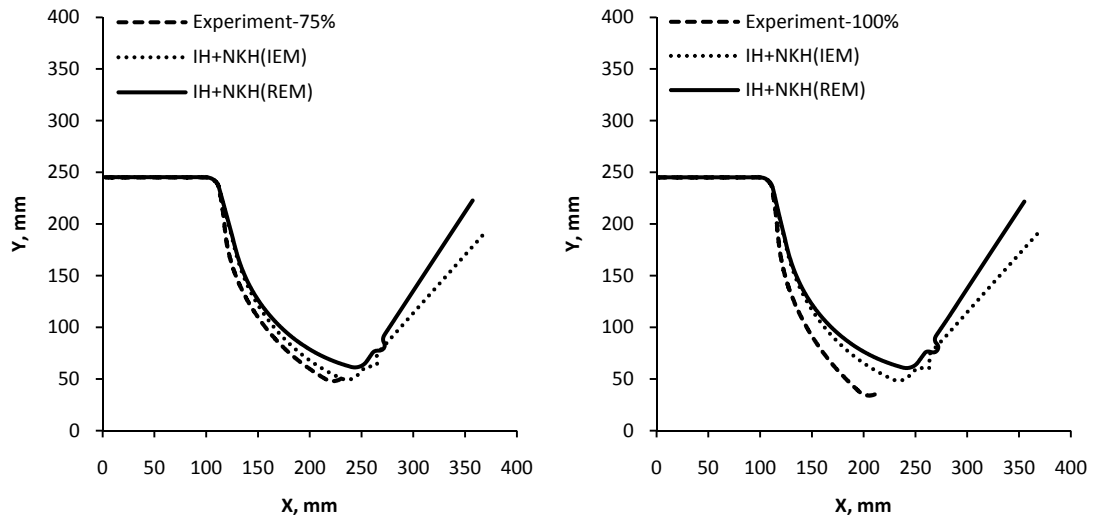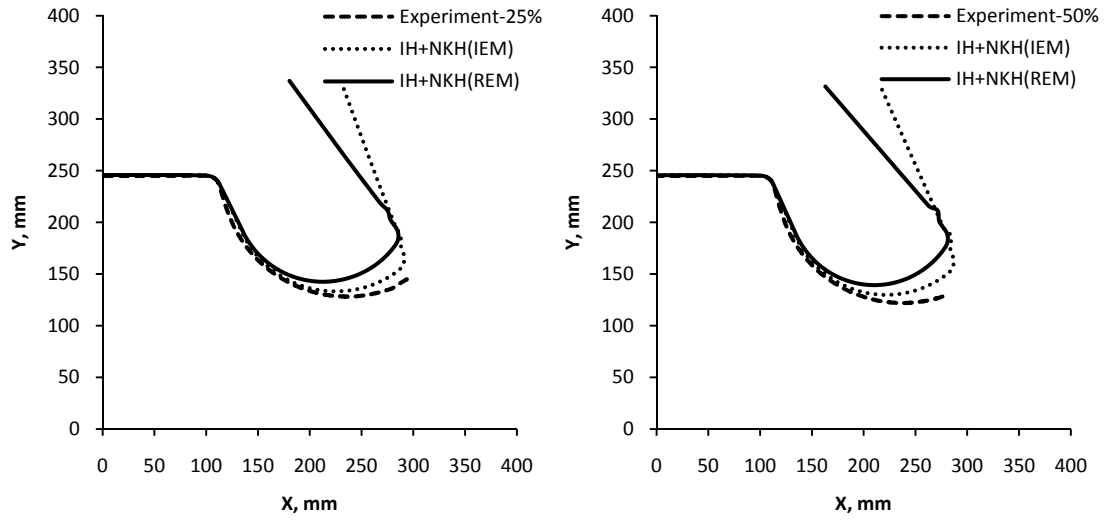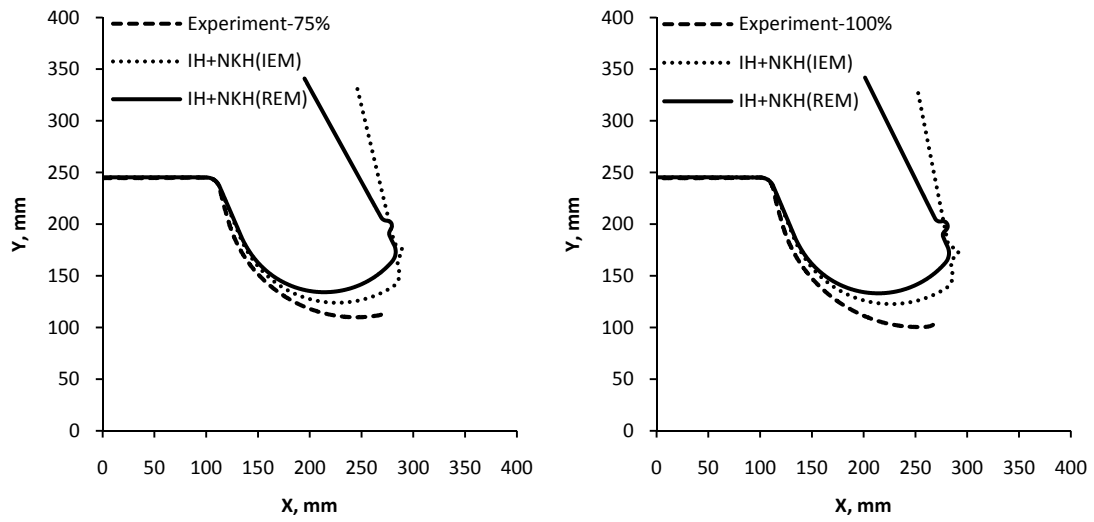

Fig. 5.46. Channel sidewall profiles predicted by the YU model for AKDQ at 75% (left) and 100% (right) drawbead penetrations
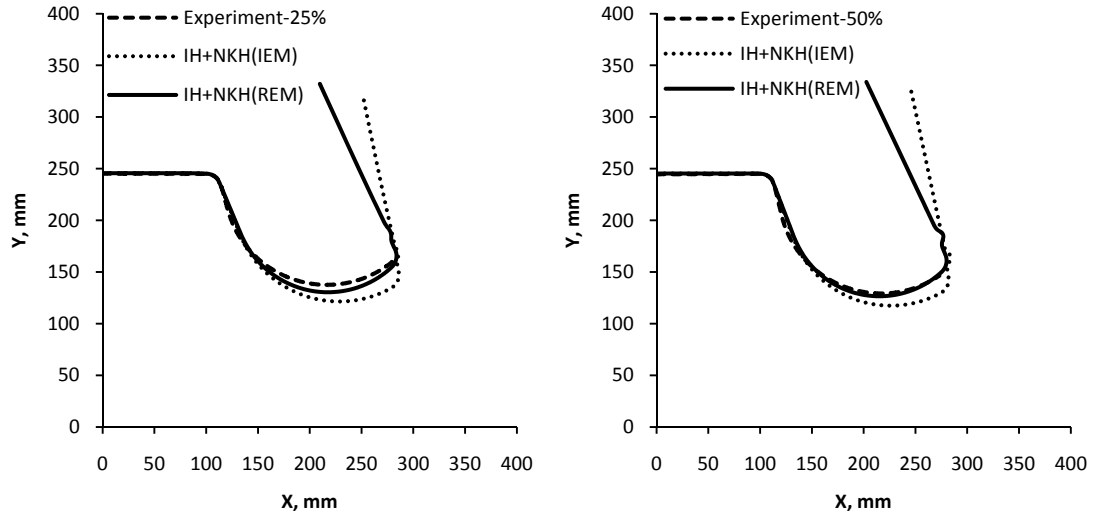
Fig. 5.47. Channel sidewall profiles predicted by the YU model for HSLA at 25% (left) and 50% (right) drawbead penetrations

Fig. 5.48. Channel sidewall profiles predicted by the YU model for HSLA at 75% (left) and 100% (right) drawbead penetrations

Fig. 5.49. Channel sidewall profiles predicted by the YU model for AA6022 at 25% (left) and 50% (right) drawbead penetrations
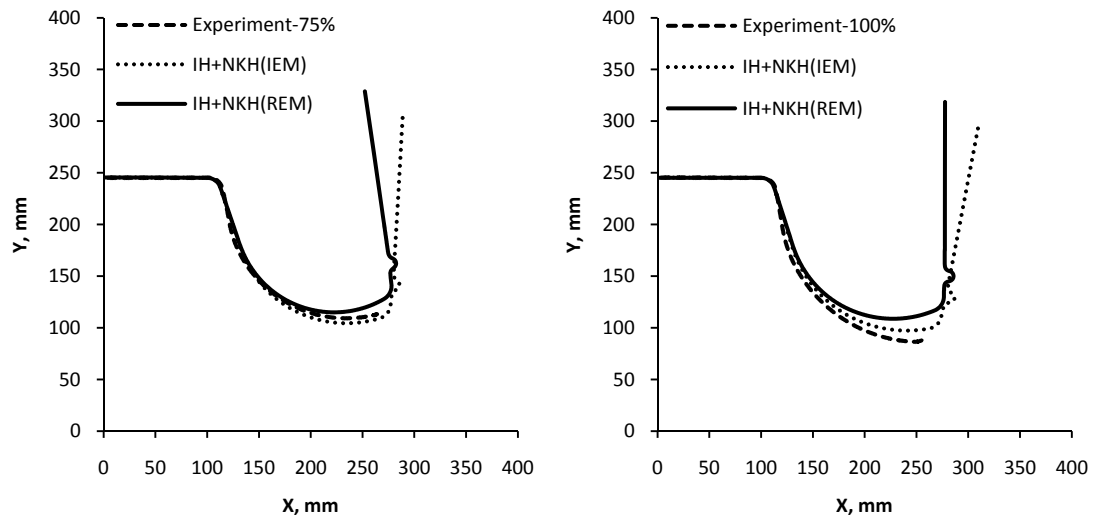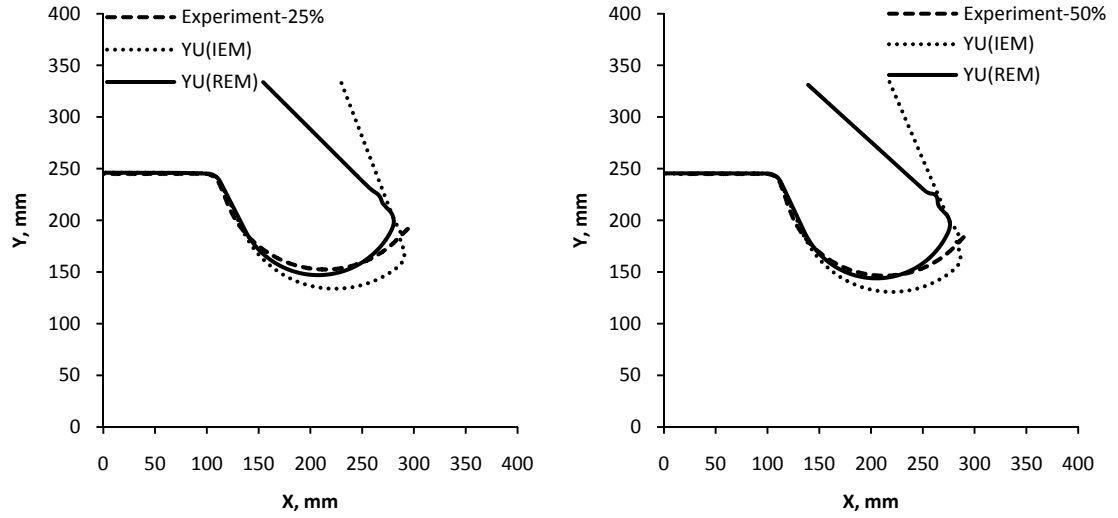

Fig. 5.50. Channel sidewall profiles predicted by the YU model for AA6022 at 75% (left) and 100% (right) drawbead penetrations

5.5.5. Yld2000-2d and YU model:

It has been reported in the literature that the simulated springback depends not only on hardening law but also on the plastic anisotropy. Geng and Wagoner [54] used four different yield functions to simulate the springback of AA6022-T4 formed in a draw-bend test. They found that the springback angle at low back forces was controlled by the hardening law, while at higher back forces the anticlastic curvature, which depends principally on yield surface shape, controlled the springback angle. The results of simulation of BM3 for AA6022-T43 (Figs. 4.49-4.50) showed that the springback profile is overestimated at larger drawbead penetrations. Since the back force increases at larger drawbead penetrations, using a more advanced yield function may improve the springback simulation. Therefore, the Yld2000-2d yield function and the YU model were used to study the effect of yield function on the springback response.

In order to study the effect of yield function on the simulated springback profile accuracy, YU model was used with Yld2000-2d function to simulate the springback of BM3 for AA6022-T43. The material parameters associated with Yld2000 and YU model are given in Tables 5.8 and 5.9, respectively. Table 5.15 shows the calculated relative error for AA6022 at different drawbead penetrations. Figs. 5.51-5.52 compare the predicted profile with Hill's function and Yld2000 function. As can be seen, there is a little discrepancy between the results obtained by Hill and Yld2000 functions. Again, the springback profile is overestimated at larger drawbead penetrations. Therefore, it seems that the hardening model dominates the amount of springback for this problem and using a more advanced yield function does not improve the results even at a larger penetration.

Table. 5.15. The percentage of relative error in prediction of springback by Yld2000+YU model for AA6022-T43

	25%	50%	75%	100%
IEM	5.09	3.98	4.50	8.63
REM	1.8	2.74	6.20	14.23
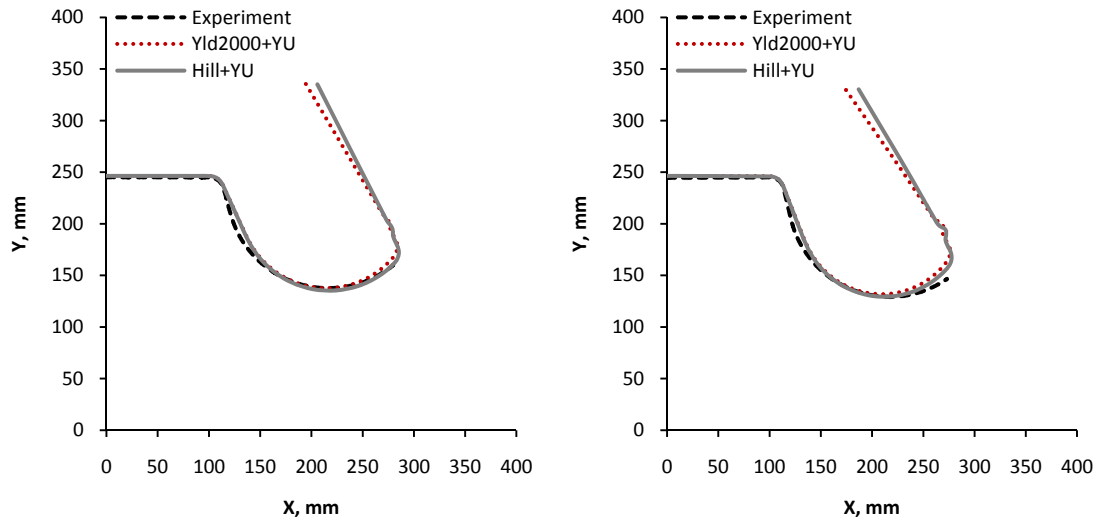
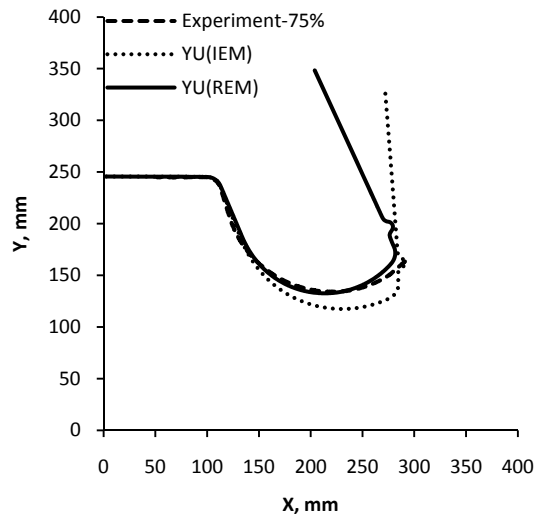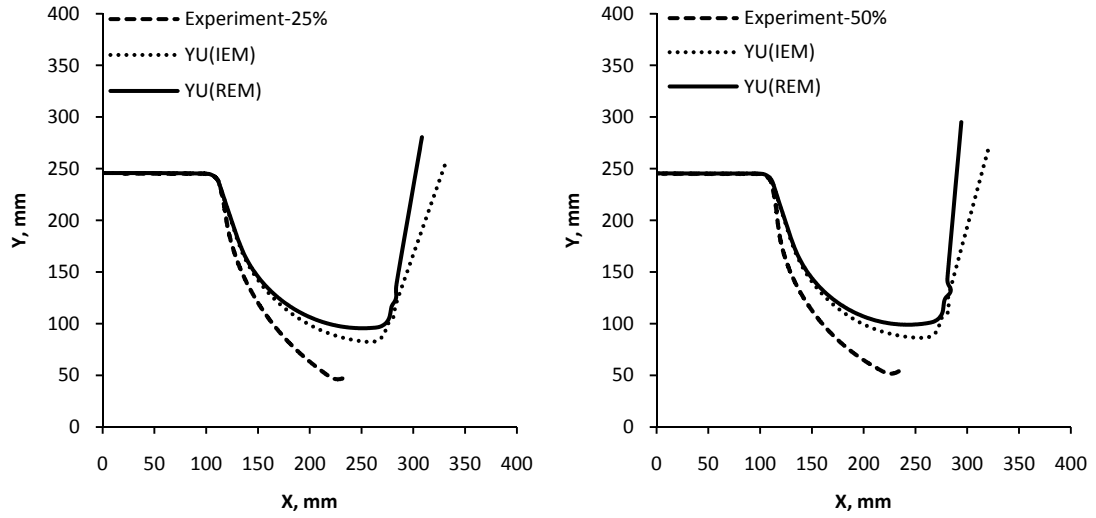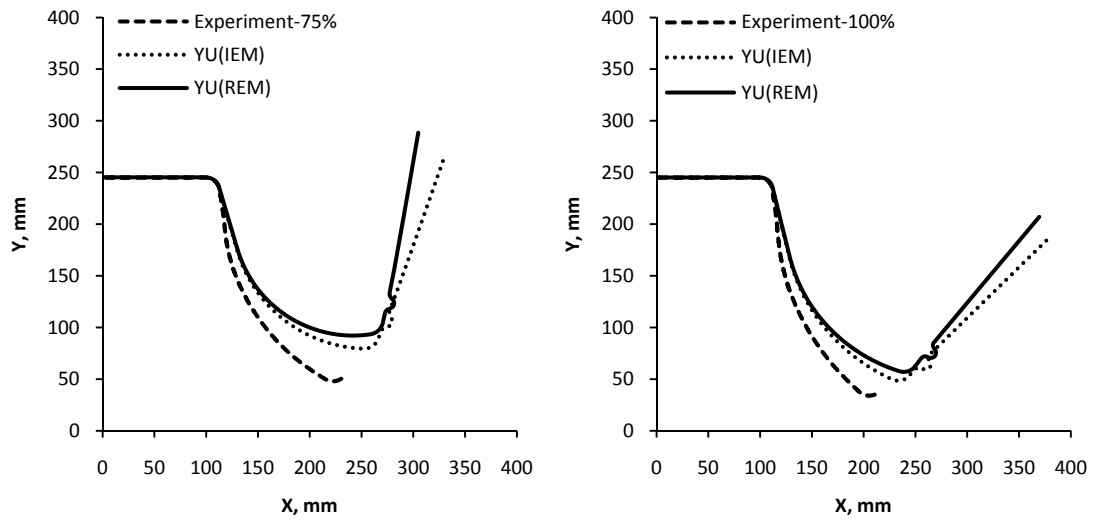Fig. 5.51. Channel sidewall profiles predicted for AA6022 at 25% (left) and 50% (right) drawbead penetrations

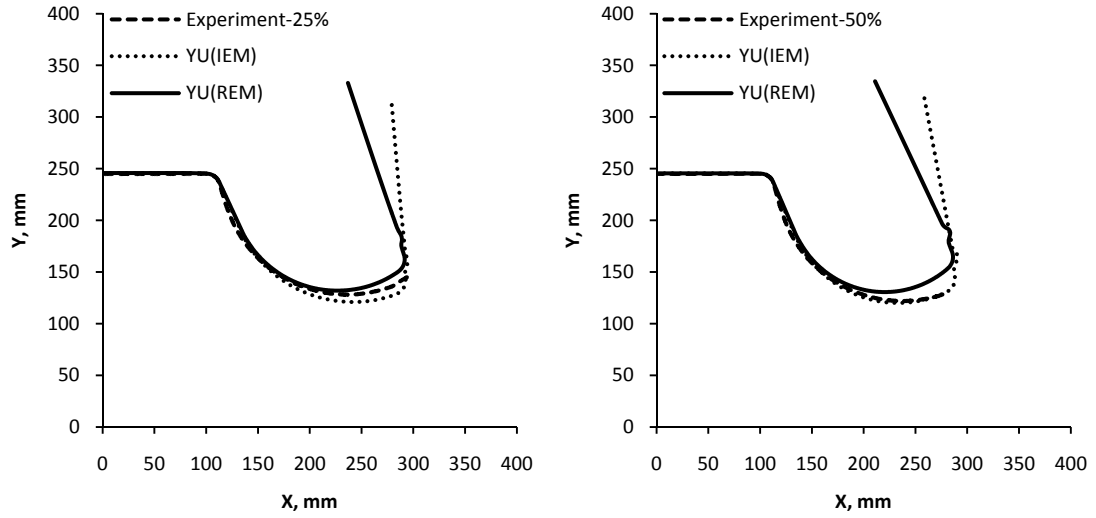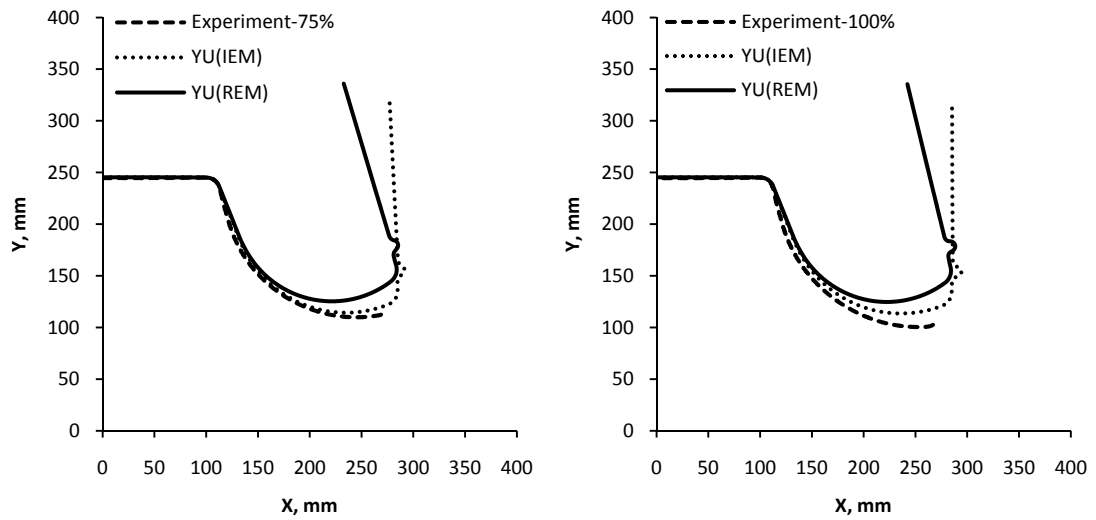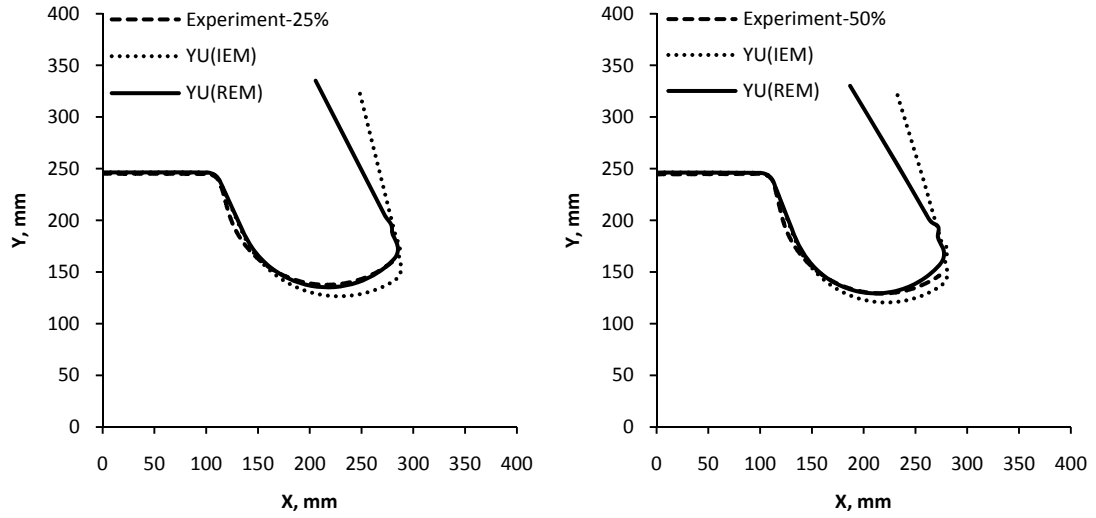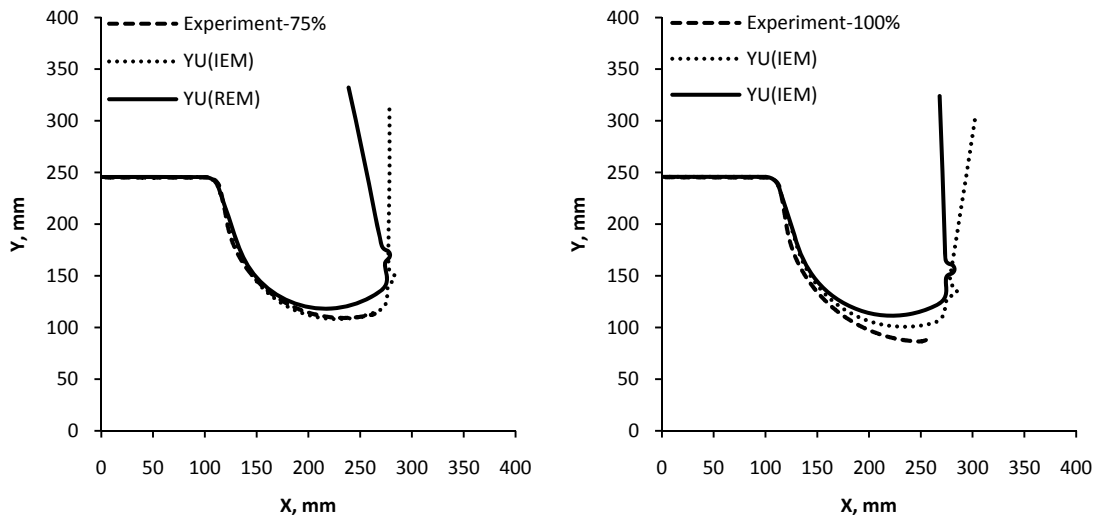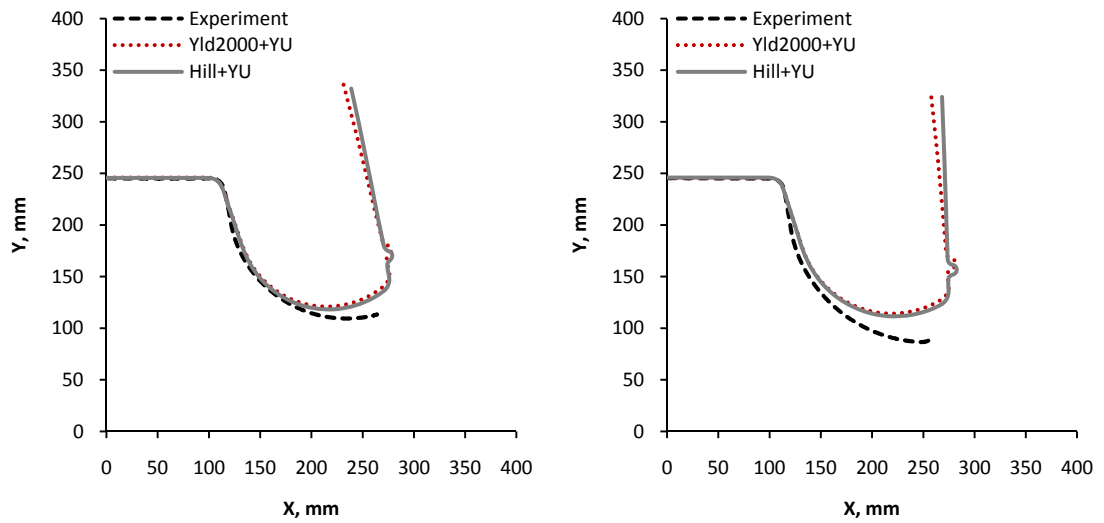Fig. 5.52. Channel sidewall profiles predicted for AA6022 at 75% (left) and 100% (right) drawbead penetrations

145

5.5.6. Punch Force

In BM3, four load cells were mounted beneath the fixed punch under the lower die in order to record the punch force during each test. The ram displacement, ram pressure and the cushion pressure in the floating binder were also recorded in real time. These data were recorded for each material, each drawbead penetration and for each channel that was formed. The punch force versus ram displacement is shown in Figs. 5.53-5.56 for all materials at different drawbead penetrations. As can be seen from these figures, the punch force increases when the ram initially starts to move, then it remains fairly constant until the end of stroke. So, in order to define the error between the simulated and experimental forces, the average punch force was determined in the steady state region (after 100 mm of ram displacement) and the error was defined as follows:

$$\text{Error} = \frac{F_{sim} - F_{exp}}{F_{exp}} \tag{5.18}$$

where F_{exp} is the experimental punch force and F_{sim} denotes the predicted punch force by simulation. The percentage of error was calculated for all materials and all drawbead penetrations and is shown in Fig. 5.57. This figure shows that the punch force is overestimated by the IH model except for HSLA at 25% drawbead penetration. The overestimation of punch force by the IH model is because this model fails to capture the Bauschinger effect and over-predicts the material response during cyclic loading. The reason for underestimating the punch force for HSLA at 25% drawbead penetration can be explained by Fig. 5.14. This figure shows that the predicted stress-response of HSLA is underestimated by the IH model because of workhardening stagnation of this material at the beginning of plastic deformation. In general, the IH+NKH and YU models improve the prediction of punch force. For DP600 and AA6022, both the IH+NKH and YU models are able to describe the cyclic behaviour of DP600 and AA6022 fairly well. As a result, both models predict almost the same profile for springback. Both these models predict similar punch forces for DP600. For AA6022 however, the punch force predicted with the IH+NKH model is different from that predicted with the YU model. For HSLA,

the punch force error predicted by YU model is relatively small at 25%. However, the punch forces predicted with the IH and IH+NKH models are better in agreement with experimental data at larger penetrations. For AKDQ, the IH+NKH and IH models predict the punch force more accurately at shallow and deep penetrations, respectively.

In general, Fig. 5.65 shows that the punch force is underestimated by the IH+NKH and YU models at deeper drawbead penetrations. It can also be observed that for some materials the punch force predicted with the IH model is more accurate than the other models. This is not generally expected because the IH model overestimates the stress-strain response of material. Perhaps the reason for this lies in the fact that the contact forces and/or friction force are not accurately calculated in the finite element simulation. For instance, if the coefficient of friction is chosen to be larger at deeper penetrations, the punch force predicted with the YU and IH+NKH models will be closer to the experimental punch force. This increases the tension in the sidewall during the forming process and results in less springback at deeper penetrations. More research is required on this issue to make sure the friction is accurately modeled in this process.
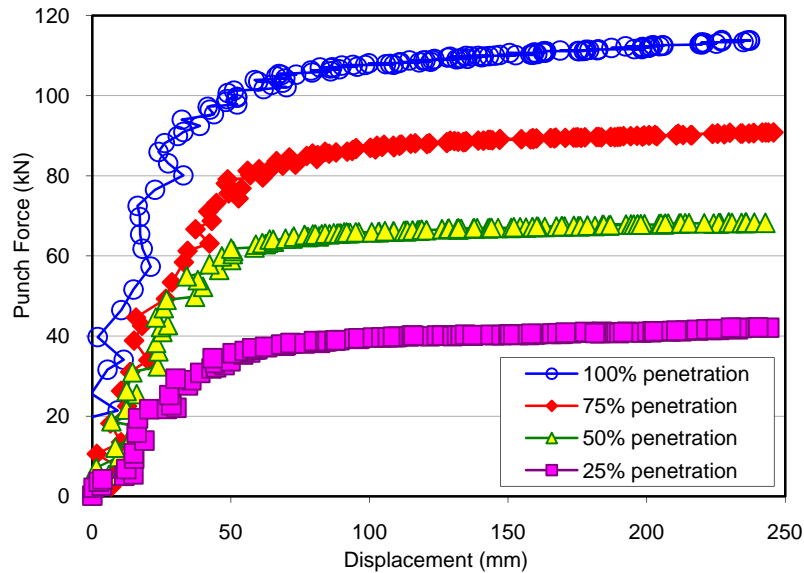
Fig. 5.53. The punch force versus ram displacement for AKDQ at different drawbead penetrations

147
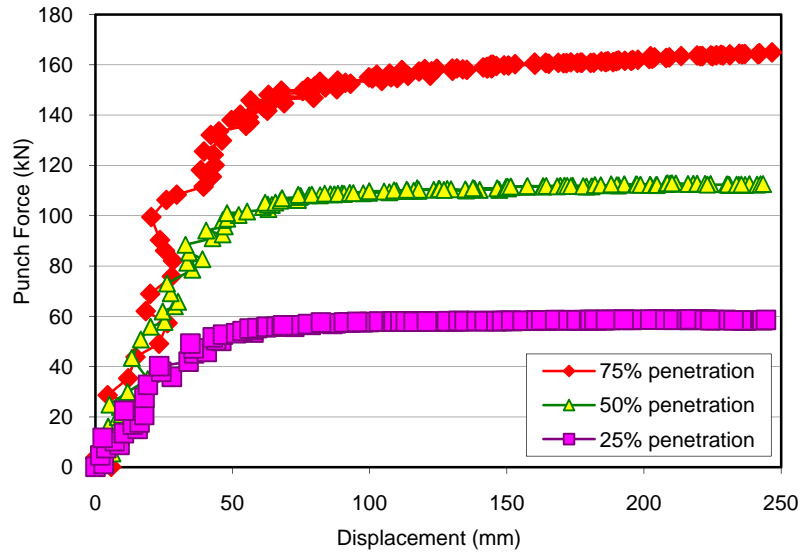
Fig. 5.54. The punch force versus ram displacement for DP600 at different drawbead penetrations
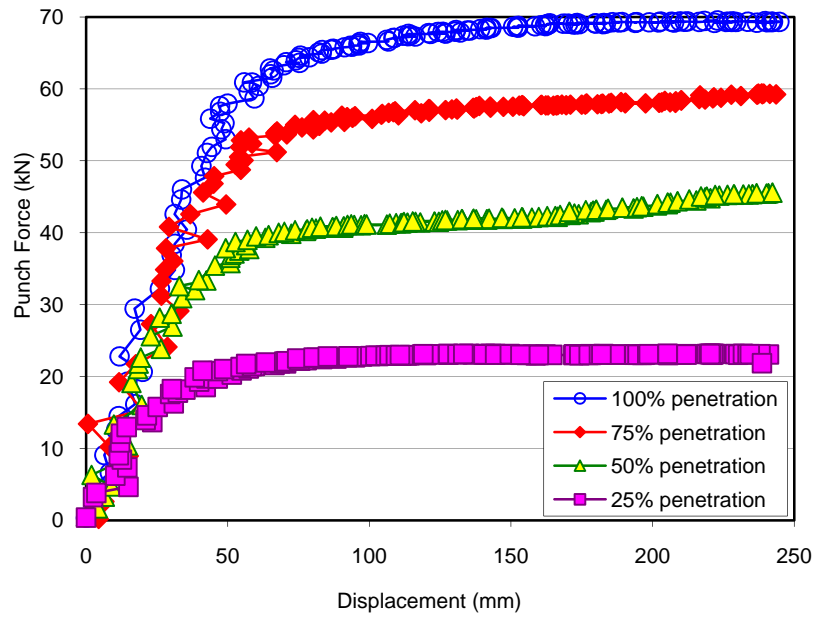
Fig. 5.55. The punch force versus ram displacement for AA6022 at different drawbead penetrations

148
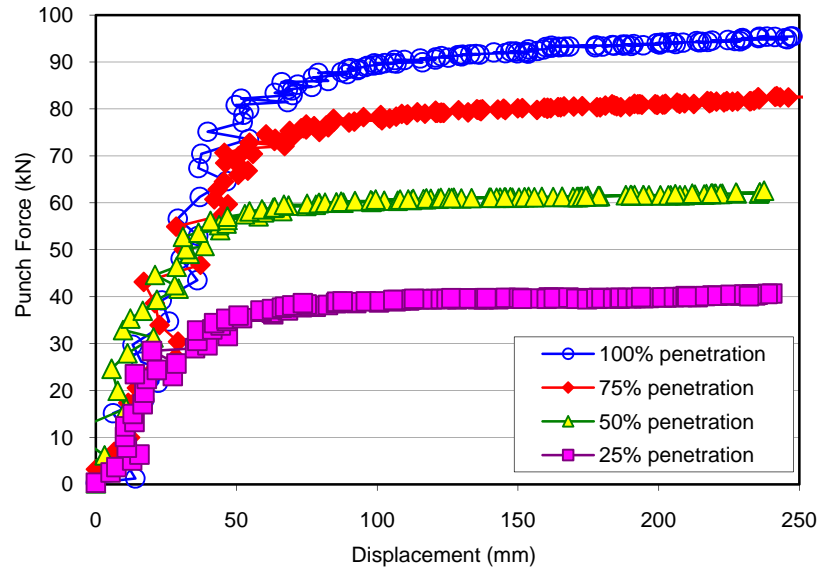
Fig. 5.56. The punch force versus ram displacement for HSLA at different drawbead penetrations
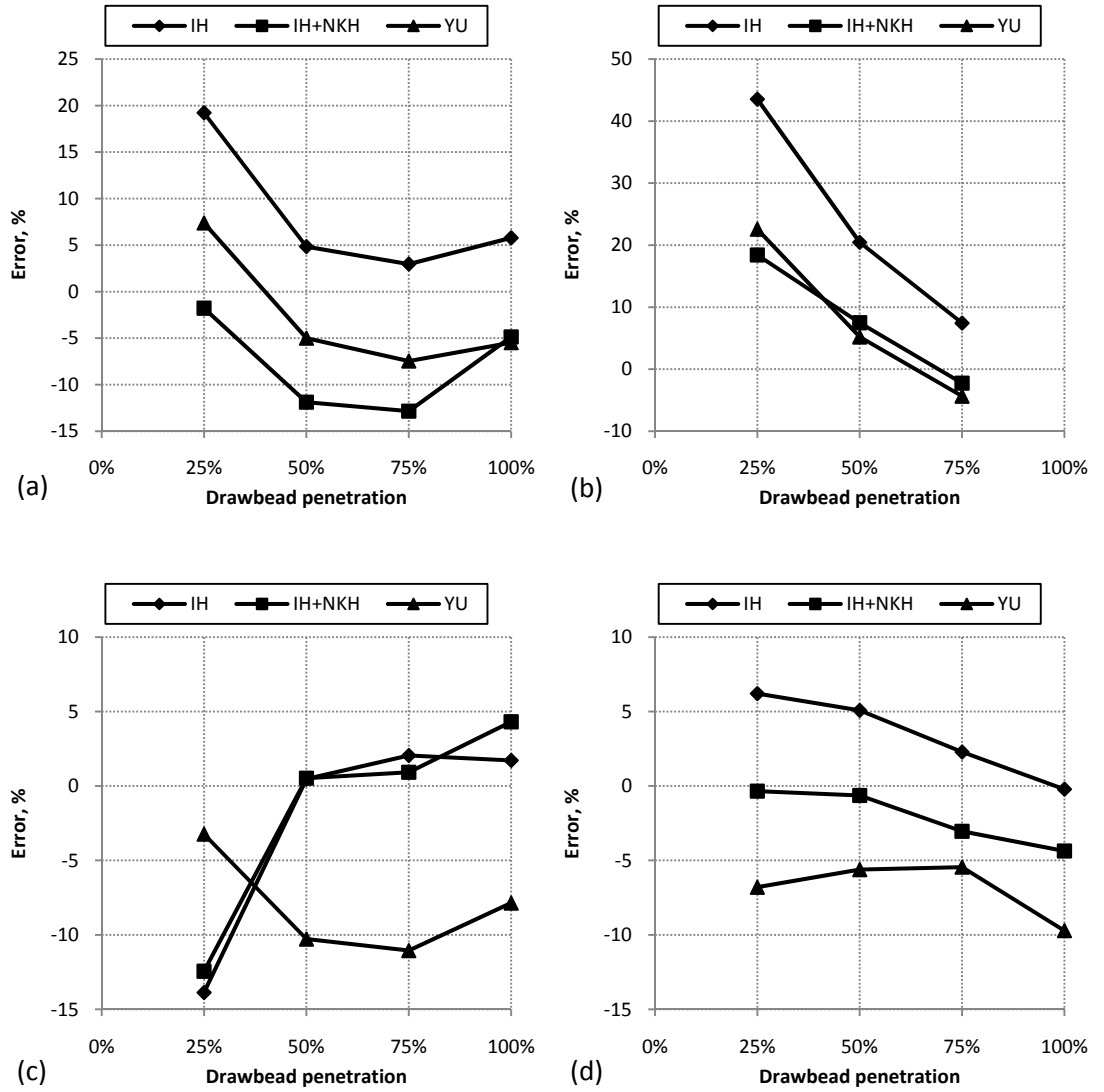
Fig. 5.57. The error in prediction of punch force: (a) AA6022, (b) DP600, (c) HSLA and (d) AKDQ

Chapter 6

Discussion

6.1. The role of hardening model on the accuracy of springback simulation:

In the previous chapter, different models were used to simulate the springback of BM3. In this section, the results obtained with each model are compared and the effect of the hardening model on the simulated profile is discussed. Hill's quadratic yield function was used with three hardening models: IH, IH+NKH and YU models. Throughout this section, it is assumed that the unloading modulus decreases during the springback stage according to Eq. (3.37).

The springback of U-shaped channel sections was obtained for four different materials. Two of these materials, i.e. DP600 and AA6022, do not show any workhardening stagnation period during cyclic loading, whereas AKDQ and HSLA show significant workhardening stagnation. In addition, the HSLA shows some workhardening stagnation during the first forward loading because of discontinuous or non-uniform yielding of this material, which is characterized by the propagation of Lüders bands. The experimental cyclic behaviour of DP600 (see Figs. 5.7, 5.12) shows that the Bauschinger effect is quite significant for this material. AKDQ shows a small Bauschinger effect as the yield stress during the stagnation period is almost equal to that in forward loading (see Figs. 5.8, 5.13). The other two materials show some Bauschinger effect during cyclic loading.

Let us first consider the stress-strain behaviour as it was predicted by different hardening laws. The IH model does not describe the cyclic behaviour of any of these

materials. The IH+NKH model describes the permanent behaviour of all materials except HSLA because this material shows both workhardening stagnation and some Bauschinger effect. For AKDQ, the predicted behaviour with the IH+NKH model is fairly close to the experimental permanent behaviour as this material does not show a large amount of Bauschinger effect. The transient response is not predicted very well with the IH+NKH model, especially when the material shows workhardening stagnation. The YU model correlates very well with the experimental response for all materials and describes both the permanent and transient behaviour fairly accurately.

Figs. 6.1-6.2 compare the springback profile simulated by IH, IH+NKH and YU models for DP600 at different drawbead penetrations. Fig. 6.3 shows the error in springback for each model. The figure shows that the error associated with the IH model increases as the drawbead penetration increases. However, the error associated with the IH+NKH and YU models decreases as the drawbead penetration increases. The YU and IH+NKH models improve the springback prediction about 3% and 8% at 25% and 75% drawbead penetrations, respectively. The main reason for improvement of springback simulation using the IH+NKH and YU models (compared to the IH model) is that these models describe the Bauschinger effect and do not over-predict the stress field in the simulation. It seems that both the IH+NKH and YU models describe the behaviour of DP600 relatively accurately and YU model has no considerable advantage over the IH+NKH model.

Fig. 6.1. The effect of hardening model on the simulated springback profile of DP600 channel sections at 25% (left) and 50% (right) drawbead penetrations

Fig. 6.2. The effect of hardening model on the simulated springback profile of DP600 channel sections at 75% drawbead penetration

Fig. 6.3. The error in springback with respect to drawbead penetration for DP600

Figs. 6.4-6.5 show a comparison between the simulated profiles obtained by each model for AKDQ at different drawbead penetrations. Fig. 6.6 shows the error associated with each model at different drawbead penetrations for this material. In general, the error in springback is much larger for AKDQ compared to DP600. For the IH+NKH model, the error for AKDQ is more than 10 times greater than the error for DP600. These results show that the springback is overestimated by all material models and the error is much larger for this material compared to the other materials. It is even more surprising to see that the error associated YU model is larger than the error associated with the IH model as the predicted stress YU model at the end of forming stage is smaller than that predicted with the IH model. The reason for this lies no doubt in the fact that the initial yield stress is rather small for AKDQ which makes the YU model predict a very early re-yielding and more plastic deformation during the springback stage. Evidently, the assumption of a constant size of the yield surface in the YU model is not realistic for low strength materials that exhibit little Bauschinger effect, such as AKDQ. Therefore, one may expect that the springback profile for AKDQ predicted with the IH+NKH model would correlate with the experimental data because this model describes the permanent

154

behaviour of AKDQ fairly well (see Fig. 5.32). However, the IH+NKH model also fails to predict the springback of AKDQ accurately. In order to determine the reason for this, the uniaxial tension was simulated using the material constants obtained from the simple shear test. Fig. 6.7 compares the experimental and simulated stress-strain response. This figure shows that the simulation overpredicts the experimental stress-strain response of AKDQ in uniaxial tension which shows that the behaviour of AKDQ in tension is different from that in shear. Therefore, it is thought that if the stress-strain curve was obtained either in uniaxial tension-compression at large strain amplitudes or in a bending-unbending test, the prediction of springback for this material will improve.

Another interesting observation is that the IH+NKH model reduces the springback error more than twice compared to the IH model for DP600. However, it does not considerably improve the results for AKDQ. The reason for this is that the decrease in yield stress during reverse loading (Bauschinger effect) is much larger for DP600 compared to AKDQ.
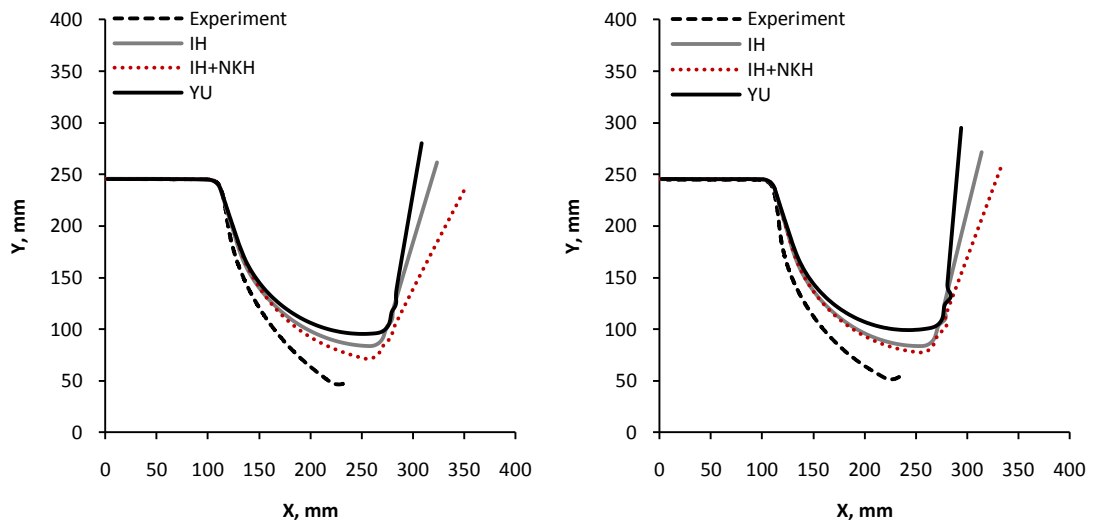
Fig. 6.4. The effect of hardening model on the simulated springback profile of AKDQ channel sections at 25% (left) and 50% (right) drawbead penetrations
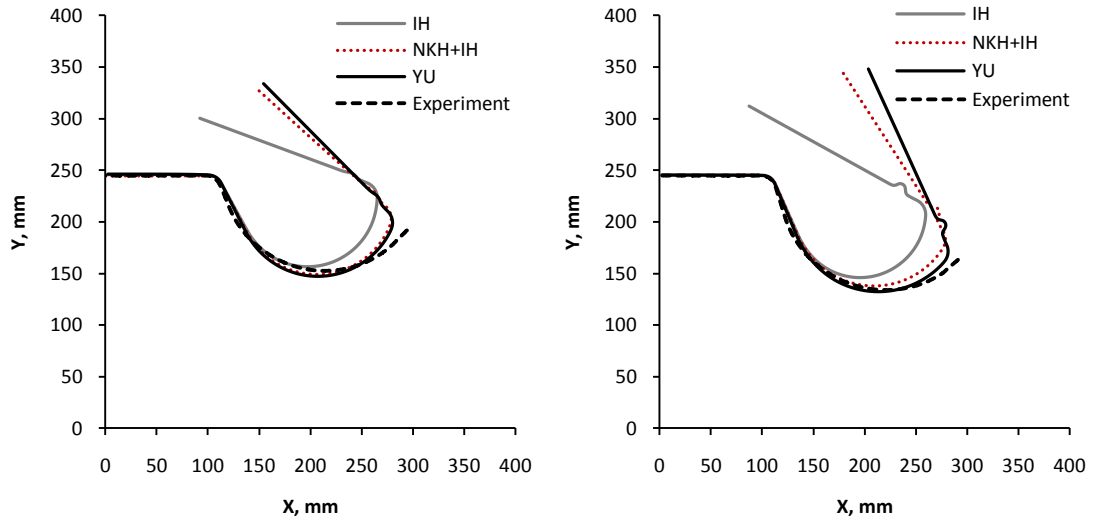
155
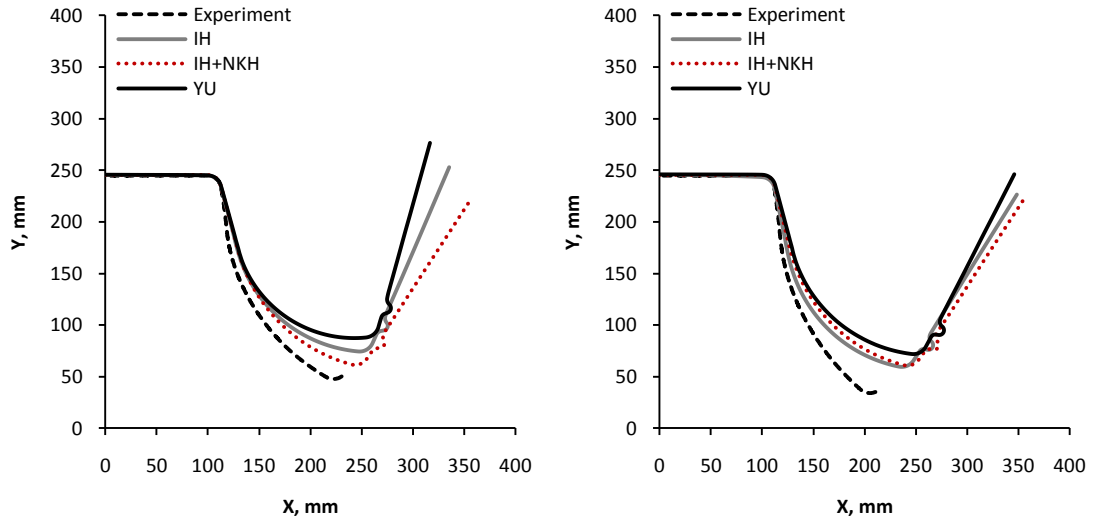
Fig. 6.5. The effect of hardening model on the simulated springback profile of AKDQ channel sections at 75% (left) and 100% (right) drawbead penetrations
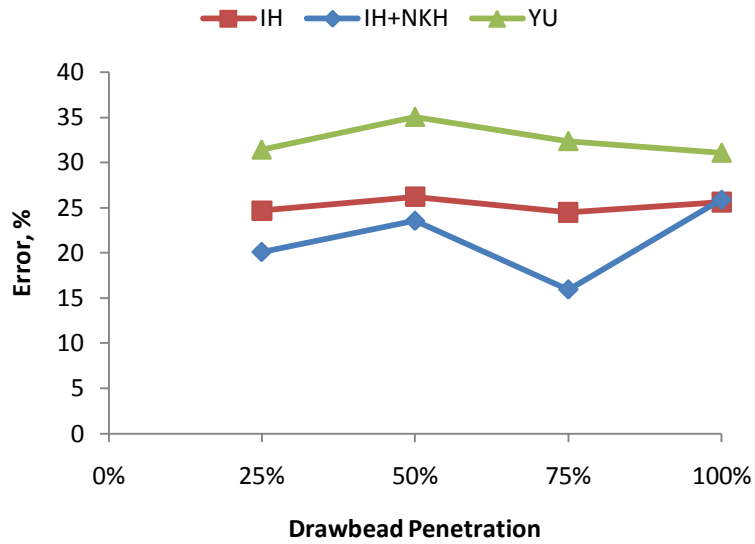
Fig. 6.6. The error in springback with respect to drawbead penetration for AKDQ

156
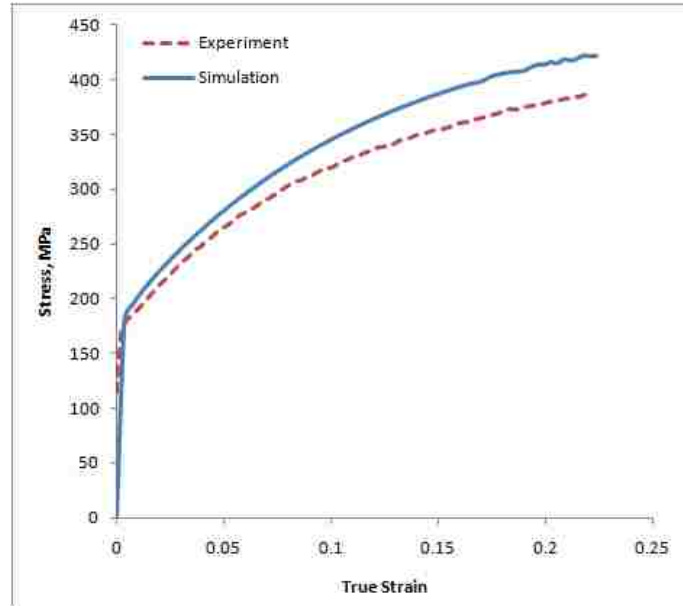
Fig. 6.7. Comparison of experimental stress-strain response of AKDQ with that obtained by simulation

The effect of the hardening model on the simulated springback profile for HSLA channel sections is shown in Figs. 6.8-6.9. The error associated with each model is also shown in Fig. 6.10. As can be seen, the best results are obtained with the YU model where the error is 2.62% at 25% and it increases up to 12.6 at 100% drawbead penetration. For the IH model, the error first decreases for 50% penetration and then increases as the drawbead penetration increases. However, the error increases as the drawbead penetration increases for the IH+NKH and YU models.
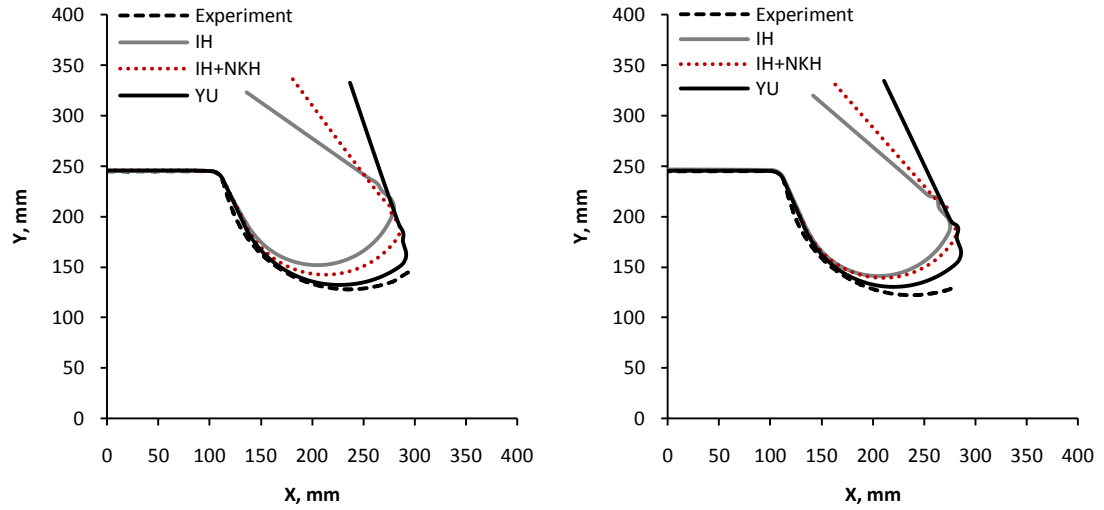
Fig. 6.8. The effect of hardening model on the simulated springback profile of HSLA channel sections at 25% (left) and 50% (right) drawbead penetrations
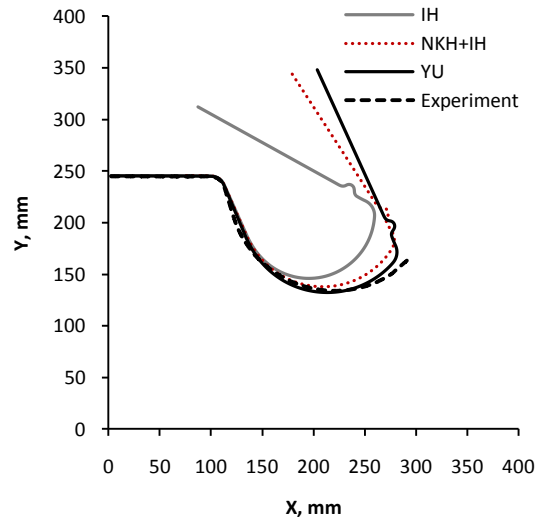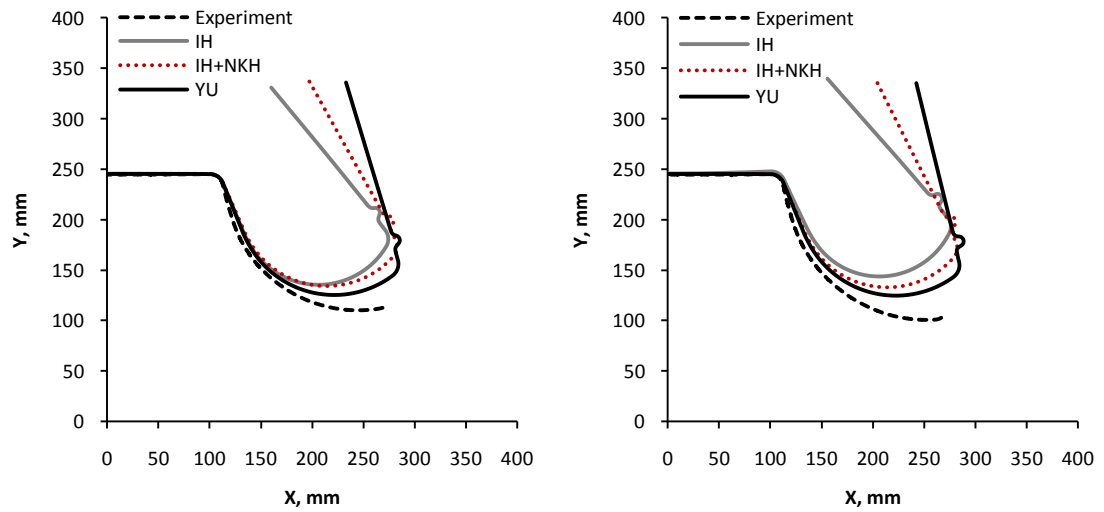

Fig. 6.9. The effect of hardening model on the simulated springback profile of HSLA channel sections at 75% (left) and 100% (right) drawbead penetrations
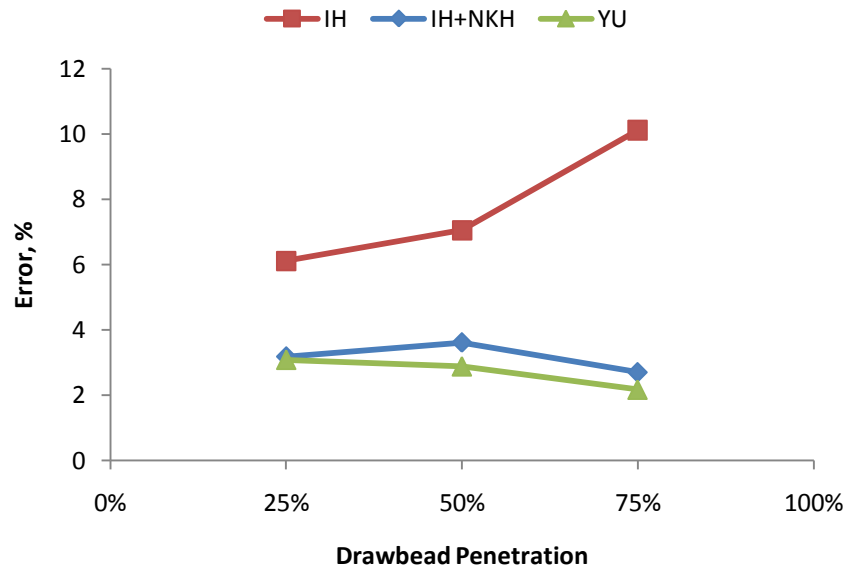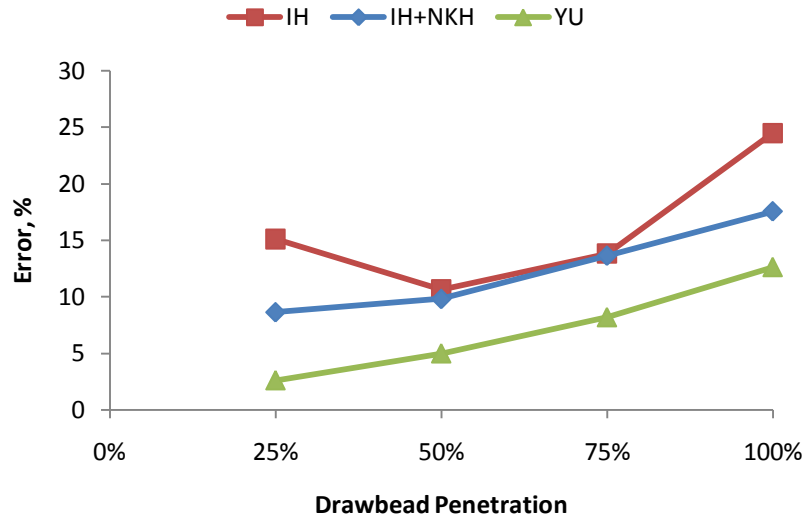
Fig. 6.10. The error in springback with respect to drawbead penetration for HSLA

The IH+NKH model improves the results compared to the IH model simply because it captures the Bauschinger effect and permanent softening. However, because this model fails to describe both the transient and permanent response of HSLA (see Fig 5.33), it is not able to predict springback accurately. The YU model significantly improves the results for HSLA compared to the IH+NKH model because it describes the cyclic behaviour of HSLA better than the IH+NKH model. However, the discrepancy between the simulation and experiment increases as the drawbead penetration increases. In order to understand the reasons for this, the loading path, punch force and springback were studied simultaneously.

Fig. 5.57 also shows that the punch force is underestimated with the YU and IH+NKH models at deep drawbead penetrations for all materials. Note that the IH+NKH model overestimates the punch force for HSLA at deep penetrations because this model fails to describe the cyclic behaviour of HSLA as shown in Fig. 5.33 which indicates that the IH+NKH model over-predicts the stress. The overestimation of springback at larger penetrations can be caused by several factors such as the material model, the element formulation, the complex contact and friction conditions.

Fig. 6.11 shows the stress-strain history of an integration point that is located outside the drawbead region at the beginning of the forming process but moves through the drawbead and up into the channel sidewall during the forming process. This history was obtained by simulation of the channel draw of an HSLA sheet using the YU model. A similar strain history, either TCTCT or CTCTC, is repeated for most of the material points that end up in the channel sidewall. In order to make sure that the material response is well predicted at all drawbead penetrations, uniaxial TCTCT test within the strain ranges shown in Fig. 6.11 are required for identification of material constants. Unfortunately, the uniaxial TC test that were carried out in this work as shown in Fig. 5.7-5.10 are not in the strain ranges of Fig. 6.11. The simple shear cyclic data was carried out at a sufficient strain range for the BM3 problem. However, the loading direction was reversed only once in this test; whereas in the BM3, the loading direction was reversed four times. So, there is no guarantee that the material response will be predicted correctly at subsequent loading reversals. It is thought that, if the cyclic stress-strain response of the material was experimentally obtained for a larger number of cycles, the hardening constants would likely reproduce the material behaviour more accurately, and consequently, the springback profile would also be predicted more accurately.

The friction model and/or friction coefficient may also be another cause of greater error at large penetrations. In general, the coefficient of friction is a function of velocity and pressure. At larger penetration, the severity of deformation and a larger pressure may increase the coefficient of friction. A greater coefficient of friction will increase the punch force and reduce the amount of springback. In order to see if a larger coefficient of friction can improve the springback simulation at deeper drawbead penetrations, the simulations were repeated using greater friction coefficients for HSLA at 100% penetration. Fig. 6.12 shows the error in springback and punch force predictions with respect to the coefficient of friction. The results show that a greater coefficient of friction (up to a certain value) improves both the punch force and the springback prediction. When the coefficient of friction is around 0.16, the punch force is accurately predicted but the springback error is 8.98%. So, this study shows that the coefficient of friction alone cannot lead to an accurate prediction of springback. Therefore, it appears that more experimental data are required on both friction and cyclic response of the material to

determine if a more accurate modeling of friction and material response leads to an accurate springback prediction for this problem.
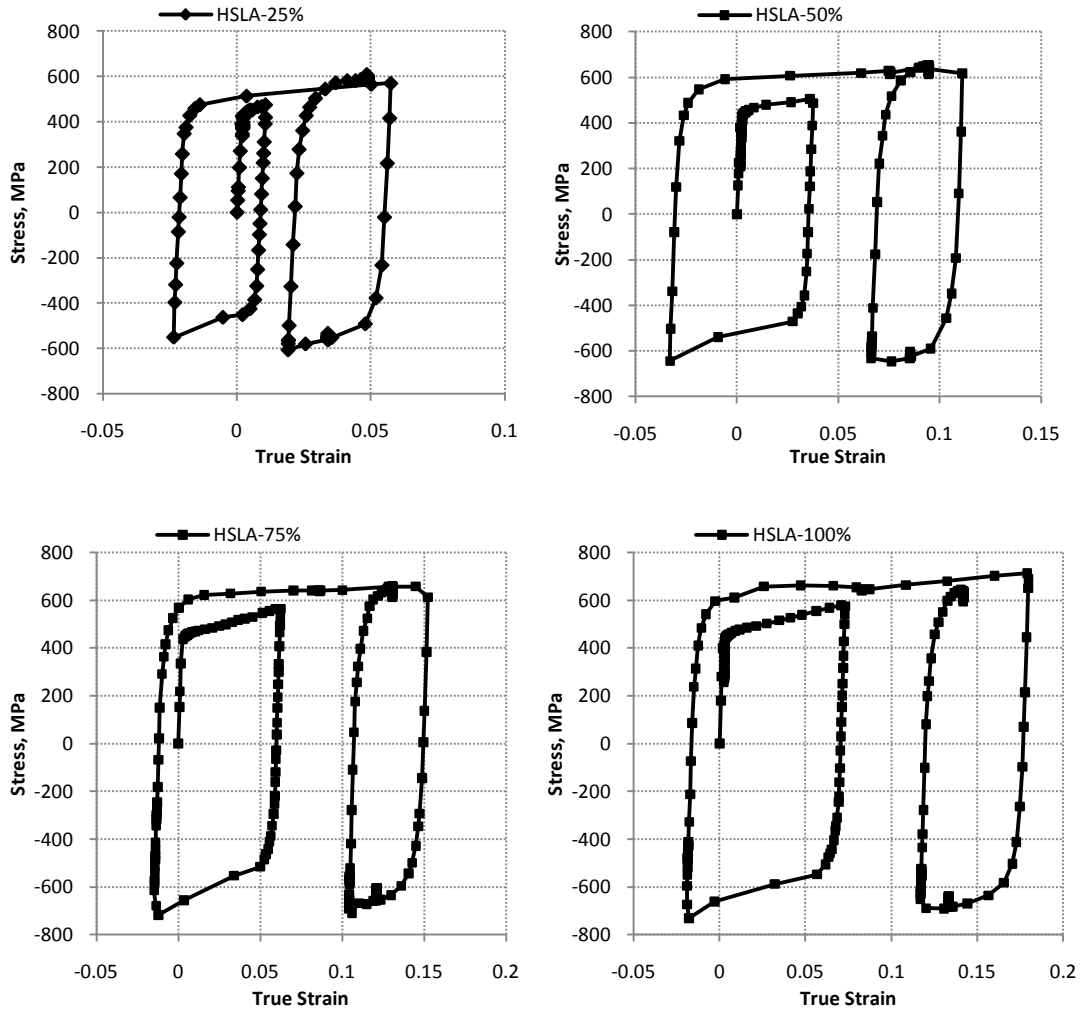
Fig. 6.11. The stress-strain history of HSLA at different drawbead penetrations
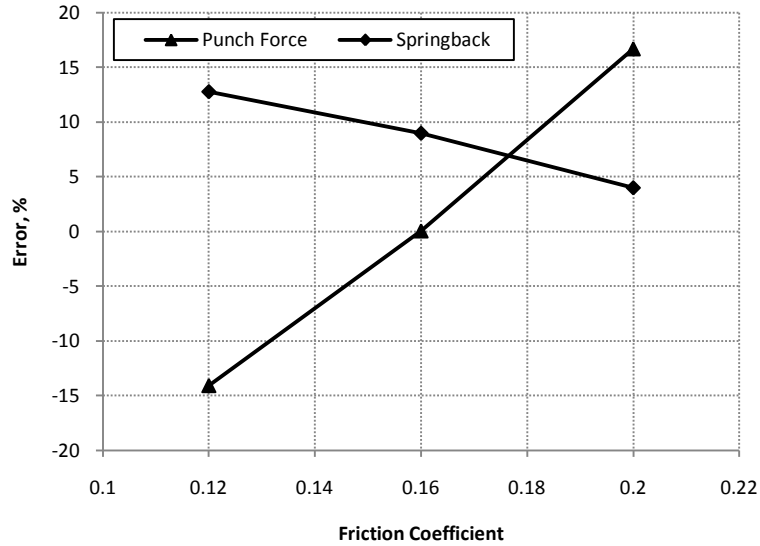
Fig. 6.12. The effect of friction on the accuracy of punch force and springback prediction for HSLA at 100% drawbead penetration

Figs. 6.13-6.14 compare the predicted sidewall profiles obtained with the IH, IH+NKH and YU models with the AA6022 experimental profiles. Fig. 6.15 also shows the error in springback for each model. For the IH and IH+NKH models, the error decreases somewhat at 50% drawbead penetration, then starts to increase as the drawbead penetration increases. For the YU model, the error for AA6022 is close to the error for DP600 and HSLA at shallow drawbead penetrations. In general, the springback errors associated with the YU and IH+NKH models are almost the same for AA6022. Therefore, it seems that the IH+NKH model is adequate for predicting the springback of AA6022 in this benchmark because this model predicts the material behaviour of AA6022 fairly well (see Fig. 5.34). It should be mentioned that the transient region is not described very well by the IH+NKH model, and therefore, the YU model may be able to improve the springback prediction in certain die geometries, e.g. small ratios of die radius to sheet thickness (R/t). In summary, the YU model does not improve the springback prediction for AA6022 in this BM3 problem. At deeper penetrations, the error increases for both the IH+NKH and YU models but this may be improved with the help of more friction data and by using cyclic stress-strain data obtained at larger strains and with more stress reversals, as discussed in the previous paragraph for HSLA.
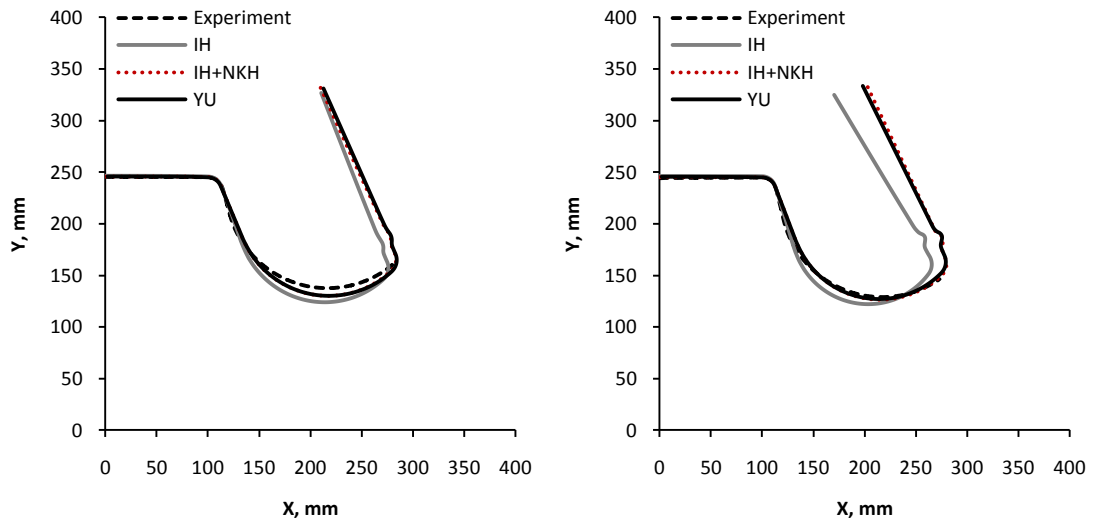
Fig. 6.13. The effect of hardening model on the simulated springback profile of AA6022 channel sections at 25% (left) and 50% (right) drawbead penetrations
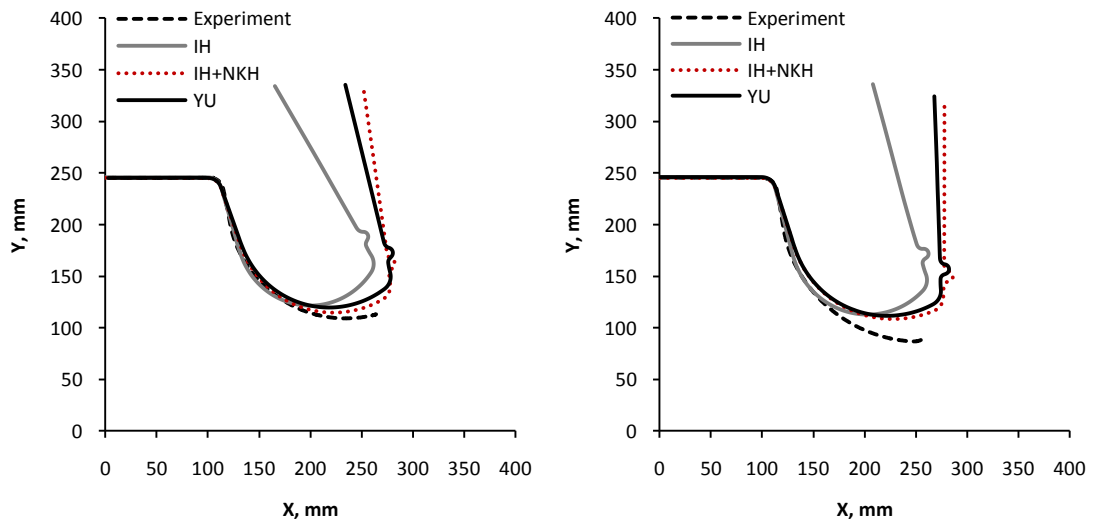
Fig. 6.14. The effect of hardening model on the simulated springback profile of AA6022 channel sections at 25% (left) and 50% (right) drawbead penetrations
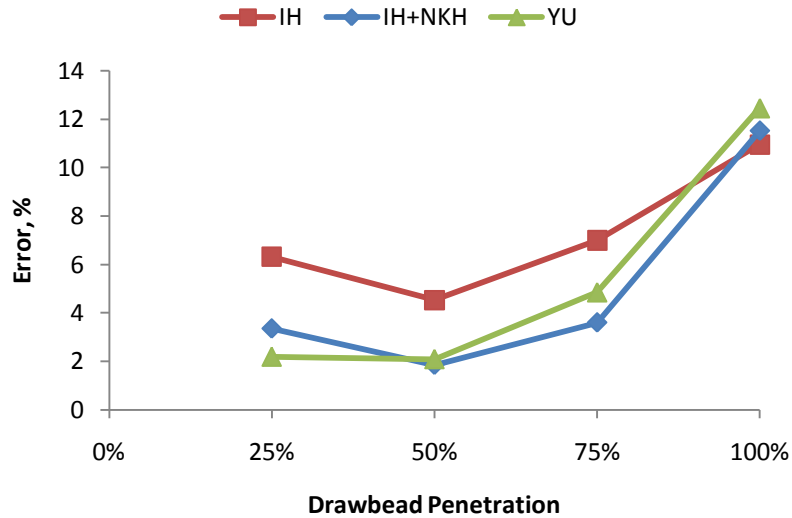
Fig. 6.15. The error in springback with respect to drawbead penetration for AA6022

6.2. Loading Path:

In general, the accuracy of the springback sidewall profile predicted with the IH+NKH model depends not only on the material behaviour but also on the loading path. For instance, the IH+NKH model is not able to accurately reproduce the behaviour of DP600 at the beginning of the reverse loading (see Fig. 5.31). If the strain path changes shortly after the first reverse loading, the stress will be overestimated by the model. In addition, if the strain path changes several times shortly after each loading reversal, the stress error will be accumulated and a larger discrepancy will be observed between the simulation and the experiment. However, as can be seen in Fig. 5.31, the stress-strain curve predicted with the IH+NKH model will eventually coincide with the experimental stress-strain curve. So, it seems that it is more important to capture the permanent behaviour of the material in order to accurately predict springback in this problem. Generally, when there is little tension in the channel sidewall, the magnitude of the plastic strain in the sidewall does not increase significantly after the last load reversal. So, the final stress-strain state of the material lies in the transient region of material response. In this case, it

164

is important that the hardening model be able to capture the transient response of the material. However, a large blank holder force, a greater drawbead restraining force and/or a large coefficient of friction may cause significant tension in the sidewall, which in turn increases the magnitude of strain in the sheet. The higher tension in the sidewall after the last loading reversal causes the stress to increase beyond the Bauschinger transient region, and in this case, it is important for the constitutive model to describe the permanent work hardening behaviour of the material.

6.3. Radius-to-Thickness Ratio:

Another condition which makes it essential to reproduce the transient behaviour is when the die radius-to-sheet thickness ratio is small. For a small die radius, the material is subjected to severe bending-unbending over the die radius, and as a result, the material may yield during springback [55]. So, the early re-yielding must be accurately described by the constitutive model. It is interesting to note that in this benchmark, the radius-to-sheet thickness ratio in the drawbead region is small, while the die radius-to-sheet thickness ratio is relatively large. It would appear then, that capturing the early re-yielding is not as important as the permanent hardening when severe bending-unbending takes place prior to the last load reversal over a large die radius.

Chapter 7

Conclusions

7.1. Summary:

In this work, the springback of a channel draw process, i.e. Benchmark #3 of NumiSheet 2005, was predicted by ABAQUS commercial software package. In order to describe the cyclic material behaviour, two different numerical algorithms were developed for numerical implementation of Yoshida-Uemori two-surface plasticity model. The first algorithm uses the governing parameter method, in which all equations are written in terms of only one unknown, and a semi-implicit integration scheme along with Hill's quadratic yield function. The second algorithm uses a fully-implicit integration scheme and assumes a general equation for the yield function. Depending on the number of stress components, this approach needs to solve several equations simultaneously. For a 3D stress space, the second algorithm needs to solve nineteen equations simultaneously: one equation for the yield function, six equations for the stress, six equations for $\boldsymbol{\beta}$ and six equations for $\boldsymbol{\theta}$. However, all equations are written in terms plastic strain increment and the procedure is summarized to solving only one nonlinear equation. So, the first approach is simpler, more computational effective and more robust. These algorithms were implemented as user-material subroutines for both ABAQUS/Standard and ABAQUS/Explicit. Both Hill's 1948 quadratic yield function and the Yld2000-2d yield function were used in the fully-implicit subroutines. Several problems were used to verify the implementation of these user subroutines. The main disadvantage of semi-implicit approach is that a small increment size should be used with

this algorithm. However, the fully-implicit approach is more stable at large increment sizes. Therefore, it can be generally suggested to use the semi-implicit approach with ABAQUS/Explicit and the semi-implicit approach with ABAQUS/Standard. The user subroutines were used to simulate the springback of benchmark#3.

Four different materials were used in the benchmark. In order to find the material constants, two types of tests were performed on these materials: *a)* cyclic tension-compression test and *b)* cyclic simple shear test. Since simple shear test was able to carry out the test at larger strain magnitudes, the stress-strain data obtained by this method were used to identify the material parameters associated with YU model. The r-values and yield stress in different directions were also used to obtain the material parameters associated with the yield function.

Finally, three different hardening models were used to simulate the benchmark: *a)* isotropic hardening, *b)* combined isotropic-nonlinear kinematic hardening, *c)* YU model. Moreover, the effect of yield function on the accuracy of springback prediction was studied for AA6022. Both Hill-48 and Yld2000-2d yield functions were used to simulate BM3 for AA6022.

7.2. Conclusions:

In summary, the following conclusions can be drawn from this work:

1. If a sufficiently fine mesh is used, the first-order solid element and shell element will result in almost the same predicted springback profiles.
2. When using shell elements, the required NIP depends not only on the material but also on the drawbead penetration. It appears that 9 integration points is sufficient for HSLA and AA6022. However, 29 and 49 integration points are required for AKDQ and DP600, respectively.

3. The coefficient of friction has a minor effect on the predicted springback profile at shallow penetrations. However, it does have a more noticeable influence on the predicted profile at deeper penetrations.

4. IH model overpredicts the springback as it does not take the cyclic plasticity phenomena into account.

5. The decrease of unloading modulus has a significant effect on the amount of springback and it is needed to be taken into account for an accurate prediction of springback.

6. IH+NKH model is able to predict the springback of AA6022 and DP600 fairly well. The profiles predicted by the YU model are very close to those obtained by the combined IH+NKH model for these materials.

7. The YU model significantly improves springback prediction for HSLA compared to the IH+NKH model.

8. None of these hardening models are able to accurately predict the springback for AKDQ. One important reason for this is that the simple shear cyclic curve was used to identify the material constants.

9. The predicted springback for AKDQ by the YU model is even larger than that obtained by the IH model which is due to the plastic deformation during springback. So, it seems that the assumption of a constant size of yield surface is not very accurate for AKDQ which has very little Bauschinger effect, a large amount of workhardening and low strength.

10. Using the Yld2000-2d yield function does not improve the springback simulation for AA6022 at large drawbead penetrations mainly because the yield stress for this material does not changes significantly at different orientations.

11. The predicted springback profile depends on the material constants which are obtained by fitting the simulation curve to that of experimental cyclic material behaviour. So, the number of cycles and the strain level in the experimental cyclic material response affects the simulated springback profile. In other words, even if the springback profile is predicted well in one particular case, e.g. shallow drawbead penetration, there is no guarantee that the predicted profile is accurate in other cases, e.g. deep drawbead penetration.

12. The error associated with numerical integration with the semi-implicit scheme increases at larger strain increments; while the error is smaller for the fully-implicit scheme at larger increments.

13. The YU model is able to accurately reproduce the material behaviour. However, it seems that it doesn't accurately predict the springback of materials with little or no Bauschinger effect such as AKDQ. So, YU model is especially suitable for prediction of springback of materials showing a considerable amount of Bauschinger effect and workhardening stagnation such as HSLA.

14. When there is a large tension in the sheet, the permanent response of material is more important to be captured compared to the transient behaviour for an accurate prediction of springback. The IH+NKH model is usually able to describe the permanent behaviour of material, especially the material with no workhardening stagnation.

References:

[1]   Ayres RA. A Process to Reduce Sidewall Curl Springback in High-Strength Steel Rails. Journal of Applied Metalworking 1984; 3:127–34.

[2]   Hishida Y, Wagoner RH. Experimental Analysis of Blank Holding Force Control in Sheet Forming. Journal of Materials and Manufacturing 1993; 2:409-415.

[3]   Sunseri M, Cao J, Karafillis AP, Boyce MC. Accommodation of Springback Error in Channel Forming Using Active Binder Force Control: Numerical Simulations and Results. ASME Journal of Engineering Materials and Technology 1996; 118:426–435.

[4]   Cao J, Kinsey B, Solla SA. Consistent and minimal springback using a stepped binder force trajectory and neural network control. ASME Journal of Engineering Materials and Technology 2000; 122:113-118.

[5]   Liu G, Lin Z, Bao Y, Cao J. Eliminating springback error in U-shaped part forming by variable blankholder force. Journal of Materials Engineering and Performance 2002; 11:64-70.

[6]   Huang M, Brouwer J. Characterization and control of the springback of advanced high strength steel. In: Proceedings of the Materials Science and Technology Conference, Vol. 4, 2005, p. 3-14.

[7]   Gan W, Wagoner RH. Die design method for sheet springback. International Journal of Mechanical Sciences 2004; 46:1097–1113.

[8]   Karafillis AP, Boyce MC. Tooling design accommodating springback errors. Journal of Materials Processing Technology 1992; 32:499–508.

[9]   Bayraktar E, Altintas S. Square cup deep drawing and 2d-draw bending analysis of Hadfield steel. Journal of Materials Processing Technology 1996; 60:183–190.

[10]   Chou I, Hung C. Finite element analysis and optimization on springback reduction. International Journal of Machine Tools & Manufacture 1999; 39:517–36.

[11]   Karafillis AP, Boyce MC. Tooling design in sheet metal forming using springback calculations. International Journal of Mechanical Sciences 1992; 34:113–31.

[12] Karafillis AP, Boyce MC. Tooling and binder design for sheet metal forming processes compensating springback error. International Journal of Machine Tools & Manufacturing 1996; 36:503–26.

[13] Buranathiti T, Cao J. An effective analytical model for springback prediction in straight flanging processes. International Journal of Materials & Product Technology 2004; 21:137-53.

[14] Yi HK, Kim DW, Van Tyne CJ, Moon YH. Analytical prediction of springback based on residual differential strain during sheet metal bending. Journal of Mechanical Engineering Science 2008; 222:117-29.

[15] Zhang D, Cui Z, Ruan X, Li Y. An analytical model for predicting springback and side wall curl of sheet after U-bending. Computational Materials Science 2007; 38:707-715.

[16] Lee MG, Kim JH, Chung K, Kim SJ, Wagoner RH, Kim HY. Analytical springback model for lightweight hexagonal close-packed sheet metal. International Journal of Plasticity 2009; 25:399-419.

[17] Li KP, Carden WP, Wagoner RH. Simulation of springback. International Journal of Mechanical Sciences 2002; 44:103-122.

[18] Wagoner RH, Li M. Simulation of springback: Through-thickness integration. International Journal of Plasticity 2007; 23:345-360.

[19] Lee SW, Yang DY. An assessment of numerical parameters influencing springback in explicit finite element analysis of sheet metal forming process. Journal of Materials Processing Technology 1998; 80:60–67.

[20] Mattiasson K, Thilderkvist P, Strange A, Samuelsson A. Simulation of springback in sheet metal forming. In: Proceedings of NUMIFORM95, Balkema, Rotterdam, The Netherlands, 1995, p.115–124.

[21] Zhan M, Yang H, Huang L. A numerical-analytic method for quickly predicting springback of numerical control bending of thin-walled tube. Journal of Materials Science and Technology 2006; 22:713.720.

[22] Lee MG, Kim D, Wagoner RH, Chung K. Semi-analytic hybrid method to predict springback in the 2D draw bend test. Transactions of the ASME, Journal of Applied Mechanics 2007; 74:1264-1275.

[23] Green DE. Description of NumiSheet 2005 Benchmark #3 Stage-1: Channel Draw with 75% Drawbead Penetration. In: Proceedings of NumiSheet 2005, CP778 Volume B, American Institute of Physics, p. 894-904.

[24] Wu HC. Continuum mechanics and plasticity, Chapman & Hall/CRC Press, 2005.

[25] Khan A, Huang SH. Continuum theory of plasticity. John Wiley & Sons Inc., NY, 1995.

[26] Hosford WF. A generalized isotropic yield criterion. Journal of Applied Mechanics 1972; 39:607-609.

[27] Hill R. The mathematical theory of plasticity. Oxford: Oxford University Press, 1951.

[28] Kojić M, Bathe KU. Inelastic Analysis of Solids and Structures. Springer, Berlin, 2005.

[29] Logan RW, Hosford WF. Upper-Bound Anisotropic Yield Locus Calculations. International Journal of Mechanical Sciences 1980; 22:419-430.

[30] Hill R. Theoretical plasticity of textured aggregates. Mathematical Proceedings of the Cambridge Philosophical Society 1979; 85:179–191.

[31] Barlat F, Brem JC, Yoon JW, Chung K, Dick RE, Lege DJ, Pourboghrat F, Choi SH, Chu E. Plane stress yield function for aluminum alloy sheets-part 1: theory. International Journal of Plasticity 2003; 19:1297–1319.

[32] Kuwabara T, Morita Y, Miyashita Y, Takahashi S. Elastic–plastic behavior of sheet metal subjected to in-plane reverse loading. Proceedings of Plasticity'95, Dynamic Plasticity and Structural Behavior, Gordon and Breach.

[33] Boger RK, Wagoner RH, Barlat F, Lee MG, Chung K. Continuous, large strain, tension/compression testing of sheet material. International Journal of Plasticity 2005; 21: 2319-2343.

[34] Yoshida F, Uemori T, Fujiwara K. Elastic-plastic behavior of steel sheets under in-plane cyclic tension-compression at large strain. International Journal of Plasticity 2002; 18: 633-659.

[35] Miyauchi K. A proposal of a planar simple shear test in sheet metals. Scientific Papers of the Institute of Physical and Chemical Research 1984; 78(3): 27–40.

[36] Miyauchi K. Bauschinger effect in planar shear deformation of sheet metals. Advanced Technology of Plasticity 1984; 1: 623–682.

[37] Genevois P. Etude expérimentale et modélisation du comportement plastique anisotrope de tôles d'acier en grandes déformations. PhD Thesis, Institut National Polytechnique de Grenoble, France, 1992.

[38] Rauch EF. Plastic anisotropy of sheet metals determined by simple shear tests, Journal of Material Science and Engineering 1998; 241: 179-183.

[39] Barlat F, Ferreira Duarte JM, Gracio, JJ, Lopes AB, Rauch EF. Plastic flow for nonmonotonic loading conditions of an aluminum alloy sheet sample. International Journal of Plasticity 2003; 19: 1215-1244.

[40] Yoshida F, Uemori T. A model of large-strain cyclic plasticity describing the Bauschinger effect and workhardening stagnation. International Journal of Plasticity 2002; 18: 661-686.

[41] Dunne F, Petrinic N. Introduction to Computational Plasticity. Oxford University press, 2005.

[42] Prager W. A New method of analyzing stresses and strains in work hardening plastic solids. Journal of Applied Mechanics 1957; 23:493–496.

[43] Ziegler H. A modification of Prager's hardening rule. Quarterly of Applied mathematics 1959; 17:55–65.

[44] Armstrong PJ, Frederick CO. A Mathematical representation of the multiaxial Bauschinger effect. G.E.G.B Report RD/B/N731, 1966.

[45] Chaboche JL. Time-independent constitutive theories for cyclic plasticity. International Journal of Plasticity 1986; 2:149-88.

[46] Ohno N, Wang JD. Kinematic hardening rules with critical state of dynamic recovery, part I: formulations and basic features for ratcheting behaviour. International Journal of Plasticity 1993; 9:375–390.

[47] McDowell DL. Stress state dependence of cyclic ratcheting behavior of two rail steels. International Journal of Plasticity 1995; 11:397–421.

[48] Jiang Y., Sehitoglu H. Modeling of cyclic ratcheting plasticity, part I: development of constitutive relations. ASME Journal of Applied Mechanics 1996; 63:720–725.

[49] Chun BK, Jinn JT, Lee JK. Modeling the Bauschinger effect for sheet metals, Part I: Theory. International Journal of Plasticity 2002; 18:571-595.

[50] Chun BK, Jinn JT, Lee JK. Modeling the Bauschinger effect for sheet metals, Part II: Applications. International Journal of Plasticity 2002; 18:597-616.

[51] Dafalias YF, Popov EP. Plastic internal variables formalism of cyclic plasticity. Journal of Applied Mechanics 1976; 98: 645-651.

[52] Krieg RD. A practical two surface plasticity theory. Journal of Applied Mechanics, Transactions of the ASME 1975; 47: 641-646.

[53] Geng LM, Wagoner RH. Springback analysis with a modified hardening model. SAE Technical Paper 2000-01-0768, Sheet Metal Forming: Sing Tang 65th Anniversary Volume, SP-1536, SAE.

[54] Geng L, Wagoner RH. Role of plastic anisotropy and its evolution on springback. International Journal of Mechanical Sciences 2002; 44:123–148.

[55] Yoshida F, Uemori T. A model of large-strain cyclic plasticity and its application to springback simulation. International Journal of Mechanical Sciences 2003; 45: 1687-1702.

[56] Lee M, Kim D, Kim C, Wenner ML, Wagoner RH, Chung K. A practical two-surface plasticity model and its application to spring-back prediction, International Journal of Plasticity 2007; 23: 1189-1212.

[57] McDowell DL. A two surface model for transient nonproportional cyclic plasticity. II. Comparison of theory with experiments. Transactions of the ASME, Journal of Applied Mechanics 1985; 52:303-308.

[58] Ohno N, Kachi Y. A constitutive model of cyclic plasticity for nonlinear hardening materials. ASME Journal of Applied Mechanics 1986; 53:395–403.

[59] Ohno N, Satra M. Detailed and simplified elastoplastic analysis of a cyclically loaded notched bar. ASME Journal of Engineering and Materials Technology 1987; 109:194–202.

[60] Xianjie Y, Qing G, Xunfang S. A study on two-surface multiaxial constitutive model of cyclic plasticity. Acta Mechanica Sinica 1993; 25:569-574.

[61] Iwata K. A two-surface cyclic plasticity model consistent with fundamental stress-strain equations of the power-law type. Nuclear Engineering and Design 1993; 139:319-326.

[62] White CS. Two surface plasticity model with bounding surface softening. ASME Journal of Engineering Materials and Technology 1996; 118:137-42.

[63] Suprun AN. A constitutive model with three plastic constants: The description of anisotropic work-hardening. International Journal of Plasticity 2006; 22:1217–1233.

[64] Choi Y, Han C, Lee JK, Wagoner RH. Modeling multi-axial deformation of planar anisotropic elasto-plastic materials, part I: Theory. International Journal of Plasticity 2006; 22:1745–1764.

[65] Choi Y, Han C, Lee JK, Wagoner RH. Modeling multi-axial deformation of planar anisotropic elasto-plastic materials, part II: Applications. International Journal of Plasticity 2006; 22:1765–1783.

[66] Rousset M. Surface Seuil de Plasticite: Determination Automatique et Modelisation. Ph.D. Thesis, Universite Paris 6, Paris, 1985.

[67] Phillips A, Tang JL. The effect of the loading path on the yield surface at elevated temperatures. International Journal of Solids and Structures 1972; 8:463–474.

[68] Wu HC, Yeh WC. On the experimental determination of yield surfaces and some results of annealed 304 stainless steel. International Journal of Plasticity 1991; 7:803–826.

[69] Khan AS, Wang X. An experimental study on subsequent yield surface after finite shear prestraining. International Journal of Plasticity 1993; 9:889–905.

[70] Francois M. A plasticity model with yield surface distortion for non proportional loading. International Journal of Plasticity 2001; 17:703–717.

[71] Vincent L, Calloch S, Kurtyka T, Marquis D. An improvement of multiaxial ratcheting modeling via yield surface distortion. ASME Journal of Engineering Materials and Technology 2002; 124:402–411.

[72] Vincent L, Calloch S, Marquis D. A general cyclic plasticity model taking into account yield surface distortion for multiaxial ratcheting. International Journal of Plasticity 2004; 20:1817–1850.

[73] Chung K, Richmond O. A deformation theory of plasticity based on minimum plastic work paths. International Journal of Plasticity 1993; 9: 907-920.

[74] Yoon JW, Yang DY, Chung K. Elasto-plastic finite element method based on incremental deformation theory and continuum based shell elements for planar anisotropic sheet materials. Computer Methods in Applied Mechanics and Engineering 1999; 174:23-56.

[75] Han CS, Chung K, Wagoner RH, Oh SI. A multiplicative finite elasto-plastic formulation with anisotropic yield functions. International Journal of Plasticity 2003; 19:197-211.

[76] Hasegawa T, Yakou T. Deformation behaviour and dislocation structures upon stress reversal in polycrystalline aluminum. Journal of materials science and engineering. 1975; 20: 267‑276.

[77] Christodoulou N, Woo OT, MacEwen SR. Effect of stress reversals on the work hardening behaviour of polycrystalline copper. Acta Metallurgica 1986; 34:1553‑1562.

[78] Dunne F, Petrinic N. Introduction to Computational Plasticity. Oxford University press, 2005.

[79] Simo JC, Taylor RL. A return mapping algorithm for plane stress elastoplasticity. Journal for Numerical Methods in Engineering 1986; 22:649-670.

[80] Simo JC, Hughes TJR, Computational Inelasticity, Springer-Verlag, Berlin, 1998.

[81] Luo L, Ghosh A. Elastic and inelastic recovery after plastic deformation of DQSK steel sheet. Transactions of the ASME, Journal of Engineering Materials and Technology 2003; 125: 237-246.

[82] Levy BS, Van Tyne CJ, Moon YH, Mikalsen C. The Effective Unloading Modulus for Automotive Sheet Steels. Proceeding of SAE 2006 World Congress & Exhibition, Detroit, MI, USA.

[83] Benito JA, Jorba J., Manero JM, Roca A. Change of Young's modulus of cold-deformed pure iron in a tensile test. Metallurgical and Materials Transactions A: Physical Metallurgy and Materials Science 2005; 36:3317-3324.

[84] Yang M, Akiyama Y, Sasaki T. Evaluation of change in material properties due to plastic deformation. Journal of Materials Processing Technology 2004; 151:232–236.

[85] Cleveland RM, Ghosh AK. Inelastic effects on springback in metals. International Journal of Plasticity 2005; 18:769–785.

[86] Morestin F, Boivin M. On the necessity of taking into account the variation in the Young modulus with plastic strain in elastic-plastic software. Nuclear Engineering and Design 1996; 162:107 116.

[87] Hibbitt, Karlsson & Sorensen, ABAQUS 6.9 users manual.

[88] Toropov VV, Filatov AA, Polynkin AA. Multiparameter structural optimization using FEM and multipoint explicit approximates. Structural Optimization 1993; 6:7‑14.

[89] Yoshida F, Urabe M, Toropov VV. Identification of material parameters in constitutive model for sheet metals from cyclic bending tests. International Journal of Mechanical Science 1998; 40: 237‑249.

[90] Yoshida F. A constitutive model of cyclic plasticity. International Journal of Plasticity 2000; 16:359‑380.

[91] Yoon JW, Barlat F, Dick RE, Chung K, Kang TJ. Plane stress yield function for aluminum alloy sheets-part II: FE formulation and its implementation, International Journal of Plasticity 2004; 20:495–522.

177

[92] Green DE, Stoughton TB, Gnaeupel-Herold T, Iadicola MA, Foecke T. Influence of drawbeads in deep drawing of plane-strain channel sections. In: Proceedings of IDDRG'06, INEGI, Porto, Portugal, 2006, p. 559-566.

[93] Thuillier S, Manach PY. Comparison of the work-hardening of metallic sheets using tensile and shear strain paths, International Journal of Plasticity 2009; 25:733-75.

[94] Li KP, Geng LM, Wagoner RH. Simulation of springback with the draw/bend test. In: Proceedings of the Second International Conference on Intelligent Processing and Manufacturing of Materials, IPMM'99 (Cat. No.99EX296), vol. 1, 1999, pp. 91-104.

[95] Hu Y, Du C. Quasi static finite element algorithms for sheet metal stamping springback simulation. In: Proceedings of NUMISHEET '99, Besancon, France: University of Franche-Compte, 1999, pp. 71– 76.

[96] He N, Wagoner RH. Springback simulation in sheet metal forming. In: NUMISHEET '96, Ohio: The Ohio State University, 1996, p.308–315.

[97] Lee MG, Kim D, Kim C, Wenner ML, Chung K. Spring-back evaluation of automotive sheets based on isotropic–kinematic hardening laws and non-quadratic anisotropic yield functions, part III: applications. International Journal of Plasticity 2005; 21:915–953.

[98] Narasimhan N, Lovell M. Predicting springback in sheet metal forming: an explicit to implicit sequential solution procedure. Finite Elements in Analysis and Design 1999; 33:29-42.

[99] Ghaei A, Taherizadeh A, Green DE. The effect of hardening model on springback prediction for a channel draw process. Proceedings of NumiSheet 2008, Interlaken, Switzerland, 2008, p. 485-491.

[100] Reid JV. Twist compression evaluation of lubricants for NumiSheet 2005 Benchmarks, Private communication submitted to the NumiSheet 2005 Materials Characterization Committee, 2005.

Flow Chart A.1.

Semi-implicit numerical algorithm for implementation of YU model

---

1. Elastic Predictor

1.1. $\sigma^{Tr} = \sigma_n + D.\Delta\varepsilon$; $\eta^{Tr} = \sigma^{Tr} - \alpha_n$; $\alpha_{n+1} = \alpha_n$

1.2. Set $IsoFac_{n+1} = IsoFac_n$

Isotropic Factor=0 during workhardening stagnation

Isotropic Factor=1 during workhardening

1.3. Check for the yield condition:

- If $(\frac{3}{2}\eta^{Tr} N \eta^{Tr})^{0.5} - Y < 0$; then set $(\bullet)_{n+1} = (\bullet)^{Tr}$ and Exit.
- Else Goto step 2.

2. Plastic Corrector

2.1. Initialize:

- $\Delta p = 0$; $\eta_{n+1} = \eta^{Tr}$

2.2. Calculate the effective plastic strain:

- $h = k.(R_{sat} - R_n).IsoFac$; $R_{n+1} = R_n + h.\Delta p$; $a_{n+1} = B + R_{n+1} - Y$
- Use Eq. (14) to find η_{n+1}
- Use Eq. (15) to find Ξ
- Calculate the residual: $Res = (\frac{3}{2}\eta_{n+1} N \eta_{n+1})^{0.5} - Y$.
- If (Res < Tol), then Goto Step 3.
- Set $\Delta p = \Delta p - \frac{Res}{f'}$ where f' denotes the derivative of f with respect to Δp.
- Goto 2.2.

3. Update

- $\theta_{n+1} = \theta_n + C(\frac{a_{n+1}}{Y}.\eta_{n+1} - \sqrt{\frac{a_{n+1}}{\bar{\theta}_n}}.\theta_n)\Delta p$

- $\boldsymbol{\beta}_{n+1} = \boldsymbol{\beta}_n + k(\dfrac{b}{Y}.\boldsymbol{\eta}_{n+1} - \boldsymbol{\beta}_n\,)\Delta p$

- $\boldsymbol{\alpha}_{n+1} = \boldsymbol{\theta}_{n+1} + \boldsymbol{\beta}_{n+1}$

- $\boldsymbol{\sigma}_{n+1} = \boldsymbol{\eta}_{n+1} + \boldsymbol{\alpha}_{n+1}$

4. Workhardening Stagnation

- $Res = \dfrac{3}{2}(\boldsymbol{\beta}_{n+1} - \boldsymbol{q}_n\,)^T \boldsymbol{P}(\boldsymbol{\beta}_{n+1} - \boldsymbol{q}_n\,) - r_n^{\,2}$

- If ($Res > 0$) Then
  - If (*IsoFac*=0), then set *IsoFac*=1 and Goto Step 2.
  - Use Eq. (31) to find $\Delta\mu$.
  - Use Eq. (29) to update $\boldsymbol{q}$.
  - Use Eq. (26) to update r.
- Else
  - If (*IsoFac*=1), then set *IsoFac*=0 and Goto Step 2.
- EndIf

Flow Chart A.2

Fully-implicit numerical algorithm for implementation of YU model

---

1. Elastic Predictor

1.1. $\boldsymbol{\sigma}^{Tr} = \boldsymbol{\sigma}_n + \boldsymbol{D}\Delta\boldsymbol{\varepsilon}; \boldsymbol{\eta}^{Tr} = \boldsymbol{\sigma}^{Tr} - \boldsymbol{\alpha}_n; \boldsymbol{\alpha}_{n+1} = \boldsymbol{\alpha}_n$

1.2. Set $IsoFac_{n+1} = IsoFac_n$

   $IsoFac$ (Isotropic Factor) =0 during workhardening stagnation

   $IsoFac$ (Isotropic Factor)=1 during isotropic hardening

1.3. Check for the yield condition:

   - If $\bar{\eta} \leq Y$; then set $(\bullet)_{n+1} = (\bullet)^{Tr}$ and Exit.
   - Else Goto step 2.

2. Plastic Corrector

2.1. Initialize:

   - $\Delta p = 0; \boldsymbol{\eta}_{n+1} = \boldsymbol{\eta}^{Tr}$

2.2. Calculate the effective plastic strain, backstress and $\boldsymbol{\eta}$:

   - If $(IsoFac = 0$); then $R_{n+1} = R_n$
   - If $(IsoFac = 1$); then $R_{n+1} = R_{sat}(1 - e^{-k.p})$
   - $a_{n+1} = B + R_{n+1} - Y$
   - Use Eqs. (4.11) to calculate the residuals: $G_1, \boldsymbol{G}_2, \boldsymbol{G}_3, \boldsymbol{G}_4$
   - If ($G_1 \& \boldsymbol{G}_2 \& \boldsymbol{G}_3 \& \boldsymbol{G}_4$)<Tolerance; then Goto Step 3
   - Use Eq. (4.28b) to calculate $\boldsymbol{\Xi}^{-1}$
   - Solve Eqs. (4.12) simultaneously to find $d\Delta p; \Delta\boldsymbol{\sigma}; \Delta\boldsymbol{\theta}; \Delta\boldsymbol{\beta}$
   - Update: $(\Delta p)_{n+1} = (\Delta p)_n + d\Delta p ; p_{n+1} = p_n + \Delta p$
     $\boldsymbol{\beta}_{n+1} = \boldsymbol{\beta}_n + \Delta\boldsymbol{\beta}; \boldsymbol{\theta}_{n+1} = \boldsymbol{\theta}_n + \Delta\boldsymbol{\theta}; \boldsymbol{\alpha} = \boldsymbol{\beta} + \boldsymbol{\theta}$
     $\boldsymbol{\sigma}_{n+1} = \boldsymbol{\sigma}_n + \Delta\boldsymbol{\sigma}; \boldsymbol{\eta} = \boldsymbol{\sigma} - \boldsymbol{\alpha}$
   - Goto 2.2.

3. Workhardening Stagnation

- $Res = \frac{3}{2}[\boldsymbol{\beta}_{n+1} - \boldsymbol{q}_n]^T \boldsymbol{P}[\boldsymbol{\beta}_{n+1} - \boldsymbol{q}_n] - r_n^2$
- If ($Res > 0$) Then
  - If (*IsoFac*=0), then set *IsoFac*=1 and Goto Step 2.
  - Use Eq. (4.22) to find $\Delta\mu$.
  - Use Eqs. (4.19, 4.20) to update $\boldsymbol{q}$.
  - Use Eq. (4.17) to update r.
- Else
  - If (*IsoFac*=1), then set *IsoFac*=0 and Goto Step 2.
- EndIf

4. Consistent Tangent Modulus:

- Use Eq. (4.32) to calculate the consistent tangent modulus

VITA AUCTORIS

NAME   Abbas Ghaei

PLACE OF BIRTH   Esfahan, Iran

YEAR OF BIRHT   1979

EDUCATION   Chamran High School,Esfahan, Iran

                     1993-1997

                     University of Tabriz, Tabriz, Iran

                     1998-2002 B.A.Sc.

                     Sharif University, Tehran, Iran

                     2002-2004 M.A.Sc.

                     University of Windsor, Windsor, Ontario

                     2006-2009 Ph.D